Doctoral Dissertation

Università degli Studi di Genova
Istituto Italiano di Tecnologia

Doctorate in Sciences and Technologies of Chemistry and Materials

Curriculum: Nanochemistry

(XXXV)

Engineering of waste Biomass-based active materials for application in current Lithium-ion Batteries and Beyond

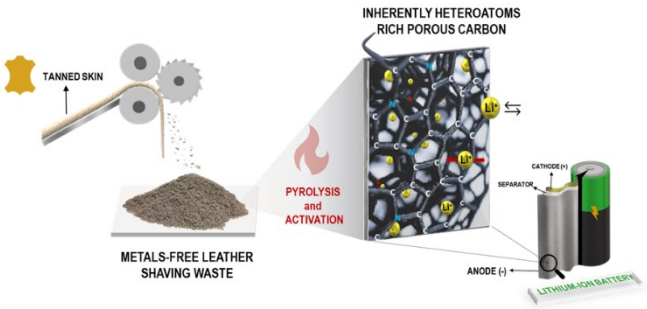

By

Pejman Salimi

Supervisor(s):
Prof. Remo Proietti Zaccaria
Prof. Paola Costamagna

March 2023

Abstract

The goal of the current thesis, which represents a significant collaborative effort between four institutions and universities (Italian Institute of Technology, University of Genoa, CA' Foscari University of Venice, and Hasselt University), is to summarize the most recent findings in the area of sustainable secondary batteries by utilizing various waste biomass through a specific carbonization treatment, or a waste-to-energy action. Since it is generally known that the components of conventional secondary batteries have an adverse effect on the environment, research on eco-friendly alternatives are both extremely desirable and necessary. In this respect, our work aims to make a significant advancement in this area, bringing us one step closer to practical lithium-ion batteries (LIBs) with minimal environmental impact.

Herein, we have tackled the sustainable batteries problem by breaking it down in its main parts, namely what kind of bio resources materials to exploit and their treatment to make them suitable to run as battery anode. Our materials choice was motivated by the desire to secondary use of waste biomass, would surely be beneficial both from an environmental and economical point of views.

In line with the philosophy of a reduced environmental impact, the engineering of biochar was based on steam and CO_2 activations, neither of them recognized as dangerous procedures. Additionally, for preparing fully sustainable and environmentally friendly LIBs anodes, deionized water and carboxymethyl cellulose (CMC) have been used as alternatives to toxic/teratogen N-methyl-2- pyrrolidone (NMP) and to biologically hazardous Polyvinylidene fluoride (PVdF), respectively. Furthermore, going towards reduced cost, we have employed water solvent and flouride-free bio-derived CMC binders. Indeed, to provide a scenario as complete as possible, the results achieved for half-cell batteries were also confirmed in a full battery configuration where $LiFePO_4$ (LFP), and sulfur cathodes were used, the latter being particularly attractive in the emerging field of sulfur-based batteries. All in all, we believe that the combination of these actions goes in the direction of the 2030 goal of having green LIBs at 100 \$ /kW h^{-1}. Last but not least, we have also provided a detailed comparison in terms of performance, where we highlight how our results outperform anything reported to date, with the intention of giving a general picture of the state-of-the-art in this field and with the desire for precise positioning of our results.

Keywords: Sustainability, Li-ion battery, Bio-based anodes, High-efficient, Next-generation batteries

ACKNOWLEDGEMENTS

I would like to express my sincere gratitude to my great supervisors Prof. Remo Proietti Zaccaria and Prof. Paola Costamagna for their patience, motivation, enthusiasm, and immense knowledge.

My completion of this project could not have been accomplished without the support of my collaborators at Università Ca' Foscari Venezia, and imo-imomec (UHasselt), Prof. Michela Signoretto, Dr. Somayeh Taghavi, Mr. Sebastiano Tieuli, Prof. Dries Vandamme, Prof. Momo Safari, Prof. An Hardy, Dr. Willem Vercruysse, Dr. Saeed Yari, and Mr. Amin Lataf.

I am also very thankful to all my colleagues including Dr. Eleonora Venezia, Dr. Mirko Prato, Dr. Silvio Fugattini, Dr. Susana Chauque, Dr. Lorenzo Carbone, Dr. Sergio Marras, Mr. Simone Lauciello, Mr. Luca Leoncino, Mr. Marco Ricci, and Ms. Shanshan Liang. Special thanks to my best friends Dr. Omid Norouzi, and Mr. Kasra Askari. We started this journey together and I had a great time with them in research on green batteries.

Last but not the least, I would like to thank my family, especially my parents, and beloved spouse *(Gorgeous Maryam)*. Their belief in me has kept my spirits and motivation high during this process.

Table of Contents

Chapter 1 . Lithium-ion batteries and Carbon: An integrated Approach to Green Energy Systems

1.1 Introduction

Before the invention of electric generators and electrical networks at the end of the 19th century, batteries served as the main source of electricity. They have a lengthy history, and their future evolution will likely be equally exciting. The historical timeline of the battery is schematically shown in Figure 1.1. A negative electrode, a positive electrode, an electrolyte, and a separator make up a battery cell, which is primarily capable of generating energy through a chemical process. In 1799, the Italian scientist Alessandro Volta made the first battery [1]. Volta's battery included alternating disks of zinc and silver (or copper and pewter) separated by paper or cloth soaked either in salt water or sodium hydroxide, which was later named 'Volta pile'[1]. Following this invention, numerous efforts have been made to advance battery technology by introducing novel chemistry, processes, and materials. Until now, many types of batteries including primary batteries (non-rechargeable) such as Alkaline, Zin-Carbon, Magnesium, etc., and secondary batteries (re-chargeable) such as Lead–acid, Nickel-Cadmium, Lithium-ion batteries, etc., have been developed and used in various applications. However, among them, lithium-ion technology has attracted considerable attention, owing to its electrochemical rechargeability, high energy density, long cycling life, acceptable rate feature, and no memory effect [2]. Figure 1.2 illustrates the history of the early development of LIBs following their introduction to the market by Sony in 1991.

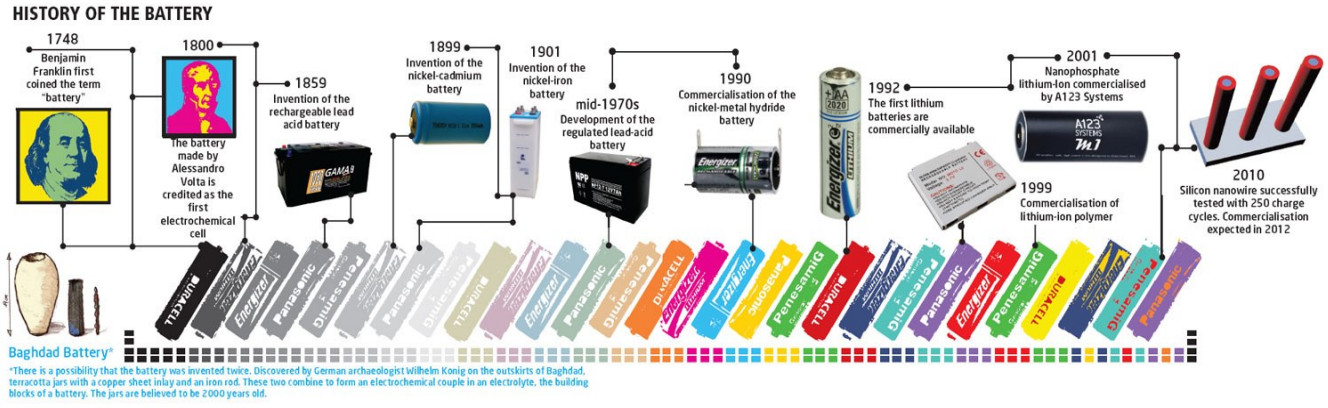

Figure 1.1. The historical timeline of the battery (https://www.upsbatterycenter.com/blog/history-batteries-timeline/).

Figure 1.2. Brief history of LIBs commercialization by 1991 [3].

The basics of electrochemical cells, the operation of LIBs, electrochemical processes, and the size of the global LIBs market are covered in this chapter. Henceforth, an overview of carbonaceous materials in electrochemical energy storage devices (EESDs) is provided.

1.2 Fundamental of Electrochemical cells

1.2.1 what are the parts of an electrochemical cell?

The figure below (Figure 1.3) shows a schematic cross-section of an electrochemical cell. Although a lithium-ion cell construction is presented below, electrochemical cells generally feature the same parts. In an electrochemical cell, the negative electrode is often a metal or an alloy. This electrode undergoes oxidation and releases electrons to the external circuit during the discharge process. Oxidation is the process through which a molecule, atom, or ion loses electrons during a reaction. On the other side, the negative electrode is decreased during recharging. It means that this electrode accepts electrons from the external circuit. During the discharge process, the negative electrode is also technically known as the anode electrode because the anode is the electrode that provides electrons where the chemical reaction takes place. Nevertheless, during charge process, the negative part gains electrons and is technically defined as the cathode. It is worth noting that, in the literature, the negative electrode refers often to the anode, and the positive electrode means cathode. The positive electrode in an electrochemical system typically contains metal oxides, metal sulfides, or oxygen. During the discharging process the positive electrode gains electrons from the external circuit, while during the re-charging cell it gives up electrons to the external circuit [4].

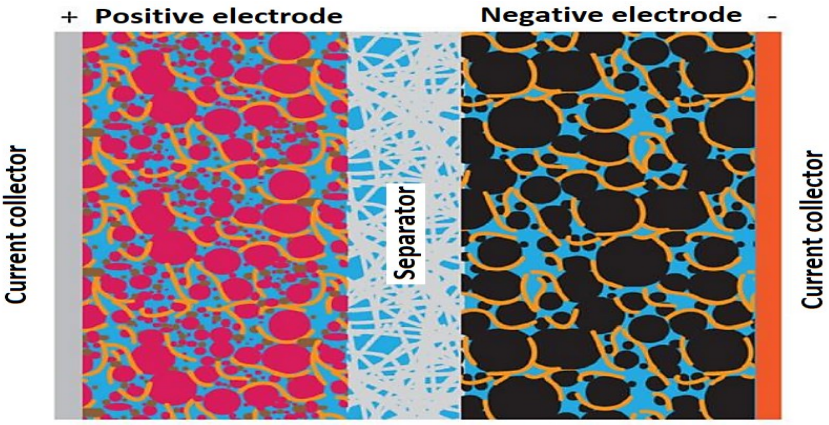

Figure 1.3. Schematic cross-section of an electrochemical cell.

Another component of an electrochemical cell is the electrolyte, which provides an internal medium for the movement of ions between the negative and positive electrodes during electrochemical reactions. The electrolyte typically consists of dissolved chemicals such as acid,

base, or salt in a solvent. The chemicals must disassociate into positive and negative ions. To prevent self-discharge, the electrolyte also needs to be an electronic insulator and an ion conductor. In most cases, the electrolyte medium acts as a medium for the movement of ions from one internal side of the cell to the other, but not for the passage of electrons. Instead, the electron follows a path that is not inside the cell. There is something between two electrodes of the cell known as the separator. Separator is an electronic insulator and thin permeable membrane with large enough pores that allow Li ions to pass through. This membrane is a crucial feature of the cell because it keeps the cathode and anode electrode particles from coming into touch physically, ensuring the safety of the cell (which would short-circuit the cell). Current collectors are yet another crucial component of an electrochemical cell. Current collectors are usually metal foils that collect electrical current generated at the electrodes. It should be noted that electrode materials are often powder form and could not directly attach to the external terminal of the cell [5].

1.2.2 Battery Specifications

The background terminology that is essential for comprehending battery operation and performance will be introduced in this section. In order to accurately define battery cells or battery packs, it is imperative for battery researchers to develop a common language [https://e-lyte-innovations.de].

Cell

Cell is the smallest electrochemical unit that delivers a voltage. This voltage can be used to power a load. The voltage of the cell is determined by the chemistry employed to create the battery components. Primary and secondary cells come in two different varieties. Although the secondary cells allude to rechargeable cells, the primary cells are not. It should be emphasized that a cell and a battery are not the same thing. A battery technically consists of many cells that are connected in series, parallel, or sometimes even series and parallel. Nevertheless, the terms "cell" and "battery" are frequently used synonymously by ordinary people and even researchers. For instance, six 2 V lead-acid cells are connected in series to form a single typical automotive lead-acid battery (12 V) [4,6].

Nominal voltage and capacity

The amount of energy that drives each moving electron is known as voltage. The voltage of a (cell) battery is determined by the mixture of active substances in the cathode and anode as well as the

level of charge. The nominal voltage of a battery is a typical voltage or average voltage of a battery cell, which is between the fully charged voltage and a fully discharged voltage. On the other hand, voltage is rather energy per unit of charge. The voltage of a typical alkaline, nickel-based secondary, and the majority of lithium-based cells is 1.2, 1.2-1.5, and over 3 V, respectively [https://electricalschool.org].

Another crucial term related to battery cells is capacity. The capacity of a battery, which is measured in ampere-hours (Ah), represents the maximum amount of energy that can be extracted from the battery under certain condition [7]. In other words, capacity refers to the amount of energy a battery can store and release during discharge. The battery capacity is affected by the following factors:

- Type, chemistry, weight, density, and size of the electrodes
- Electrolyte
- Temperature
- Charge and discharge rates

State of charge (SOC) and Depth of discharge (DOD)

SOC conveys the battery's level of charge in relation to its capacity. SOC is expressed as %. 100% indicates that the battery is fully charged, whereas 0% indicates that the battery is completely empty. A different type of SOC that displays the level of discharge is depth of discharge (DOD) [8].

Open-circuit voltage (OCV)

OCV is the electrical potential difference between two device terminals while there is no load being applied. The battery's state of charge, state-of-charge, cell assembly, temperature, etc. all affect the open-circuit voltage [9].

Power density and energy density

Energy density (Wh kg^{-1}) refers to the amount of energy in a given mass (or volume) whereas power density (W kg^{-1}) means the amount of energy flow per unit of mass (area, and volume) and per unit of time. An energy-dense system can store a lot of energy in a small volume of matter. A high energy density does not necessarily mean a high-power density [https://energyeducation.ca]. A battery with a high energy density with low power density is able to perform for a longer period

in comparison with capacitor with high power density and low energy density [10]. Figure 1.4 depicts the Ragone plot for different energy storage systems. Ragone plot demonstrates the relationship between energy and power density and according to this, the electrochemical storage devices need to be improved from the energy and power density points of view to competing with combustion engines [11].

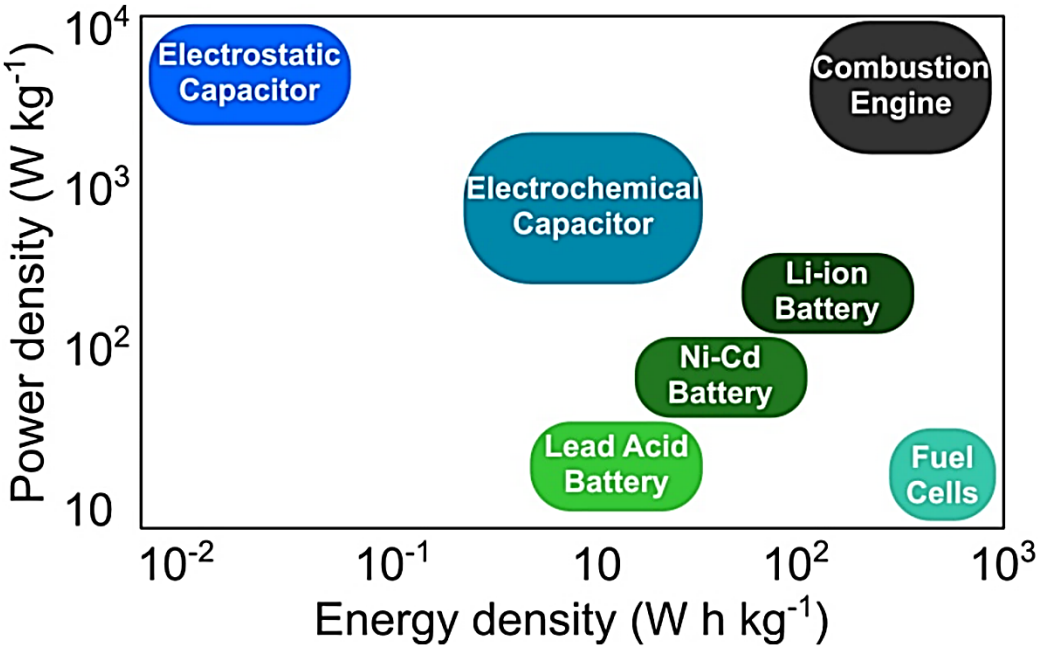

Figure 1.4. Ragone plot for various energy storage systems [11].

C-rate

The C-rate of a battery cell is the level of constant current charge or discharge which is used to measure the speed at which a battery is fully charged or discharged. In theory, charging at a C-rate of 1C means that the battery is charged from 0-100% in one hour. 4C-rate means that the full charge of a battery cell takes 15 minutes [5]. When the theoretical capacity of the researched material is unknown, current density per unit of mass (mA/g) is a frequent alternative to C-rate for expressing the rate of charging and discharging.

Coulombic efficiency (CE)

A general definition of CE, this parameter expresses the ratio of discharge capacity overcharge capacity of a specific electrode in a cell. Because the charge/discharge capacity of a cell is measured by the total charge flow to/from the electrode, CE can be expressed as the ratio between

the amount of Li^+ ions or electrons inserted into the cathode and the amount of Li^+ or electrons de-inserting from the cathode in a full cycle [12]. In full cell LIBs, the CE% can be defined as follows:

$$CE\% = \frac{Discharge\ capacity}{Charge\ capacity} \times 100$$

or

$$CE\% = \frac{Total\ number\ of\ e^-\ (\text{or}\ Li^+)\ back\ to\ cathode}{Total\ number\ of\ e^-\ (\text{or}\ Li^+)\ departing\ from\ cathode} \times 100$$

Equation 1.1

Cycle life and Rate capability

The number of discharge-charge cycles that the battery can experience before it fails to meet specific performance criteria. Cycle life is estimated for specific charge and discharge conditions. The battery's cycle life is influenced by factors such as temperature, DOD, SOC, and charge/discharge C-rate [13]. The Rate capability expresses the maximum charge/discharge rate of a battery or cell. This rate capability test is typically conducted at a range of C-rates to determine a battery's or cell's capacity at a given current. High power can be produced by a cell with excellent rate capability because it experiences less polarization (voltage loss) even under high current loads.

Solid electrolyte interphase (SEI)

Currently available lithium-based batteries are made up of three primary components: the anode electrode (typically, graphite, carbon, or metallic Li), the cathode electrode (typically metal oxides such as LFP[1], NMC[2], LCO[3], LMO[4], etc.), and an electrolyte to provide an electrical insulation environment for Li ions mobility ((typically lithium salt such as $LiPF_6$ dissolved in an organic solvent (EC[5]:DMC[6])) [14]. The negative terminal of such batteries operates at potentials near the equilibrium potential of lithium which is in −3.04 V vs. standard hydrogen electrode [15]. The chosen electrolyte should therefore be stable under such extreme reducing conditions. Organic solvents such as EC – the most used solvent in the current LIBs- along with the salt are reduced through cathodic reactions at the negative electrode. This results in the formation of SEI, a

[1] $LiFePO_4$
[2] $LiNi_{0.5}Mn_{0.3}Co_{0.2}O_2$
[3] Lithium Cobalt Oxide
[4] $LiMn_2O_4$
[5] ethylene carbonate
[6] Dimethyl carbonate

passivation layer on the electrode surface that is a crucial component of the electrochemical process (Figure 1.5) [16]. This layer contains both organic and inorganic compounds, and is heterogeneous and mainly amorphous. The SEI layer is conductive to Li^+ but electrically insulator to electron flow. The advantages of this layer are the batteries' safety enhancement by protecting the anodes from Li dendrite growth on metallic Li or continuous graphite exfoliation in LIBs [17]. However, by producing heat during the charge/discharge cycle and raising the battery's internal resistance, which is linked to a rapid capacity drop during cycling, the thick SEI layer lowers the battery's performance [18]. The SEI layer's presence is essential for the security and stability of LIBs.

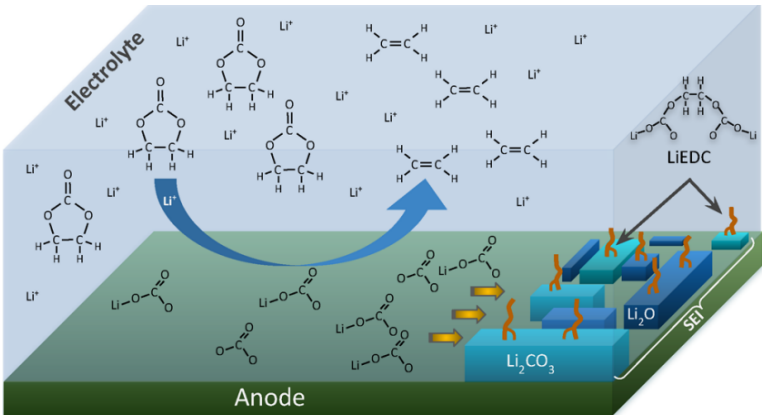

Figure 1.5. SEI layer formation in LIBs [15].

1.3 Electrochemical techniques

1.3.1 Charge and discharge

The operation and long-term performance of batteries are heavily dependent on charging and discharging. An external circuit receives electricity from the battery during discharging, and the anode releases Li ions during an oxidation process that moves to the cathode. The newly formed ions' electrons move in the reverse direction, flowing into the circuit that is powering the electrical or electronic device (https://www.electronics-notes.com). Through this action, chemical energy is transformed into electrical energy. In contrast to discharging, the charging process involves the return of electrons from the cathode through the electrolyte to the anode [19]. The electrical energy is then produced by combining the Li ions and the electrons from the external circuit. Lithium cobalt oxide (LCO), for instance, loses some of its lithium ions during the charging of an

LCO/graphite cell, resulting in a less lithium-containing molecule that is still chemically stable. These Li ions are intercalated, or stored, on the anode side in the gaps between the molecules of the graphite molecular lattice (https://predictabledesigns.com). It should be noted that the charging procedure is not entirely efficient because some energy is lost as heat during the charging process. More heat is produced as a result of the increased charge and discharge C-rate [20]. Figure 1.6 demonstrates the discharge curve (polarization curve) of an electrochemical cell. Battery polarization, which takes place throughout the discharge process, determines how a battery behaves (https://www.batterypowertips.com). During discharge, batteries experience a drop in terminal voltage (V_t). The drop in V_t is associated with several factors:

1) An IR or ohmic polarization drop occurs when current flows over the internal resistance of the battery, resulting in a drop in cell voltage. When the C-rate goes up, the IR drop also goes up.
2) Activation polarization set on by the charge-transfer reaction's kinetic barriers.
3) Concentration polarization arisen from the resistance faced by the mass transfer (diffusion) process by which ions are transported across the electrolyte from one electrode to another.

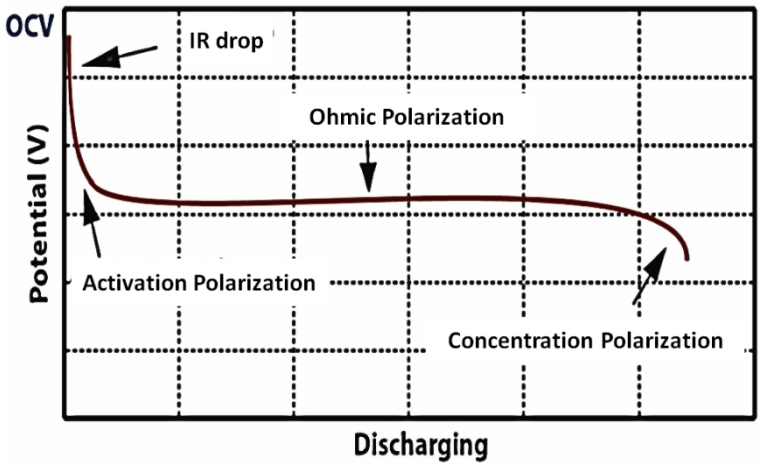

Figure 1.6. Discharge curve (polarization curve) of an electrochemical cell.

It should be noted that temperature has a significant impact on how well LIBs function. At either low or high temperatures, LIBs cannot be charged. LIBs typically operate at a temperature of about 25 °C. Working at a temperature below 25 °C results in lower voltage and reduced capacity

because the Li-ion movement rate is affected by less energy being given. On the other hand, a greater temperature enables an improvement in the mobility of Li ions, which facilitates access to the electrolyte and Li ions diffusion and increases energy, but reduces the battery's cycle life [21,22].

There are three main charging methods for batteries:

- Constant current (CC): The battery is charged at a steady current while maintaining a voltage that is equal to the battery's max terminal voltage.
- Constant voltage (CV): The battery is charged at a predefined constant voltage.
- Constant current-Constant voltage (CC-CV): This method is a combination of constant current and constant voltage.

1.3.2 Cyclic voltammetry (CV)

Cyclic voltammetry is a fundamental analytical technique among electrochemical methods which is extremely beneficial to comprehend the reactions in LIBs. The following data will be gathered with the use of the CV technique [6]:

- Reversibility or irreversibility of the chemical reaction
- Determination of the reduction/oxidation potential
- Qualitative and quantitative analyses for unknown substances.
- Analysis by changing test conditions (scan rate, Temperature, etc.)

The CV approach involves linearly varying the voltage applied to an electrode, which results in a little amount of current linked to an electrochemical reaction at the electrode interface. The ability to determine whether a chemical reaction is reversible or irreversible is the merit of the CV method, as was previously mentioned. In a reversible process, the rate of electron transfer is fast enough at the electrode surface, thus the peak potential (E_p) is independent of the variation of scan rate (Figure 1.7). However, in a quasi-reversible process (e.g., Li ions intercalation), the peak potential is a function of scan rate due to the limitation of electron transfer kinetics (Figure 1.7). The cyclic voltammogram of the quasi reversible process demonstrates gradual peak shifts to higher potential values [23].

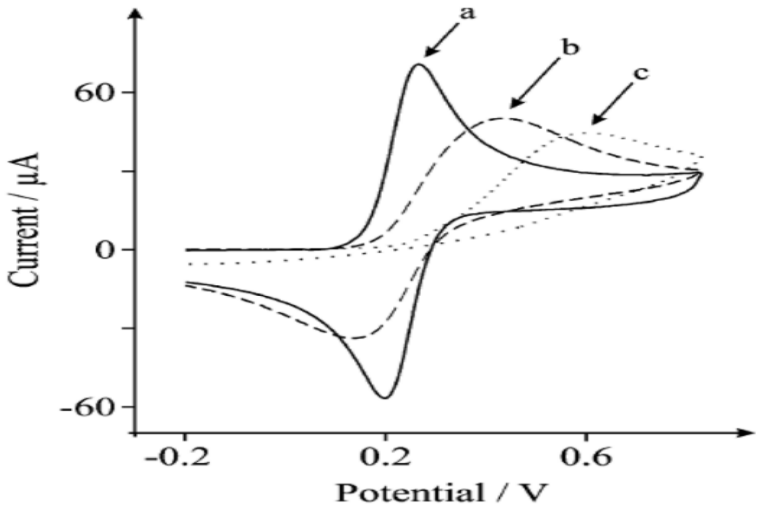

Figure 1.7. Cyclic voltammogram of reversible, quasi reversible, and irreversible electron transfer [23].

Electrode particle size, electrolyte condition, electrode thickness, scan rate, and temperature are variables influencing voltammetric curve shape [24].

1.3.3 Electrochemical Impedance Spectroscopy (EIS)

EIS is a commonly used non-destructive method to examine the physical and chemical processes in LIBs [4]. EIS is a metric of electrical flow resistance that can be used to assess AC systems. According to the various relaxation times, the EIS approach may efficiently break down complex electrochemical processes into a number of simple processes. It should be highlighted that the system needs to be in a steady state for EIS measurements. A periodic disturbance of current or a potential with modest amplitude can be used to excite the electrochemical process at different frequencies [25]. The impedance of the electrochemical system is determined by measuring the response (current or potential) of the system to this perturbation. Figure 1.8 demonstrates a typical Li-ion cell EIS measurement presented in the Nyquist plot. With a separate feature for each fundamental process that makes up the overall electrochemical mechanism, this figure contrasts the imagined and actual portions of the impedance. The inductive element observed in the high-frequency domain of the spectrum can be related to the wires connecting the cell to the geometry of the cell and cell windings [26]. The high-frequency region corresponds to the sum of internal ohmic resistances, including the electrolyte, active material, current collectors and electrical contacts. The electrochemical reactions taking place at the electrode/electrolyte interfaces inside

the cell, which include resistance and capacitance, are linked to the mid-frequency region's observed arcs [26]. Lithium (de-)insertion happens concurrently with double layer (dis)charging at each electrode, while lithium transport via the SEI occurs concurrently with dielectric polarization [26]. Therefore, this domain is related to anode/cathode charge transfer, and anode/cathode SEI. In the LIBs, the low-frequency region mainly refers to solid-state Li-ion diffusion in the electrodes [25], known as Warburg diffusion element.

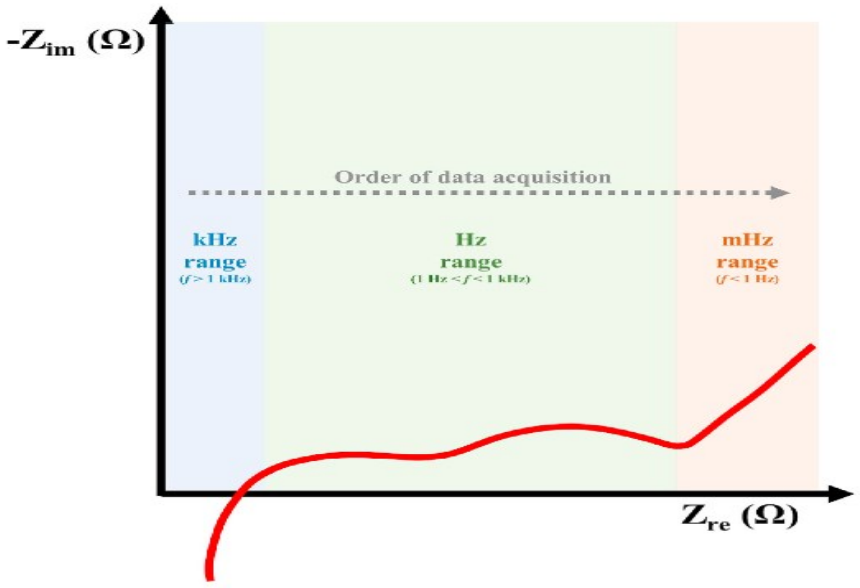

Figure 1.8. A typical Nyquist plot of commercial Li-ion cell [25].

The EIS technique makes it possible to quickly and efficiently collect significant values from each component in the cell. EIS is a useful method for examining how battery system reactions and aging work as well.

1.4 Global lithium-ion battery market size

With a compound annual growth rate (CAGR) of 15.1%, the market for LIBs is expected to surpass USD 40 billion in 2019 and reach $85.72 billion in 2026. [https://www.prnewswire.com]. It should

be highlighted that the 2019 Nobel Prize in Chemistry was given for the creation of this battery technology because of the significance of LIBs. The first, and second largest regions in LIB's market in 2021 was Asia, and North America, respectively [https://www.prnewswire.com].

The primary factor driving LIBs' market expansion is the inclusion of high energy density features brought about by the usage of Co, Ni-based cathodes in LIBs. Through 2026, the LIB market's nickel manganese cobalt oxide (NMC) chemical sector is expected to increase at an 18% annual rate (https://www.gminsights.com). Increasing penetration of EVs and rising acceptance of light electric vehicles will stimulate the demand for this material. Nickel manganese cobalt is one of the most successful cathode combinations in LIBs. Nickel and manganese are combined to enhance each other's strengths which can be custom-made to work as power and energy cells. Lithium iron phosphate (LFP) and lithium cobalt oxide (LCO) also are the most used cathode materials in LIB's market (Figure 1.9a) (https://www.gminsights.com). Although, NMC batteries have slowly occupied the position of LFP credited to their high energy density, the use of phosphates in LFP batteries avoids concerns of cost and environmental contamination. Therefore, LFP could be considered the best choice to design a sustainable battery. In addition to cathode materials, anode, electrolyte, aluminum foil, and copper foil, are some of the key LIBs' components that determine the cost of the battery. Figure 1.9b demonstrates the cost of each material that affects the final cost of the LIBs (https://www.gminsights.com).

The energy density of the LIBs is 100-265 Wh/kg or 250-670 Wh/L (mainly depending on the cathode materials used), which is one of the highest energy densities of any battery technology. The primary factor that has made LIBs the most popular batteries for use in electric vehicles, computers, mobile phones, and other devices is their high energy density. Lowering the final cost of LIBs increases demand for these batteries. Materials, and production techniques, overhead expenses, and significant expenditures in these battery systems are among the causes prompting a decline in LIBs prices. By 2030, the price of LIB with a combined cost for cell and pack would fall to US$76 per kWh, according to a Navigant Consulting Research (https://www.prnewswire.com).

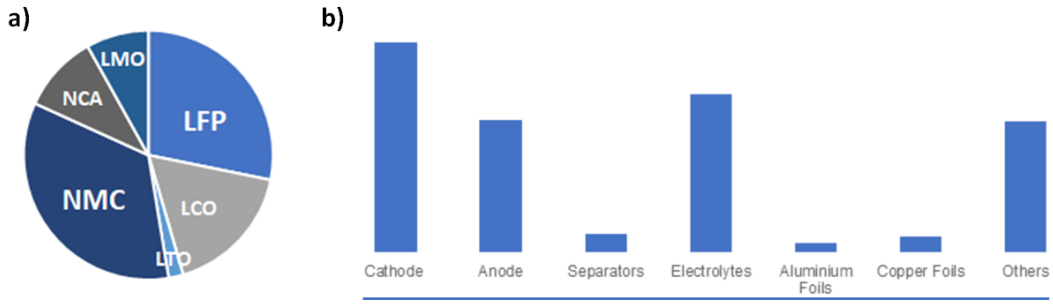

Figure 1.9. a) the most common cathode electrodes in LIBs' Market, and b) the key LIB's components regarding their cost [www.gminsights.com].

1.5 Carbon anode materials for application in LIBs

There is an increasing need for low-cost, high-performance materials due to the LIBs' use in electric cars and portable electronic gadgets. Cathode and anode electrodes are two crucial parts of LIBs. Before covering Hard Carbon's (HC) structure, chemistry, Li-ion storage methods, difficulties, and viewpoint in this part, let's take a quick look back at how carbonaceous materials were developed for use as the anode in LIBs.

1.5.1 Carbonaceous materials

Carbonaceous materials including graphite, soft carbon (SC), and HC are a practically viable candidates for application as the anode in LIBs. These materials had a great influence on the launch of the first commercial LIBs which were based on graphite anode (derived from petroleum coke) and $LiCoO_2$ cathode [27]. Up to now, graphite has been the most popular anode material for commercial LIBs.

We should note the contribution of the scientists in presenting the carbon-based materials in LIBs. One of the pioneers who initially presented a new family of interstitial compounds generated from graphite in 1972 was Michael Armand [28]. J.O. Besenhard and Eichinger proposed the reversible intercalation of Li ions into the cathodic oxides and graphite in late 1970 [28]. Nevertheless, due to the lack of an appropriate electrolyte, the graphite anode still was not considered a good choice for LIBs. The electrochemical intercalation and de-intercalation of Li ions into/from the graphite anode was later discovered by Yazami and Tiuzion in 1982 through experimental investigations [29]. However, because graphite and the propylene carbonate electrolyte were incompatible at the

time, its usage in LIBs was still constrained [30]. Exfoliation of the graphite in the electrolyte causes battery failure. Akira Yoshino identified the first practical example of such carbonaceous material for LIBs in 1985 [31]. He proposed that as-prepared petroleum coke with a low degree of graphitization and a certain crystalline structure shows structurally stable electrochemical behaviour with the electrolyte of LIBs. This discovery enabled the commercialization of LIBs by the Japanese Sony Corporation in 1991 [27]. The compatibility of graphite electrodes with another kind of carbonate-based electrolyte, ethylene carbonate, was discovered through further research. Long cycling life of graphite is enabled by the development of SEI on the graphite anode without exfoliation [32]. This development led to improve graphite anode-based LIBs' performance, thus laying the foundations for their debut of them in the markets. Nonetheless, the low theoretical capacity (372 mAh g^{-1} vs Li^+/Li) and poor rate capability of graphite hinder using it in advanced battery technology [33,34]. The next task for researchers in this field of study has been to investigate different carbonaceous materials to address the issues with graphite in LIBs. Figure 1.10 demonstrates the most important discoveries of carbonaceous materials from birth and applied to the first commercial LIBs.

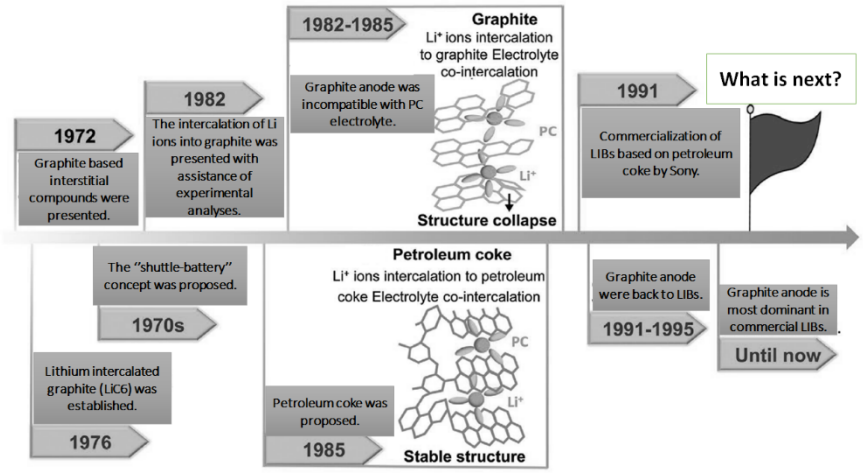

Figure 1.10. Brief historical timeline of carbonaceous materials in LIBs.

The application of HC for the current and upcoming generations of LIBs has been regarded as one of the promising carbonaceous materials among many other types. Because of their distinctive physical and chemical characteristics, HCs provide great cycle stability and capacity in LIBs.

Table 1.1 compares three different types of carbonaceous materials primarily from a physical and electrochemical perspective. In the following part, we focus on the structures of HCs, understanding Li-ion mechanisms in HCs, challenges, precursors, and modification methods of HCs.

Table 1.1. The main comparison of graphite, soft carbon, and HC from physical and electrochemical points of view.

Material	**Graphite**	**Soft carbon**	**Hard carbon**
Raw materials	**Natural graphite/pitch/petroleum coke**	**Pitch/petroleum coke**	**Resin/pitch/biomass**
Carbonization temperature	2500–3000 °C	1000–1500 °C	<1500 °C
Crystal structure (*Lc*) [nm]	>80	2–20	1.1–1.2
Interlayer distance [nm]	~0.335	0.34–0.37	0.37–0.42
True density [g cm^{-3}]	~2.2	~2.2	1.4–1.8
Compacted density of electrode [g cm^{-3}]	1.5–1.8	~1.2	0.9–1.0
Expansion rate of electrode (%)	~10	1-10	~1
Charge capacity at low temperatures and fast-charging performances	-15 °C/3 C	-20 °C/10 C	-50 °C/>10 C
Cycling stability	Medium	Significantly capacity drop at high temperature	High
Initial Coulombic efficiency	High	High	Low
Safety	Good	Excellent	Excellent
Application in battery	Li-ion	Li-ion	Li/Na/K-ion
cost	Low	Medium	High

1.5.2 Typical structure of HCs

HCs are referred described as "non-graphitizable" carbon because they contain curved graphene sheets that cannot be flattened to further stack into graphite even at temperatures exceeding 3000 °C [35]. The predecessors' interlayer cross-linking or the presence of C-O-C bonds is what causes HCs to be amorphous [36]. The "failed cards" model, which suggests that HCs contain small graphite sheets, amorphous domains with defects, and pores, is the most widely recognized theory regarding their structure [37,38]. The spherical, wirelike, or porous structure are three morphological traits of HCs, which are stemmed from HCs' precursor (Figure 1.11). The anisotropic hexagonal carbon layers in HCs leads to form many open or closed pores [35]. Figure 1.12 demonstrates the structural difference between graphite, SC, and HC.

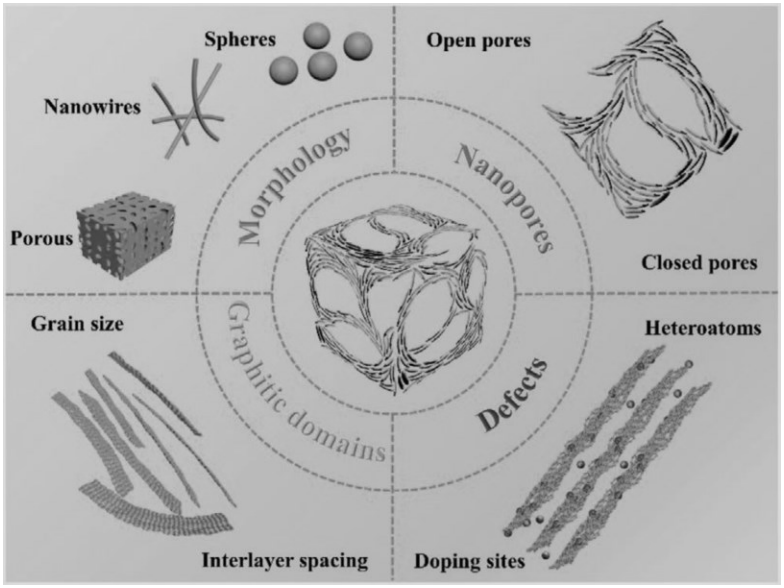

Figure 1.11. Three morphological traits of HCs [39].

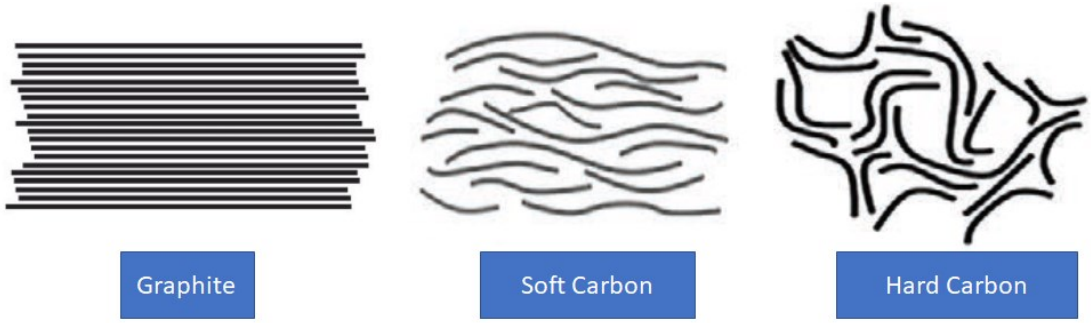

Figure 1.12. Structural difference of graphite, SC, and HC.

Some conventional characterization analyses such as Raman spectroscopy, X-ray Powder Diffraction (XRD), and N_2 adsorption/desorption can give quantitative structure properties of HCs such as degree of graphitization, average interlayer spacing, crystallite size, porosity, and specific surface area. The figure below (Figure 1.13a) demonstrates the Raman spectra of graphite, SC, and HC. The 2D band at around 2685 cm^{-1} is not observed for HCs, indicating that the number of graphite crystallites is decreased. The broad D band located around 1360 cm^{-1} is associated with the edges, defects, and disorders of carbonaceous materials [40]. On the contrary, the G band at about 1600 cm^{-1} corresponds to the graphitic layers and shows sp2 hybridized carbon [41]. The intensity ratio of the D band and G band (I_D/I_G) can be applied to determine the level of disorder in the carbon. A sharp rise of the D band shows disordered carbon materials with more defects. From the Raman spectra, it can be concluded that HC and SC are turbostratic carbon materials with lower degrees of graphitization compared to graphite. The XRD patterns (Figure 1.13b) indicates two broad diffraction peaks located at around 25°, and 43° associated with (002) and (100) lattice planes, respectively. HC demonstrates a shift to lower degrees (002) in comparison with SC, and graphite. This proves that the structure of HC is more disordered (with increased average interlayer spacing (d_{002})) than SC, and graphite [42]. Additionally, the XRD peaks have a wider characteristic in HC due to smaller average crystallite sizes in HC than in SC and graphite [43].

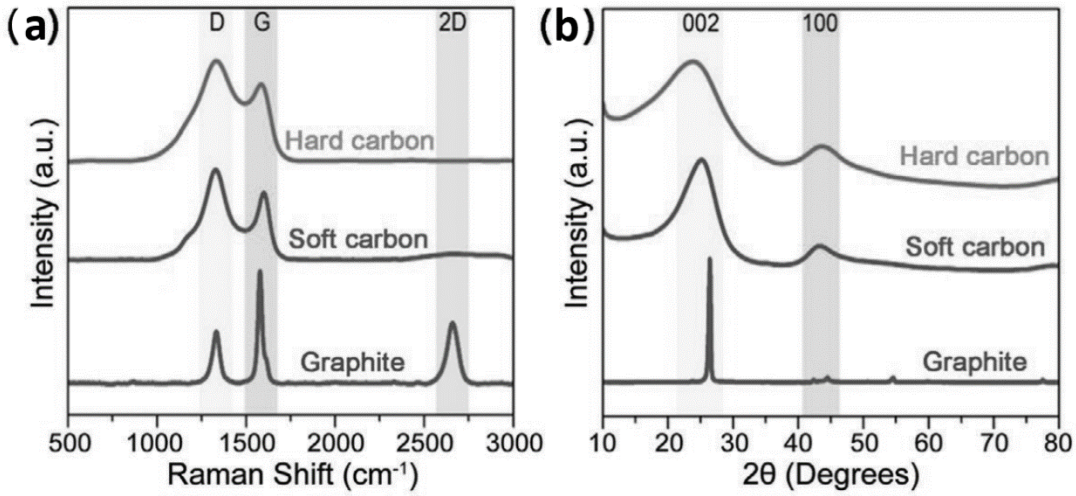

Figure 1.13. a) Raman spectra and b) XRD spectra of graphite, SC, and HC [36].

HCs also have a higher specific surface area than graphite, resulting from ample defects, microporosity, and turbostratic structure [44]. Benefiting from these properties, HCs usually possess a higher capacity than graphite in alkali batteries [45]. It is worth noting that the graphitization, porosity, and interlayer space of HCs can be easily tuned by varying thermal treatment conditions, making it a potential carbon anode for battery application. Generally, porosity, surface area, crystallinity, elemental composition, etc., are influencing factors that determine the electrochemical performance parameters. Bio-based carbon materials have a high specific surface area, and thus part of the low voltage capacity (below 0.1 V) will be sacrificed due to a large amount of SEI formation, particularly for LIBs [44]. The mentioned features are being explored to further investigate the right balance between porous and graphitic structures for elaborating electrochemically optimized carbons for the alkali metal ion storage technology.

1.5.3 Li ions storage mechanism in HCs

High capacity, outstanding cycleability, and promising rate capability are the major characteristics of HCs that make them desirable candidates for employment in LIBs [36,46]. Although these depend on the carbon sources (feedstock properties) and treatment procedure, HCs often exhibit superior electrochemical performance than graphite (the most frequently used anode electrode in the industry). This electrochemical performance in LIBs could be explained through Li-ion storage mechanisms in these materials. It should be noted that, due to the complex microstructure, the existence of pores, edge sites, graphitic crystallite size, defects, and heteroatoms in HCs, the Li ions storage mechanism in them is still under discussion [47,48]. The schematic representation of Li ions being stored in HC is shown in Figure 1.14. Two typical reaction pathways for Li ions intercalation into HCs were proposed using the microstructure and charge/discharge profile of HCs. First, Sato et al. proposed a model in 1994. This model says that the occupation of ionic sites and covalent sites on carbon layers, and the formation of Li_2 covalent molecules with a saturated state of LiC_2 lead to high energy (Figure 1.15) [49]. The second reaction mechanism for Li^+ was proposed by Besenhard and his coworkers in 1998. In addition to graphitic domains, they thought that cavities of HCs could also host Li ion electrochemical processes [50].

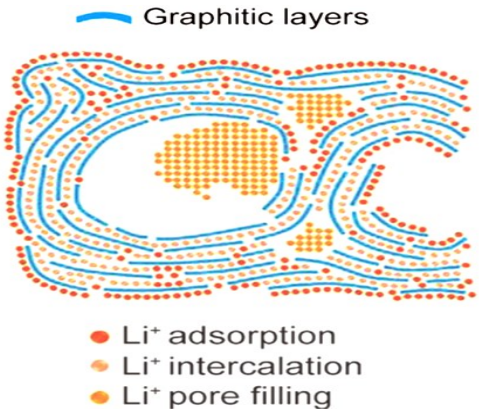

Figure 1.14. The schematic illustration of Li ions storage in HCs.

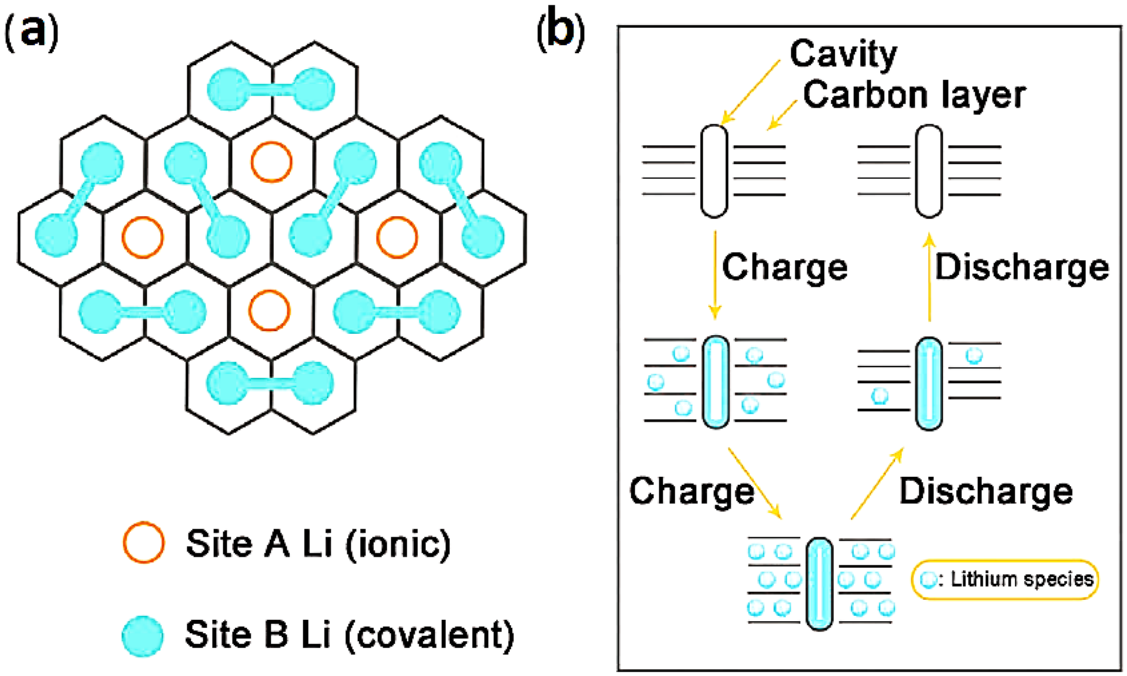

Figure 1.15. Typical reaction mechanisms for Li ions intercalation into HCs, a) the model suggested by Sato et al in 1994 [49]*, and b) the model proposed by Besenhard and his coworkers in 1998* [50].

In addition, the charge/discharge profile of carbonaceous materials (graphite, SC, and HC) reflects the distinct intercalation/de-intercalation behaviour of Li ions [51,52]. The constant current discharge/charge patterns of these materials are shown in Figure 1.16. The typical staging profile of a graphite electrode shows that its maximum capacity is found at low voltage plateau regions.

[50]. However, for HCs, the intercalation of Li ions begins around 0.8 V vs. Li/Li+. There is no discernible plateau but instead a downward slanted, demonstrating that no visible staging phenomena occurs as Li ions intercalate HCs. The structural differences of HCs can be used to explain a variety of electrochemical phenomena. The disordered structure and highly crystalline graphite offer non-equivalent, and equivalent sites, respectively, both in electronically and geometrically [53]. It should be pointed out that HCs reveal a larger voltage delay compared to SC, and graphite [50]. In comparison with HCs, SCs show a higher starting voltage (1.0 V vs. Li/Li^{+}). They lack a noticeable low voltage plateau, like HCs, though. Additionally, the voltage and capacity are roughly linearly connected, and the discharge profile is substantially steeper than that of HCs. As a result, the capacities are lower and the average oxidation voltages are greater.

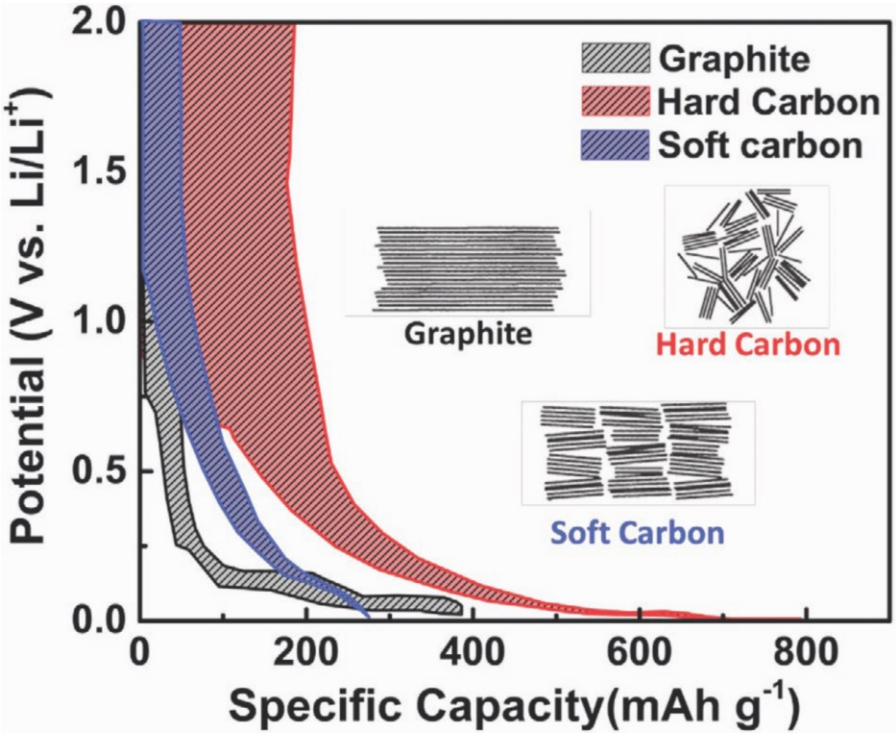

Figure 1.16. Galvanostatic charge/discharge profiles of graphite, HCs, and SCs.

In-situ characterization and computer modeling may potentially provide us with more thorough and organized details about the Li ion storage process in HCs. Li ions are essentially stored in HCs in three steps, as shown in Figure 1.14:

1) Li ions up taking in nanopores
2) Li ions adsorption at defect sites

3) Li ions intercalation into the graphitic layers

In-situ XRD analysis of the electrochemical behaviours of Li ions confirmed a reduction in the (002) peak intensity at the slanted voltage region caused by the intercalation of Li^+ ions between graphitic layers [54]. An "intercalation-filling process" for HCs was postulated by in-situ small-angle X-ray scattering (SAXS) investigation of the behaviours of Li ions within the low voltage plateau. These studies along with experimental and theoretical simulations revealed that the adsorption of Li ions on defects or edge sites led to the slanted capacity of the high-voltage region. On the other hand, the plateau capacity of the low-voltage region mainly stemmed from the electrochemical intercalation of Li ions into the graphitic layers [55]. Figure 1.17a demonstrates the diffusion coefficients of Li ions in porous carbon which it is very sharp initially before reaching the minimum state. The initial large value of diffusion coefficients shows the physical adsorption of Li ions that they easily diffuse in the high voltage range. Afterward, the diffusion coefficient is decreased (as the discharge potential decreases), suggesting the domination of chemical adsorption of Li ions. Figure 1.17b provides evidence in favor of the notion that Li ions adsorb and intercalate at the low voltage plateau and slanted voltage area, respectively [56]. Other similar studies also proved the adsorption-intercalation model [38,57]. Based on experimental observations and theoretical calculations, it has been confirmed that Li ions preferentially adsorbed on defects, edges, and microporous surfaces (slanted high-voltage capacity), and then intercalated into graphitic layers (low-voltage plateau region). Despite many researchers believe in the “adsorption intercalation” mechanism, some research results are inclined to support the “intercalation-adsorption” mechanism [54,57]. This difference of opinion has been caused by the complex structural makeup of HCs, which may present new chances for researchers to understand more about the Li storage mechanism of HCs and develop high potential electrodes with improved Li ion storage.

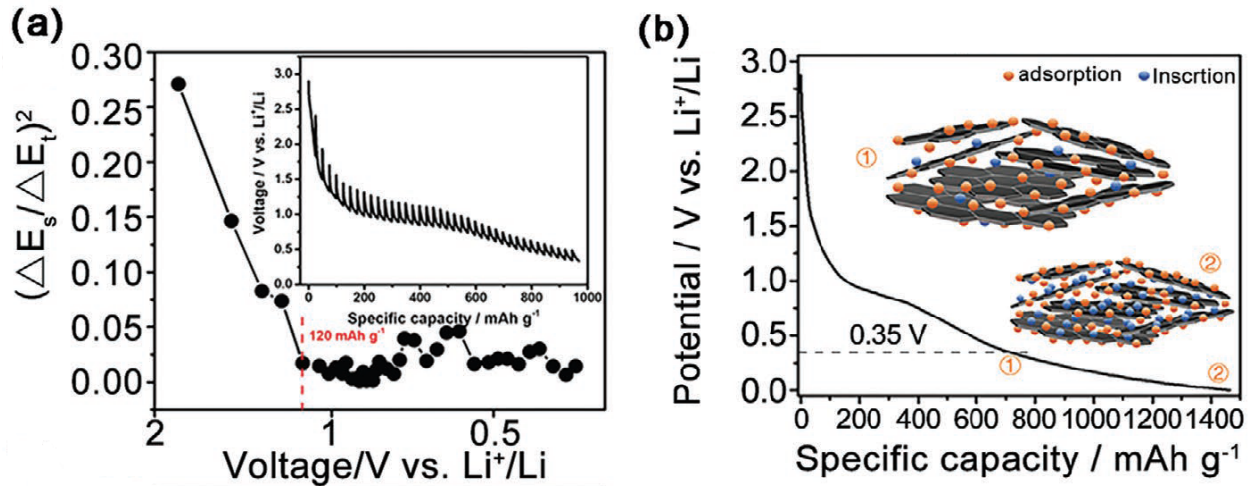

Figure 1.17. a) Diffusion coefficient of Li ions in porous carbon. Inset is the potential galvanostatic profile of intermittent titration technique in the first cycle. b) Galvanostatic profile and schematic of Li ions storage in porous carbon [56].

1.5.4 HCs' precursors

Engineering/synthesis/treatment settings and precursor texture have a significant impact on the microstructures and electrochemical performances of HCs in LIBs [58–60]. Resin-based, pitch-based, and biomass-based are the three main precursors to make HCs for LIBs' application. Figure 1.19. a) Schematic of the synthesis of phosphorus-doped resin-based HCs. b) Rate capability and c) cycling performance of undoped (HC-700) and doped (PHC-700) samples [64]. Figure 1.18 illustrates the main characteristics of the precursors that are frequently employed to create carbon-based electrodes for alkali batteries [61]. From the practical point of view, graphite shows the highest efficiency because of having a reasonable price/performance ratio. However, if great electrochemical battery performance is taken into account, resin may be a superb choice. Phenolic resin-based HCs are lower-cost than resin and can work as anode materials for LIBs and supercapacitors [62]. Resin is normally a solid or extremely viscous substance of synthetic or botanical origin that can be converted into polymers. It is typically made up of combinations of organic chemicals (https://goldbook.iupac.org). The heteroatom doping strategy also can bring positive electrochemical effects for the electrochemical performance of HCs by changing of electronic structure, increasing conductivity, introduction of different active/defect sites and functional groups for Li^+ ions adsorption, and the increased interlayer distance [63]. The creation of

phosphorus-doped resin-based HCs employing phosphoric acid as a crosslinking agent and phosphorus supply as well as epoxy resin as a crosslinking and curing agent is a successful example of this strategy (Figure 1.19a) [64]. The physical and electrochemical analyses revealed that the introduction of P species enabled the Li^+ ions adsorption, and the formation of LixPCy, leading to the reversible capacity of 1294.8 mAh g^{-1} with a high ICE, excellent rate capability, and long cycle life (Figure 1.19b,c).

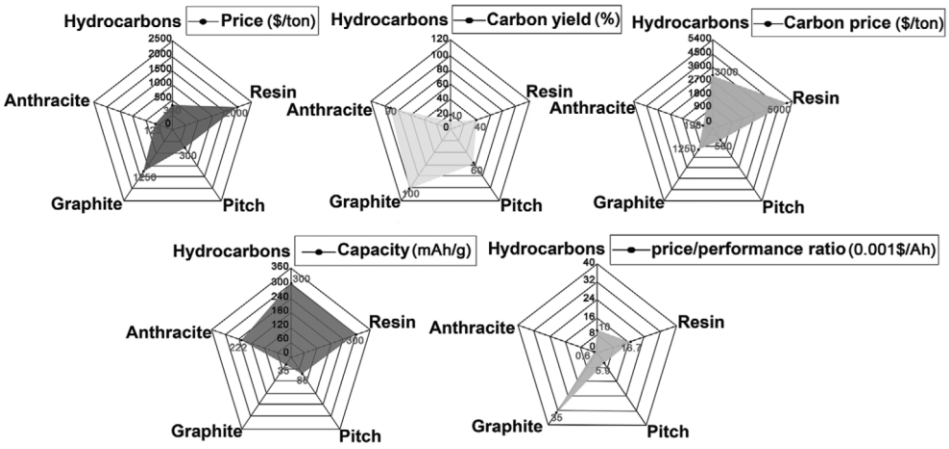

Figure 1.18. The major features of commonly used precursors to fabricate carbon-based electrodes [61].

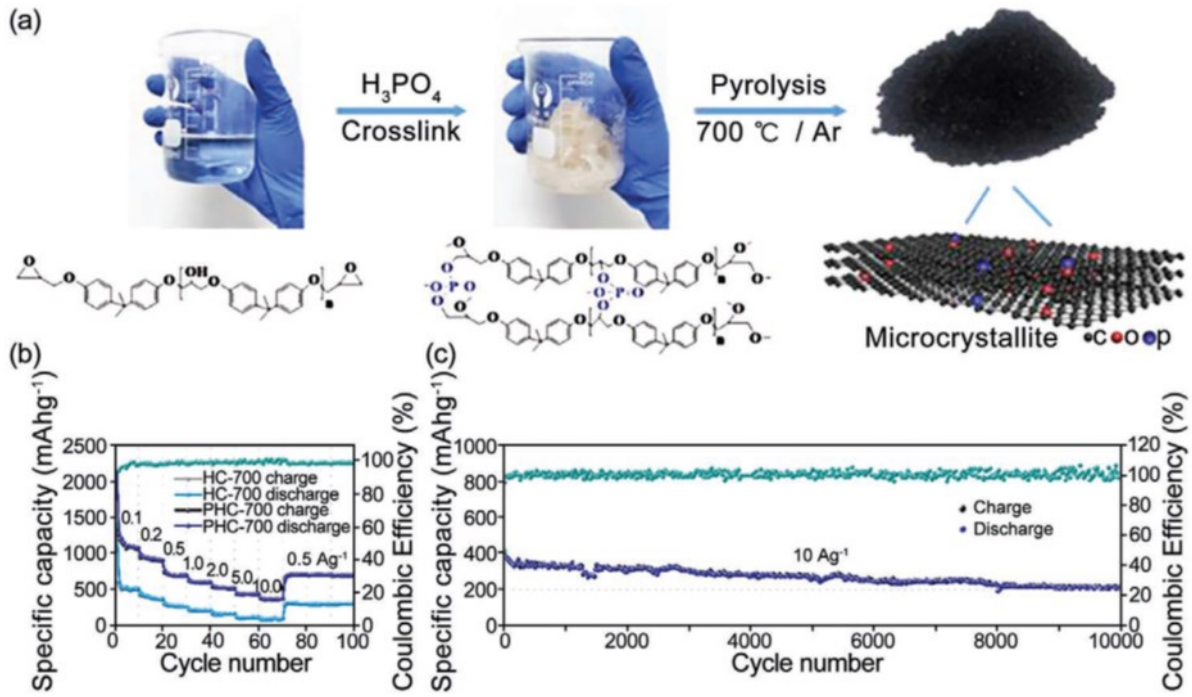

Figure 1.19. a) Schematic of the synthesis of phosphorus-doped resin-based HCs. b) Rate capability and c) cycling performance of undoped (HC-700) and doped (PHC-700) samples [64].

Pitch is regarded as another source to get HCs. It may be manufactured or natural and generated from plants, coal tar, or petroleum [65]. Pitch can be used to make HCs at a low cost and with high carbon residue rates. The direct carbonization of pitch, however, results in the formation of a structure resembling graphite because of the hydrocarbons and nonmetallic compounds present in pitch [66]. Therefore, the generation of oxygen-rich active sites before pitch carbonization is a solution to form HCs [67]. Guo et al., suggested a simple two-step oxidation/carbonization method to prepare HC from coal tar pitch [68]. The pitch-based HC material's structural investigation found that it had a weakly crystalline structure with some contacted microcrystallites that resembled graphite (Figure 1.20a). Additionally, from the electrochemical point of view, this sample showed the reversible capacity of 350.8 mAh g^{-1}, after 30 cycling at 37.2 mA g^{-1} (Figure 1.20b). Similar investigations demonstrated that the electrochemical characteristics of pitch-based HC in LIBs may be greatly impacted by the oxygen concentrations [69]. Despite the benefits of pitch precursor, the mechanism underlying the cross-linking oxidation process is still being debated. To optimize the pitch-based HCs for use in LIBs, the pre-oxidation and carbonization processes must be precisely modulated.

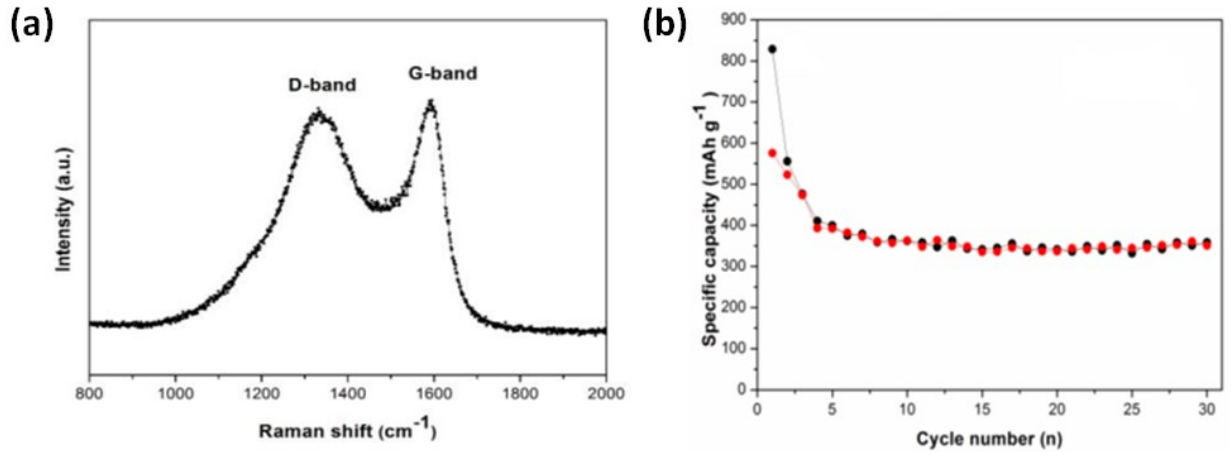

Figure 1.20. a) Raman spectrum, and b) the cycling performance of pitch-based HC in lithium half-cell batteries [68].

1.5.5 Biomass-based HC

The third HCs precursor is biomass that has captured immense interest for application as anode materials for LIBs because of their favorable properties, including easy availability, sustainable production, low-cost and environmental friendliness. Considering the growing importance of such materials and the increasing number of research activities (Figure 1.21) in this area, this part presents a brief overview of studies that investigated biomass-materials in LIBs.

As a definition for biomass, we can say that biomass is organic, which it is made of material that comes from living organisms, such as plants and animals. Plants, wood, and waste are the most common biomass materials which have been used for energy applications [70]. These are referred to as biomass feedstocks, and biomass will be accessible as a renewable energy source for as long as these materials are present on earth. It is crucial to note that biomass energy can also be produced from non-renewable resources.

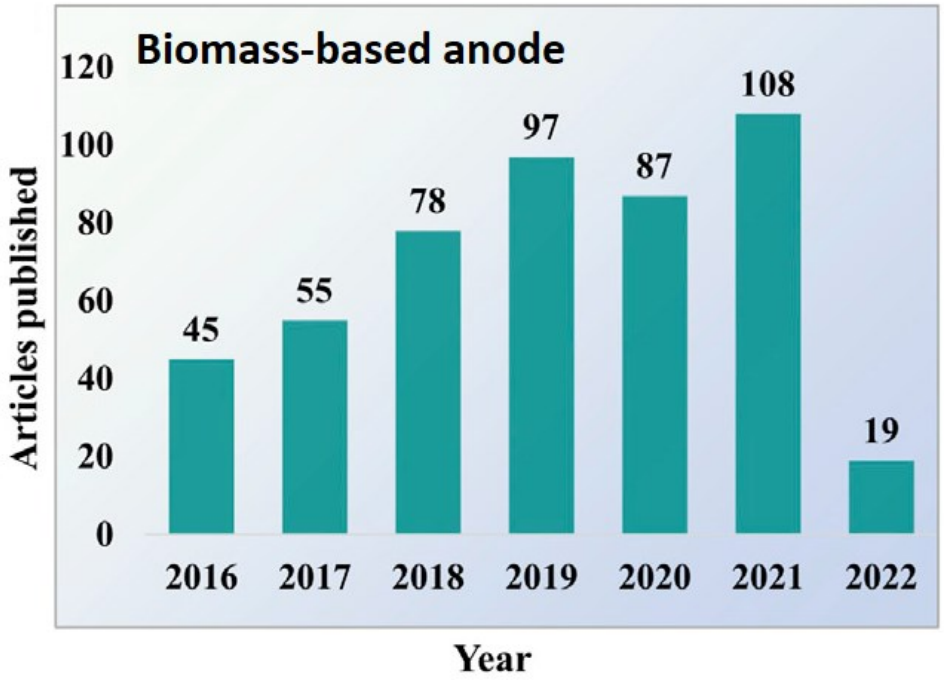

Figure 1.21. Number of publications on biomass-derived materials as anodes for LIBs' application from 2016 to March 2022 [71].

Biomass materials include all types of biologically produced materials. Figure 1.22 demonstrates the biomass resources in nature which are abundant, including energy crops, agricultural crops, and their residues, wood and wood wastes, municipal, industrial, and animal wastes, aquatic plants, and algae [72]. Typically, biomass has the capacity to store chemical energy from solar energy in the plant tissue through the process of photosynthesis. Because of this, biomass energy is also regarded as the primary source of renewable energy, along with solar, wind, hydroelectricity, and geothermal energy. More importantly, though, using this energy will lower CO_2 emissions [73]. Nowadays, a variety of uses for biomass energy, including the production of electricity and the fueling of vehicles, are common [74]. The most common products from biomass are biochar and activated carbons (ACs). In addition to biochar, and AC, biomass also can be converted into liquid or gas fuel, such as bioethanol or biodiesel, which have wide range use of applications [75]. Biochar is often produced by burning (carbonization) and pyrolysis (low oxygen). These procedures frequently result in very porous structures with a large specific surface area, which can be beneficial for a variety of applications. In agriculture, for instance, biochar may be used to absorb nutrient cations and anions for the growth of soil-beneficial microbes, resulting

in soil fertilization and providing significant agricultural benefits [76]. Another by-product of the pyrolysis of biomass is ACs, which are used for water purification, ground and municipal water treatment, power plant, landfill gas emissions, precious metal recovery, and electrodes for electrochemical energy devices and typically have higher specific surface area than biochar [77]. Although biomass materials have been used in various applications so far, the fundamental challenge is always the same: how to enhance performance through structural optimization. In order to respond to this query, it is necessary to have a solid understanding of the mechanisms that lead to the production of high-performance chemical feedstocks, which will enable us to meet the difficulties associated with energy and the environment.

Figure 1.22. Various resources of biomass [78].

1.5.6 Conversion methods of Bio-based HCs

To transform biomass into viable forms of energy utilization, a variety of techniques have been used. The primary variables that influence the choice of conversion process include the kind and quantity of biomass feedstock, the intended form of the energy, or end-use needs, environmental standards, economic conditions, and project-specific factors [79]. Basically, all the processes can be grouped into two categories, i.e., thermochemical methods (such as combustion, gasification, and pyrolysis) and biochemical method (e.g., fermentation and anaerobic digestion) [79]. One of the most important processes for energy recovery is pyrolysis, which involves thermally degrading a solid (or a liquid) into smaller volatile molecules. This process generates a number of products, including char, oil, and gas, at high temperatures and without oxygen [80]. Due to the thermal

pyrolysis, the remaining solid char shows different features in comparison with the pristine biomass. Through well designed synthesis processes, this solid char can be utilized to create a variety of carbon-based materials, including activated carbon, porous carbon, nanostructured carbons, carbon nanotubes, and graphene [81–84]. Activation methods and agents can modify/change the texture, structure, and surface functional groups of the resultant biochar [85]. Physical activation, chemical activation, and hydrothermal carbonization are the three main synthesis techniques used to produce carbon-rich compounds from renewable biomass feedstock. Herein, we briefly explain the mentioned conversion methods.

Physical activation

To physically activate carbon precursors, two stages are often required. The raw material is first carbonized (at a temperature of around 700 °C) using a pyrolysis process, which increases surface area and decreases the degree of polymerization and crystallinity by thinning the particle size. [86]. The controlled gasification process takes place after the second phase at significantly higher temperatures (>800 °C) in the presence of oxidizing gases such CO_2, steam, air, or CO_2/steam/air mixes. Due to the complexity of the reaction environment, the mechanistic understanding of pyrolysis is limited [87]. Cellulose, hemicellulose, and lignin are the main constituents of the biomass (raw material, especially lignocellulosic biomass) [88]. During the pyrolysis process, water loss takes place in the first stage (<100 °C). At higher T (220 to 315°C), hemicellulose degrades, leading to the formation of the basic structure of char. In comparison with cellulose, hemicellulose has a random, amorphous structure with lower molecular weight and little strength. The third stage, which is connected to the pyrolysis of cellulose, is the consolidation of the char structure, which happens between 315 and 400 °C. Decomposition of lignin covers a wide range of temperatures from 150 to 900 °C [89]. It should be noted that only pyrolysis is not enough to have rich porous with high surface area carbon because often disorganized carbon (formed from the decomposition of tars during the pyrolysis process) occupies the pores of the char. Thus, a subsequent activation process at high T (800-1000 °C) is vital to remove the disorganized material, resulting in a well-developed and accessible interconnected porous structure [89]. Physical activation with CO_2/steam as a clean and feasible technique can be a good option to achieve key desirable properties [90,91]. The main disadvantage of physical activation is the high consumption of energy because of running analysis at extremely high T. Figure 1.23 demonstrates the activation of wheat straw by a two-step method [92].

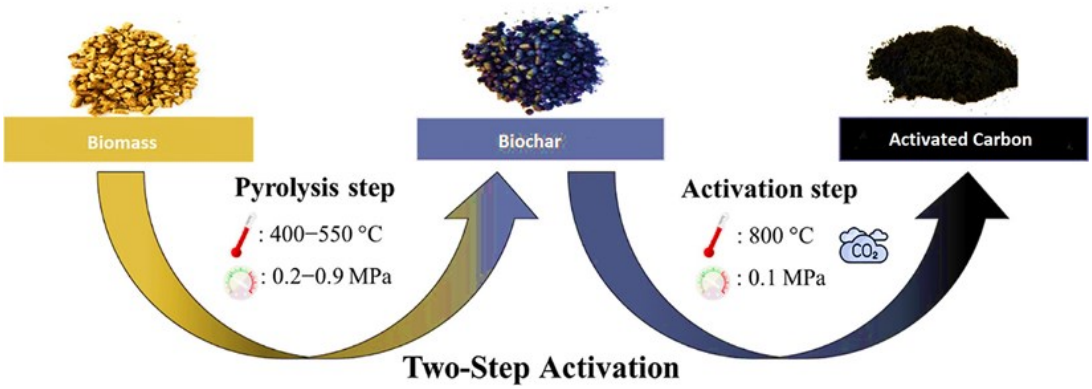

Figure 1.23. Obtaining activated carbon from wheat straw biomass by two-step method (pyrolysis and CO_2 activation) [93].

Chemical activation

ACs can exhibit acidic, basic, or neutral properties depending on the surface functional groups. Consequently, modifying biochar chemically involves changing its natural surface functional groups. Between 400 and 900 °C, chemical activation often occurs in a single phase that combines heat treatment with chemical compound activation, such as HCl, $ZnCl_2$, H_3PO_4, K_2CO_3, KOH, NaOH, etc. [94,95]. In comparison with physical activation, chemical treatment brings advantages from different points of view such as lower conversion temperature, higher carbon yield, and porosity with high specific surface area [74].

KOH is a highly developed activator with a microporous structure that has a mild activation temperature compared to other activators, producing high yields [96]. Due to these qualities, KOH has been the most often used activator agent since 1978. It is worth noting that when a material is employed for energy storage or conversion devices, a high specific surface area and a clearly defined micropore/mesopore pore size distribution are regarded as critical properties. The mechanism of KOH activation is still not fully understood. However, the chemical activation mechanism can be summarized as follows: 1) KOH, K_2CO_3, and K_2O etch carbon fragments via the redox process to create the pore network. 2) As a result of the activation process, gaseous is created that reacts with carbon; 3) the carbon lattices will expand as a result of the intercalation of metallic potassium (K) into the carbon framework, resulting in the development of porosity [97]. It is reported that O-containing groups, such as C–O and –OH groups, have the greatest effects on the chemical activation process. Because these groups may react with KOH during the activation

process. Therefore, the chemical interactions between oxygen (or O-containing species) and KOH should be considered during activation Additionally, it is established that KOH reacts with active O-containing species during the pyrolysis of biomass to eliminate the majority of the O-containing groups [98]. This causes a number of vacancies to arise. Additionally, vacancies are produced when KOH reacts with more durable carbon fragments. In order to supply oxygen, OH- from KOH can then fill these vacancies, leading to the formation ofmany new O-containing groups in the biochar. Figure 1.24 depicts a potential chemical reaction route of KOH activation during biomass pyrolysis.

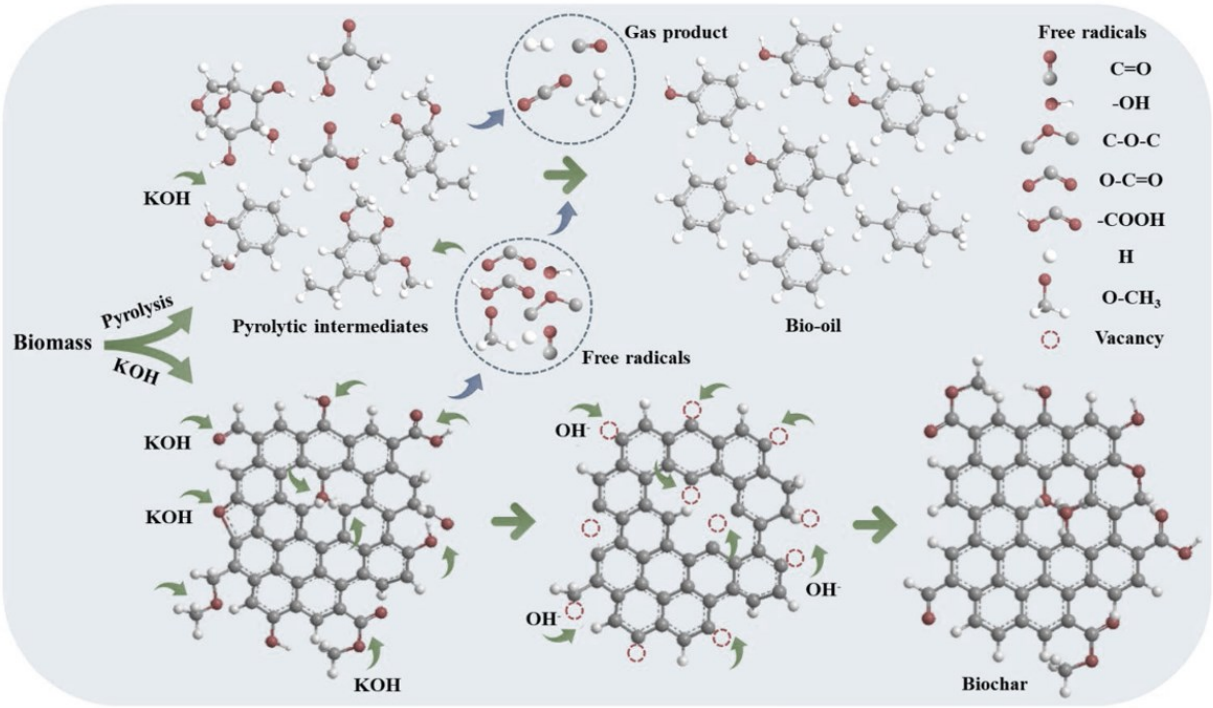

Figure 1.24. Possible mechanism of KOH activation during pyrolysis of biomass [98].

In addition to KOH, other activation agents, such as HNO_3, HCl, H_3PO_4, NaOH, etc., have an impact on the conductivity, graphitization level, and heteroatom content of carbon materials. For instance, oxidants agents typically increase disorders, increase oxygen concentration, and decrease the conductivity of carbon materials which can negatively impact on the stability of the sample in EESDs [99]. On the other hand, reductant agents such as NH_3 could be a good option for the chemical treatment of carbon materials for application in EESDs [100]. Moreover, it has been reported that HCl treatment of biochar after pyrolysis can remove great amounts of collapsed

structures on the biochar surface (Figure 1.25), leading to carbon-rich material with a high surface area that is desirable for Li ions insertion/de-insertion [101].

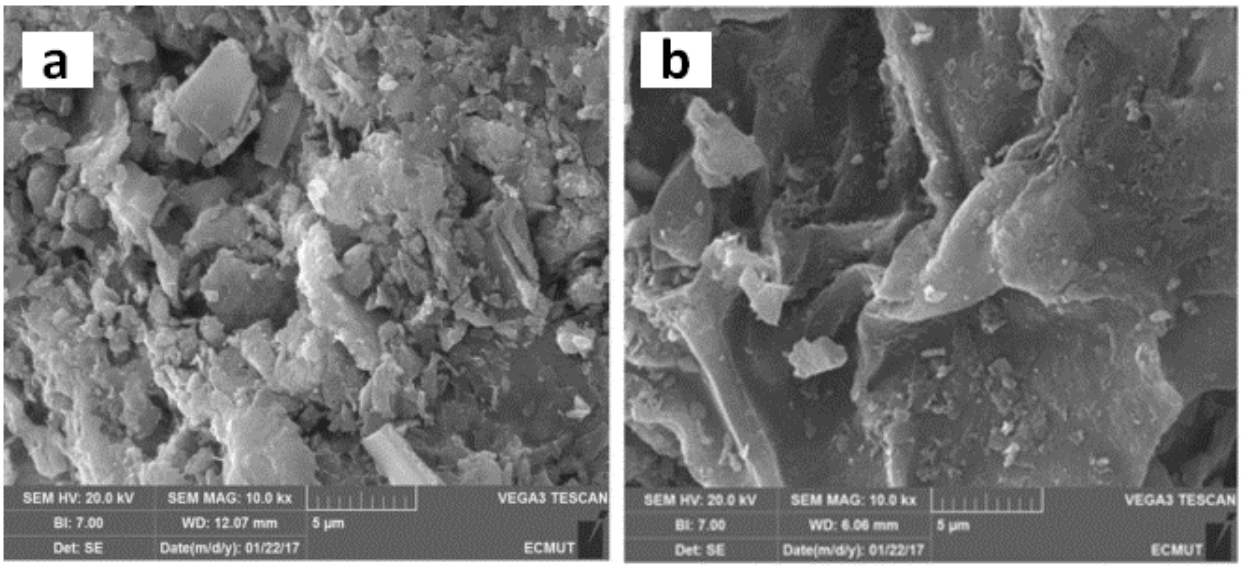

Figure 1.25. SEM images of the biochar, before a) HCl modification, and b) after HCl modification [101].

Hydrothermal Carbonization

Hydrothermal carbonization (HTC) is a technique to convert wet biomass into energy (Figure 1.26) and chemicals without pre-drying, involving raw feedstock with hot, pressurized water. Compared to pyrolysis or gasification, which are recognized as common thermal treatments, the process operates at lower temperatures. The temperature range where HTC carbonization occurs is 180–250 °C [102]. In 1913, cellulose was initially transformed into coal-like compounds using the HTC process. HTC provides a practical, affordable, and environmentally friendly method for carbonizing biomass precursors such fungus, pine cones, tobacco rods, and bagasse [103].

The HTC method's reaction pathways have been the subject of numerous studies, although some scientists think that the method's chemical process is still not entirely understood [104]. However, it can be inferred from the earlier findings that, although other reactions like dehydration, decarboxylation, or condensation are involved, hydrolysis is the key factor controlling HTC [104]. Hemicellulose, cellulose, and lignin are broken down into smaller parts during the hydrolysis process, enabling the subsequent reactions (dehydration and decarboxylation) to lower the H/C and O/C ratios, which are essential for producing a solid product that resembles coal [105].

Additional processes, such decarboxylation, enable the breakdown of carboxyl-carbonyl groups and release the majority of the final fuel gas's composition (i.e., CO_2 and CO) [104]. Hydrochar (carbon-rich part), liquid product (formic acid, lactic acid, furfural, phenol, guaiacol, acetic acid), and the gas (CO_2, CO, CH_4, or H_2) are the three main phases of the HTC process [106]. Although HTC is a low-cost method of producing carbonaceous materials from biomass, the resulting carbon often has low specific surface area and low porosity.

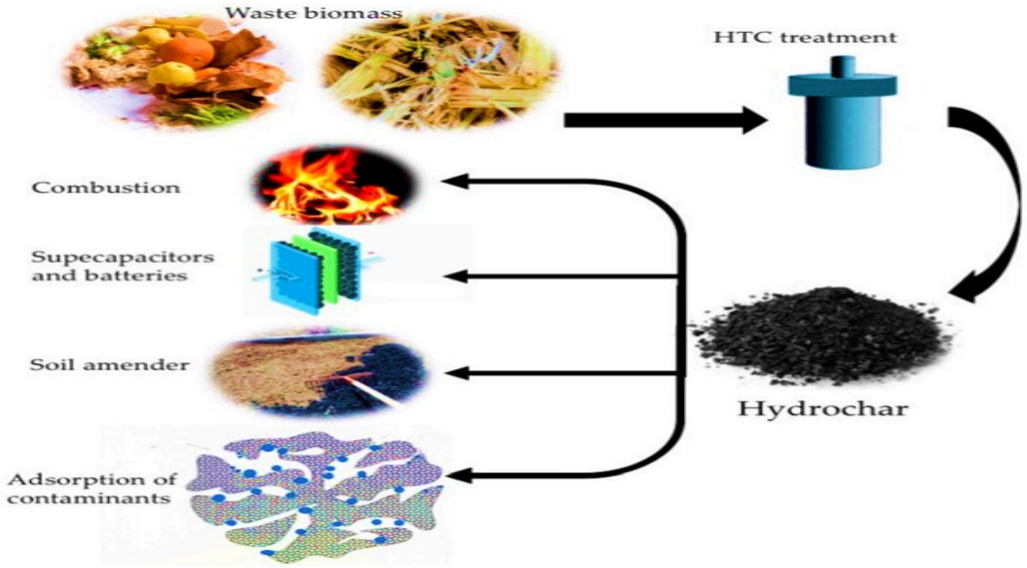

Figure 1.26. Conversion of wet biomass into energy by HTC method [107].

1.5.3 Challenges of HCs

Although the benefits of HCs (cheap, plentiful, eco-friendly, and high specific capacity) for use in alkali metal-ion batteries are inevitable, there are still a few major obstacles preventing their widespread application in practical applications (Figure 1.27). One of the main issues is the low initial coulombic efficiency (ICE) of HCs, which is caused by the ions' irreversible adsorption on the pores and defect sites (particularly in half-cells) [108]. For the use of HCs in the battery sector, stable SEI layers and ICE are crucial. Low ICE is typically a result of electrolyte decomposition to create the SEI in the first cycle and poor reversibility of the lithiation/de-lithiation reaction. Alkali ions have an adsorption-insertion storage mechanism in HCs as an intercalation-type anode material, as was previously mentioned. In order to have more active sites and boost a battery's

specific capacity, the existence of defects and surface functional groups is essential. Nevertheless, these defects and surface functional groups (Figure 1.28) may cause a side reaction and irreversible absorption between defects/surface functional groups and alkali ion, leading to a large initial capacity loss in the initial cycle. Additionally, theoretical studies demonstrated that defects in carbon layers cause ions to trap and create a repulsive electric field, which lowers the ICE by interfering with the continuous ion flux [109]. As a result, the surface structure has a significant impact on how easily the ions may intercalate and de-intercalate [110].

There are ways to optimize the structure and thickness of the SEI layers in order to improve ICE. Since the electrolyte composition mostly determines the SEI layer properties of HCs, altering the electrolyte's solvents, salts, and additives may have some impact on the ICE [111,112].

The undesirable rate performance of HCs is another major reason hindering the wide application of HC anodes. For HCs in alkali-based batteries, a considerable amount of the capacities is delivered at low voltage plateaus with slow ionic diffusion. At high current densities, HC losses the plateau capacity (for example, <0.1 V vs. Na/Na^+) which results in poor rate capability in half cells and lower energy/power density in full cells [113,114]. HC anodes with high initial capacities also have been shown fast capacity decay after several cycles. The instability of the SEI layer (increasing the thickness, changing composition, and morphology) formed on the HC anodes increases the ohmic resistance and blocks the ionic diffusion, leading to high voltage hysteresis and causing capacity drop [39]. The other reason of the low electrochemical performance of HCs is associated with co-intercalation of solvent molecules together with the exfoliation of the graphite layers.

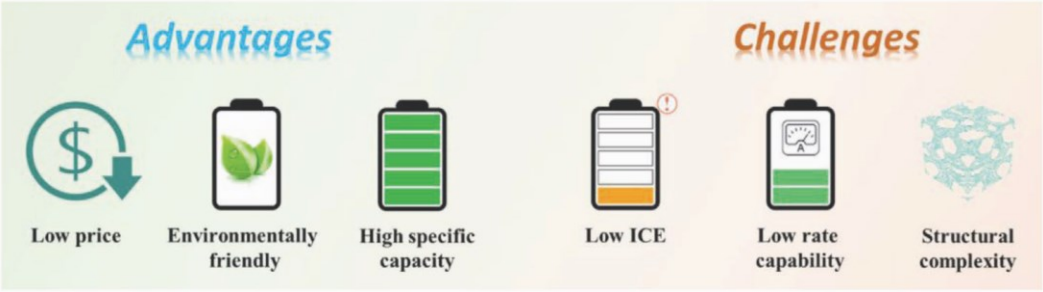

Figure 1.27. Advantages and challenges of HCs for application in alkali metal-ion batteries.

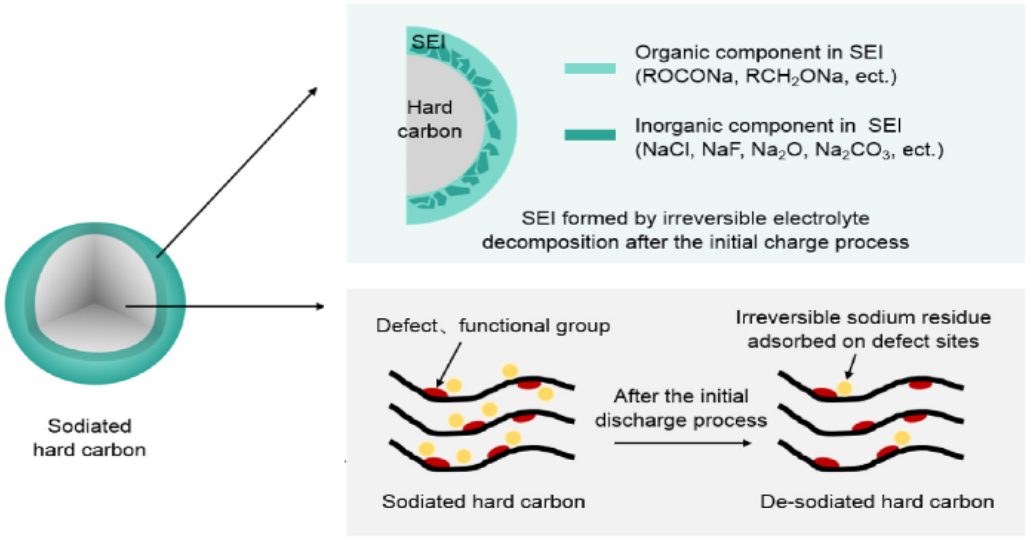

Figure 1.28. The factors leading to low ICE of HCs in akali-based batteries.

A full understanding of the HC's structure, reactivity with the electrolyte, ion transport, and storage mechanisms is vital to improving HCs' performance in LIBs. It is important to estimate and compare the theoretical and experimental capacities of HC. Even though several studies have been conducted, HC performance can still be enhanced. Due to the complexity of HC and the shortcomings of the characterisation methodologies, these materials are still far from lithium battery market. For the purpose of increasing capacity and ICE, HC defects and porosity are crucial. On the other hand, a clear strategy to fully utilize the Li storage capability is to increase the interlayer spacing of HC.

Despite significant advancements, more work needs to be done to engineer biomass structures in order to create devices that are suitable for real-world use. In fact, it is acknowledged that finding an effective approach for the use of waste biomass in the field of energy storage will create a new paradigm for widespread manufacture of green batteries, making the suggested plan appropriate for realistic scenarios. In this research, we have broken down the issue of sustainable batteries into its component elements, namely what kind of biomass waste materials to use and how to prepare them for application as battery anodes. In order to address the circular economy, another crucial environmental issue, we choose our materials accordingly. The need for scalability has also been taken into account in our deliberations. We assessed the proposed waste biomass' electrochemical

performance in both half-cell and full-cell LIBs configurations, giving us the broadest possible view of the anode electrode behaviour. In addition to analysing the materials in conventional LIBs, we offered a first-reported approach for designing the next-generation of LIBs (lithium-metal free (LiMF)) based on an amorphous hard carbon anode. However, further optimization is still needed to develop fast-charging LiMF based on sulfur chemistry, which will be important for the EVs and emerging markets such as drones and aviation.

Chapter 2 . Sustainable conventional lithium-ion batteries based on waste biochar as the anode electrode

Section 2.1 The effects of steam and CO_2 activations on the structural and electrochemical properties of Metal-free tannery waste biochar

In this chapter, we tackle the sustainable batteries topic by addressing its most defining aspects, namely what kind of waste material should be employed and its treatment for realizing performant battery anodes. In this regard, we focus on leather shaving waste (LSW), as it is an important waste element in many economies, hence resulting in an advantageous choice both from an environmental point of view and in terms of circular economy. Herein, especially metal-free LSW is used to introduce an innovative kind of eco-friendly anode for lithium-ion batteries (LIBs). A pyrolysis process of the waste material is adopted to form biochar, followed by its texture engineering through either steam or CO_2, both of them recognized as safe and environmentally friendly procedures. Indeed, these procedures develop hierarchical micro/mesopores in the biochar and modify the amount of oxygen-containing functional groups on its surface, which can lead to high performance anodes. In this respect, when water-based solvent and carboxymethyl cellulose (CMC) binder are employed, the fabricated electrode discloses high initial capacities and remarkable electrochemical stability in lithium-metal half-cells. In particular, the steam-activated electrode demonstrates a specific discharge capacity of 735 mAh g^{-1} after 1000 charge and discharge cycles at 0.5 A g^{-1}. This anode electrode also secures an excellent initial capacity and acceptable cycling stability in full-cell LIBs where a high mass $LiFePO_4$ loading cathode is employed. The results reported here represent a noticeable improvement with respect to the state of the art, hence demonstrating the enormous potential associated with the green re-use of wasting materials in important sectors such as energy storage.

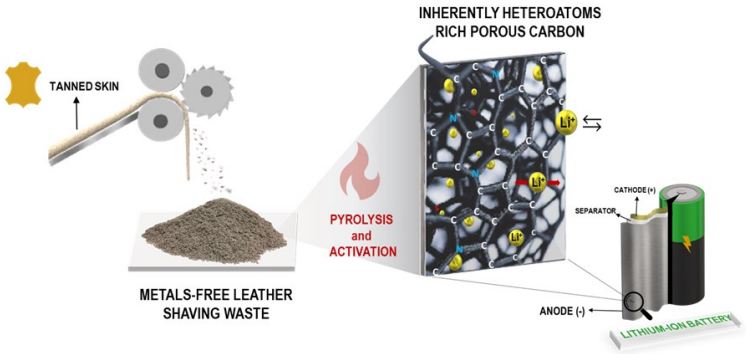

2.1.1 Introduction

The ever-growing demand for electrical energy related to the requirement to move towards sustainable and alternative energy sources, has driven the research to design and develop high-performance energy storage devices [115].

LIBs are now considered as the most popular energy storage system for portable electronic devices and transportation applications [41,116]. Among different types of energy storage devices, LIBs have shown superior electrochemical performance associated with high energy density, stability after long-term cycling, good rate capability, and no memory effects [117–119]. However, LIBs still face several challenges, particularly in electrode performance, which play a crucial role in battery efficiency [120]. Although conventional electrodes such as graphite, which is used as an anode part in commercial batteries, possess several advantages including low cost, high conductivity, and high cyclic and thermal stability, yet they could not meet the future needs of the battery industry [121]. The low theoretical capacity of 372 mAh g^{-1}, the poor diffusion kinetics of lithium (Li), the formation of lithium dendrites at low temperatures or high rates, are the main disadvantages of graphite electrodes for application in LIBs [87]. Most importantly, graphite relies heavily on fossil fuel-based precursors and harsh or energy-intensive synthesis [87,122,123]. Furthermore, the next-generation anodes based on Sn, Si, Ge, Fe, or Co, still has some drawbacks such as poor cyclic stability, large volume changes during charge and discharge processes, and large irreversible capacity that limit their application in the next prevalent generation of energy storage systems [124,125]. As an available natural resource, biochar (carbon-based materials obtained from biomass or industrial waste pyrolysis) has been considered as a high potential alternative to the abovementioned electrodes, to address the electrochemical performance, and environmental and economic concerns [87,126]. Biochar is categorized as non-graphitic/non-graphitizable carbons, and, its performance in LIBs' electrodes is highly dependent on its pore structure [127]. Several methods have been developed for biochar activation (i.e., pores formation combined to the change of the amount of functional groups containing heteroatoms on the biochar surface) and to design of hierarchical porous structure such as physical or chemical activation and activation using templates [128–131]. Biochar materials possess a crystalline disorder wherein the carbon sheets cross-links are rotated to each other. Through the activation process, the cross-links can be broken forming free layers carbon, an ideal situation for the introduction of heteroatoms such as O, N, and S. This heteroatoms insertion occurs especially at the outer region of the carbon

sheets configuration, while the internal region undergoes an ordering process known as localized crystallization. Physical activation using steam, CO_2, or air can enlarge the volume of biochar pores, and trigging the formation of micro-meso-macro hierarchical porous structure. Due to the formation of a hierarchical porous structure, and to the presence of optimum heteroatoms content such as N, O, H, S, Mg, and K, the lithiation capacity and stability of the activated biochar LIBs can be improved compared to those obtained by non-activated biochar [99,132,133].

In our earlier research, we discovered that biochar made from the green algae Cladophora glomerata is more electrochemically stable and capable in LIBs and supercapacitors than graphite [41,134]. In this work, the activated carbon obtained from pyrolysis of metals-free leather shaving waste (by LIFE GOAST technology, Green Organic Agents for Sustainable Tanneries) is investigated as anode electrode in LIBs. Leather industry plays a very important role in our society from socio-economic point of view. There are approximately 10,000 tanneries in the world producing leather more than 6.5 million tons per year. Even though the leather industry uses a by-product from the meat industry as raw material, it is considered as an activity demanding for integrated prevention and control of pollution [135]. Along the entire process from raw skins/hides to finished leather, a huge amount of solid and water wastes are generated. The solid wastes include fleshings, raw trimmings, shavings, buffing dust, etc. One of the most abundant solid wastes (ca. 25% in weight of leather) generated throughout the leather tanning is the shaving waste. Leather shaving is a mechanical process that aims to reduce the tanned skin to specific thickness prior to tanning and finishing. Such product is mainly made of collagen and tanning agent used [136]. At the present time, over 85 % of the world leather formation is from chrome tanned [137]. Consequently, large amounts of chromium-containing shaving wastes need to be treated and disposed. The major concern about the management of this kind of solid waste is ascribed to chrome content, which makes the convention disposal methods, such as landfilling and incineration, not a practicable solution. Therefore, many efforts have been developed in recent decades for promoting eco-friendly/alternative leather production and more effective waste management. Herein, shaving waste resulted from LIFE GOAST tanning technology is proposed as low-cost precursors for the preparation of carbon material as anode for LIBs. LIFE GOAST technology is established on the combination of innovatory chemicals and protocol which allows forming Chrome-Free leather with high quality. Since GOAST leather processing is 100% organic,

no heavy metals will be included in the shaving waste and into the biochar and activated carbon obtained.

The potential use of leather waste in lithium metal batteries was studied for the first time by Ashokkumar et al. [138]. After 40 charge and discharge cycles, the produced collagen-based electrode showed a reversible capacity of 327 mAh g^{-1} at the low current density of 0.05 A g^{-1}. Biochar derived leather waste was also demonstrated to be a highly efficient catalyst for oxygen reduction reaction, and a high specific capacitance for three electrode-based supercapacitor [139,140]. Despite the significant progress made, attempts to engineer the structure of biomass are still crucial for practical applications.

Here, we provide a sustainable method for creating inventive electrodes for half-cell and full-cell LIBs using waste from chrome-free leather shaving. This study's primary objective is to investigate and compare the physical characteristics of biochar made from leather waste using various methods (such as steam and CO_2 gas flow) in order to fabricate high potential electrodes for use in real LIBs. More importantly, for preparing a fully sustainable and environmentally friendly anode electrodes for LIBs, deionized water and carboxymethyl cellulose (CMC) have been used as alternatives to toxic and teratogen N-methyl-2- pyrrolidone (NMP) and biologically hazardous Polyvinylidene fluoride (PVdF), respectively [141]. Additionally, a much lower price of the water solvent and the flouride-free bio-derived CMC binder, compared to NMP and PVdF respectively, and applying $LiFePO_4$ (LFP) in full cell LIBs bring us closer to the goal of achieving a price forecast of 100 $ / kWh for greener LIBs in 2030 [142–144]. Besides, preparation of the water-based electrodes doesn’t need a controlled environment and, due to the higher vapour pressure of water in comparison with NMP, the water-based electrode drying is much faster [145].

2.1.2 Experimental Section

2.1.2.1 Synthesis of Tannery Waste Activated Carbons biochar

The pyrolysis process was carried out by a laboratory-scale prototype plant (Carbolite custom model EVT 12/450B). The experimental equipment consists of a vertical tubular furnace split into two halves along its length. The pyrolysis was performed in a fixed bed quartz tube equipped with a porous septum to hold the sample and to let the gas pass through, at the same time. The end flange of the quartz tube was connected to the quenching system through a heated outlet pipe (ca.

200°C) to prevent condensate build-up. The quenching system consisted of a first condenser, water-cooled at 20°C, which was linked to a series of glass condensers, cooled at 0°C in an ice bath, for collecting the condensable fraction.

The output of the condenser was directly connected to GC-TCD injector using an automatic sampling valve for the continuous non-condensable fraction analysis (out of this work). Additionally, a trap filled with quartz wool and magnesium perchlorate was located at the outlet of the quenching system in order to retain non-condensed products and water before the chromatography analysis. The furnace temperature was controlled using an electrical heater and a PID temperature controller. N-type thermocouples were used to measure both temperatures of the furnace and the quartz tube reactor. The desire inert gas flow (N_2) was set using a Brooks mass flow controller. The schematically pyrolysis plant is reported in Figure 2.1.

In a typical run, approximately 40 g of leather shaving waste (LSW) was placed into the reactor. The feedstock used was supplied by PASUBIO S.p.A. tannery (Arzignano, Italy). Before pyrolysis treatments, the LSW was sieved to < 0.250 mm and then air-dried for 48 h. Afterwards, the feedstock was pyrolyzed under nitrogen flow of 100 mL/min at 700°C with a heating rate of 5°C/min, and residence time of 30 minutes. The obtained biochar was labeled as LSW-Biochar.

The LSW-Biochar was then physically activated by steam (LSW-ACS) or CO_2 (LSW-ACC) flow. For synthesizing LSW-ACS, LSW-Biochar was treated at 800 °C under 57 vol.% steam/ N_2 mixture for four hours, with a total gas flow of 160 mL/min. LSW-Biochar was activated under the same reaction circumstances as LSW-ACC, but CO_2 gas flow was used as the activating agent instead. After that, 1.0 M HCl solution and deionized water was used to remove the contaminants from the biochars' surface.

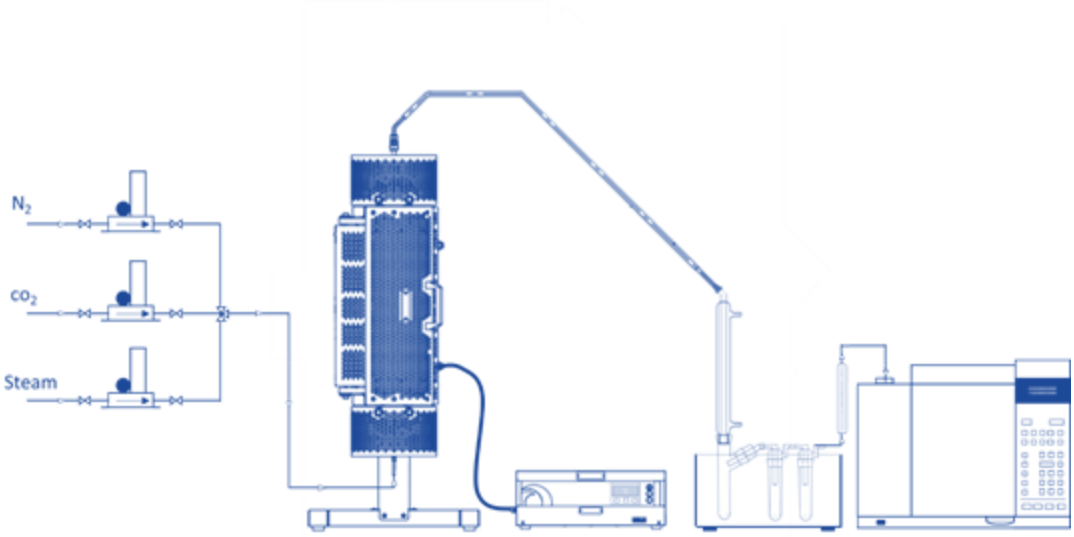

Figure 2.1. The schematically laboratory-scale prototype.

2.1.2.2 Material Characterization

The oxygen content was calculated by difference after the CHNS elemental analysis was completed using the UNICUBE organic elemental analyzer (Elementar). Thermogravimetric analysis (TGA 8000 PerkinElmer) was used to determine the ash content in accordance with ASTM-D7582 protocol. Surface functionality was examined by Attenuated Total Reflection Fourier Transform Infrared Spectroscopy (ATR-FTIR) using a Perkin Elmer Frontier FT-IR spectrometer over a wavenumber range of 400-4000 cm^{-1} at room temperature and resolution of 4 cm^{-1}. To investigate the existence of heteroatoms and their binding to the carbon matrix X-ray photoelectron spectroscopy (XPS) was carried out with a Kratos Axis Ultra DLD spectrometer equipped with a monochromatic Al Kα source (15 kV, 20 mA). Nitrogen physisorption measurements were performed at -196 °C using a Micromeritics Tristar II Plus sorptometer (MICROMERITICS USA). The samples (~100 mg) were outgassed at 200 °C for 2 hours before the sorption experiment. The BET and Langmuir equations were used to compute the surface area, and the total pore volume (V_{tot}) was estimated using the amount of N_2 that was adsorbed and P/P_0 (absolute pressure/saturation vapour pressure) values that were close to 0.98.

To ascertain the crystallinity, mineral content, and degree of order/disorder in the samples' structures, an X-ray diffractometer (XRD, Malvern PANalytical Empyrean) outfitted with a 1.8

kW CuK sealed ceramic tube and a Renishaw in-Via Micro Raman system with a 532 nm laser source were utilized.

Using a JEOL JSM-6490LA SEM Analytical (low-vacuum) scanning electron microscope, the morphology of non-activated and activated carbons was examined (SEM). The activated samples were further examined using a JEOL JSM-7500 FA (Jeol, Tokyo, Japan) field emission scanning electron microscope (FE-SEM) while operating at an acceleration voltage of 5 to 10 kV and taking secondary electrons into consideration for improving the morphological structures.

2.1.2.3 Electrode Preparation and Cell assembly

By combining 70wt% (activated)biochar material, 20wt% conductive carbon black agent, and 10wt% CMC as the binder, the electrodes were made using an environmentally friendly process. The mixture was ground in a mortar to form a slurry, and then deionized water was added as a solvent. The mixture was then stirred until it became a completely homogeneous slurry. The slurry was then cast using the doctor blade process on a copper foil at a thickness of 200 µm. The electrode foil was dried for 3 h at 80 °C. Thereafter, the dried sheet was punched into circular discs with a diameter of 15 mm. The electrode discs were then vacuum-dried using a Buchi apparatus for a further 12 hours at room temperature. The discs were then transferred in an argon-filled glove box (MBraun) with oxygen and water content below 0.1 ppm at the end of this procedure. The active substance had a mass loading of between 0.8 and 1 mg cm^{-2}. Lithium metal chips served as the anode, a microporous membrane (Celgard 3501) served as the separator, and 1.0 M $LiPF_6$ solution in a 1:1 (V/V) ratio of ethylene carbonate: dimethyl carbonate (LP30) used as the electrolyte (Merck, battery grade) for the cell assembly.

To investigate the performance of the biowaste in full-cell LIBs, we selected the LSW-ACS anode electrode because of its good electrochemical stability in half cell studies. This electrode was pre-lithiated before being coupled to a commercial LFP (NEI corporation) as the cathode. The mass loading of single-coated LFP cathode on aluminum foil was 14.5 mg cm^{-2}. To assure strong reversibility of LSW-ACS vs lithium metal, the pre-lithiation of the LSW-ACS anode was conducted with a discharge at the extremely low current density of 0.05 A g^{-1} (based on LSW-ACS active mass). After the discharge process, Li/ LSW-ACS cell was disassembled, and the LSW-ACS electrode was rinsed with dimethyl carbonate in the argon-filled glove box. Afterward, the full-cell was assembled in the LSW-ACS: LFP mass ratio of 1:3.6; the ratio number is based on

the capacity ratio Q_{Anode}:$Q_{Cathode}$ at low current density. It should be noted that the anode's active mass loading was changed to 4 mg cm^{-2} for the full cell. The same electrolyte and separator that were used in the half cell were also employed in the full-cell assembly. The laboratory-scale preparation of the electrodes and testing in 2032 coin-cells are schematically depicted in Figure 2.2.

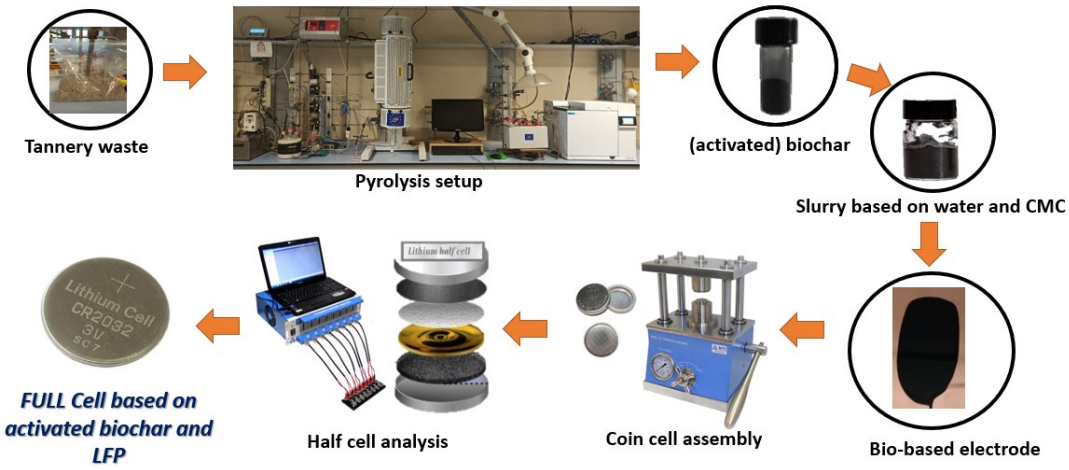

Figure 2.2. The schematically laboratory-scale preparation of the electrodes and testing in 2032 coin-cells.

2.1.2.4 Electrochemical measurements

2032 coin cells were used for the CV measurements, which were carried out at a scan rate of 0.05 mV s^{-1} with a potential range of 0.01-3.00 V. The half cells underwent charge/discharge experiments using a constant current (CC) technique. Based on the mass of the biowaste active material, the specific capacity of the half cells was assessed. Additionally, the CC condition was used for full-cell analysis in the 1.5–3.9 V range at 0.1 current-rate (equal to 0.1 C – 1C=170 mA /g_{LFP}). Electrochemical Impedance Spectroscopy (EIS) was also used in the frequency range from 10 kHz to 100 mHz at an open circuit with a 10 mV Alternating Current (AC). The obtained impedance spectra were analysed using Boukamp software, with a Chi-square goodness fit (χ^2) below 10^{-4}. A BCS-805 BioLogic equipment was used to conduct all of the electrochemical tests at room temperature.

2.1.3 Results and Discussion

2.1.3.1 Biochar and activated biochar characterization

Table 2.1 reveals the CHNS elemental analysis of the samples. The activation processes with steam and CO_2 entail oxidation reactions, which cause the production of porosity, as is commonly reported in the literature [146]. According to Table 2.1, the activation process with either steam or CO_2 determines the removal of nitrogen and sulfur from the pristine biochar, thus increasing the carbon content in the resulting samples. Particularly, steam activation appears to remove more sulfur and nitrogen than the CO_2 method. This feature can be attributed to the water molecule's lower size compared to CO_2 molecules, which makes it easier to activate through the diffusion of steam into the porous network [147]. Since both nitrogen and sulfur are helpful for enhancing lithium storage and enhancing reversible capacity, LSW-ACC currently seems to be the material of choice [148]. However, when O and C are included in the elemental analysis, the situation appears to shift in favor of LSW-ACS. Indeed, when CO_2 and steam are employed as oxidizing agents, they alter the functional groups on the active surface that contain oxygen. Our research indicates that LSW-ACC has a greater O/C ratio than LSW-ACS, indicating that CO_2 activation has produced more O-containing functional groups on the carbon surface. Importantly, a high content of O can reduce the stability of the biochar, hence negatively affecting its electrochemical response [149]. Analysis was done on how the activating agents affected the degree of carbonization. After the activation process, a large decrease in the H/C ratio suggests that the carbon structure is becoming more and more aromatic and carbonaceous [150]. The LSW-ACS sample has a lower H/C ratio than the LSW-ACC sample, which suggests a higher level of carbonization and a more condensate structure, both of which can improve the LSW-ACS sample's electrochemical stability.

Table 2.1. CHNS elemental analysis of LSW-Biochar, LSW-ACS, and LSW-ACC.

Sample	C [%]	N [%]	H [%]	S [%]	O [%]	Ash [%]	H/C	O/C
LSW-Biochar	71.6	11.0	1.8	1.1	5.8	8.7	0.025	0.08
LSW-ACS	77.8	4.0	1.3	0.6	4.7	11.6	0.016	0.06
LSW-ACC	73.4	7.4	1.3	1.0	5.3	11.6	0.018	0.07

ATR-FTIR was then applied to qualitatively analyse the functional groups on the carbon surface after the activation process. In the ATR-FTIR spectra of Figure 2.3, the weak intense band around 3600 cm^{-1} is due to the vibrations of O–H functional groups [151]. A strong band is observed at approximately 1600 cm^{-1}, which may be generated by the aromatic C=C stretching vibration and C=O stretching of conjugated ketones and quinones [152,153]. Although the IR profiles of the activated samples and the original biochar are comparable, it is still feasible to detect minor variations in the wavenumber range between 2300 cm^{-1} and 800 cm^{-1}, which is indicative of the surface functional groups of the structural network. The bands between 1700 cm^{-1} and 2300 cm^{-1} indicate carboxyl and carbonyl groups. The broad band in the 1400–900 cm^{-1} region is associated with a series of overlapping absorption bands stemmed from the contemporary presence of C–O bonds that are typical of alcohol, phenol, and ether bridges occurring between the aromatic rings and the nitrogen group component (N–C, N-COO) [41,154]. Interestingly, these overlapping bands undergo a change in shape and intensity upon the occurrence of the activation process (blue and red lines), demonstrating a different distribution of nitrogen and oxygen functional groups on the material surface. Specifically, for LSW-ACC (red line), the maximum of absorption shifts to a lower value (near 1140 cm^{-1}) than the pristine biochar (1210 cm^{-1}). The shift might be explained by a negligible N-bond contribution to the absorption band, in line with the decreased nitrogen content discovered by CHNS elemental analysis. The aforementioned overlapping bands are faint peaks at 1220, 1120, and 1020 cm^{-1} when LSW-ACS (blue line) is instead taken into account, indicating a reduction in the number of surface functional groups compared to LSW-ACC.

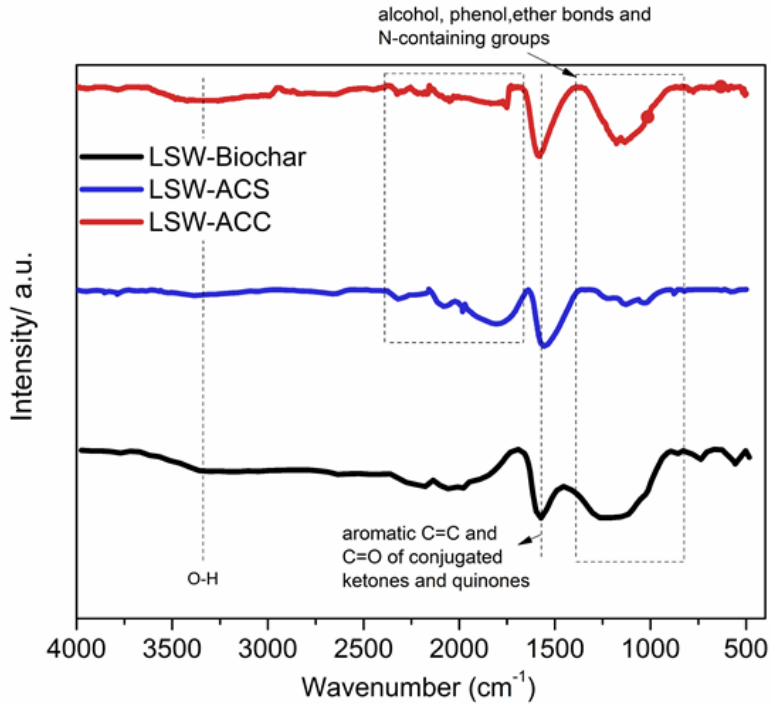

Figure 2.3. ATR-FTIR spectra of LSW-ACC, LSW-ACS, and LSW-Biochar.

By using XPS, the effective heteroatom doping of LSW-Biochar was examined. Figure 2.4 indicates X-ray photoemission high-resolution spectra on oxygen, nitrogen, and sulfur energy regions, together with the results of the best-fit procedure. Analysis of the N 1s region shows that N is effectively bound to carbon in several states (Pyridinic N, Amino N, Pyrrolic N, Graphitic N). The low intensity peak at 402.6 ± 0.2 eV suggests that some nitrogen atoms are in the form of oxygenated compounds: pyridine N-oxide [155]. Four different chemical states are fitted to the sulfur signal. The fitting demonstrated that the primary source of sulfur is either C-S-C or thiophene (peaks at 163.70, and 164.5 eV). The presence of a peak at 532.6 eV in the O 1s spectrum is associated with oxygen atoms in various oxygen groups, including C= O, O-C-O and O=C-O [156]. It is essential to mention that the carbonized biowaste contains additional elements, such Mo, in addition to the S, N, and O groups.

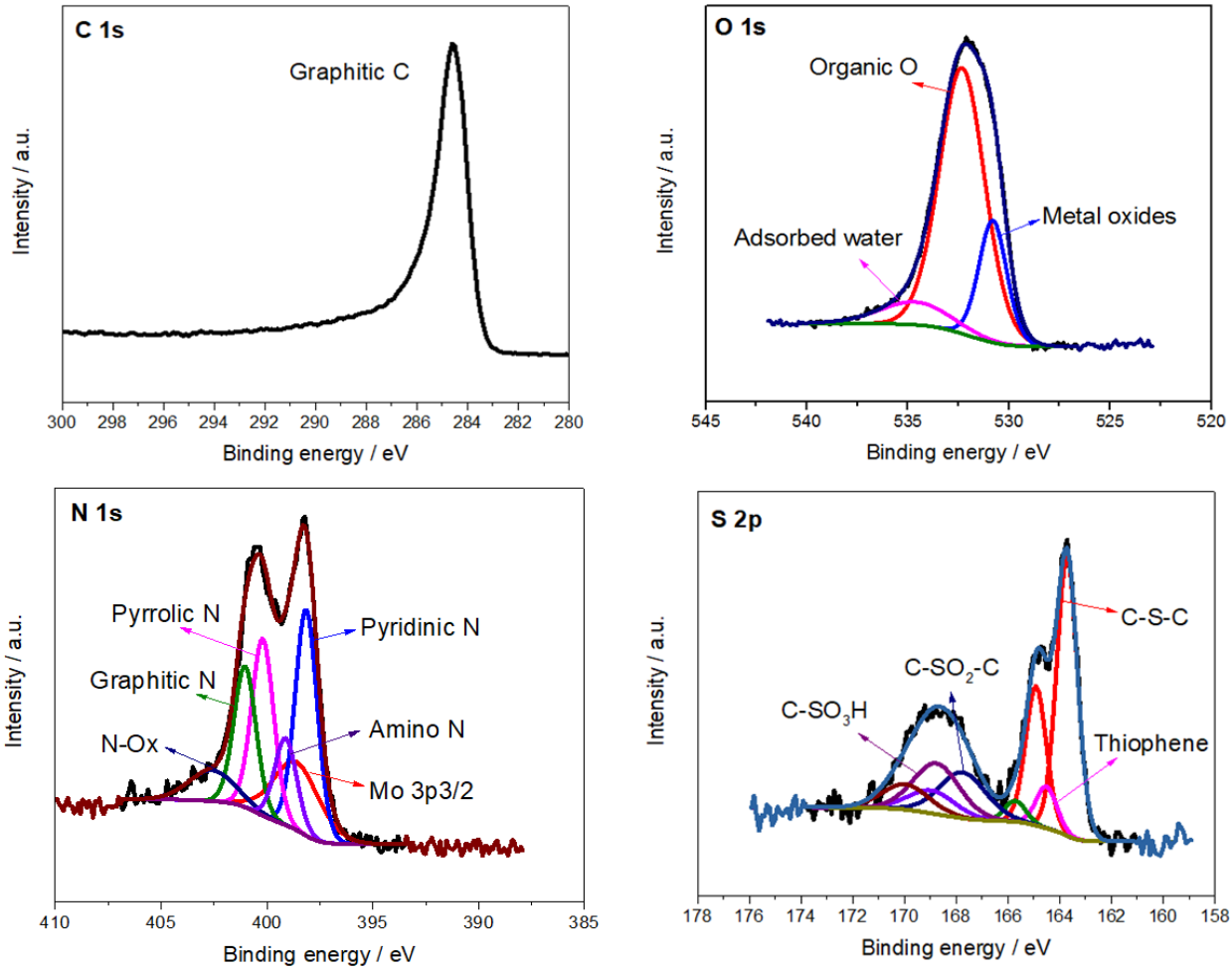

Figure 2.4. XPS spectrum of LSW-Biochar. C 1 s XPS spectrum, O 1s XPS spectrum, and N 1 s XPS spectrum, S 2p XPS spectrum.

Figure 2.5 shows nitrogen physisorption analysis which it was carried out to recognize the surface area and pore size distribution of the samples. The isotherm of the pristine LSW-Biochar (in the inset of Figure 2.5) does not match with any profile in the IUPAC classification. According to the findings, LSW-Biochar has a very low surface area and total pore volume that are typical of non-porous materials. These results can also be discovered in a variety of materials, such as carbon samples produced by the pyrolysis of waste from the leather-processing industry [157]. As depicted in Figure 2.5, the N_2 adsorption-desorption isotherms of the activated carbons show a composite nature, exhibiting the combination of type I and type IV isotherms with an apparent hysteresis loop of type H4. This suggests the co-existence of a micro and mesoporous structure. The initial region of reversible micropore filling is followed by multilayer physisorption and

capillary condensation. A micro/mesoporous activated carbon with a slit-like pore structure typically has a profile like this [152].

Both activated samples present high surface areas, large pore volumes, and wide average pore sizes (as summarized in Table 2.2). According to the BET surface analysis, the surface areas of LSW-ACS and LSW-ACC are equal to 726 and 858 $m^2\ g^{-1}$, respectively. Both activated samples' high surface area and hierarchical distribution of micro- and mesopores could offer a large number of sites for charge-transfer reactions and for cutting the diffusion time for lithium ions, respectively.

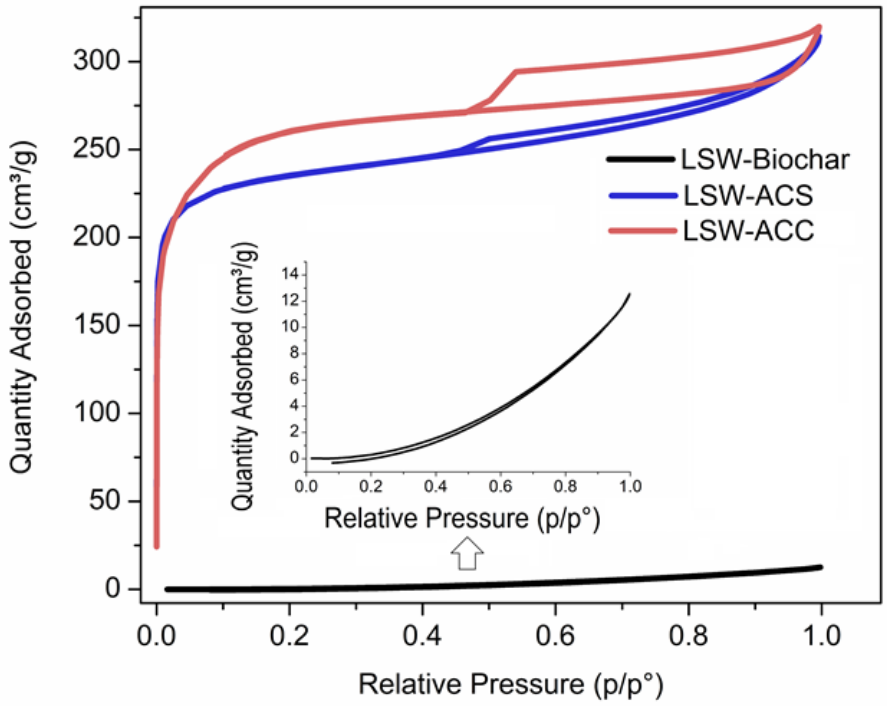

Figure 2.5. Nitrogen adsorption-desorption isotherms of LSW-ACC (red line), LSW-ACS (blue line), and LSW-Biochar (black line).

Table 2.2. Results of nitrogen physisorption analysis.

Sample	S_{BET} $(m^2 g^{-1})$	$S_{langmuir}$ $(m^2 g^{-1})$	S_{micro} $(m^2 g^{-1})$	V_{tot} $(cm^3 g^{-1})$	V_{micro} $(cm^3 g^{-1})$	V_{meso} $(cm^3 g^{-1})$
LSW-ACS	726	1.029	865	0.45	0.27	0.18
LSW-ACC	858	1.165	975	0.48	0.29	0.19

Figure 2.6 exhibits the XRD patterns of the carbonized materials. The patterns show the same features observed in most disordered carbon materials [158]. Two prominent broad diffraction peaks are present at 2θ 25° and ~44°, which are related to the (002) and (100) reflection planes [159]. The shape of these peaks confirms the presence of a disordered turbostratic carbon structure [160]. According to the Bragg's law [161], the interlayer distance of graphitic layers (d_{002}) is calculated in the range ~0.351 - 0.359 nm. Additionally, the thickness (L_c), and the average width of the graphitic domains (L_a), calculated using the Scherrer equation [162], are very similar for all samples, ~0.95 - 1.01 nm for L_c, and 2.08 - 2.37 nm for L_a. Table 2.3 reports the parameters calculated from each sample. Based on these results, the carbonized samples are estimated to be composed by ~3 stacked graphene layers (i.e., 0.98/0.36= 2.72) [163]. In addition to (002) and (100) reflections, several sharp peaks are present in the XRD patterns, which can be associated with some inorganic phases such as NaCl (ICSD- 41439), probably arising from HCl used in the synthesis process, and crystalline SiO_2 (quartz (ICSD 83849), and Trydimite (ICSD 176)), typical contaminations present in quartz reactors.

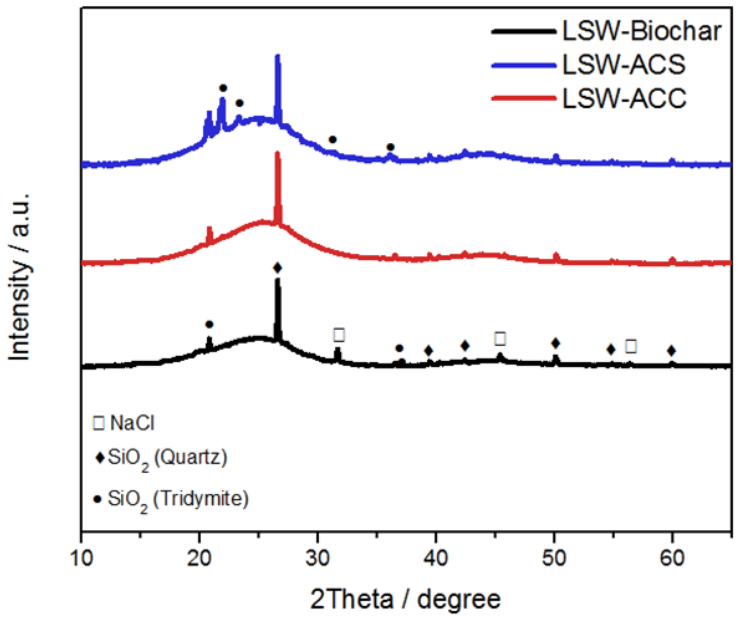

Figure 2.6. XRD patterns of LSW-ACS, LSW-ACC, and LSW-Biochar.

The interlayer distance of graphitic layers (d_{002}) is calculated by using Bragg equation:

$$\lambda = 2d_{002}\sin\theta \qquad \textit{Equation 2.1}$$

Here, λ is the wavelength of the X-ray beam.

The thickness (L_c), and the average width of the graphitic domains (L_a) of the carbonized samples are calculated according to the Scherrer's equation:

$$L_c = 0.89\lambda/(\beta_{002}\cos\theta_B) \; ; \; L_a = 1.84\lambda/(\beta_{100}\cos\theta_B) \qquad \text{Equation 2.2}$$

where λ is the wavelength of the X-ray beam, β is the peak width at half-maximum intensity (FWHM in radians), and θ_B is the Bragg angle (in degrees).

Table 2.3. Parameters calculated from the XRD patterns.

Sample	L_a (nm)	L_c (nm)	d_{002} (nm)	FWHM (002)	FWHM
LSW-Biochar	2.37	0.98	0.359	8.22	7.38
LSW-ACC	2.20	1.01	0.351	7.95	7.96
LSW-ACS	2.08	0.95	0.358	8.43	8.41

Raman spectroscopy (Figure 2.7) was then carried out for the LSW-Biochar, LSW-ACS, and LSW-ACC electrodes to determine the carbon order and the number of defects. The broad D band located around 1360 cm^{-1} is related to the edges, defects, and disorders of carbonaceous materials [40]. The graphitic layers, on the other hand, are represented by the G band at roughly 1600 cm^{-1}, which exhibits sp^2 hybridized carbon [40,164]. The amount of disorder in the carbon may typically be estimated using the I_D/I_G ratio (I_D/I_G is proportional to the disorder) [165]. In this respect, the I_D/I_G ratio for LSW-ACC is equal to 0.91, a value higher than the corresponding ratio for LSW-ACS (I_D/I_G= 0.88). This disparity shows that LSW-ACC has a lower graphitic order, presumably as a result of the significant amounts of S and N elements present in the graphene layers [149]. Another important quantity to consider is $I_D/(I_D+I_G)$ which describes the ratio of defects along the whole graphene sheets [166]. The $I_D/(I_D+I_G)$ value of LSW-Biochar, LSW-ACC and LSW-ACS are 0.50, 0.48 and 0.47, respectively. These results reveal that the activation process and the elevated temperature can slightly diminish the number of defects. The higher defect density in LSW-ACC compared to LSW-ACS supports the idea that the degree of graphitization decreases with the increase of defect concentration. In this respect, and as previously reported [167], the amount of defects introduced by N atoms into carbon structures increases the number of active sites for Li storage. Although both defects and a high degree of ordered graphitic carbon can affect

an electrochemical material's performance, a trade-off between the two needs to be determined when evaluating a material's overall electrochemical performance [148,167].

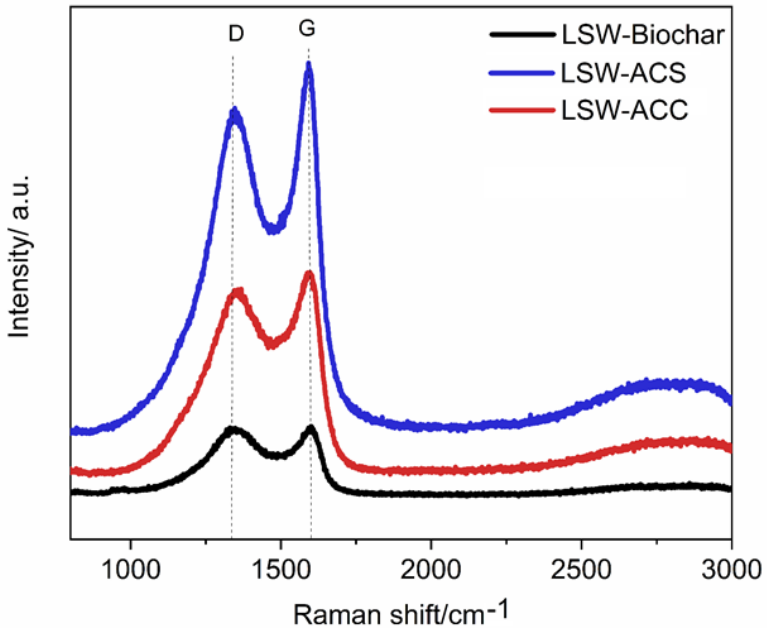

Figure 2.7. Raman patterns of LSW-ACS, LSW-ACC, and LSW-Biochar.

Scanning electron microscope (SEM) and field emission scanning electron microscope (FESEM) pictures were used to monitor the morphology of the activated carbon samples. According to the SEM images in Figure 2.8a, LSW-Biochar exhibits a morphology like glass shards fragments with no apparent pores on the surface. This finding implies that a well-defined porosity cannot be produced by pyrolysis alone. As opposed to this, a visible porosity can be seen in the activated samples. SEM and FESEM images of LSW-ACS in Figure 2.8(b-d) show an uniform distribution of olive-shaped pores on the biochar surface [134]. Additionally, LSW-ACS appears to have higher order porosity than LSW-ACC, which is consistent with the findings of elemental, Raman, and N2 adsorption-desorption isotherm investigations. The higher order porosity of LSW-ACS vs. LSW-ACC is associated with the smaller dimension of the H_2O molecule [168,169]. Indeed, its small dimension makes H_2O more effective than CO_2 in the removal of non-carbonaceous materials, therefore leading to the formation of high order micro-porous structures on the biochar surface [139]. This is confirmed by Figure 2.8(e-g), where is shown an irregular surface of LSW-

ACC given by different pores dimensions and channel sizes, and related to the higher amount of N, O, and S (Table 2.1). Additionally, it seems that using CO_2 as an activation agent causes the biochar surface to develop more mesopores than micropores. This would support the results of the earlier Raman investigation, which showed that LWS-ACC had a higher amorphous grade than LWS-ACS.

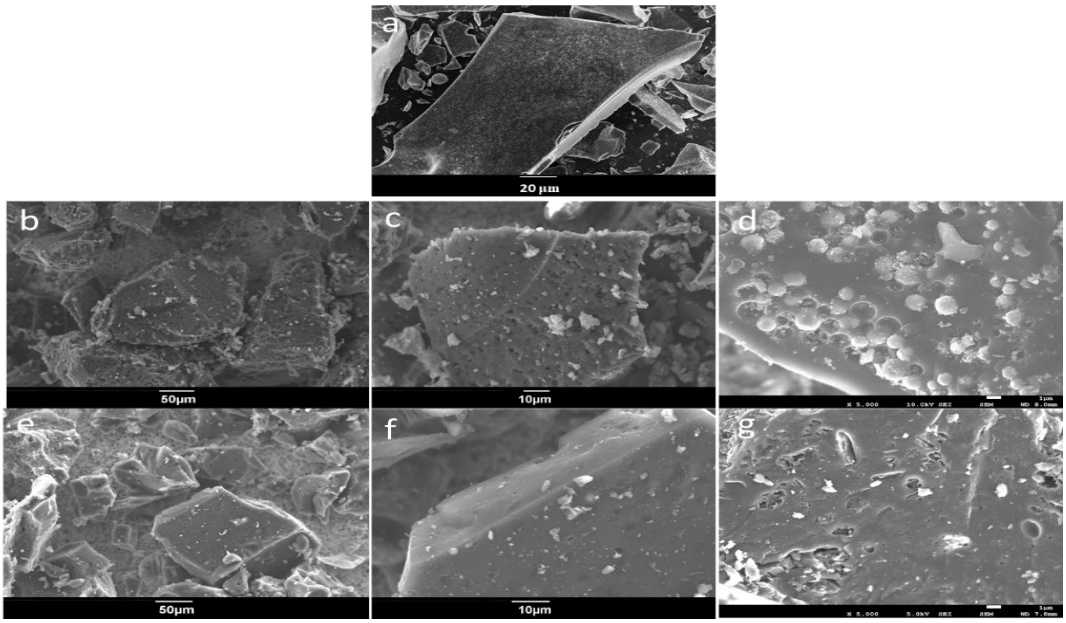

Figure 2.8. SEM image of LSW-Biochar (a), SEM (b, c), and FESEM images (d) of LSW-ACS sample. SEM (e, f), and FESEM images (g) of LSW-ACC sample.

2.3.1.2 Electrochemical performance of biochar and activated biochar

Galvanostatic charge-discharge cycling, CV, and EIS techniques were used to assess the electrochemical performance of LSW-Biochar, LSW-ACS, and LSW-ACC electrodes. By using CV analysis with a 0.05 mV s^{-1} scan rate, the electrochemical processes of the LSW-Biochar, LSW-ACS, and LSW-ACC electrodes were evaluated during the first 10 cycles. Figure 2.9(a-c) shows two reduction peaks at around 1.5 and 0.7 V in the first cycle which are related to the irreversible reaction of the electrolyte with surface functionalities of the bio electrodes, and solid electrolyte interface (SEI) formation, respectively [170,171]. Because of the high level of nitrogen content in the LSW-Biochar and LSW-ACC electrodes, the cathodic peaks at around 0.7 V are not clear meaning that the surface of the electrode is relatively resistant to electrolyte degradation [148]. After completing bio electrodes lithiation, the anodic peak related to their de-lithiation is

clear at about 0.2 V [119]. In LSW-Biochar and LSW-ACS electrodes, also a broad oxidation peak at about 1 V is obvious that could be associated with the faradic capacitance on the surface/edge sites of the biochar product [172]. Besides, during the oxidation process in LSW-Biochar, a narrow peak is appeared at around 2.4 V which could be related to the transformation of Li_xS into the polysulfides [149]. Both the LSW-ACS and LSW-ACC electrodes, in contrast to LSW-Biochar, show a significant amount of overlap in the succeeding cycles, confirming the great reversibility and electrochemical stability of the activated electrodes.

The galvanostatic charge-discharge profiles of LSW-Biochar, LSW-ACS, and LSW-ACC at a current density of 0.1 A g^{-1} relative to the weight of the biowaste active material are shown in Figure 2.9(d-f). The initial discharge specific capacity of LSW-ACS is 1520 mAh g^{-1}, while its first charge specific capacity is 645 mAh g^{-1}, which led to an initial coulombic efficiency of 42.4%. However, the LSW-ACC electrode achieves an initial coulombic efficiency of 38.3%, which is attributed to the electrode's first discharge specific capacity of 2063 mAh g^{-1} and its first charge specific capacity of 789 mAh g^{-1}. The non-activated electrode shows the low initial specific discharge and charge capacities of 487 and 194 mAh g^{-1}. The LSW-ACS and LSW-high ACC's surface area, development of porosity, and creation of numerous micro- and mesopore defects and vacancies during the activation process, which provides more active sites for storing Li ions, are all factors that contribute to the remarkable higher initial capacity of activated electrodes compared to the LSW-Biochar [173].

Figure 2.9f demonstrates the visible plateau at around 1.6 V during first discharge. This plateau supports the presence of additional elements, such as N, O, and S, in the activated samples by CO_2 compared to LSW-ACS and is connected to the irreversible reaction of the electrolyte with surface functional groups of LSW-ACC. A certain amount of the heteroatoms could affect the electron density around N and O atoms, which leads to more Li ions holding [174].

Although both activated electrodes show low initial coulombic efficiencies, the second cycle efficiency increases to around 96% and after the initial cycles, the coulombic efficiencies enhance dramatically to the range of 99%, demonstrating the excellent stability of the activated electrodes. The low initial coulombic efficiency is a common phenomenon for turbostratic porous carbon structure [175]. The main causes of the observed initial efficiency are the electrolyte degradation on the large specific surface area of LSW-ACS and LSW-ACC electrodes (plateau at about 0.7 V

during the first discharge process in galvanostatic charge-discharge profiles), and the irreversible reduction of functional groups like dioxygen and oxygenated present in the turbostratic porous biowaste-based electrodes [174,176].

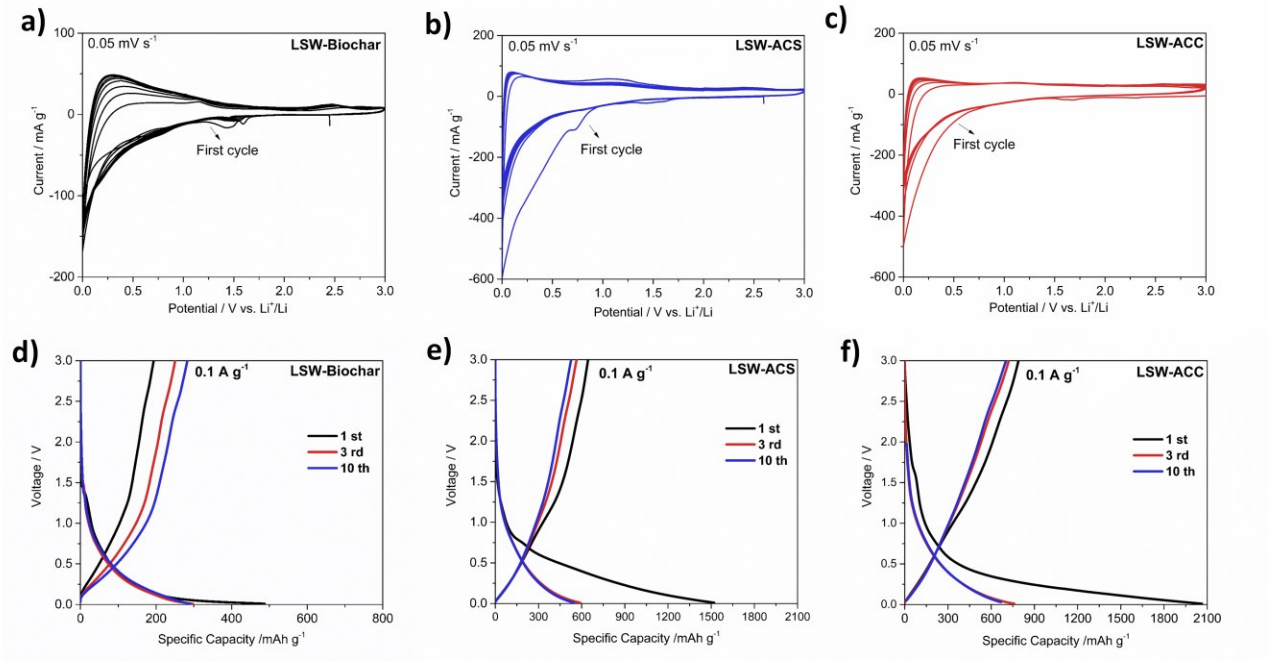

Figure 2.9. (a-c) CV curves of the biowaste electrodes at a scan rate of 0.05 mV s^{-1}. (d-f) Galvanostatic charge-discharge profiles. Performed in the lithium-metal half cells at room temperature within 0.01-3 V. (a, d) LSW-Biochar, (b, e) LSW-ACS, and (c, f) LSW-ACC.

Figure 2.10a shows the rate performance of LSW-Biochar, LSW-ACS, and LSW-ACC over cycling at different current densities. At 0.1, 0.2, 0.5, 0.7, 1, and 2 A g^{-1}, the specific discharge capacity of LSW-ACS is around 600, 490, 410, 380, 350, and 280 mA h g^{-1}, respectively, while for LSW-ACC the specific discharge capacity returns values around 760, 630, 500, 450, 407 and 319 mA h g^{-1}, respectively. At all the measured current densities, the non-activated electrode, in contrast, offers much lower reversible capacities. This demonstrates that through changing the surface properties of the biochar, such as surface texture, surface area, and porosity through CO_2 and steam activations, promote reversible Li-ion storage. Finally, when the current density rolls back to 0.1 A g^{-1}, all three electrodes show an excellent capacity retention of 100%.

The cycling performance of biowaste electrodes at 0.5 A g^{-1} (equivalent to ~1.4 C vs. graphite) is reported in Figure 2.10b. While the cell containing the LSW-Biochar electrode only exhibits an

initial discharge capacity of 100 mA h g^{-1} at 0.5 A g^{-1}, the cells with activated biochars exhibit an initial discharge capacity of roughly 400 mA h g^{-1} at the same condition. The low capacitance of the LSW-Biochar electrode is associated with its low surface area and non-porous structure that provide less active sites for Li-ions storage compared to LSW-ACS and LSW-ACC. Interestingly, the activated carbon-based electrodes exhibit capacity increase after the initial charge-discharge cycling process. This behaviour was also seen in earlier research using N, O-rich porous carbons made from biomass as an electrode for LIBs [125,177,178]. After many oxidation/reduction events, the electrolyte could have easy access to the electrodes' uncovered micro and mesopore sites, which could explain this behaviour [179]. Another factor is the decrease in internal resistance during cycling, as demonstrated by the Nyquist plots of LSW-ACS and LSW-ACC (Figure 2.11, Table 2.4). Finally, after 1500 charge and discharge cycles, LSW-Biochar, LSW-ACS, and LSW-ACC could still maintain 108, 625, and 267 mA h g^{-1}, respectively.

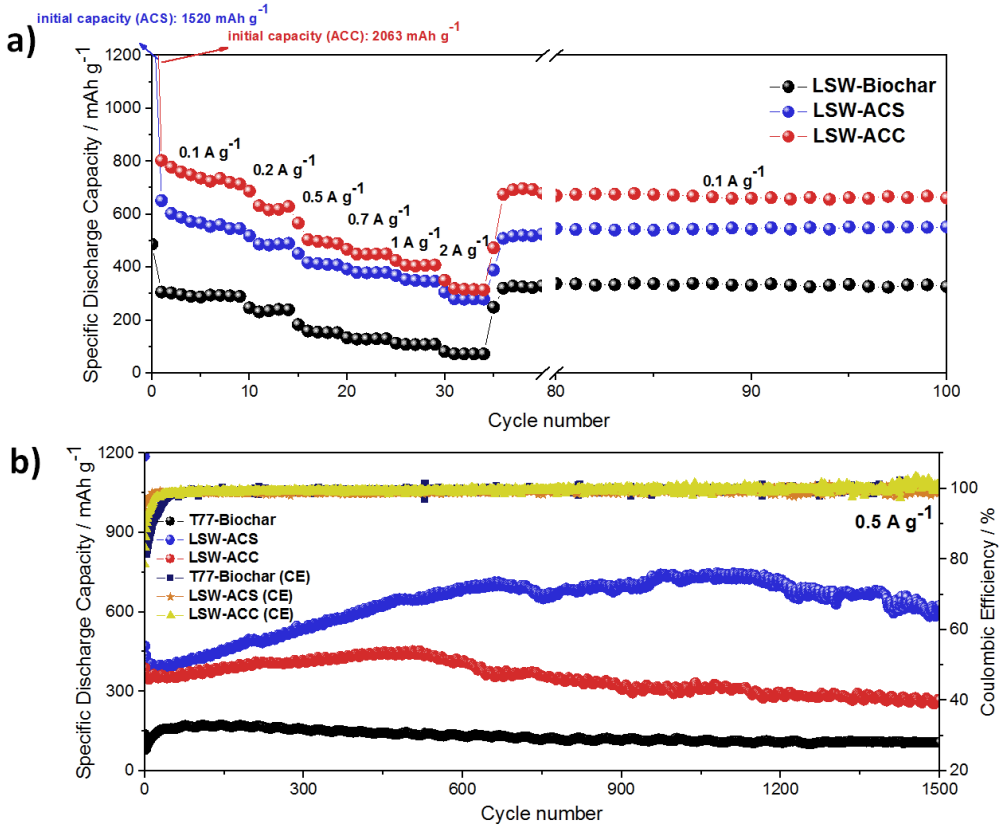

Figure 2.10. a) Rate capability of the carbonized samples over cycling at current density of 0.1, 0.2, 0.5, 0.7, 1, and 2 A g^{-1}, and b) cycling performance (current density of 0.5 A g^{-1}) of the carbonized samples performed in lithium-metal half cells at room temperature within 0.01-3 V. CE: coulombic efficiency.

The AC impedance was measured during cell assembly and after 500 cycles of 0.5 A g^{-1} cycling in order to determine why the LSW-ACS electrode had higher electrochemical stability than the LSW-ACC electrode as well as the cause for the capacity increase of the activated electrodes after cycling. The physical quantities resistance of the charge transfer kinetics through the electrode/electrolyte interface and the SEI film on the activated electrodes may be measured through EIS analysis and are two parameters that affect how well the electrodes operate in LIBs. The Nyquist plots in Figure 2.11a (fresh state) exhibit a semicircle in the middle frequency region that shows the charge transfer resistance (R_{ct}) in the electrolyte/electrode interface and a sloped line in the low-frequency region (Warburg impedance). The resistance of the electrolyte (R_s) is located before the first semicircle. The resistance of the SEI layer that forms during the first cycle on the surface of the electrodes can be determined by looking at the Nyquist plots after cycling. The numerical values of R_s, $R_{sei,}$ and R_{ct} (Table 2.4) were calculated by an equivalent circuit model (Figure 2.11b, c) obtained from Boukamp software. Before cycling, the R_s, and R_{ct} for both activated electrodes are around 10 and 50 Ω, respectively. However, after 500 cycling, R_{ct} is decreased to 8.6 and 15 Ω for LSW-ACS, and LSW-ACC, respectively. The decreased R_{ct} for both electrodes after cycling compared to that in the fresh condition reveals that the electrolyte can easily access unexposed micro- and mesopore sites after a number of oxidation/reduction reactions. Additionally, the lower R_{ct}, and R_{sei} values of LSW-ACS electrode compared to LSW-ACC demonstrate the better electrical conductivity and faster charge transfer kinetics during cycling process in very condensate structure of LSW-ACS with the fewer heteroatoms content and a higher degree of graphitization.

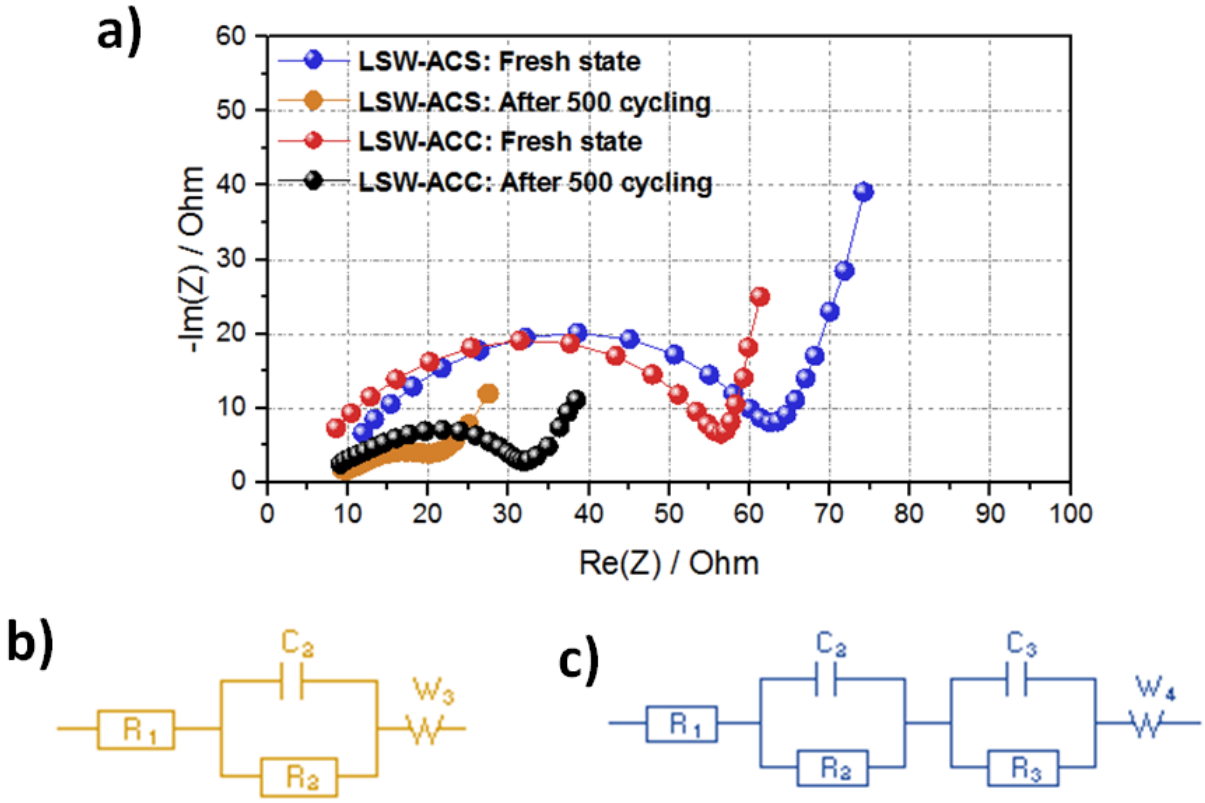

Figure 2.11. a) Nyquist plot of LSW-ACS, and LSW-ACC at fresh state, and after 500 cycling at 0.5 A g^{-1}. Equivalent circuit used to fit the experimental impedance spectra for b) fresh state, and c) after cycling.

Table 2.4. The fitting values of R_s and Rct, and R_{sei} for LSW-ACS and LSW-ACC at fresh state and after 500 charge and discharge cycles run at 0.5 A g^{-1}.

State	Resistance (Ω)	LSW- ACS	LSW-ACC
Fresh	R_s	12.9	9
	R_{ct}	49.7	45.9
After 500 cycles	R_s	8.9	8.7
	R_{ct}	8.6	15
	R_{sei}	4	6.9

To be noticed that a direct comparison between Figure 2.10a, and Figure 2.10b reveals what might appear as a controversial behaviour when observing the ratio between the specific capacities of LSW-ACC and LSW-ACS. Indeed, while in Figure 2.10a the electrochemical response of LSW-ACC is better than LSW-ACS, the opposite appears to occur in Figure 2.10b. The explanation lies in the low-rate activation performed in Figure 2.10a, where the initial test was performed at 0.1 A

g^{-1}, whereas in Figure 2.10b the test was immediately set at 0.5 A g^{-1}. As shown in Figure 2.12, we conducted the same type of analyses on the samples to support this theory, starting at an initial rate of 0.1 A g^{-1}.

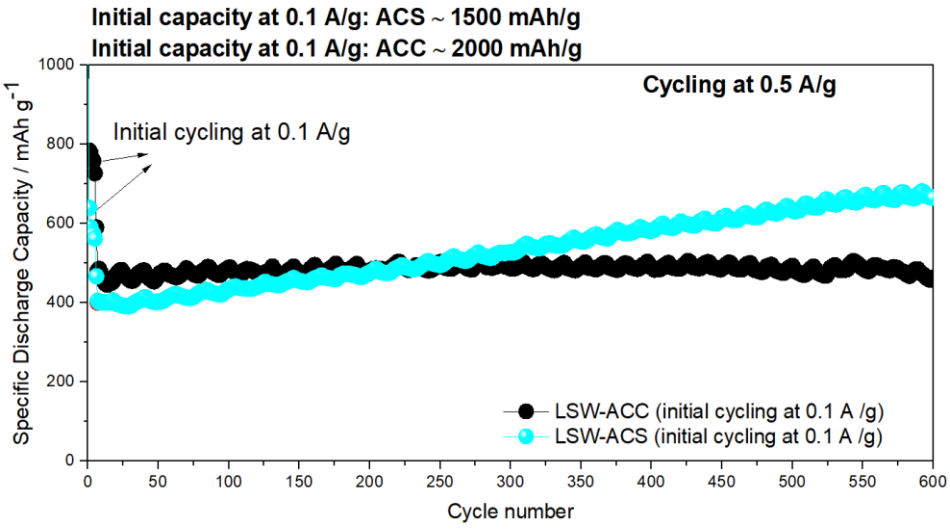

Figure 2.12. Specific discharge capacity for both samples, LSW-ACC and LSW-ACS at 0.5 A g^{-1} after an initial cycling at 0.1 A g^{-1}, performed in lithium-metal half cells at room temperature within 0.01-3 V.

The most significant recent publications that utilize biomass materials for anode preparation in lithium half cell batteries are listed in Table 2.5. The findings demonstrate the huge potential associated with the environmentally friendly reuse of waste materials in LIBs, showing how the sustainable strategy for material and electrode preparation in this work constitutes an upgrade compared to many articles reported to date. It should be highlighted that past studies frequently overlooked the environmentally favorable option.

The remarkable outcomes obtained here could be attributed to the designed materials' robust structural integrity, efficient porous architecture, and optimal heteroatom content (N, O, and S). These characteristics do, in fact, enhance the electrode's electrochemical performance by offering a suitable number of active sites.

Table 2.5. Comparison of the preparation methods and the main electrochemical criteria of different waste-based anode electrodes in Lithium half-cell batteries.

Sample	Preparation method	Initial discharge capacity (mA h g^{-1}) at low current density	Current density (A g^{-1}) & corresponding reversible capacity (mA h g^{-1}/Cycles)	Refs.
Tannery	Pyrolysis at 700 °C and CO_2 activation	2063 at 0.1 A g^{-1}	0.5 & 452 / 450th	*This work*
	Pyrolysis at 700 °C and steam activation	1520 at 0.1 A g^{-1}	0.5 & 625 / 1500th	
Rice husk	Multi-step heat treatment and carbonization under Ar gas at 600 °C	1627 at 0.075 A g^{-1}	0.075 & 757 / 150th	[180]
Wheat straw	KOH activation and carbonization at 800 °C in the inert N_2 atmosphere	797 at 0.037 A g^{-1} (0.1 C)	0.037 (0.1 C) & 310/ 100th	[181]
Leather	Carbonation at 1000 °C under Ar atmosphere	~750 at 0.05 A g^{-1}	0.05 & 327/ 50th	[138]
Garlic peel	KOH activation and carbonization at 850 °C in the Ar atmosphere	1825 at 0.05 A g^{-1}	0.1 & 540/ 100th	[182]
Corn stalk core	Calcination at 550 °C under N_2 atmosphere and KOH activation	1614.1 at 0.075 A g^{-1}	0.075 & 504/ 100th	[183]
Bamboo shoot hulls	Heat treatment and carbonization at 600 °C under Ar atmosphere	1319 at 0.2 A g^{-1}	3 & ~250/ 1000th	[184]
Hazelnut shell	Annealing under Ar/H2, carbonization at 900 °C, laser irradiation	1108 at 0.01 A g^{-1}	0.01 & 578/ 20th	[185]
Rice husk	Carbonization at 600 °C under N_2 atmosphere and hydrothermal NaOH treatment	1647 at 0.075 A g^{-1} (0.2C)	0.075 & 502/ 100th	[186]
Tannin-furanic resins	Heat treatment and carbonization at 1000 °C under Ar atmosphere	605 at 0.05 A g^{-1}	0.4 & 134/ 200th	[187]
Spruce Hard Carbon	H_3PO_4 activation and pyrolysis at 1100 °C	~385 at 0.037 A g^{-1} (0.1 C)	0.037 A g^{-1} (0.1 C) & ~300/ 400th	[188]
Tea-seed shells	calcination at 800 °C under flow and KOH activation	913 at 0.037 A g^{-1} (0.1 C)	0.037 (0.1 C) & 537/ 100th	[189]
Coffee ground	Carbonization at 800 °C under N_2 atmosphere	764 at 0.1 A g^{-1}	0.1 & 262/ 100th	[190]

The outcomes obtained with lithium-metal half-cells were subsequently validated in a full-cell configuration to give a scenario as complete as possible. Specifically, the full-cell employed high mass LFP loading as cathode, LSW-ACS as anode, and LP30 as electrolyte. Figure 2.13a displays the galvanostatic charge-discharge curves of the LSW-ACS/LFP full-cell during the 1st, 5th, 20th, and 50th cycles in the voltage range of 1.5 - 3.9 V at 0.1 C. At the first cycle, the charge and discharge capacities are 169, and 159 mA h g^{-1}, respectively, providing a coulombic efficiency as high as 94%. The average working potential of the cell is approximately 3.4 V. Interestingly, the outcomes are consistent with data that was previously published using a full-cell system with a low mass LFP loading and a graphite anode [191]. As shown in Figure 2.13b, after 50 cycles of charge/discharge, the biowaste-based full-cell maintains 80% of its initial capacity with a coulombic efficiency above 98%. The initial capacity and durability of the LSW-ACS/LFP full-cell are compared to those of state-of-the-art full-cell LIBs using graphite in Table 2.6. The table indicates that one of the promising choices for use as an anode material for lithium metal-free bio-based batteries is the biochar produced from leather waste using the engineering method described here.

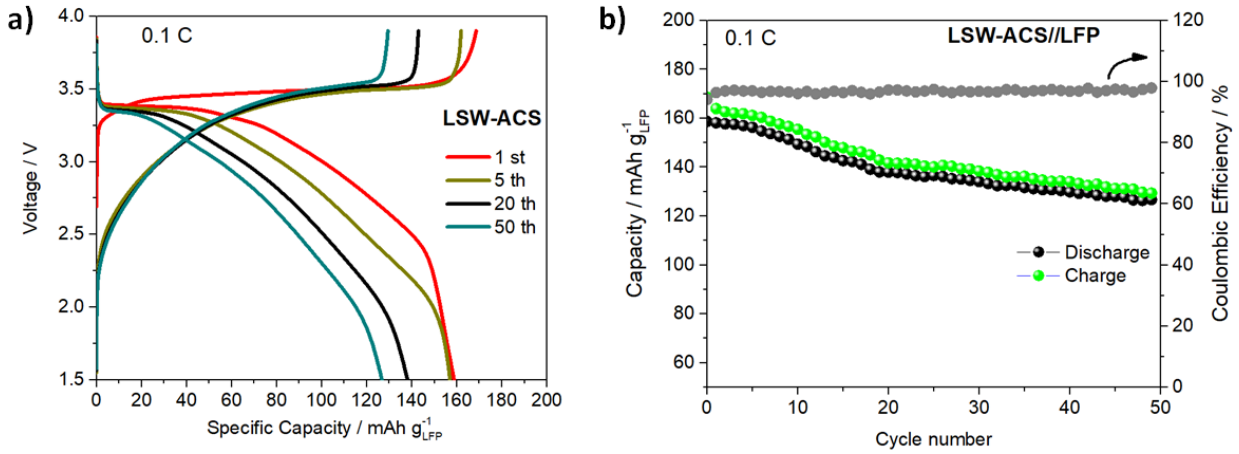

Figure 2.13. a) Galvanostatic charge-discharge profile, and b) cyclic performance of LSW-ACS/LFP full-cell in the range of 1.5 – 3.9 V at 0.1 C (1C= 170 mA /g_{LFP}), and room temperature. LFP= 14.5 mg cm^{-2}, LSW-ACS= 4 mg cm^{-2}. The specific capacity of the cell is reported according to LFP active mass.

Table 2.6. Electrochemical comparison of different LFP cathodes using different carbon-based anodes in LIBs full cells.

Full cell system	Rate (C)	Initial discharge capacity (mA h g^{-1})	Durability/ cycles	Refs.
LFP / A-pBC[1]	0.1	159	77% at 0.1 C / 40th	[192]
LFP / graphite	*0.5*	*127*	*65% at 0.5 C / 40th*	[191]
LFP / graphite	*0.5*	*~ 90*	*~ 89% at 0.5 C / 12th*	[193]
LFP / graphite	*0.2*	*~ 134*	*24% at 0.2 C / 100th*	[194]
LFP / graphite	*0.1*	*121*	*52 % at 2 C / 1000th*	[195]
LFP / LSW-ACS	*0.1*	*159*	*80%* at 0.1 C / 50th	*This work*

2.1.4 Conclusion

The physical and electrochemical characteristics of carbon material (biochar) made from waste chrome-free leather shavings were examined in this work for potential applications in LIBs. The desire to address environmental sustainability and the circular economy served as the main motivation. In this regard, a fully environmentally friendly and sustainable design process for bio-based electrodes that can be evaluated in both half- and full-cell configurations was created. In particular, two environmentally friendly activation methods were employed, based either on H_2O or CO_2. For both cases, the assembled lithium-metal half-cells have demonstrated good rate capability and cycling performance, with the H_2O-based cell providing the best long cycling result. Furthermore, as a practical example, a full-cell based on high mass LFP loading cathode and a H_2O-activated anode was realized. The findings revealed a 160 mA h g^{-1} initial discharge capacity

with acceptable cycle stability at 0.1 C. The promising performance described in this work is related to the activated biochars' hierarchical micro/mesopore structure, high specific surface area, heteroatoms-doped (N, O, and S), interlayer spacing, and defects. We think that this effort is a significant step in the right direction and brings us one step closer to having functional LIBs with minimal environmental effect. Finally, it is important to note that these discoveries are not limited to conventional LIBs and might be widely applicable to various electrochemical energy storage technologies, such as Na-ion batteries, Lithium-metal free sulfur batteries, or fuel cells.

Section 2.2 Food waste biochar as an alternative to graphite: Extraordinary stable Full LIBs with cattle bone anode

In the last decades, numerous scientific papers have been focusing on various types of biomasses and biowastes for application in lithium-ion batteries (LIBs). Indeed, it is recognized that carbon deriving from sustainable resources can be a promising alternative to current commercial materials for energy storage devices, particularly for LIBs. However, most of the research in LIBs' filed has been considering bio-based material in half-cell configuration. Here, we tackle the sustainable full-cell LIBs topic by addressing its most defining aspects, namely what kind of waste material should be employed and the electrode design for realizing LIBs with high performance. The material of choice, cattle bone, is categorized among the most abundant biowaste materials, thus the secondary use of this kind of material could be beneficial for the economy and environment. In this study, the factors affecting the full cell performance have been precisely identified and optimized to maximize the electrochemical performance of the cell. According to this, full-cell LIBs based on carbonized cattle bone anode and $LiFePO_4$ cathode reveal extraordinary cycling life at even high current rates. These promising results may fill up important knowledge gaps on the design of practical sustainable batteries. In this respect, the amount of cattle bone waste produced each year worldwide opens a paradigm for massive battery production, hence making the proposed scheme suitable for realistic scenarios.

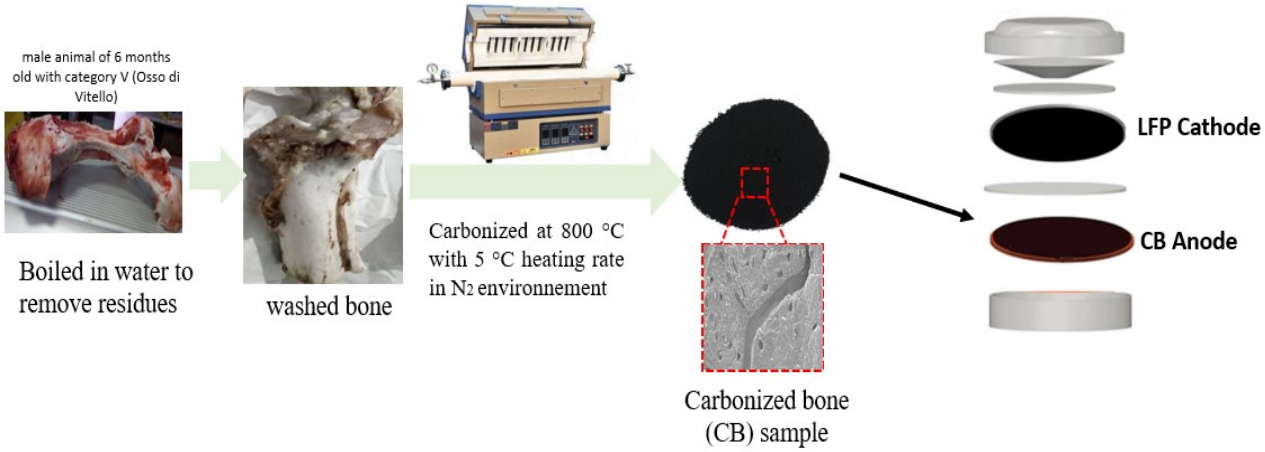

2.2.1 Introduction

In the last decades, numerous research papers have been focusing on various types of biomasses or biowastes for application in lithium-ion batteries (LIBs) [196]. It has been shown that carbon derived from sustainable resources is a promising candidate as replacement of standard graphite in energy storage sector [197]. However, most of the literature remains at the half-cell level, particularly in LIBs [183].

The non-graphitizable structure of carbonized biowaste/biomass (biochar) formed by amorphous/pseudo-graphitic nanodomains makes biochars an ideal ingredient for secondary batteries, particularly LIBs [87]. Apart from their important electrochemical properties, carbonized biobased materials are also low cost and available in great abundance, making this approach an optimal sustainable solution [198].

Animal bone is among the most abundant biowaste materials. According to a recent report, the global meat industry produces 130 billion kg of animal bone per annum with over 10% produced in the European Union [199]. The animal bone's composition is a valuable source for the development of diverse materials for advanced applications. Specifically, bone is an organic-inorganic composite that contains 22–45% collagen and 50–74% hydroxyapatite by weight [200], considered as a precursor for the preparation of high defect and low-cost porous carbon materials [201]. In the current study, cattle bone (CB) waste has been thermally treated and used as the anode electrode part for full-cell LIBs design.

One of the major challenges that full LIBs face is capacity decay during storage and charge-discharge cycling. Side effects may include decreased coulombic efficiency, decreased cell usable capacity, and increased cell impedance. Chemical degradation, which is known to be the primary cause of lithium loss in well-made LIBs, is the term used to describe cell performance degradation caused by side reactions. During charge and discharge, the solid-state diffusion of lithium atoms in and out of host electrode particles causes diffusion induced stresses and volume changes in the electrode particles. Depending on the operating conditions, these stresses may cause mechanical fatigue and fracture of the electrode particles, isolation of the electrode particles from the composite matrix, or SEI fracture [202]. The capacity balancing between the anode and cathode is crucial to reduce chemical degradation of the electrodes, which increases the full cell's

performance. The different ratios may significantly vary the cell voltage and its delivered capacity [203]. Thus, the balancing should be precisely performed to avoid the overcharge of the battery and plating of the anode which causes safety issues and deteriorates the system's cycle life. In this study, the factors affecting the full-cell performance have been precisely identified and optimized to maximize the electrochemical performance of the cell. Herein, we report an extraordinary cycle life LIBs based on the biowaste anode and $LiFePO_4$ (LFP) cathode. This battery technology is not dependent on critical raw materials such as manganese, cobalt and nickel. Finally, with respect to the electrochemical performance, the designed full-cell reveals specific capacities of 155, 140, 95, and 65 mAh /g_{LFP} during long cycling at 1, 2, 5, and 10C, respectively.

2.2.2 Experimental section

The details of the synthesizing process for the biochar production, and methods used for structural and electrochemical characterization in this part can be found elsewhere [197,198].

The CB electrode was fabricated with environmentally-friendly process with the assistance of carboxymethyl cellulose (CMC) and deionized water. The deionized water and CMC binder have been used as replacements for toxic N-methyl-2- pyrrolidone (NMP) and biologically hazardous polyvinylidene fluoride (PVdF), respectively. CB powder (70 wt%) was mixed with 20 wt% of conductive carbon black agent, and 10 wt% of CMC. After grinding, the mixture was dispersed into deionized water to make a homogenous slurry. Then, the obtained slurry was casted on the copper current collector (10 µm thickness) using doctor blade, then dried on the hot plate (3 h at 60 °C). Afterward, the electrodes disks were cut out with diameter of 12 mm. The punched electrodes were further dried using a Buchi apparatus for 4 h at 80 °C. The active mass loading of the electrodes was about 1-1.5 mg cm^{-2}.

The cathode electrode was fabricated by mixing the commercial LFP (NEI corporation), carbon black (Super P) and PVdF with a weight ratio of 80:10:10 in NMP. Then, the cathode slurry was coated on the aluminium current collector. The active mass loading of the LFP electrodes was about 2 mg cm^{-2} after drying.

The CV and galvanostatic charge and discharge analyses of Li/CB half-cell, and CB/LFP were performed in the potential/voltage range of 0.01-3 V, 0.8-3.9 V; respectively.

The 2032 coin cell, Celgard 2400 separator, and carbonate electrolyte (1M $LiPF_6$ in EC: DMC (LP30)) were used for the electrochemical analyses. All the electrochemical analyses were done at room temperature.

2.2.3 Results and discussion

2.2.3.1 Structural characterization of CB

Fourier transform infrared spectroscopy (FTIR) analysis was performed to explore the chemical composition of the carbonized sample (Figure 2.14a). The broad peak at 3281 cm^{-1} is related to the stretching vibration of OH due to adsorbed moisture. The bands at 872, 1414, and 1456 cm^{-1} are associated with the stretching vibrations of the carbonate group (CO_3^{-2}). The dominant band at 1007 cm^{-1} and the band at 961 cm^{-1} are for the stretching vibration of the phosphate group [204]. Furthermore, the peaks at 700 and 2014 cm^{-1} may be related to the N-C-N deformation and stretching modes of the cyanamide species which arise through the combustion of the nitrogen-containing compounds of the bone structure [205].

For clarity, the presence of heteroatoms was examined by X-ray photoelectron spectroscopy (XPS) analysis (Figure 2.14b). The peaks of C1s, O1s, Ca2p, and P2p are clear in the CB sample. The atomic percentage of C1s, O1s, Ca2p, and P2p for the carbonized sample is 37.82%, 39.17%, 13.28%, and 9.72%, respectively.

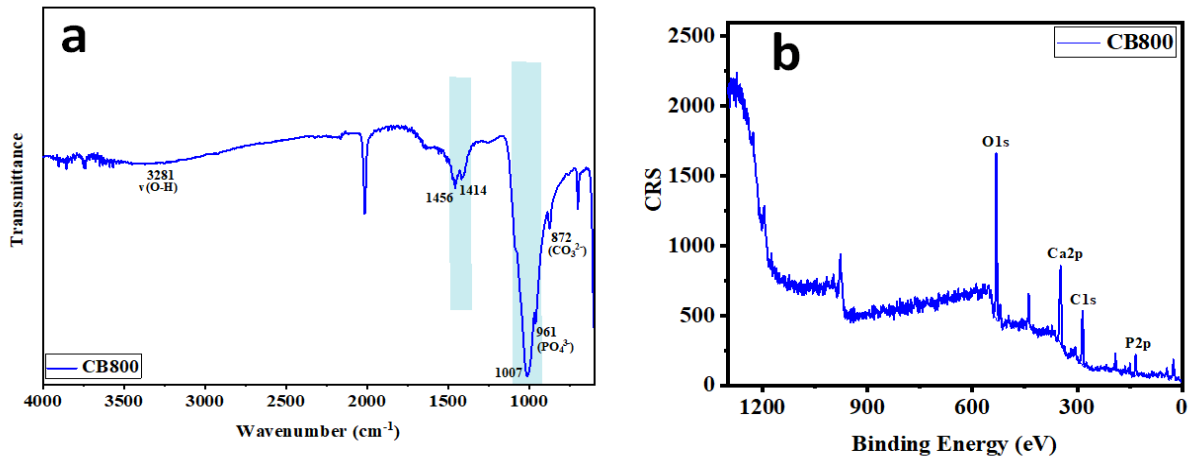

Figure 2.14. a) FTIR spectrum, and b) survey scan of XPS spectrum of CB.

X-ray diffraction (XRD) spectrum (Figure 2.15a) of the CB demonstrates the peaks which are associated with the characteristic peaks of standard hydroxyapatite (reference card (ICDD- 01-074-9761)) [206]. In the Raman spectra (Figure 2.15b), two prominent peaks at around 1350 cm^{-1} (D-band), and 1600 cm^{-1} (G-band) correspond to disordered or turbostratic structure, and sp^2-hybridized carbon of CB, respectively [197]. The intensity ratio between D-band and G-band (I_D/I_G) is used to quantify the disordered degree of sample. According to this equation, CB indicates a value of 0.85. This number confirms the high defect density in the sample due to the self-doped architectures of CB with O element and other elements such as Ca, and P.

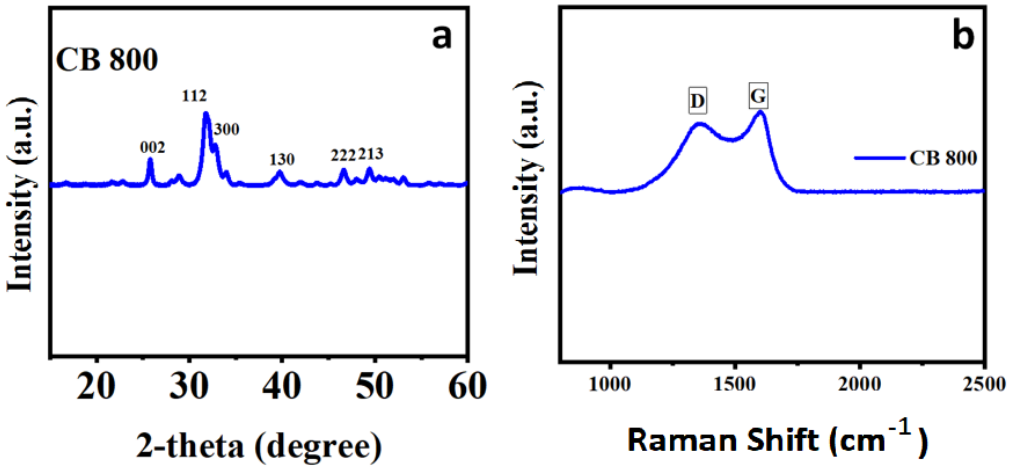

Figure 2.15. a) XRD pattern and b) Raman spectrum of CB.

To confirm and further evaluate the overall carbonized bone structure, scanning electron microscope (SEM) images of CB sample were acquired (Figure 2.16). The sample shows a porous structure consisting of a fibrous texture and highly interlinked longitudinal and transversal microchannels. Additionally, CB demonstrates the presence of longitudinal microchannels characteristic of the Haversian canals, that run throughout the bulk bone structure along its axis, and of transversal pores [207].

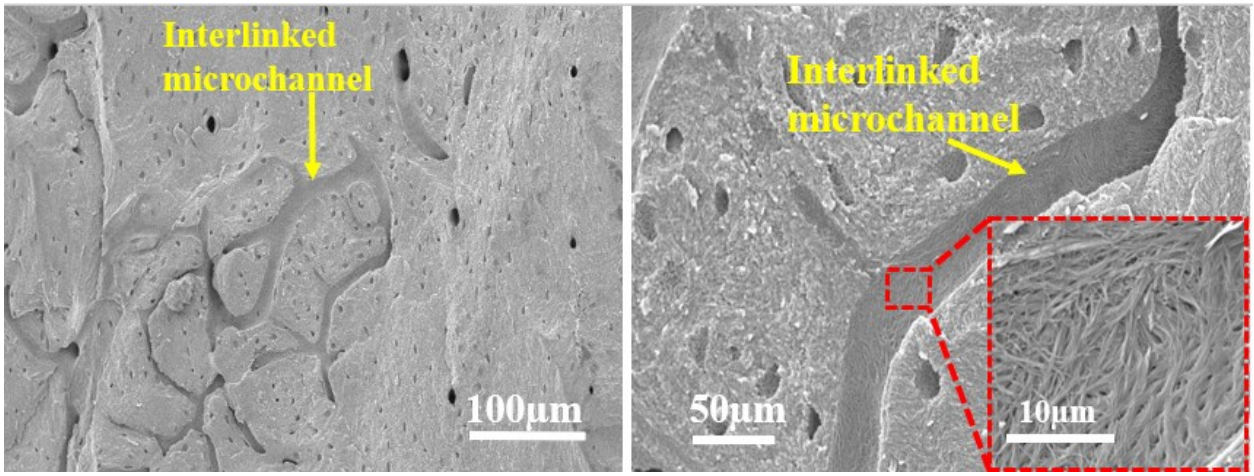

Figure 2.16. Cross-sectional SEM images of CB at different magnifications, showing the interlinked microchannels combined with fibrous-like structure and smaller pores of CB. Insets: Surface morphology of the microchannels at higher magnification.

The BET analysis also revealed the presence of mesopores within CB in the range from 3 to 20 nm, which can be attributed to the empty spaces between collagen fibres and the hydroxyapatite crystals [208]. The specific surface area of the sample is 136.4 m^2 g^{-1}.

Figure 2.17 demonstrates the contact of electrolyte (LP30) with CB electrode. The electrode shows a rapid wetting behaviour, leading to promote ion transportation.

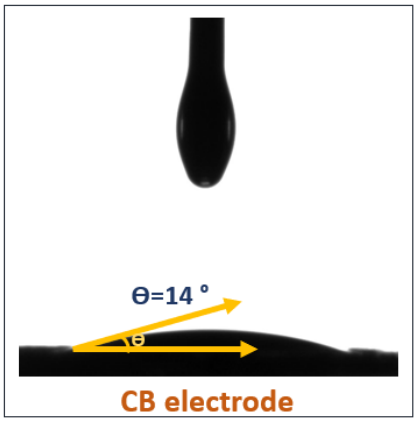

Figure 2.17. Contact Angle of the electrolyte on CB electrode

2.2.3.2 Electrochemical Performance

This study belongs to a line of research focusing on full-cell LIBs based on biowaste anode materials. Accordingly, electrochemical activity of CB firstly was investigated in lithium half-cell configuration (Figure 2.18). Secondly, we have extended the potential use of the carbonized biowaste in full LIBs, employing LFP cathode. Galvanostatic charge and discharge cycling demonstrates the high initial discharge capacity of ~ 2300 mAh g^{-1}, with initial coulombic efficiency (ICE) of 37% at 0.1 A g^{-1} (Figure 1.28b).

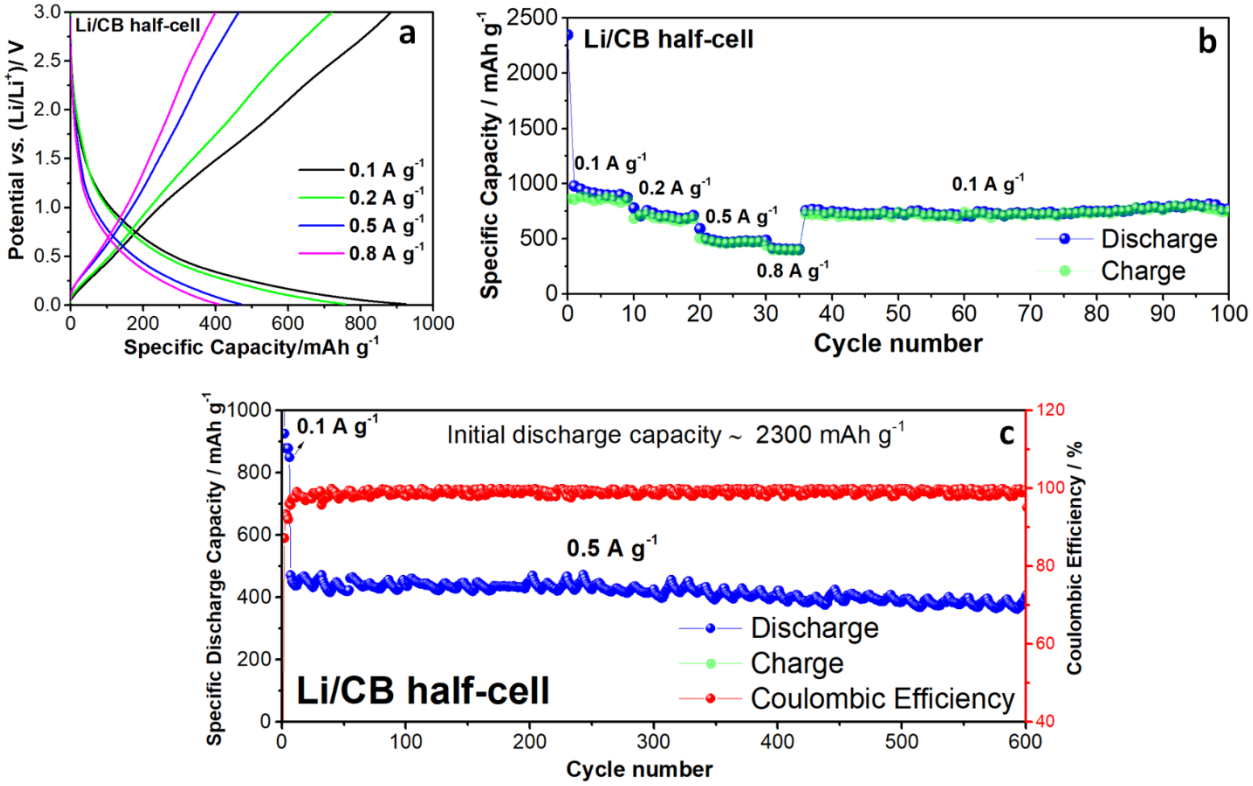

Figure 2.18. Electrochemical performance of the CB electrode in lithium half-cells. (a) Galvanostatic charge/discharge profiles for the 2nd cycle at different current densities. (b) Rate-performance, and (c) cycling performance at 0.5 A g^{-1}. All the analyses were performed in the potential range of 0.01-3 V at room temperature. Electrolyte: LP30.

The low ICE originates from solid electrolyte interphase (SEI) film formation during the first reduction process. Moreover, this anode exhibits good capacity in different current densities (900,

720, 470, and 410 mAh g^{-1} at 0.1, 0.2, 0.5, and 0.8 A g^{-1}) (Figure 2.18a). When rolling back in the current density of 0.1 A g^{-1}, the slight capacity drop is observed compared to initial cycling, exhibiting the relatively good reversibility of the designed electrode. At the current density of 0.5 A g^{-1}, the cycling performance of the CB electrode during 600 charge and discharge cycling was analysed. The Li/CB cell presents the average specific discharge capacity of 417 mAh g^{-1}, with 84% capacity retention upon cycling (Figure 2.18c). It is documented that presence of oxygen group in the electrode leads to fast redox process [209]. Additionally, the high surface and porous architecture of CB are the other main reasons behind the observed capacity and electrochemical stability of Li/CB battery.

Figure 2.19 demonstrates the CV behaviour of the Li/CB half-cell at the various scan rates. The typical broad peaks are clear which are similar to that of most disordered carbon in lithium battery application [122]. During, lithiation process, a cathodic peak associated with the lithiation process is observed at about 0.1 V [210]. Moreover, an anodic peak (at 0.2 V) also is related to de-lithiation of the CB [210]. By increasing the scan rates, the electrode's current is increasing, indicating the potential of CB material for application at high current rates.

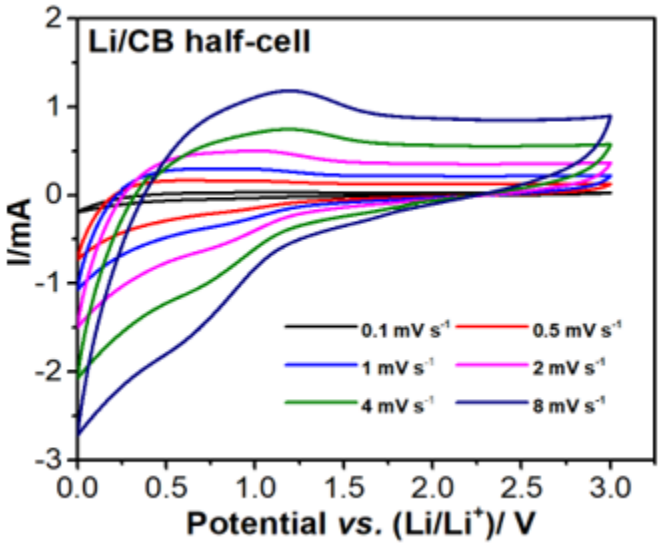

Figure 2.19. CV curves of CB electrode at different scan rates ranging from 0.2 to 8 mV s^{-1}. The test was performed in RT with LP30 electrolyte. Potential range: 0.01-3 V.

After analysing the CB potential as the working electrode in half-cell configuration, the full-cell setup was designed by combining CB electrode with LFP cathode. The full-cell assembly was based on the direct contact electrochemical method (DC-EM) [211] of CB *VS*. Lithium metal to prelithitae CB electrode. With this strategy, CB electrode was placed in direct contact with Lithium metal chips in the cell containing LP30 electrolyte. The lithiation step forms an SEI layer on the anode surface, preventing Li ion loss during the first discharge of the full cell. Moreover, in this research, an attempt is made to optimize the mass ratio balancing between the anode and cathode. The cells were assembled with the different anode to cathode mass ratio. The cathode loading was the same in all cells (~2 mg), thus ratio balancing was adjusted by changing the anode mass loading (from 0.7 mg to 2 mg). The best performance was obtained when the anode/cathode capacity ratio was ~2 (according to the stable capacity of anode and cathode at 0.5 A g^{-1}, and 0.5 C, respectively). With high anode/cathode ratio (>2), the LFP cathode provided a capacity of 140 mAh g^{-1} and lower stability that that of the cell with anode/cathode ratio ~2. Even the cell with low anode/cathode ratio (<2) revealed lower capacity and stability in comparison with the cell with ratio >2. Here, the results of the optimized cell have been provided and discussed. Figure 2.20 shows the CV profile of the pre-lithiated CB/LFP full-cell at the scan rate of 0.1 mV s^{-1} in the voltage range of 0.8–3.9 V. During positive voltage sweep (at ~ 3.5 V), Li-ions insert into biochar electrode, and Li-ion extraction occurs within LFP cathode. During the negative sweep, the peak at ~ 3.3 V is related to Li-ions intercalation (into LFP cathode), and Li-ions de-intercalation (from CB) [212]. During the 2^{nd}, and 3^{rd} cycling, the peaks (at ~ 2.8 V during charging and at ~ 2.5 V during discharging process) could be due to the two-step of Li-ion insertion/ Li-ion extraction into/from the electrodes [213]. The voltage difference of 0.2 V between the positive and negative peaks corresponds to electronic polarization.

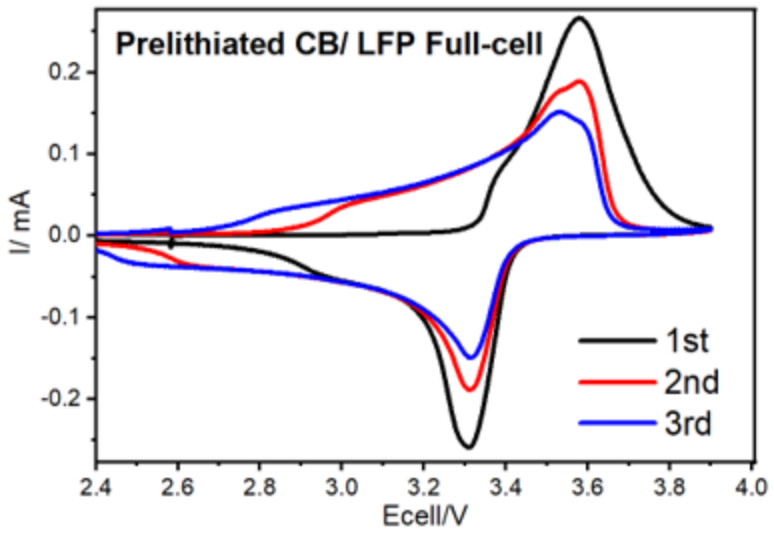

Figure 2.20. The CV profile of pre-lithiated CB/LFP full-cell at the scan rate of 0.1 mV s^{-1} in the voltage range of 0.8–3.9 V. The analyses were performed at room temperature. Electrolyte: LP30.

Figure 2.21a, b demonstrates the long cycling tests of the full-cell by varying C-rates from 1 C to 10 C, then again to 1 C to find the cell's stability. At a high applied current, the capacity would be decreased due to the polarization overpotential increase. Figure 2.21a reveals the initial discharge capacity (based on cathode active mass) around 160 mAh g^{-1}, which is very close to the theoretical capacity of LFP versus Li/Li^+. By increasing the C-rate to 2 C, a very low-capacity drop is observed. Furthermore, when the C-rate changes from 2 C to 5 C, the capacity

fade is 25%. The slight change in capacity also is clear by shifting C-rate from 5 C to 10 C. Moreover, the full-cell discloses a reversible capacity of 140 mAh g^{-1} (1C) after 1750 cycles along with rate capability test. Besides, the cell presents an average CE of 99.62%. Figure 2.21c reports the gravimetrical energy density of the CB/LFP cell at 0.5 C according to cathode mass, and overall mass of cathode and anode. Considering the active mass of cathode, the output gravimetrical energy density of the cell is 480 Wh Kg^{-1}. On the other side, the energy density of the cell still is promising (295 Wh Kg^{-1}) when the weight of both electrodes is considered. The obtained energy and reversibility of the CB/LFP full-cell at high operation current rates outperforms the results for similar batteries published in literature so far. A comparison of the main electrochemical criteria of LFP-based LIBs reported recently is shown in Table 2.7. The results obtained here are in line with those reported by Xu et al [214]. They proposed that the low capacity loss in the cells balanced with relatively higher capacity anode can be explained by two possible stress-related mechanisms:

i) As anode loading increases, current density on the anode surface decreases, potentially reducing electrode particle cracking during cycling. (ii) Increasing anode loading reduces anode utilization, which reduces electrode particle expansion and contraction during lithiation and de-lithiation, thereby reducing mechanical degradation.

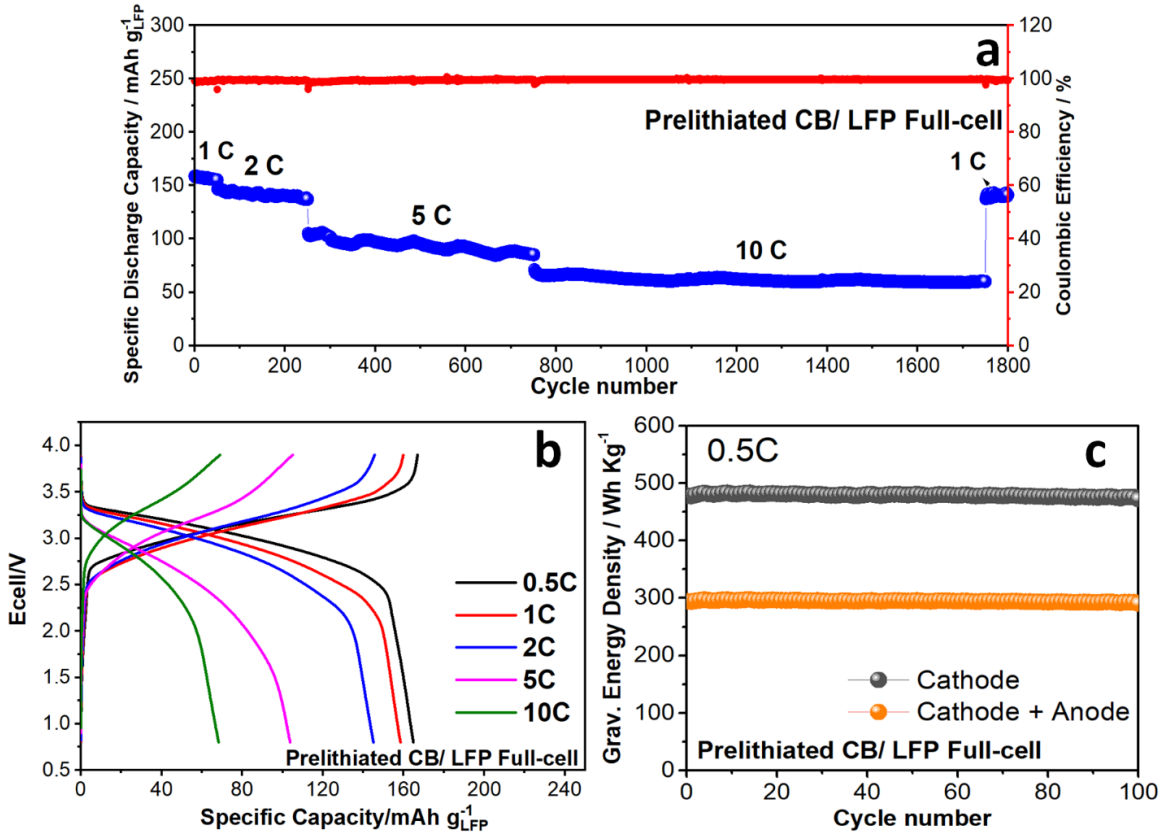

Figure 2.21. The electrochemical results of pre-lithiated CB/LFP full-cell in the voltage range of 0.8–3.9 V. (a) long-term cycling test at various C-rates (1C= 170 mA /g_{LFP}), (b) Galvanostatic charge-discharge profile of the cell at different C-rates, and (c) gravimetrical energy density according to the mass of cathode active material, and overall mass of cathode and anode (active material). The analyses were performed at room temperature. Electrolyte: LP30. LFP= 2 mg ($d_{electrode}$=11 mm), CB= 1.3 mg ($d_{electrode}$=12 mm).

Table 2.7. Comparison of the main electrochemical criteria of LFP-based LIBs reported recently.

Anode	Mass ratio (anode: cathode)	ICE%	Working voltage (V)	Initial discharge capacity (mAh g^{-1})	Specific capacity (mAh g^{-1}) at different rates	Reference
Sn-C	1:2	-	2.8	150	120 at 3C	[215]
Graphene	1:4	89	3	165	160 at 1C	[216]
TiO_2 hollow nanofibers	1:1.3	68	1.4	140	110 at 0.1 A g^{-1}, 80 at 0.2 A g^{-1}, 50 at 0.5 A g^{-1}, and 30 at 1 A g^{-1}	[217]
Binary $Li_4Ti_5O_{12}$ -$Li_2Ti_3O_7$	-	-	1.8	125	75 at 0.08 A g^{-1}	[218]
$ZnFe_2O_4$ -C	1:1.5	-	2.1	120	80 at 9.6C	[219]
Si-Graphene	-	83.2	3	157	130 at 1C	[220]
Ge	-	93	2.8	105	90 at 0.5C	[221]
Carbonized biowaste	1:1.5	80	3	167	165 at 0.5C, 155 at 1C, 142 at 2C, 95 at 5C, 65 at 10C	This work

2.2.4 Conclusion

In summary, the cattle bone waste has been considered as the active anode material to couple with LFP to design sustainable full LIBs. The inherent heteroatoms, high surface area, the interlinked microchannels and hierarchical porous structure of carbonized cattle bone made it a promising electrode for application in rechargeable batteries. In this study, the factors affecting the full-cell performance have been precisely identified and optimized to maximize the electrochemical performance of the cell. The engineered full-cell LIBs based on cattle bone biowaste anode and LFP cathode revealed very stable capacity during long cycling, which could be related to stress reduction on oversized anode electrode through Li intercalation/ de-intercalation. This study turns the attention toward the practical utilization of the food waste in the lithium-ion technology. In particular, the present research not only deals with the application biowaste in the energy sector

but also presents an innovative and sustainable way for food waste management contributing to the United Nation's sustainable development goals.

Chapter 3 . Biochar and beyond conventional LIBs: Lithium-metal free sulfur battery based on brewer's spent grain biochar anode

The realization of stable lithium-metal free (LiMF) sulfur battery with an amorphous carbon anode and lithium sulfide (Li_2S) cathode can surpass the low energy densities of conventional Lithium-ion batteries (LIBs). Herein, we propose a full-cell which combines carbonized brewer's spent grain (CBSG) anode and Li_2S-graphene composite cathode (Li_2S@Gr). This design approach is particularly attractive for applying cost-effective and safe anode materials based on waste biomass in emerging battery technologies. The systematical investigation reveals the good compatibility of the biomass electrode with ether-based electrolyte (as the most common electrolyte for lithium-sulfur battery). The sample exhibits the stable capacity of 350 mAh g^{-1} at 0.1 A g^{-1} along long cycling at difference current densities. The novel CBSG/ Li_2S@Gr full-cell displays the initial charge and discharge capacity of 726 and 537 mAh g^{-1} at 0.05C with a coulombic efficiency of 74%. Moreover, it discloses a reversible capacity of 330 mAh g^{-1} (0.1C) after 325 cycling at increasing C-rates of 0.1, 0.2, 0.5, and 1C. Comparison with the literature, CBSG/ Li_2S@Gr battery system could be considered as a promising system for energy storage technologies.

3.1 Introduction

The emergence of electric vehicles (EVs) requires high electrochemical energy storage devices (EESDs) with low cost [222]. Domination of high-performance EVs in the global automotive market reduces the application of fossil-fuel-based vehicles tackling the negative impact of CO_2 emissions according to the European Protocol in the Transportation Sector. Nowadays, lithium-ion batteries (LIBs) are almost exclusively power sources for EVs [1,222]. However, the inadequate-range transport of EVs powered by current LIBs, with an energy density of around 250 Wh kg^{-1}, is the main situational barrier preventing the purchase of EVs by consumers [223]. In this situation, Lithium-sulfur batteries (LSBs) as LIBs' family could be considered as one of the most promising alternatives to current LIBs. The high theoretical gravimetrical energy density of 2600 Wh kg^{-1} and low-cost LSBs could promise a sustainable battery value chain for many applications, especially for the emerging markets such as drones and aviation. Additionally, due to its abundant natural supply and high theoretical capacity of 1675 mAh g^{-1} based on the following chemical reaction, sulfur is regarded as an element that is good to the environment [224,225]:

$$S_8 + 16Li^+ + 16e^- \leftrightarrow 8Li_2S \qquad \textit{Equation 3.1}$$

Nevertheless, a number of challenges have prevented the broad commercialization of LSBs [226]. In conventional LSBs, sulfur and lithium metal act as cathode and anode electrodes, respectively [227,228]. In the process of the redox process, lithium dendrites form and grow on the surface of the metal, creating a short circuit that causes spontaneous combustion in the cell [229]. Additionally, the battery's capacity fades quickly and its coulombic efficiency is low due to the unstable solid-electrolyte interface (SEI) layer caused by the direct reactivity of the lithium metal with polysulfides (PSs) in the electrolyte [230]. The insulating properties of sulfur and Li_2S/Li_2S_2, volume expansion, and low conductivity of sulfur on the cathode side also lead to an increase in polarization during the electrochemical operations [231,232]. Another major hurdle to the practical use of lithium metal-based sulfur battery arises from the high solubility of polysulfides (PSs) in organic electrolytes, leading to irreversible loss of sulfur active material, and finally cell failure [224,233].

Replacing sulfur with its lithiated counterpart (Lithium Sulfide) greatly improves the LSBs' performance [234]. Lithium Sulfide (Li_2S) is mechanically stable at maximum volume state and

doesn’t exhibit volumetric expansion in the initial charge process [229,235]. In addition, Li_2S possesses higher thermal stability compared to sulfur [236]. The insertion of Li_2S into porous conductive hosts utilizing a variety of synthetic techniques at high operational temperatures is made possible by the melting stability of 938 °C [236,237]. More importantly, Li_2S cathode can be paired with various anode materials beyond lithium metal and make a safe Lithium-metal free (LiMF) battery for practical application [238–240]. However, Li_2S's electrical and ionic conductivities are quite low, which causes the cell's cycle stability to be poor and causes a large charge transfer resistance at the interface between the Li_2S cathode and the electrolyte [234]. Additionally, the inevitable formation of PSs in the cathode prevents the full utilization of the active material [241]. The PS degradation results in long-term capacity deterioration because it disperses into the electrolyte and diffuses to the anode electrode [242].

Anode electrode is equally important to overcome the fundamental limitations of LSBs including safety, and low practical energy density. Other than elemental lithium, anode materials such graphite, silicon, tin, and metal oxides can be employed to avoid the safety concern with the lithium-based sulfur battery [243–247]. For instance, metal oxide nanoparticles release toxic ions, with consequent damage of the living organisms [34,35]. On the other hand, graphite as one of the most employed anode materials in LIBs, undergoes exfoliation in conventional ether-based electrolytes, thus making it unsuitable for metallic lithium replacement [36,37] (ether-based electrolytes are needed for sulfur-based batteries as sulfur is not stable in traditional carbonate-based electrolytes [38],[39]). It is critical to identify an anode material that is compatible with ether-based electrolytes that combines safety, environmental friendliness, cheap cost, and good performance.

Carbons derived from pyrolysis of biomasses are promising alternatives to standard graphite electrode for application in electrochemical energy storage devices (EESDs). Their non-graphitizable structure with amorphous/pseudo-graphitic nanodomains [70], which is advantageous for electrochemical processes in LIBs, is a specific advantage of these materials. More interestingly, bio-based carbon’s precursors are mainly renewable, green, cheap and abundant [87]. Following our previous studies [124,134,197,248,249], we demonstrated the great potential of EESD technology's green re-use of waste (spent) materials. Herein, we suggest the use

of carbon material derived from brewer's spent grain (BSG), an abundant solid industrial waste, to address the technical challenges related to anode electrodes in next-generation of LIBs.

Nowadays, around 85% of all solid waste produced in brewing industry is BSG more particularly barley grain husks coming from wort production step. BSG is constituted of lignocellulose (i.e. cellulose, lignin and arabinoxylans) rich in protein, lipid, fiber, vitamins and minerals [250]. According to the latest "BarthHass Report 2020", the world beer production in 2020 is estimated in 1820 million hL [https://www.barthhaas.com/en/campaign/barthhaas-report-2021]. It was reported that between 14 and 20 kg of BSG for each hL of produced beer are formed during the brewing process [251]. Therefore, an average of 30.940 million tons of this biomass can be produced each year. Due to the high content of nitrogen-containing nutrients in BSG, it has been used as the feed of animals [251] and in agricultural products such as compost or fertilizers [252]. However, high content of moisture in the wet BSG leads to the microbial contamination especially from filamentous fungi needing high-cost conservation processes. Therefore, energy generation from BSG could be another possible and significant application [251]. As reported by Luna-Lama et al. [44], the evaluation of potential scalability requires a deep analysis where the cost of residue biomass, the availability of the feedstock, the simplicity of the procedure as well as the employed solvents and reagents, should be carefully taken into account. In view of these considerations, the methodology proposed in the present work could be considered potentially scalable to an industrial level due to the low cost and readily available feedstock. Through the thermochemical decomposition in an inert atmosphere (pyrolysis process), BSG converts to bio-oil and bio-gas and produces solid residue rich in carbon, named biochar. In the present study, we observed that the biomass-based electrodes might contribute to the design of stable long-term LIBs with the potential to replace the state-of-the-art anodes by electrochemical analysis of our developed Li/biochar half-cell in an ether-based electrolyte. On the other hand, this research discloses bio-based carbon as a possible candidate for future battery technology anodes, due to its stability and compatibility in emerging battery technology environment. The stable electrochemical behaviour of the studied hard carbon derived from biomass resources could be attributed to different factors: (i) the wider average interlayer spacing with respect to graphite, (ii) the presence of pyridinic N and quaternary N atoms along with oxygen group, and (iii) cross-linked carbonaceous clusters. Indeed, the increased interlayer spacing could lead to a greater Li-ions storage within the carbon structure. It is documented that the functional groups increase the conductivity of the carbon material and

introduce the extra free electrons next to the carbon atoms that can accelerate the redox reactions [149,253,254]. Additionally, cross-linked structures cause biochar's extraordinary stability in an ether electrolyte environment [255].

The main objectives of this study are:

- Application of the by-product through BSG pyrolysis as anode material in emerging battery technologies
- Systematic physical and electrochemical investigations of CBSG anode to reveal its compatibility with the electrolyte condition of sulfur batteries
- Combining the CBSG anode with Li_2S@Gr cathode to fabricate LiMF battery to overcome the major challenges posed by LSBs such as safety concerns and short cycling life

3.2 Experimental section

3.2.1 Materials synthesis

3.2.1.1 Synthesis of CBSG

CBSG was obtained by employing a laboratory-scale prototype plant (Carbolite custom model EVT 12/450B), as reported in the previous chapter. The pyrolysis of BSG (< 2 mm in size) was carried out by heating up the sample till 700°C at 5°C/min under a 100 mL/min nitrogen flow. The temperature was maintained constant at 700°C for 30 minutes. Afterward, the CBSG powder was centrifuged in a 1.0 M HCl solution, then grinded and sieved down to ~90 µm.

3.2.2 Materials characterization

Kratos Axis Ultra DLD spectrometer equipped with a monochromatic Al K source was used to perform X-ray photoelectron spectroscopy (XPS) analysis on the chemical structure and heteroatom binding states of the CBSG sample (15 kV, 20 mA). The UNICUBE organic elemental analyser (from Elemental) was used to measure the total carbon, nitrogen, hydrogen, and sulfur (CHNS) contents of the CBSG active material, and the oxygen content was estimated from the difference. The ash content was determined following the ASTM-D1102 protocol. The surface functionality of CBSG was investigated by Fourier Transform Infrared Spectroscopy (FTIR) using

Perkin Elmer Spectrum One spectrometer with a wavenumber range of 400-4000 cm^{-1} at room temperature with a resolution of 4 cm^{-1}. The carbon sample and KBr were completely combined to create the pellets. Malvern PANalytical Empyrean X-ray diffractometer (XRD) with 1.8 kW CuK sealed ceramic tube and Renishaw in Via Micro Raman with 532 nm laser source were used to analyze the sample's crystallinity, mineral content, and degree of order/disorder. Using field-emission scanning electron microscopy (FESEM-JEOL JSM-7500FA), the surface morphology and energy dispersive spectroscopy (EDS) of the electrodes and CBSG powder were examined.

3.2.3 Electrode and electrolyte preparation

3.2.3.1 CBSG Electrode preparation

The CBSG electrodes were prepared by mixing 70wt% of the active material (CBSG), 15wt% of conductive carbon black agent (Imerys), and 15wt% of carboxymethylcellulose (CMC, Dalian Chem) working as binder. The mixture was mechanically stirred to create a slurry after being evenly ground. Using the Doctor-Blade technique, the film electrode was successively cast on copper foil with a 10 µm thickness before being dried on a hot plate for three hours at 60 °C. The electrodes were dried, then punched into 15 mm-diameter disks and dried for an additional 4 hours at 80°C using a Buchi device. The prepared electrodes were then kept in a glove box filled with argon (MBraun). About 0.7 to 0.9 mg cm^{-2} of active mass were loaded.

3.2.3.2 Electrolyte preparation

1 mol kg^{-1} (m) lithium bis(trifluoromethanesulfonyl)imide (LiTFSI, Sigma-Aldrich) and 0.5 m lithium nitrate ($LiNO_3$, Sigma-Aldrich) were combined in a solution with 1,3-dioxolane (DOL, Sigma-Aldrich) and 1,2-dimethoxyethane (DME, Sigma-Aldrich) in a weight ratio of 1:1 as the electrolyte (from here on named DOLDME-LITFSI-$LiNO_3$). The DOL and DME solvents were dried on molecular sieves for ten days prior to the preparation of the electrolyte. An MBraun argon-filled glovebox was used to stir the prepared electrolytic solution for 24 hours.

3.2.4 Electrochemical characterization

The electrochemical characterization was performed by employing 2032 coin cells. The amount of electrolyte was normalized to ≈15 $\mu L_{electrolyte}/mg_{active\ material}$ for both half-cell and full-cell measurements. For the electrochemical testing, a microporous polymeric membrane (Celgard 2400) was employed as a separator. In addition, lithium chips (15.6 mm, MTI Corporation) were employed as the counter electrode and reference electrode for the electrochemical studies of the Li/CBSG and Li/Li_2S@Gr half-cells. The cells were assembled in an argon-filled MBraun glovebox with H_2O and O_2 levels lower than 0.1 ppm. The Li/CBSG half-cells were analysed with constant current (CC) protocol in the potential range of 0.01 - 3 V at the current densities of 0.1, 0.2, 0.5, 0.7, 1, and 2 A g^{-1}. Based on the weight of the active material in the CBSG electrode, the current density was determined. The cyclic voltammetry (CV) measurement of the lithium-metal half-cell was carried out at the scan rate of 0.1 mV s^{-1} in the 0.01 - 3 V potential range for CBSG. Electrochemical Impedance Spectroscopy (EIS) technique was used for Li/CBSG half-cells in the frequency range from 10 kHz to 100 mHz with a 10 mV alternating current. In order to assemble the full-cells, a direct contact electrochemical method (DC-EM) [256] was used to prelithiate the CBSG electrode by keeping it in direct contact with a metallic Li chip in presence of the electrolyte for 8 h (see Figure 3.1). Subsequently, the lithiated CBSG electrode was rinsed with DME solvent and dried in an inert environment. Afterward, the lithiated CBSG/ Li_2S@Gr full-cell was assembled according to the mass ratio of 1:1.35, corresponding to the active material weights of Li_2S@Gr: CBSG. For the mass balancing, the starting capacity of each electrode at low current density/rate in half-cell design was taken into account. The galvanostatic cycling test of CBSG/ Li_2S@Gr full-cell was carried out at the current rates of 0.05C (58 mA g^{-1}), 0.1C (116 mA g^{-1}), 0.5C (583 mA g^{-1}), and 1C (1166 mA g^{-1}) in the voltage range 0.8 - 2.6 V. The specific gravimetric capacity of CBSG/ Li_2S@Gr full-cell were calculated based on the Li_2S mass. The CV analysis of the CBSG/ Li_2S@Gr full cell was performed between 0.8 V and 3 V at the scan speed of 0.1 mV s^{-1}. The whole electrochemical characterization was obtained at room temperature by employing a BCS-805 multichannel battery unit by BioLogic.

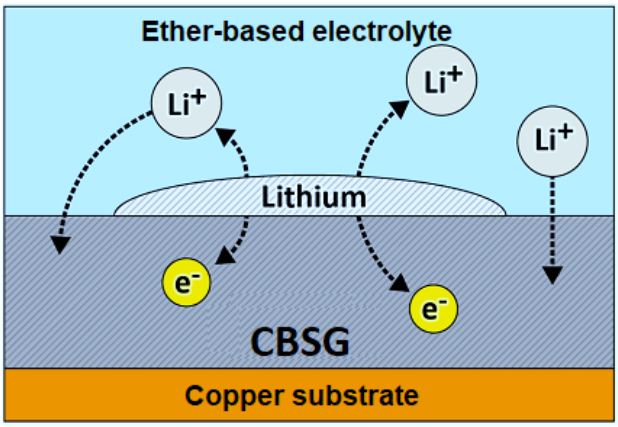

Figure 3.1. Direct contact electrochemical method (DC-EM) for CBSG prelithiation.

3.3 Results and Discussion

3.3.1 Materials characterization

The elemental analysis of the CBSG anode was performed to determine the weight percentage of C, N, H, S, and O in the sample, with the values reported in Table 3.1**.** The C, N, H, and O amounts resulted to be 73.6 wt%, 4.7 wt%, 1.9 wt% and 12.9 wt%, respectively. In contrast, the S content is minimal at values below 1 wt%. The presence of N and O within the sample is known to contribute to the expansion of the interlayer spacing of the graphitic carbon domains, thus providing extra active sites for accommodating Li-ions [257]. Furthermore, the hybridization of N lone pair electrons with the π electrons of C increases the electronegativity of the electrode forming favourable binding sites for Li storage [87]. Last but not least, it has been established that Li-ions can bond close to H atoms in CBSG electrodes [51].

Table 3.1. Elemental analysis of CBSG.

Sample [%]	C	N	H	S	O	Ash
CBSG	73.6	4.7	1.9	0.1	12.9	6.8

The functional and doped groups of CBSG were qualitatively analysed by FTIR (see Figure 3.2) and XPS (Figure 3.3). In the spectra of FTIR, there is a very weak band at almost 3600 cm^{-1} which

is related to the vibration of hydroxyl groups [258]. The band at around 1542 cm^{-1} is associated with the stretching vibration of aromatic C=C and C=O and also stretching of C=O groups of conjugated ketones and quinones [153]. The existences of oxygen and nitrogen-containing functionalized groups and doped heteroatoms in the biochar surface and skeleton could be demonstrated by a series of intense, broad and overlapped bands in the range of 1400-900 cm^{-1}. In particular, the bands at this region are assigning to the C–O bonds of phenol, alcohol, ether bridging, aromatic rings, and the presence of N–C, N-COO groups. In addition, the bands at 2850 and 2920 cm^{-1} are related to the C–H of alkenes, while the band at 800 cm^{-1} is due to aromatic C–H out of plane vibrations [41]. Figure 3.3a-c presents X-ray photoemission high-resolution spectra on oxygen, and nitrogen together with the results of the best-fit procedure. According to the analysis of the O 1s region, O is associated with carbon in both organic and metal-oxide forms. The presence of N atoms in several coordination modes, including pyridinic N, amino N, pyrrolic N, and graphitic N, is further demonstrated by the XPS spectrum of N 1 s. In addition to C, N, H, and O, XPS also reveals the presence of residues of Mo, Cl, Si, In, Al, Pb, and Ca, among other elements (they are grouped as Ash in Table 3.1).

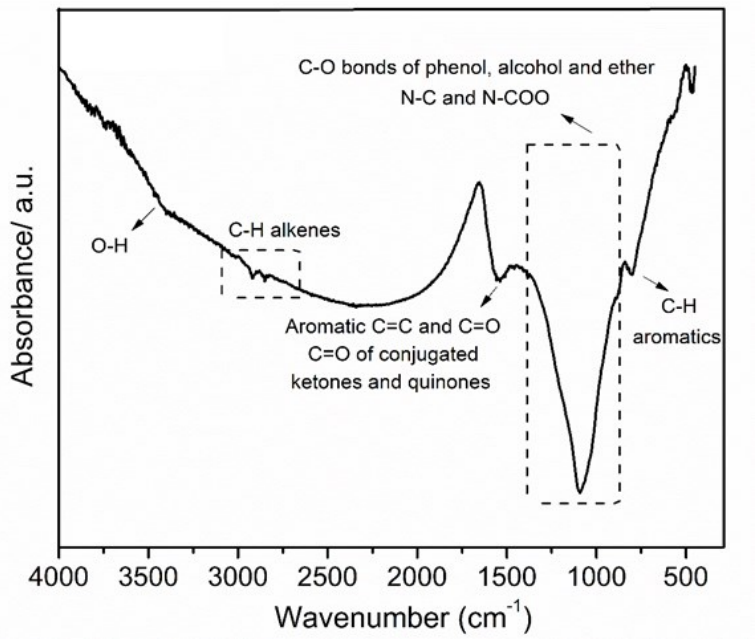

Figure 3.2. FTIR spectrum of CBSG.

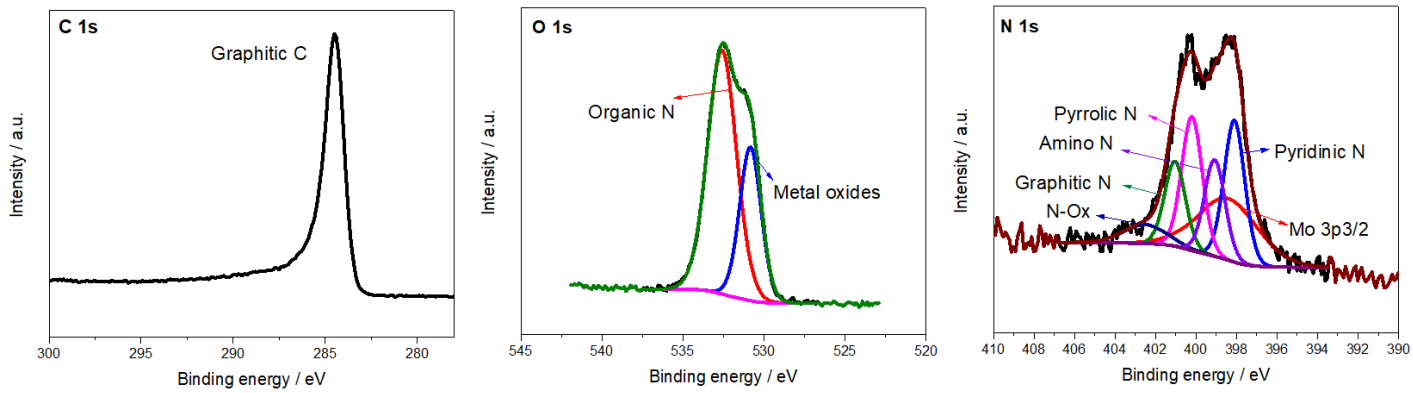

Figure 3.3. XPS spectra of CBSG material relative to: (a) C 1s, (b) O 1s, and (c) N 1s spectra.

To ascertain the degree of order/disorder and defects of the carbon layers of CBSG, XRD and Raman studies were performed. The (002) and (100) planes, respectively, are represented by a strong peak at about 2°=23° and a weak peak at about 2°=44° in the XRD pattern of Figure 3.4a [254]. The broad form and low intensity of the peaks indicate the CBSG's amorphous quality [257]. The Raman spectrum of Figure 3.4b shows the presence of two prominent peaks at around 1350 cm^{-1} (D-band) and 1600 cm^{-1} (G-band) corresponding to disordered or turbostratic structure and sp^2-hybridized carbon of CBSG, respectively [259]. The sample's level of disorder is determined by the I_D/I_G intensity ratio between the D- and G-bands [101]. In particular, I_D/I_G value of 0.82 is found for the CBSG sample. According to this value, the biochar exhibits graphitic properties as well as a disordered configuration, which is consistent with the XRD examination. Generally speaking [197], the degree of graphitization decreases with the increase of defects concentration (which is proportional to the ratio I_D/I_G). In this regard, the presence of N, O, and S atoms leads to numerous carbon structure defects and thus increases the number of active sites for Li storage. Although both defects and a high degree of ordered graphitic carbon might affect the performance of the electrochemical cell, a trade-off needs to be determined when it comes to the overall electrochemical evaluation of a material. High graphitic order is linked to enhanced cell stability, especially at high C-rates, and high disorder specifically is related to higher initial capacities [197,260].

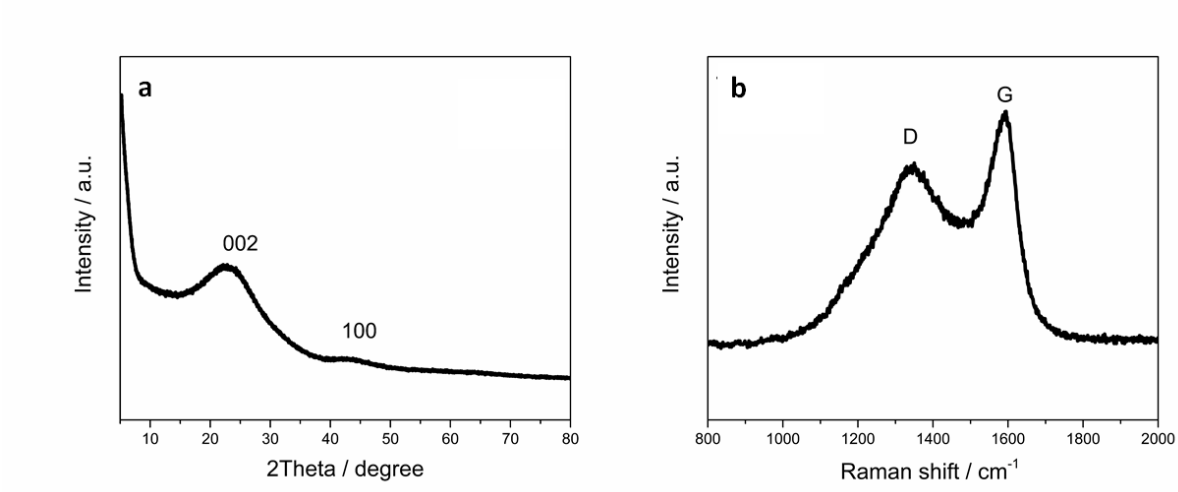

Figure 3.4. (a) XRD pattern, and (b) Raman spectrum CBSG sample.

The N_2 adsorption-desorption (Figure 3.5) reveals a low specific surface area equal to 2.4 $m^2\ g^{-1}$ and a pore volume density of 0.036 $cm^3\ g^{-1}$ for the CBSG sample, resulting in the appearance of an isotherm curve that is typical of non-porous materials [261]. In good agreement with N_2 adsorption-desorption analysis, the FESEM image of Figure 3.6a exhibits a low porosity, indicating that using the pyrolysis process alone to create porous structures is insufficient. Although it is generally known that increasing the surface area of carbon-based anodes can increase their capacity [87], recent studies have also reported about the benefits of non-porous carbonaceous materials as electrodes for LIBs [190,262,263]. Because fewer solid electrolyte interphase (SEI) layers form in non-porous structures, less electrolyte is actually consumed, which increases the stability and initial coulombic efficiency of biochar anodes [190,262,264]. The element mapping of CBSG powder also shows the distribution and presence of O, S, N in the biochar Figure 3.6b.

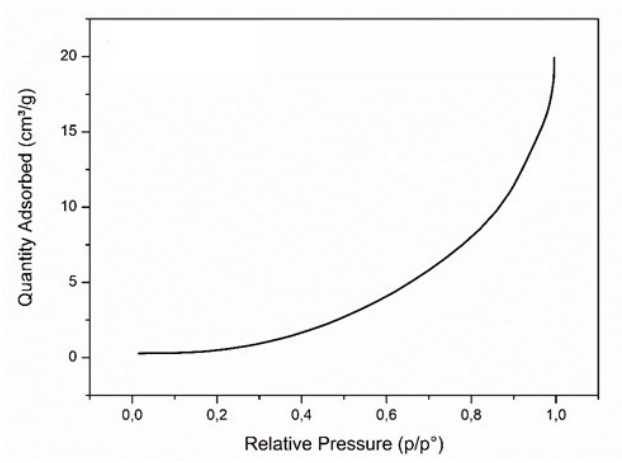

Figure 3.5. BET analysis of CBSG.

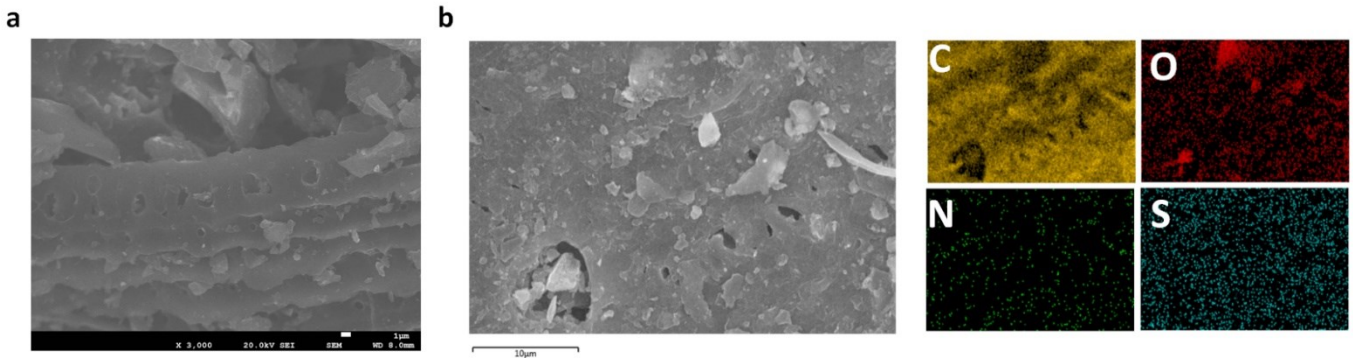

Figure 3.6. a) FESEM and, b) element mapping of CBSG.

3.3.2 Electrochemical characterization

Li/CBSG half-cell

The design of a novel biochar-based anode for use in LiMF sulfur batteries is the major objective of the current work. So, in an ether-based electrolyte, a preliminary examination of the electrochemical performance of the CBSG electrode in a lithium half-cell configuration was conducted. For this investigation, in particular, DOLDME-LITFSI-$LiNO_3$, the most common electrolyte in sulfur-based batteries, has been used. The CV behaviour of the CBSG electrode is shown in Figure 3.7. The cathodic reduction curve during the first cycle exhibits a peak at 1.7 V that is related to the $LiNO_3$ decomposition [265]. The peak at around 0.55 V during the initial reduction is associated with SEI formation on the CBSG electrode surface because of the electrolyte degradation [149,265]. The aforementioned peaks (at 1.7 V and 0.55 V) disappear in

the subsequent cycles, confirming the stability of the formed SEI layer. Finally, the presence of two peaks at around 0 V (cathodic peak) and 0.2 V (anodic peak) correspond to the lithiation and the de-lithiation of CBSG electrode, respectively [266]. It should be noticed that the significant overlap between the third and tenth cycles reveals the suggested electrode's low electrochemical polarization and strong reversibility when used with the preferred electrolyte.

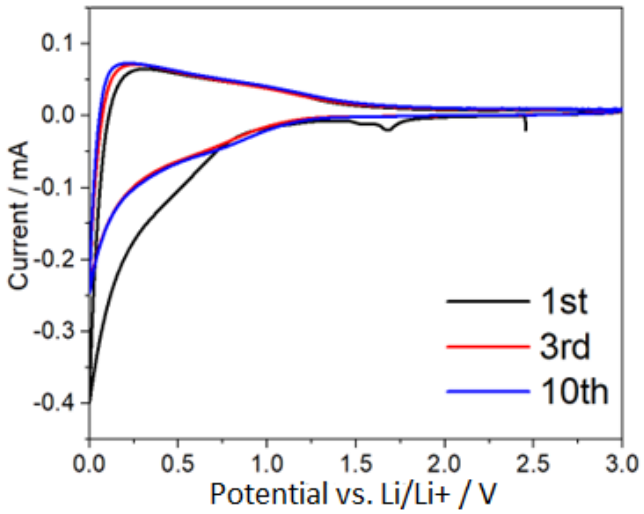

Figure 3.7. Cyclic voltammetry curves of CBSG in half cell configuration at the scan rate of 0.1 mV s^{-1}. The tests were performed in the potential range of 0.01- 3V at room temperature using a DOLDME-LITFSI-$LiNO_3$ as electrolyte.

Rate capability and long-term cyclic stability at a specific current density were investigated to further electrochemically evaluate the CBSG electrode in the ether-based electrolyte. The rate capability test (Figure 3.8a and b) was carried out by increasing the current density from 0.1 to 2 A g^{-1} and then back down to 0.1 A g^{-1}, to examine the capacity recovery following analyses of high current densities. The charge-discharge profiles of the CBSG electrode at increasing current densities are shown in Figure 3.8a. Moreover, Figure 3.8b depicts the specific discharge capacity vs. cycle number. The Li/CBSG half-cell achieved a specific discharge capacity of 348, 271, 219, 212, 195, 152 mAh g^{-1} at 0.1, 0.2, 0.5, 0.7, 1, and 2 A g^{-1}, respectively, indicating a coulombic efficiency approaching 99%. As anticipated, raising the current density lowers the specific capacity, perhaps as a result of an increase in polarization. The capacity and cycling life of the CBSG electrode are steady once the current density is reset to 0.1 A g^{-1} (348 mAh g^{-1} over 315

cycling). EIS and ex-situ SEM investigations were performed to better understand which processes contribute to the stability of the Li/CBSG half-cell (Figure 3.9 and Figure 3.10).

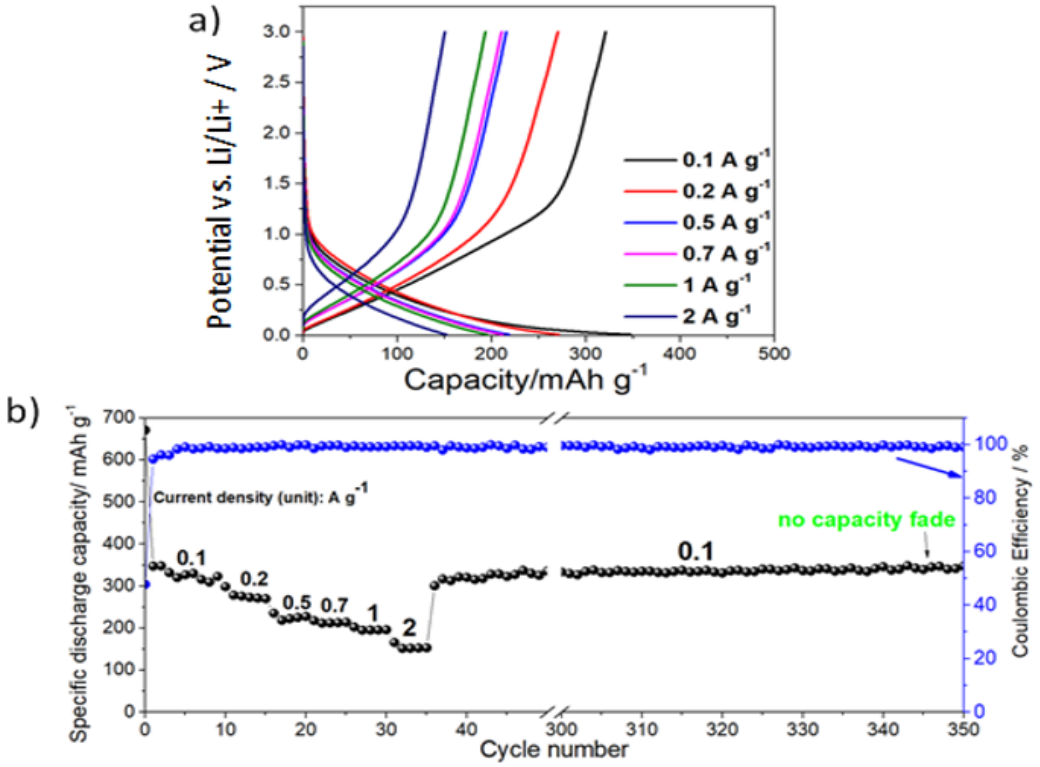

Figure 3.8. (a) Galvanostatic charge-discharge profile relative to the 2nd cycle analysed at each current density and (b) Rate capability performance (discharge specific capacity upon cycling number and related coulombic efficiency) of CBSG at a current densities of 0.1, 0.2, 0.5, 0.7, 1, and 2 A g^{-1}. The tests were performed in the potential range of 0.01- 3V at room temperature using a DOLDME-LITFSI-$LiNO_3$ as electrolyte.

Figure 3.9 shows the Nyquist plot of Li/CBSG half-cell, in both its fresh state and after the rate capability test. After cycling, the cell's overall internal resistance falls from 53.1 Ω in the fresh state to 20 Ω, indicating an improvement in the kinetics of the cell. In fact, this reduction may indicate that lithium ions are moving favourably within the CBSG electrode through the electrolyte and the SEI coating [117]. Here, R_s is electrolyte resistance, R_{ct} corresponds to charge transfer resistance, R_{SEI} stands for solid electrolyte interphase resistance, CPE1 relates to surface film

capacitance, CPE, and CPE2 associate with double layer capacitance, and W_0 is warburg impedance related to the lithium-ion diffusion within the electrode.

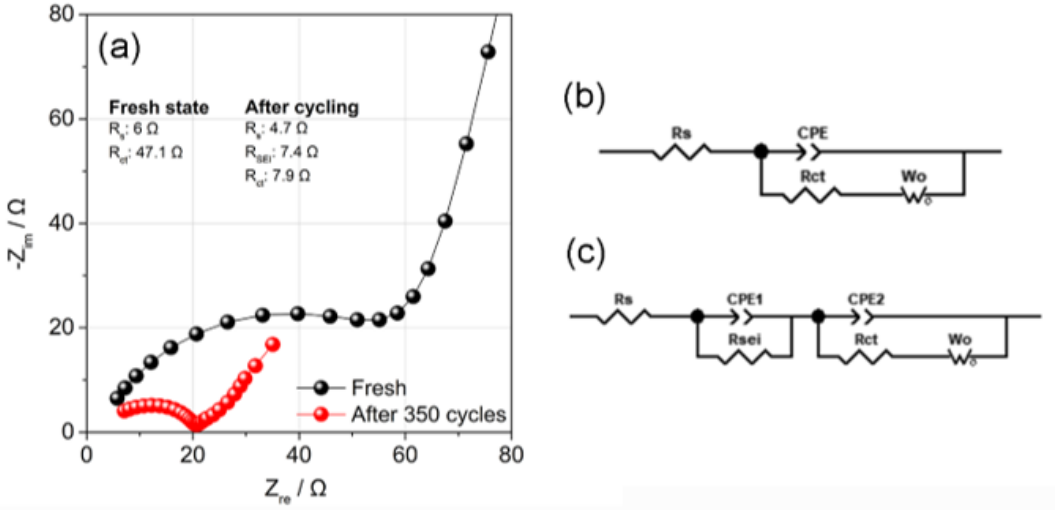

Figure 3.9. (a) Nyquist plot of Li/CBSG half-cell. In inset, the resistance values obtained through the modelled equivalent circuits reported in (b) for the fresh state and in (c) after the rate capability test. Electrolyte: DOLDME-LITFSI-$LiNO_3$.

Figure 3.10 depicts the results of an ex-situ SEM study of the CBSG (top and cross-sectional views), which was done to look for any structural changes that might have occurred as a result of the Li insertion and extraction after extensive cycling. The morphological investigation indicates negligible volume changes and pulverization of the CBSG electrode after cycling, thus confirming the robustness and compatibility of the suggested anode material in the ether-based electrolyte.

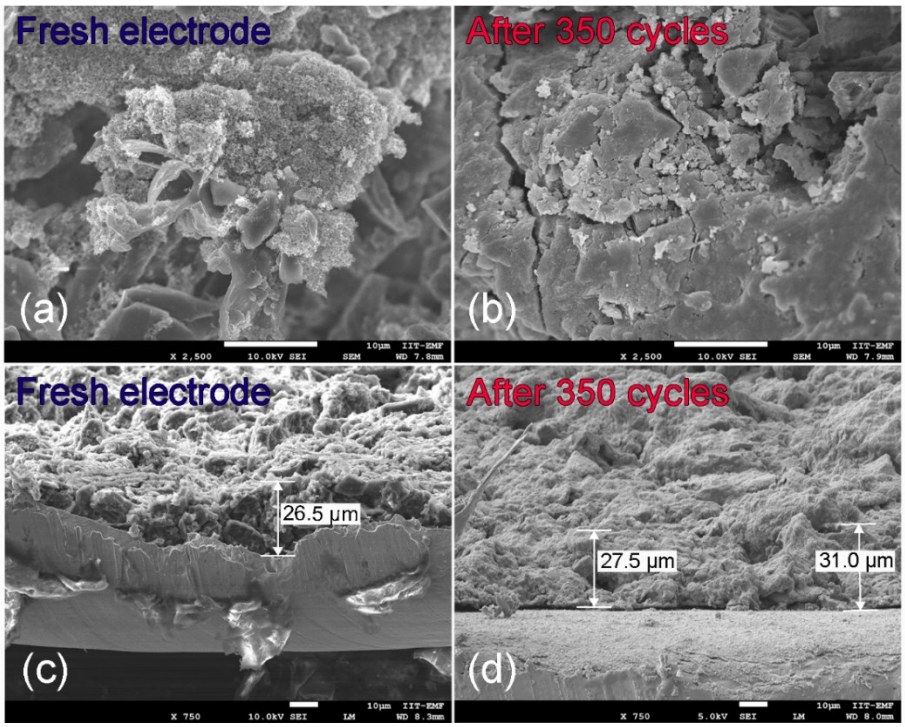

Figure 3.10. (a) and (b) top and (c) and (d) cross-sectional views of Ex-situ SEM of CBSG in pristine state and after cycling (350 cycles at different current densities). Electrolyte: DOLDME-LITFSI-$LiNO_3$.

The long cycling test of the Li/CBSG half-cell was also analysed at 0.5 A g^{-1} (1.3 C-rate if compared to graphite), as shown in Figure 3.11. Here, the CBSG electrode reveals a stable specific capacity around 205 mAh g^{-1} over 400 cycles, with a coulombic efficiency equal to ~99%. Table 3.2 compares the performance achieved by our designed electrode vs. graphite when conventional ether-based electrolyte is considered. In contrast to graphite, which can only cycle for a few tens of cycles, CBSG exhibits superior electrochemical behaviour and is particularly capable of extensive cycling (>400 cycles).

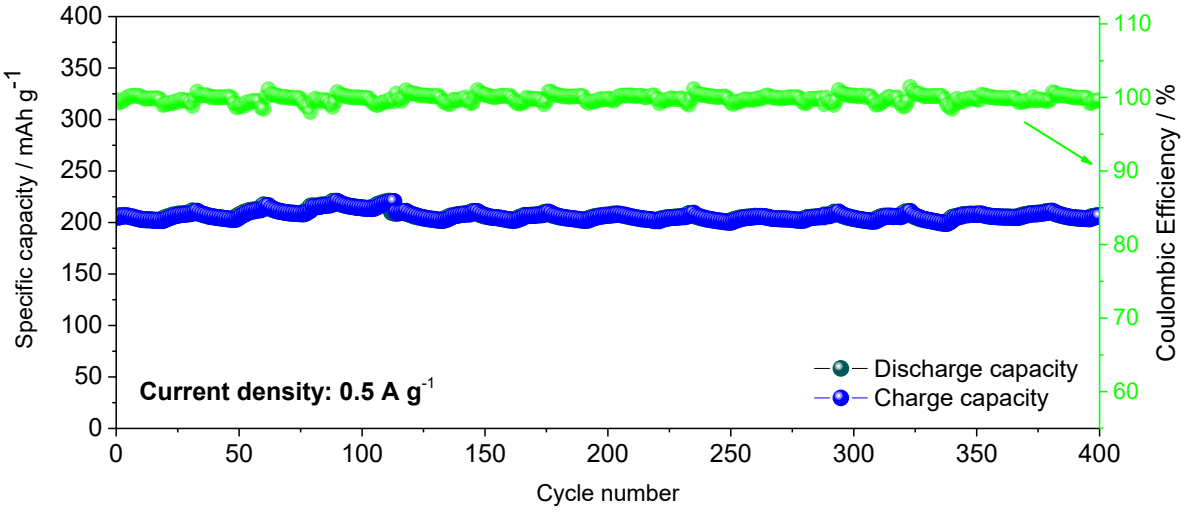

Figure 3.11. Cycling response of Li/CBSG half-cell at the current density of 0.5 A g^{-1} in the potential range of 0.01- 3V at room temperature. Electrolyte: DOLDME-LITFSI-$LiNO_3$.

Table 3.2. Electrochemical performance of CBSG vs. graphite in Lithium half-cell configuration with ether-based electrolyte for application in sulfur-based batteries.

Half-cell system	Solvent	Salt	Initial and second discharge capacity (mAh g^{-1})	Reversible discharge capacity (mAh g^{-1})	Ref.
Li/ CBSG	DOL:DME	1 m LiTFSI + 0.5 m $LiNO_3$	671 – 347 at 0.1 A g^{-1}	205 after 400 cycles at 0.5 A g^{-1}	**This work**
Li/ Graphite	DOL:DME	1 M LiTFSI + 1 wt% $LiNO_3$	506 - 333 at 0.1 C	~ 320 after 60 cycles at 0.1 C	[267]
Li/ Graphite	DOL:DME	1 M LiTFSI + 1 wt% $LiNO_3$	400 (0.1 C) - 270 (0.2 C)	~ 250 after 40 cycles at 0.2 C	[268]
Li/ Graphite	DOL:DME	1 M LiTFSI	450 - ~ 100 at 0.1 C	Significant capacity drop after 2 cycles	[269]
Li/ Graphite	DOL:DME	5 M LiTFSI	400 - 370 (0.1 C)	~ 370 after 5 cycles at 0.1 C	[269]
Li/ Graphite	DOL:DME	6 M LiTFSI	360 - ~ 360	~ 360 after 7 cycles	[270]
Li/ Graphite	DOL:DME	3 M LiTFSI	~ 400 - ~ 220 (0.1 C)	220 after 40 cycles at 0.1 C	[243]

To compare the electrochemical performance of our designed biochar electrode with graphite, we also analyzed behaviour of commercial graphite in the electrolyte condition of sulfur batteries. Figure 3.12 shows the galvanostatic charge/discharge profiles of commercial graphite (from NEI corporation) at different current densities in the ether-based electrolyte. Graphite shows the huge capacity drop after the initial cycles. After cell disassembly, we found that graphite was completely

separated from copper current collector (Figure 3.12, inset). Exfoliation of graphite because of intercalation of solvent molecules and lithium salts in graphene planes is the main reason of this low performance.

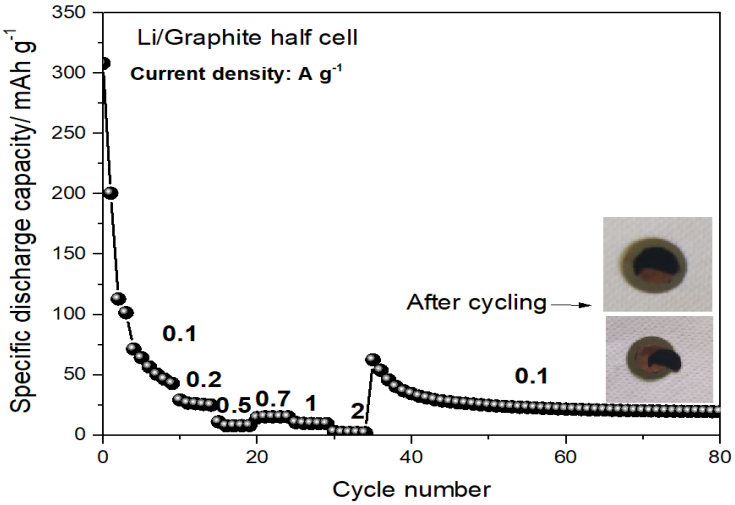

Figure 3.12. Galvanostatic charge/discharge profiles of Li//graphite cell at various current densities during different cycles. Electrolyte: ether-based electrolyte (DOLDME-LITFSI-$LiNO_3$). Potential window: 0.01–3.0 V vs. Li/Li^+. Operational temperature: room temperature.

CBSG/ Li_2S@Gr full-cell

In order to explore the eligibility of the biochar electrode as metallic-lithium substitute in a full-cell configuration, the CBSG electrode was employed as negative electrode in a LiMF sulfur battery. Li_2S@Graphene composite (Li_2S@Gr) was also synthesized to work as the cathode side. In the Appendices section, the synthesis procedure, the structural properties, and electrochemical behaviour of this sample are provided. The CBSG electrode was prelithiated before the full-cell assembly using the method described in the Experimental Section (see Figure 3.1). The formation of SEI on the electrode surface as a result of the prelithiation process increases the cell's initial coulombic efficiency, reversibility, and cyclic stability [271]. Figure 3.13a and b report the rate capability performance of the CBSG/ Li_2S@Gr cell showing the specific discharge capacity vs. cycle number and the voltage profiles, respectively. The test was carried out by increasing the current from 0.05C to 1C (= 1166 mA g^{-1}) through 0.1 and 0.5C over 400 cycles. The first charge profile in Figure 3.13b shows a hump as a result of the low initial activation potential at 2.4 V needed to fully extract the Li ions from Li_2S during the first charging cycle. The differential capacity-voltage profile and CV test (Figure 3.13c) were analyzed to verify this phenomenon.

Here, a strong peak that appeared during the oxidation of Li_2S@Gr supports the theory that the nano-sized Li_2S was activated at 2.4 V. The inset of Figure 3.13c shows the CV profile of CBSG/ Li_2S@Gr full-cell during oxidation and reduction processes. During the anodic scan, two peaks appeared at ~2.0 V (identified as Peak 1) and at 2.5 V (Peak 2), associated with the Li_2S oxidation to elemental sulfur, through low and the high-order PSs [267]. Two peaks may be seen when the scan is reversed, at approximately 2.25 V (Peak 3) and 1.8 V (Peak 4). The first one is related to cyclo-S_8 reduction to high-order lithium PSs, while the second one is related to the production of the discharge products Li_2S and Li_2S_2 as a result of further PSs reduction [268,272]. The charge-discharge profiles of Figure 3.13b reveal an initial charge and discharge capacity of 726 and 537 mAh g^{-1} at 0.05C, respectively, resulting in an initial coulombic efficiency of 74%. Furthermore, by increasing the current rate, and consequently the cell polarization [225], the CBSG/ Li_2S@Gr shows a capacity of 412, 350, and 300 mAh g^{-1} at 0.1, 0.5 and 1C, respectively. Interestingly, the cell demonstrated a steady profile for 300 consecutive cycles and delivered 73% of its 0.1C capacity at 1C with a coulombic efficiency that was almost 100% (Figure 3.13a). The cell recovered a discharge capacity of about 355 mAh g^{-1} once the current was reduced to 0.1C, demonstrating the improved reversibility and cycle stability of the CBSG/Li_2S@Gr system.

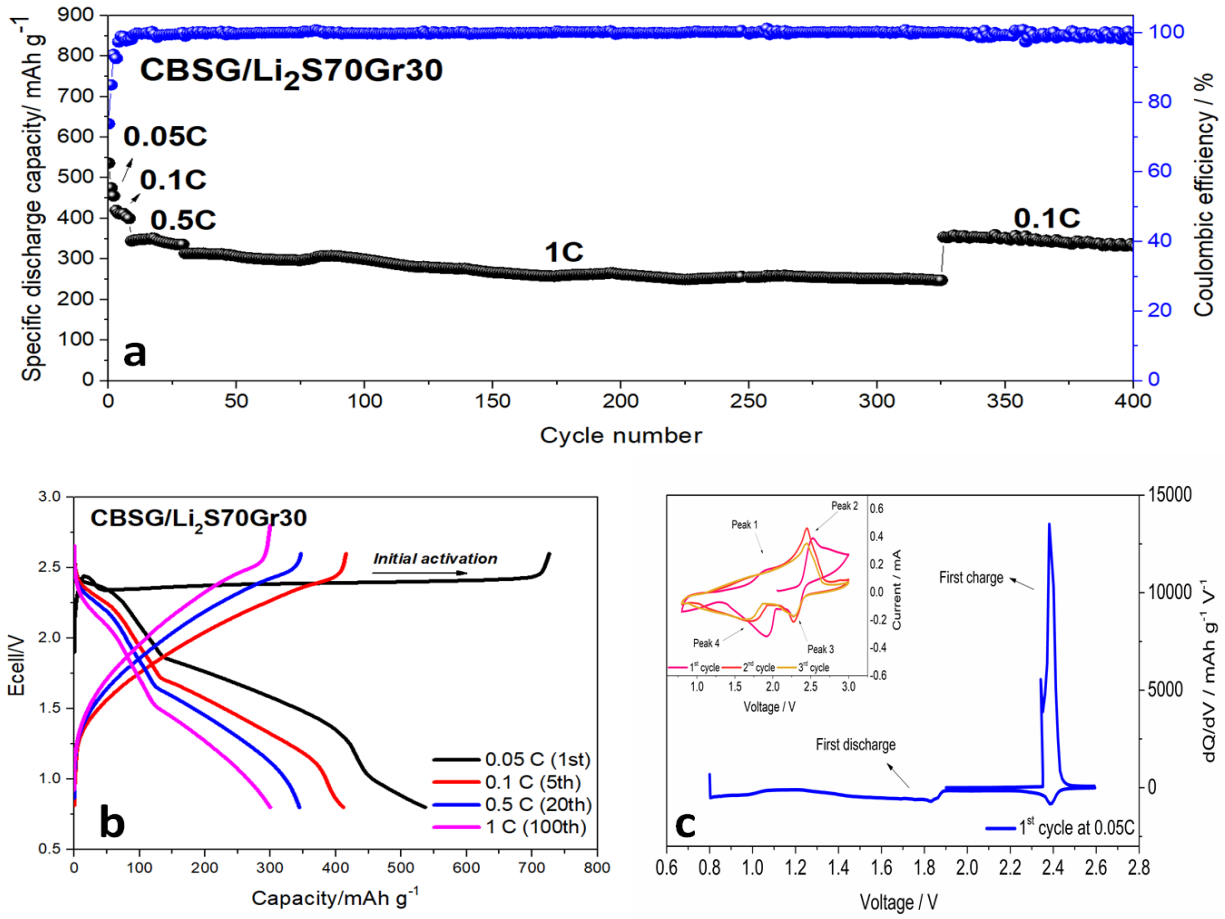

Figure 3.13. (a) Long rate cycling (discharge specific capacity upon cycle number and related coulombic efficiency) of CBSG/ Li_2S@Gr full-cell. The specific capacity of the cell is reported considering the Li_2S mass. (b) Corresponding charge-discharge profiles. (c) Differential capacity profile of the CBSG/ Li_2S@Gr full-cell obtained from the first charge cycle at 0.05C during the rate capability test; in inset, CV test carried out at a 0.1 mV s^{-1} scan rate. All the tests are performed in the voltage range of 0.8- 2.6 V at room temperature. Electrolyte: DOLDME-LITFSI-$LiNO_3$.

The CBSG/ Li_2S@Gr full-cell underwent a galvanostatic charge-discharge test at 1C, and the results are shown in table in Figure 3.14. The full-cell reveals a relatively stable behaviour upon cycling, with an initial discharge capacity of 280 mAh g^{-1} which slowly decreases down to 210 mAh g^{-1} after 350 cycles. The formation of a stable SEI layer on the CBSG surface could be responsible for the reduction of the PS shuttle effect thus leading to the observed performance [273].

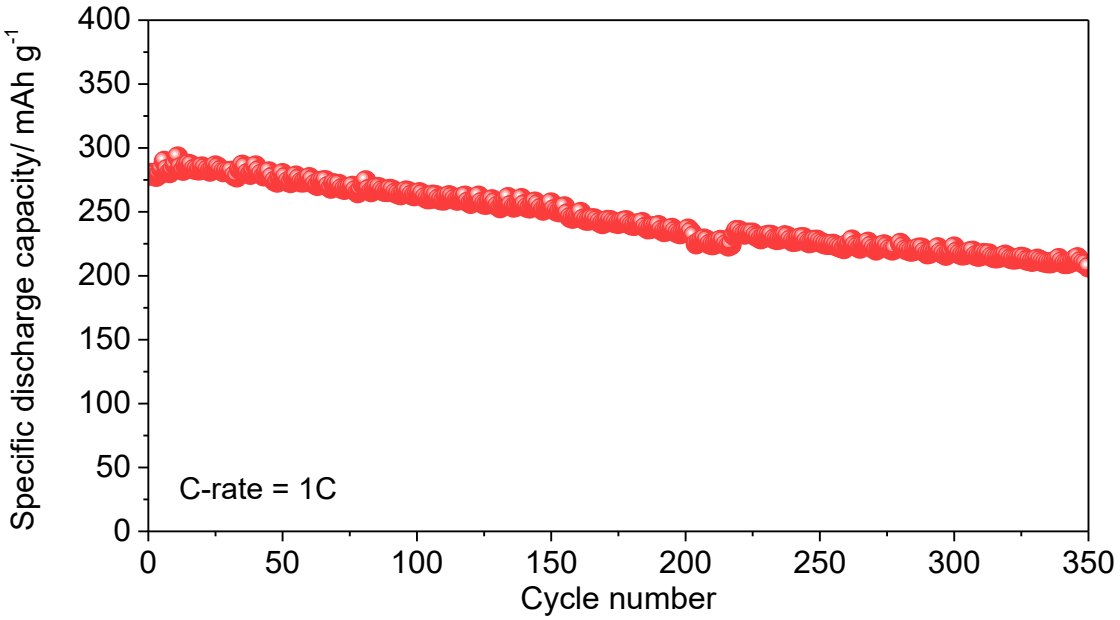

Figure 3.14. Cycling performance of the CBSG/ Li_2S@Gr full-cell at 1C. The tests is performed in the voltage range of 0.8 - 2.6 V, at room temperature, and after an initial activation at low C-rate (C/10). The specific capacity of the cell is calculated considering the Li_2S mass. Electrolyte: DOLDME-LITFSI-$LiNO_3$.

Finally, in Table 3.3 the main electrochemical results of the CBSG/ Li_2S@Gr full-cell are compared with the data obtained for LiMF batteries exploiting Li_2S as cathodic active material. Based on the data, we can draw the conclusion that the strategy proposed in this study offers a novel and promising method to design sustainable and cost-effective electrodes for the next-generation of LIBs.

Table 3.3. Electrochemical performance of LiMF sulfur batteries (full-cell) based on lithium sulfide cathode.

Cathode	Anode	Average working voltage (V)	Capacity (mAh g^{-1}) @ cycle number	Ref.
Li_2S@Gr	CBSG	~ 1.7 at 0.1C	~ 340 @ 400 at 0.1C (after cycling at various C-rates), and ~ 210 @ 350 at 1C	**This work**
Li_2S@MCMB	Si-O-C material	~ 1.4 at 0.2C	~ 280 @ 50 at 0.2C	[274]
Thermally exfoliated graphene–Li_2S	Si thin film	~ 1.6 at 1C	~ 450 @ 30 at 1C	[275]
Li_2S@C composite	Graphite–solid electrolyte composite	~ 2 at 0.01C	~ 650 @ 10 at 0.01C	[276]
Li_2S@porous carbon	Graphite	~ 1.9 at 0.1C	~ 268 @ 30 at 0.1C ~ 173 @ 100 at 0.5C	[267]
Li_2S@graphene nanocapsule	Graphite	~ 1.8 at 0.1C	~ 440 @ 200 at 0.1C	[238]
Li_2S@MXene/graphene	Fe_3O_4/CNs	~ 1.7 at 0.2C	~ 430 @ 50 at 0.2C	[245]
Li_2S-rGO	MnO_2-rGO	~ 1.7 at 0.2C	~ 470 @ 150 at 0.2C	[244]
Li_2S@Carbon aerogel	TiO_2	~ 2.3 at 0.1C	370 @ 200 at 0.1C	[277]
Li_2S@Carbon aerogel	Graphene	~ 2.2 at 0.1C	200 @ 200 at 0.1C	[277]
Li_2S	Si-C	-	very low @ 200 at 1C	[278]
Mo-Li_2S-graphene	Si-C	~ 2.2	463 @ 200 at 1C	[278]

3.4 Conclusion

Here, a new pathway is presented to achieve highly efficient, environment friendly and safe lithium-metal free (LiMF) sulfur batteries, with the primary goal of avoiding the negative impact of metallic lithium for application in LSBs. In this study, an eco-friendly and low-cost material based on brewer's spent grain (BSG) is used as anodic active material for application in sulfur full-cell configuration. In a typical ether-based electrolyte, the naturally N- and O-doped biochar displayed a steady electrochemical behaviour. The biochar material demonstrated improved electrochemical performance due to the large average interlayer spacing, the presence of pyridinic/quaternary N atoms coupled with oxygen-containing groups, and the cross-linked carbonaceous clusters. Additionally, a straightforward recrystallization technique was used to create a Li_2S-few layer graphene-based composite material for the positive electrode. This composite material was activated during an initial cycle at a low C-rate without the need of a high voltage. LiMF cells were then assembled by coupling the prelithiated CBSG and the Li_2S@Gr composite, used as anode and cathode, respectively. The developed LiMF cell had a coulombic efficiency of 74% with initial charge and discharge capacities of 726 and 537 mAh g^{-1}. During the electrochemical measurements, the proposed system showed outstanding cycle stability upon Li insertion/de-insertion. This work offers the first-reported approach for designing sulfur batteries based on a biochar anode. However, further optimization is still needed to develop fast-charging LiMF based on sulfur chemistry, making it suitable for more mass-critical fields of application such as aviation, drone, and EVs.

"This chapter is a slightly modified version a paper (https://doi.org/10.1002/eem2.12567) published in Energy & Environmental Materials and has been reproduced here with the permission of the copyright holder"

- *In this chapter, Li_2S@Graphene composite (Li_2S@Gr) was used as the cathode side to combine with biowaste-based anode electrode to make a Lithium-metal free sulfur battery. In the Appendices section, the synthesis procedure, the structural properties, and electrochemical behaviour of this sample are provided.*

Chapter 4 . The electrochemical behavior of biochar and activated biochar derived from spent common ivy in the lithium-metal free sulfur batteries

Lithium-sulfur batteries have emerged as sustainable replacements for current lithium-ion batteries (LIBs). The commercial viability of this battery technology is still in doubt due to the use of a highly reactive lithium-metal anode and complex electrochemistry of the sulfur cathode. Herein, we propose a sulfur-based battery (particularly, lithium-metal free sulfur batteries) that is free of a metallic lithium anode, and other critical raw materials. In order to assess the importance of the type of anode as an alternative to metallic lithium, two biomass-based anode electrodes (biochar and activated biochar) derived from spent common ivy were compared from structural and electrochemical points of view. The use of biomass-derived materials is promising in the new battery system because of their numerous advantages, such as strong physical and chemical adsorptions, abundant sources, low cost, and environmentally benign. Both biochar and activated biochar exhibited good electrochemical compatibility in the electrolyte condition of sulfur batteries. Surprisingly, ivy biochar (i.e., the sample with no post-treatment) revealed better performance in comparison with the activated biochar, reaching the stable capacity of 400 mA h g^{-1} at 0.1 A g^{-1}, and long lifespan (>400 cycles at 0.5 A g^{-1}). Our results demonstrated that surficial oxygen functional groups positively affect the capacity and cycling performance of the electrodes which led to increase the d-spacing graphitic layer, strong interaction with solid electrolyte interphase layer, and better ion transportation. Finally, biochar with high content of functional groups such as nitrogen and oxygen, was coupled with sulfur cathode to fabricate lithium-metal free sulfur batteries.

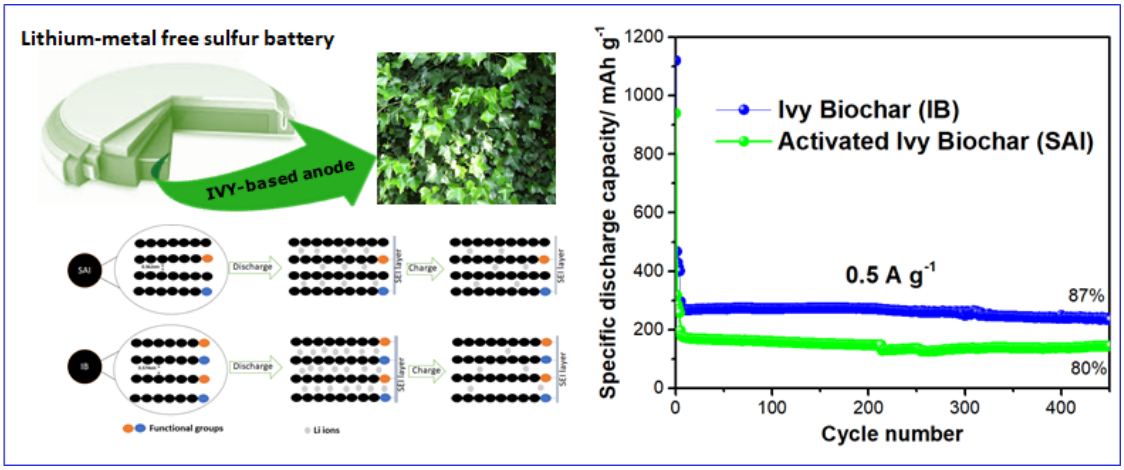

4.1 Introduction

Significant use of fossil fuels (petroleum, coal, natural gas, etc.) and the fast increase in the world's population led to global warming and numerous negative environmental impacts, which inspired many researchers to call for more efficient, sustainable, and secure ways to store energy. Developing renewable energy storage systems has been considered a key tool to avoid the negative impacts of conventional energy resources [279]. However, some renewable energy sources, such as solar and wind, are erratic and unstable, making them difficult to use in our daily life as soon as feasible [280]. Nowadays, rechargeable batteries attracted a great attention for large-scale electrical energy storage applications [22]. Lithium-ion batteries (LIBs) have gained significant consideration throughout the past three decades among the various types of rechargeable batteries for a wide range of applications, including portable devices and electric vehicles [281]. They are also appropriate for usage in the aerospace and aviation sectors [282]. However, for these battery technologies, there is a critical need to enhance the electrochemical performance of the active materials, which are in charge of the storage mechanism, in terms of their cost and environmental impact, as well as their capacity, energy density, and cycling stability. One of the most used anode materials in LIBs is graphite which has poor theoretical capacity (372 mA h g^{-1} vs. Li/Li^{+}), and cannot fulfil the need of future battery [211]. The other technical barrier of graphite is its poor compatibility with the ether-based electrolyte (most common electrolyte for sulfur-based batteries) [234].

A promising alternative to current anode electrodes is carbon obtained from biomass resources such as peanut shells, rice husks, green and brown algae, etc [41,97,283–286]. This carbon is known as biochar and it is mainly the solid residue from the pyrolysis procedure [287]. Biochar can be derived from spent biomass or industrial waste. It possesses non-graphitic/non-graphitizable structure with some heteroatoms, and disordered configuration of cross-linked carbon sheets [127]. The interesting characteristic features of biochar are their adjustable surface area, pore structure, and excellent electronic conductivity [87]. It is worth noting that, according to the life cycle assessment, the use of waste materials as input material for biochar production, would result in significant environmental benefits in line with the context of a circular economy [288]. Additionally, biowaste is still under-utilized and frequently burned outdoors, which disrupts

carbon neutrality and pollutes the environment by producing CO_2, volatile organic compounds, and oxides. Therefore, reusing biowaste for energy purposes is one sustainable approach.

One promising, novel biomass (waste) stream in this regard would be the common ivy, Hedera helix L.. Currently it is used for the preparation of herbal cough-syrups, as coverage in green walls, due to its large content of extractable pharmaceutically active compounds (hederacoside C and α-hederin) [289]. Moreover, it is also applied in vertical greenery systems in urban environments, where it has positive effects on urban air quality and reduces the urban heat island effect[290]. These vertical greenery systems require regular trimming, which would generate a substantial biomass residue streams which has proven to be an ideal feedstock for high-quality biochar production [291].

Based on our previous research [292], the high potential of biochar for application in next-generation batteries (i.e., Lithium-metal free sulfur (LiMFS) technology) has been revealed. In that study, brewer's spent grain (BSG) has been employed as the anodic active material after the pyrolysis procedure to couple with the Li_2S cathode. The inherently N, O-doped biochar displayed the stable capacity around 350 mA h g^{-1} after 315 cycling in the ether-based electrolyte. Additionally, it has been proved that engineering biochar through either steam or CO_2 activation enhances the electrochemical performance of the bi-based electrode in conventional LIBs [197]. The higher surface area, and more hierarchical distribution of micro/mesoporous of the activated sample in comparison with those of the unmodified biochar, are the main reasons behind the better electrochemical performance of the activated sample. Indeed, activation can provide plenty of sites for charge-transfer reactions and shorten the diffusion length of lithium ions.

LiMFS as the next-generation LIBs, which is not dependent on critical raw materials (i.e., manganese, cobalt and nickel) should be considered one of the most promising alternatives to current LIBs [229]. This battery technology avoids the use of metallic lithium, providing a safer and longer life system in comparison with lithium-based sulfur batteries. Additionally, sulfur with high gravimetrical energy density[293] is naturally abundant, making a very promising concept for sustainable battery value chains for many applications, especially for emerging markets such as drones and aviation.

Although many studies are done, especially for the application of biochar in conventional batteries, today, there is a need to investigate the electrochemical behaviour of biochar-based anode

materials in the next-generation battery environment. The main objective of this research is to comprehend the electrochemical behavior of (activated) biochar as an anode material to allow the further development of next-generation battery technology. More specifically, we aim to understand how the biochar/ activated biochar properties affect the electrochemical performance of the next-generation LIBs. Herein, we show that the presence of the surficial oxygen functional groups positively affects the capacity and cycling performance of the electrodes. The biochar and activated biochar show different performances in the ether-based electrolyte, owing to their unique properties such as the amount of heteroatoms contents, degree of graphitization order, distance space between graphitic layers, etc. For instance, the initial discharge capacity of IB is around 1200 mA h g^{-1} with 87% capacity retention along 450 cycling at 0.5 A g^{-1}. While SAI reveals the initial capacity of 1000 mA h g^{-1} with 80% capacity retention at the same condition. The better performance of biochar with more O-containing species than that of activated biochar could be associated with the strong interaction between the ether or carbonyl groups and the solid electrolyte interphase (SEI) formed on the electrode.

4.2 Experimental section

4.2.1 Synthesis of biochar and activated biochar based on spent common ivy

The freshly harvested common ivy trimmings were dried at 105 °C and subsequently shredded in a Retsch SM100 (Retsch, Haan, Germany) cutting mill to 10x10 mm. Pyrolysis experiments were conducted in a modified rotary kiln reactor, type RSRC 120-1000/11 Nabertherm (Lilienthal, Germany) at 700 °C. The reactor consisted of a screw feeder (biomass input rate 350-400 g/h) that fed an indirectly heated tilted rotary kiln. The kiln's rotational speed and inclination were adjusted to have a particle mean residence time of approx. 15 minutes, particle residence times for this reactor were modeled before [294]. Pyrolysis exhaust gases were incinerated in an afterburner.

The produced biochars where ball milled in a Retsch S1 plantery ball mill (Retsch, Haan, Germany) before activation to increase the contact surface between the steam and biochar. After this the biochar was placed into a home-built stainless steel (AISI 310) rotating screw reactor [294]. The reactor was heated to 800 °C under nitrogen atmosphere (70 ml/min), at 20 °C/min until 700 °C/min when a holding time of 30 min was applied, hereafter heating continued at 10 °C/min to minimize temperature overshoot upon reaching the activation temperature of 800 °C.

Physical activation with steam was done at 800 °C for 60 min, steam was added continuously until the steam-biochar ratio was 1:1 wt%. After this samples were cooled under N_2-atmosphere.

4.2.2 Material Characterization

The CHNS elemental analysis was carried out using a Thermo Electron Flash EA1112 elemental analyzer (ThermoFisher Scientific, Waltham, USA) to quantify the main heteroatoms' content in the samples. The oxygen content was then calculated by difference ash obtained by ASTM-D7582 D2866-94 protocol [295]. Surface functionality was investigated using Attenuated Total Reflection (ATR) ((MIRacle ATR, PIKE Technologies) coupled to a Fourier Transform Infrared Spectroscopy (FTIR) (Vertex 70v FT-IR, Bruker). An X-ray diffractometer (XRD, Malvern PANalytical Empyrean) outfitted with a 1.8 kW CuK sealed ceramic tube and a Renishaw in-Via Micro Raman system with a 532 nm laser source were used to determine the crystallinity, mineral content, and degree of order/disorder in the biochar and activated biochar.

The morphology of non-activated and activated biochar was examined using a JEOL JSM-6490LA SEM Analytical (low-vacuum) scanning electron microscope (SEM).

The biochar's and activated carbon's textural characteristics were determined by measuring the N2-physisorption isotherms at 77 K with a Tristar II 3020 surface area analyzer (Micromeritics, Norcross, USA). Prior to the measurement, the sample was dries under nitrogen flow at 150 °C for 16 h. The specific surface area (S_{BET}) was calculated using the Brunauer-Emmett-Teller theory.

4.2.3 Electrode Preparation, Cell assembly, and Electrochemical measurements

The IB and SAI electrodes were prepared according to the protocol reported in the chapter 2 [197]. The active mass loading of the anode electrodes was in the range of 2-3 mg cm^{-2} (thickness is around 50 microns). In a full cell configuration, the sulfur electrode was coupled with the IB electrode (best sample from the electrochemical point of view). The sulfur electrode was prepared by straightforward method mixing 60 wt% sulfur powder (Sigma Aldrich), 30 wt% carbon super C65 (Imerys), and 10 wt% binder (polyvinylidene difluoride (PVdF) from Solvay). N-methyl-2-pyrrolidone (NMP, Sigma Aldrich) was applied as a solvent for slurry preparation. Then, the slurry was ball milled for 15 min at a speed of 1000 rpm, and then casted by Doctor-Blade onto Aluminum foil and dried 3h at 60°C. The electrode foils were punched into 10 mm diameter disks, resulting in active mass loading (sulfur) around 1 mg cm^{-2}.

The conventional ether-based electrolyte (i.e., 1 mol kg^{-1} lithium bis(trifluoromethane)sulfonimide salt (LiTFSI) with the addition of 1% of lithium nitrate ($LiNO_3$) dissolved in a mixture 1:1 w/w of 1,3-dioxolane (DOL) and 1,2-dimethoxyethane (DME)) was used in this study. The electrolyte will be named DOLDME-LiTFSI-$LiNO_3$. The amount of electrolyte was ≈10 $\mu L_{electrolyte}/mg_{active\ material}$ for all electrochemical analyses.

To investigate the performance of the IB anode the LiMFS battery, IB (d=12.6 mm, and ~2 mg) was prelithiated to provide a source of lithium for the system. The prelithiation was done with a current density of 0.1 A g^{-1} (based on the IB active mass) in the same ether-based electrolyte. The detailed information on the prelithiation is reported elsewhere [197]. The IB electrode was rinsed with DME solvent in an argon-filled glove box after cell disassembly and dried for 30 min. Afterward, the sulfur cathode with a mass of 0.9 mg (d=10 mm) was selected to couple with IB anode.

For the half-cell analyses, lithium chips (15.6 mm, MTI Corporation) were used as reference and counter electrodes. The cells were assembled in an argon-filled MBraun glovebox with H_2O and O_2 levels lower than 0.1 ppm. The Li/IB, and Li/SAI half-cells were analyzed with constant current (CC) protocol in the potential range of 0.01-3 V. The Li/Sulfur cell was also assembled and galvanostatic charge and discharge carried out at 0.1C (C= 1675 mA g^{-1}) in the potential range of 1.6- 2.8 V. Finally, the LiMFS cell using IB as anode was electrochemically analyzed in the voltage range of 0.8-2.8 V. The cyclic voltammetry (CV) measurement of the IB and SAI in the half-cell configuration was carried out at different scan rates of 0.1 mV s^{-1} in the potential range of 0.01-3 V. Electrochemical Impedance Spectroscopy (EIS) technique was used at OCP for the half-cells in the frequency range from 10 kHz to 100 mHz with a 10 mV alternating current. All the electrochemical characterization was done at room temperature by employing a BCS-805 multichannel battery unit by BioLogic.

The electrolyte contact angle with the IB, and SAI electrodes was measured using the Data physics OCAH 200 contact angle goniometer.

4.3 Results and Discussion

4.3.1 Structural characterization

The CHNS elemental analysis of the biochar and activated biochar is reported in Table 4.1. CHNS elemental analysis of IB, and SAI samples.. The type of biomass, the pyrolysis and activation

settings, and each pre- and post-treatment step affect the levels of each element and ash in the samples. As reported in literature [146], the activation processes with steam entail oxidation reactions through the diffusion of steam through the porous network, resulting in porosity increase. Herein, SAI (activated biochar) shows less content of nitrogen and oxygen compared to IB (biochar). This is because of the activation process which leads to remove of heteroatoms and increase the carbon content. The steam activation has altered the functional groups on the biochar, particularly contents of oxygen and nitrogen. After the activation process, a large decrease in the H/C, O/C, and N/C ratios has been made. The greater O/C and N/C ratios propose higher doped and surface polar functional groups, which improve the hydrophilicity of the biochar, while the higher H/C ratio predicts more aromatization in the structure of biochar. According to our previous work[197], we observed that a high content of oxygen and nitrogen can reduce the stability of the electrode in the electrolyte condition of conventional LIBs, hence negatively affecting its electrochemical response.

Table 4.1. CHNS elemental analysis of IB, and SAI samples.

Sample	C [%]	N [%]	H [%]	S [%]	O [%]	Ash [%]	H/C	O/C	N/C
IB	76.46	1.94	1.77	-	11.72	8.11	0.023	0.15	0.025
SAI	79.40	0.94	0.88	1.75	4.70	11.41	0.011	0.07	0.011

The functional groups on the samples were also analyzed by FTIR (Figure 4.1a). The IR profiles of the activated biochar and the original biochar are very similar. The peaks at around 2925 and 2855 cm^{-1} are associated with CH_2 asymmetric and symmetric stretching [296]. The bands between 1950 cm^{-1} and 2180 cm^{-1} are related to carboxyl and carbonyl groups [197]. The band at around 1740 cm^{-1} is indicative of the C=O stretching vibration (lignin and hemicellulose) [297]. A band at 1630 cm^{-1} which is more intense in the IB sample is due to the NH_2 deformation in primary amides [298]. The bands between 1100 cm^{-1} and 1300 cm^{-1} are associated with residual signal of C-O-C holocellulose, syringyl, and C-O stretch in lignin and xylan [299,300]. Some bands also are clear below 1000 cm^{-1}, corresponding to aromatic C-H out of plane bending vibration [152,301].

Figure 4.1b exhibits the XRD of the IB and SAI samples which is similar to patterns observed in most disordered carbon materials [158]. There are two distinct broad diffraction peaks at 2θ~24°

and 2θ~44° that are related to the (002) and (100) reflection planes, respectively [159]. Based on Bragg's law ($\lambda=2d_{002}\sin\theta$) [161], the interlayer distance of graphitic layers (d_{002}) is calculated for the samples. The average graphitic interlayer spacing of IB yields a value of 0.374 nm, which is 3.3 % larger relative to the equilibrium spacing of SAI (0.362 nm). In addition to the (002) and (100) reflections, there are other peaks in the XRD patterns that can be related to some inorganic phases, including crystalline SiO_2 (quartz (ICSD 83849) and Trydimite (ICSD 176), typical contaminations found in quartz reactors.

In addition to XRD, IB and SAI samples were analyzed by Raman spectroscopy with a 532 nm laser excitation source to see changes in carbon microstructure during the activation process. The IB and SAI profiles demonstrate two different peaks at ~1340 cm^{-1} and ~1584 cm^{-1} (Figure 4.1c). The peak at 1335 cm^{-1} refers to D band, associated with the disorder and defect of the samples [302]. The later peak is related to G band, showing the stretching vibration of sp^2 carbon plane [303]. The surface defects or amorphous degree of the biochar has been increased by activation that may arise from the formation of aromatic methyl structure [304]. Moreover, the intensity ratio of the D band to the G band (I_D/I_G) increases from 0.88 to 1.01 after activation, indicating that the IB contains more C=O or C=C groups [305].

The monographs of the biochar and activated biochar were analyzed by SEM. Figure 4.1d shows that both samples have a heterogeneous, rough, and uneven surface. Figure 4.1e illustrates the nitrogen physisorption profile of the IB and SAI samples, which was carried out to recognize the surface area and porosity. The isotherms are composite in nature, exhibiting a combination of type I and type IV isotherms (IUPAC classification) with an evident type of H4 hysteresis loop. This suggests that a micro and mesoporous structure coexist. Following the initial region of reversible micropore filling, multilayer physisorption and capillary condensation occur. This is the typical profile of a micro/mesoporous activated carbon with a slit-like pore structure [306]. As summarized in Table 4.2. Results of nitrogen physisorption analysis., both samples reveal high surface areas. According to the BET surface analysis, the specific surface areas (SSA) of IB and SAI are equal to 284.8 and 627.6 $m^2\ g^{-1}$, respectively. Although activated biochar has higher surface area compared to the biochar, this analysis also demonstrated that only pyrolysis at 700 °C is high enough to achieve porous structure with relatively high surface area. The high surface area and distribution of micro- and mesopores provide many active sites for charge-transfer reactions and for cutting the diffusion time for Li ions.

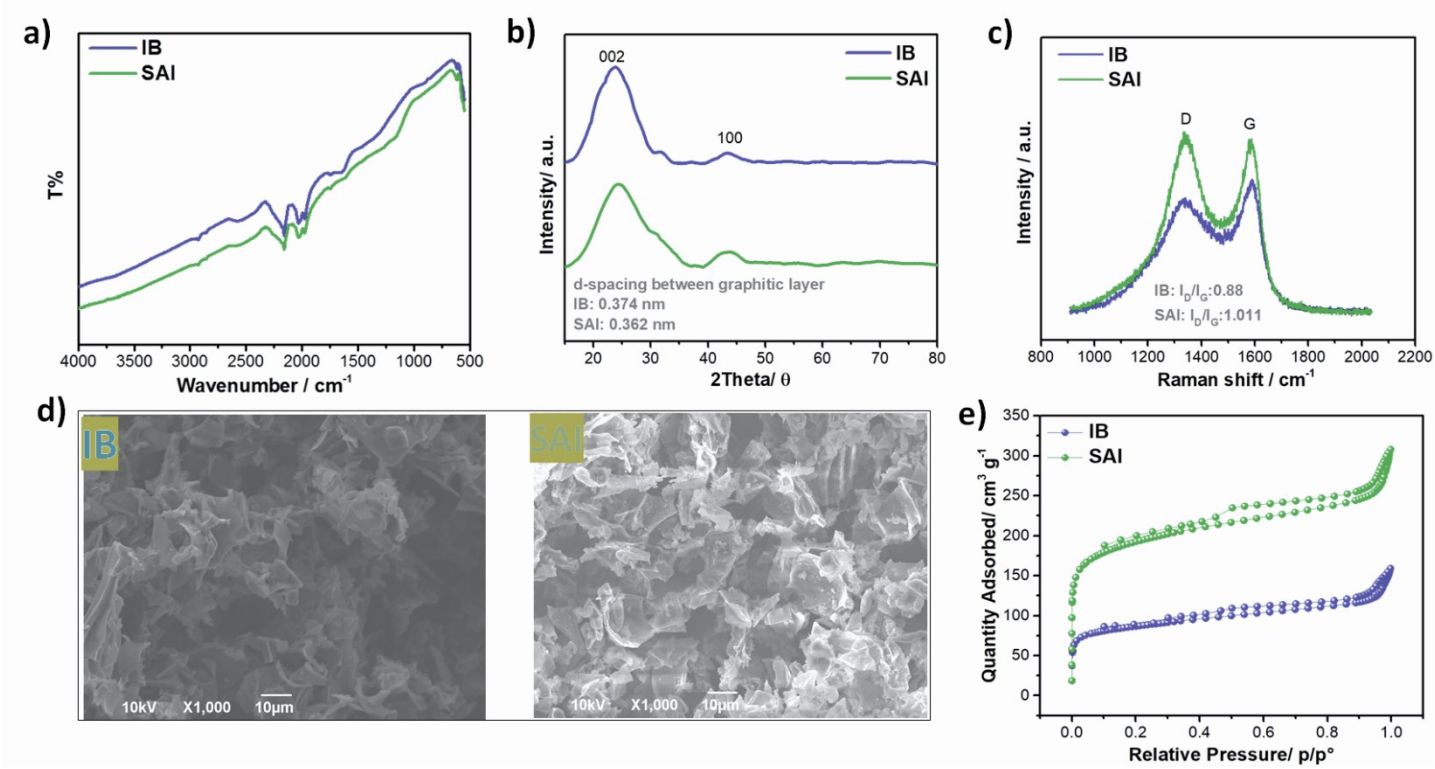

Figure 4.1. ***a)*** *FTIR spectra,* ***b)*** *XRD patterns,* ***c)*** *Raman spectra, and d) SEM images of IB, and SAI. e) Nitrogen adsorption-desorption isotherms of IB, and SAI.*

Table 4.2. Results of nitrogen physisorption analysis.

Sample	S_{BET} $(m^2 g^{-1})$	$S_{langmuir}$ $(m^2 g^{-1})$
IB	284.8	459.1
SAI	627.6	1002.1

4.3.2 Electrochemical characterization

In this part, the electrochemical performance of the biochar and the activated biochar will be discussed through electrochemical techniques such as CV, galvanostatic charge/discharge, EIS, and GITT. Figure 4.2a, and b demonstrate the CV curves of the IB and SAI electrodes in half cell configuration versus metallic lithium at a scan rate of 0.1 mV s^{-1}. During the first reduction, two peaks appeared in the IB electrode (at ~2.25, and 1.8 V) which are related to the irreversible reaction of the ether-based electrolyte with the surface functional groups of IB, confirming the

existence of more heteroatoms such as oxygen, and nitrogen[170] in IB compared to those with SAI electrode. Additionally, the other irreversible peak at 1.5 V is associated with $LiNO_3$ decomposition [265]. Both electrodes exhibit identical characteristics and a broad reduction peak at around 0.7 V, indicating the formation of an SEI film on the electrode surface [307]. This peak has not disappeared in the subsequent cycles (particularly for SAI electrode), which is attributed to the incomplete stabilization of the SEI layer during first reduction. Additionally, two redox peaks can be seen at about 0.01 V (cathodic peak) and ~0.2 V (anodic peak), which represent the lithiation and de-lithiation of the electrodes, respectively [308]. Furthermore, a broad oxidation peak at around 1.1 V is clear in the IB sample which could be related to the capacity current on the surface/edge sites of the biochar. Interestingly, both electrodes (especially, IB) demonstrate almost overlapped curves from the 3rd to the 10th cycle, meaning a good reversibility of the redox processes.

Galvanostatic charge-discharge of the samples are provided in Figure 4.2c, and d. The non-activated biochar and activated biochar show an initial discharge capacity of 1185 mA h g^{-1}, and 1004 mA h g^{-1}, at 0.1 A g^{-1}, respectively. Additionally, the IB electrode achieves an initial coulombic efficiency (ICE) of 40%, whilst the ICE is 31% for the SAI. The lower ICE of the SAI electrode compared to that of IB could be caused by the higher SSA of activated biochar, which would promote an excessive amount of electrolyte decomposition in the high potential zone. Furthermore, low ICE is a typical characteristic of turbostratic porous carbon structures [42]. Despite the fact that both electrodes exhibit low ICE, the third's cycle efficiency raised to about 98%, and 94% for IB, and SAI, respectively. After the first few cycles, the coulombic efficiencies increased dramatically to the range of 99%, illustrating the good stability of the electrodes.

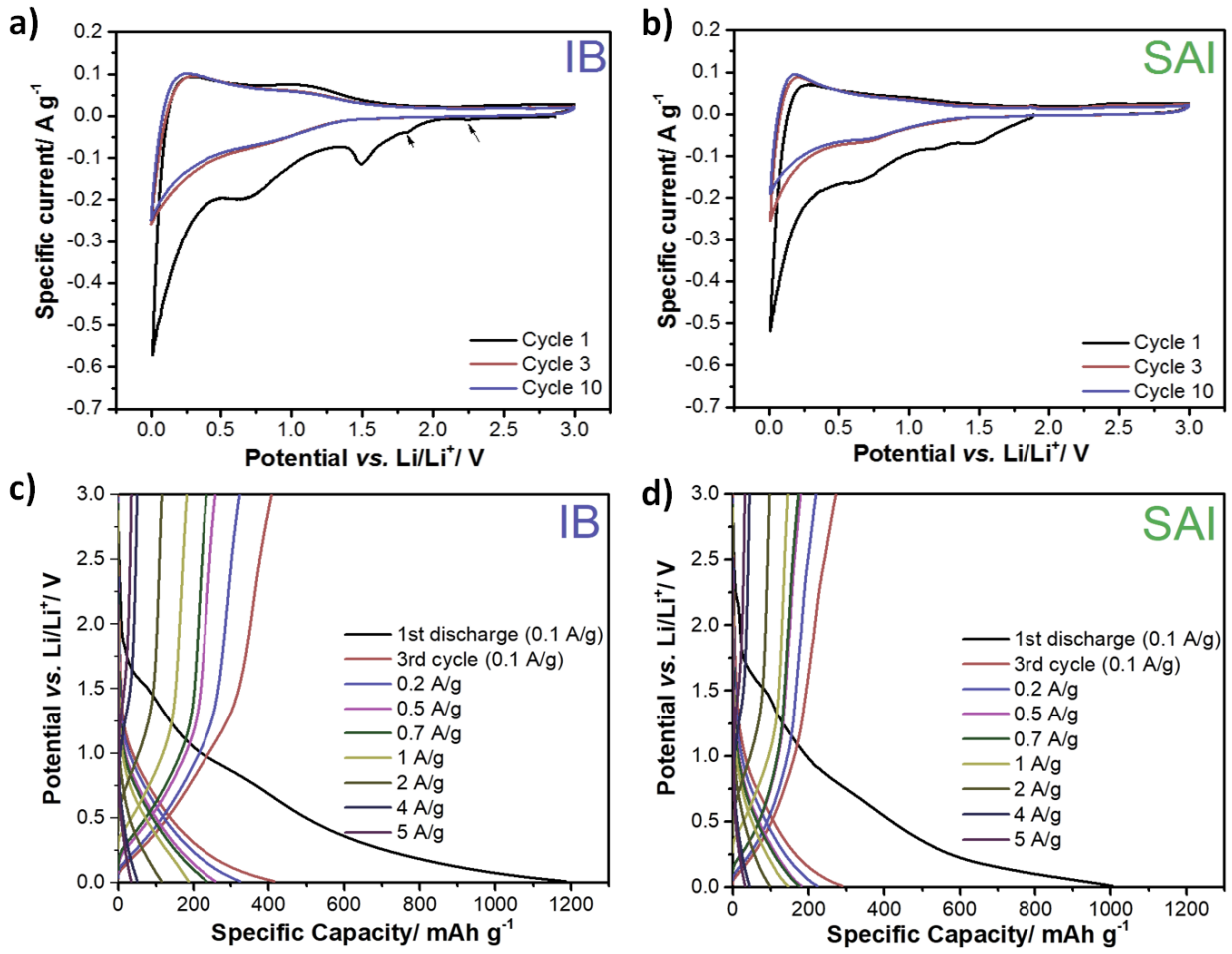

Figure 4.2. a) and b) CV curves of the IB and SAI electrodes at a scan rate of 0.1 mV s^{-1}. (c, and d) Galvanostatic charge-discharge profiles of IB, and SAI electrodes, performed in lithium-metal half cells at room temperature within 0.01-3 V.

Figure 4.3 reveals the discharge capacity contributions of the two specifics potential ranges (slanted and plateau). Figure 4.3a shows the similar behaviour for both electrodes with more contribution of slanted capacity (above 0.1 V) compared to plateau capacity (below 0.1 V). According to recent studies, the high-potential slanted region could be related to lithium-ion adsorption at the defects and functional groups, while the low potential plateau region is associated with lithium-ion intercalation into the graphitic layers of the carbon-based electrodes [309,310]. Lithium-ion adsorption on defects and edge sites of the carbon surface is the dominant storing mechanism in both cases. Herein, the IB sample presents more contribution of plateau capacity than that of SAI electrode which could be related to the more graphitization order in IB (as discussed in Raman spectroscopy section). Figure 4.3b, and c demonstrate that both slanted and

plateau capacities decrease by increasing the current densities due to the polarization increase. Interestingly, at higher current densities (i.e., 2, 4 and 5 A g^{-1}), both IB, and SAI electrodes exhibit similar behaviour. From these results, we find out that diffusion of the lithium-ions in defects, and edge sites of (activated) biochar is more than that of the intercalation into the graphitic layer. Additionally, under fast charge and discharge, there is not sufficient time to intercalate lithium-ions into graphitic layer of the electrodes. That is why, SAI electrode shows less capacity drop by increasing current densities compared to IB electrode (Figure 4.3a).

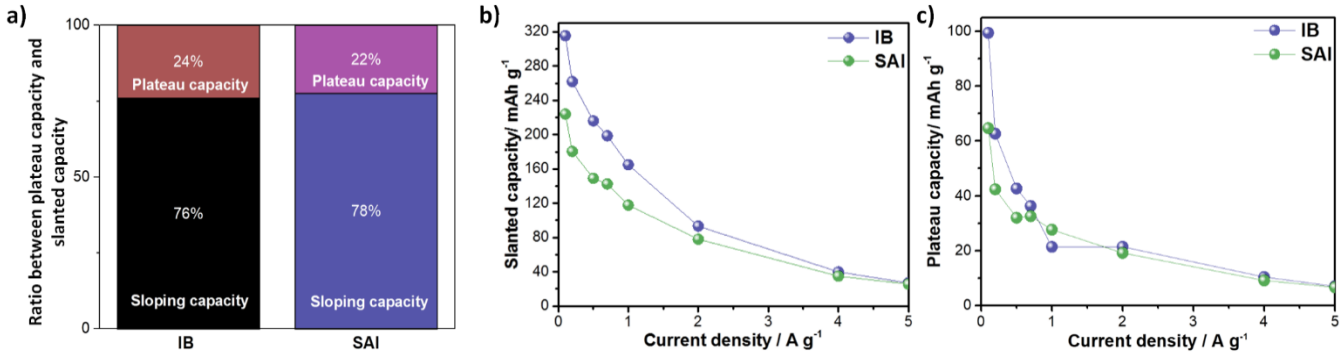

Figure 4.3. a) The capacity contribution for two different potential ranges of IB and SAI electrodes, corresponding to the 3rd discharge. b) Slanted capacity, and c) plateau capacity of the electrodes at various current densities.

Figure 4.4a exhibits the rate performance of IB and SAI electrodes over cycling at various current densities. At 0.1, 0.2, 0.5, 0.7, 1, 2, 4 and 5 A g^{-1}, the specific discharge capacity of IB is around 390 (0.1), 325 (0.2), 260 (0.5), 235 (0.7), 188 (1), 112 (2), 50 (4), and 34 mA h g^{-1} (5). On the other hand, the activated biochar presents the specific discharge capacity values around 272 (0.1), 224 (0.2), 181 (0.5), 175 (0.7), 145 (1), 97 (2), 44 (4), and 32 mA h g^{-1} (5). At all current densities, the non-activated electrode offers higher reversible capacities. This could be related to the presence of more heteroatoms in the IB structure and the larger d-spacing graphite layer of IB (0.374 nm for IB in comparison with 0.362 nm for SAI) which provide more active sites for lithium adsorption and diffusion. Additionally, when current density recovered to 0.1 A g^{-1} after cycling at different current densities, IB electrode showed no capacity drop (compared to 10th cycle at 0.1 A g^{-1}) in comparison with 4% capacity reduction in the case of SAI. However, at higher current densities of 1 A g^{-1}, the delivered capacities of IB and SAI are very close. This negligible capacity difference reflects to insufficient intercalation of Li ions into graphitic layer of the electrodes under

fast reduction. In other words, at higher current densities, lithium ions adsorption on the defect and edge sites of the carbon surface is the more dominant storage mechanism than that of observed at lower rates.

Figure 4.4b demonstrates the cycling performance of the electrodes in the electrolyte condition of typical sulfur batteries at 0.5 A g^{-1} (equivalent to ~1.4 C vs. graphite). It is commonly known that (activated) biochar-based electrode expands in volume when lithium ions become embedded in it during redox reactions. Also, the structure will be somewhat subsided when the lithium ions are released from the substance [311]. Compared to bulk material, this structural collapse of the porous material happens more readily. Herein, the material's microstructure gradually becomes stable, and in the 10^{th} cycle (at 0.5 A g^{-1}), the specific discharge capacity of IB and SAI was held constant at 268, and 173 mA h g^{-1}, respectively. The cells with non-activated and activated biochars exhibit the average specific discharge capacity of 260.8, and 147.1 mA h g^{-1} during 450 cycling, respectively. Additionally, the capacity fade is 13, and 20% for Li/IB, and Li/SAI cells. To better understand the electrochemical behavior of the IB and SAI in the ether-based electrolyte, the EIS analysis was carried out every 100 cycles (at 0.5 A g^{-1}) to find out the changes of resistance of SEI film (R_{SEI}). The impedance spectra of the cells are depicted by the Nyquist plots (Figure 4.5a, b), which include two semicircles and a long-inclined line (Warburg impedance) at high and low frequencies, respectively. The numerical values of the R_{SEI} were calculated according to the equivalent circuits reported in our previous work [292]. Although both electrodes demonstrate very low R_{SEI} variation upon cycling (Figure 4.5c), IB shows more stable film formation which could be related to the strong interaction between the surface oxygen functional groups of IB and the SEI layer. Additionally, in comparison with SAI, IB has lower charge transfer resistance at the electrode-electrolyte interface (second semi-circle in every 100 cycles). Furthermore, the overall impedance (size of the semi-circles) of IB also is smaller than that of SAI. Next, the swelling effect of the electrolyte was investigated by contact angle determinations for both electrodes (Figure 4.6). The IB shows a rapid wetting behavior ($\Theta = 15°$)) toward the electrolyte, whereas the SAI displays a slower wetting response ($\Theta = 26°$). These findings reveal that the oxygen functional groups are beneficial to lithium-ions insertion/de-insertion into/from biomass-based electrode during discharging and charging, therefore the cell prepared with IB electrode with more oxygen functional groups shows higher capacity with excellent stability.

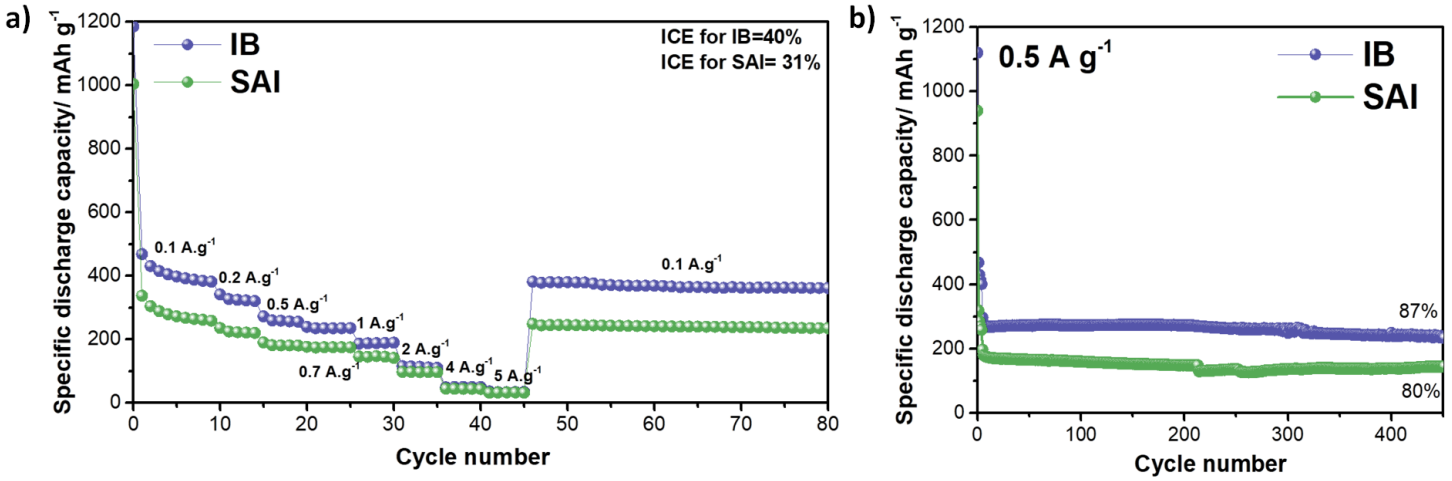

Figure 4.4. a) Rate capability of the IB and SAI over cycling at various current densities, and b) cycling performance (current density of 0.5 A g^{-1}) of the samples performed in lithium-metal half cells and activated at low current density at room temperature within 0.01-3 V. ICE: initial coulombic efficiency.

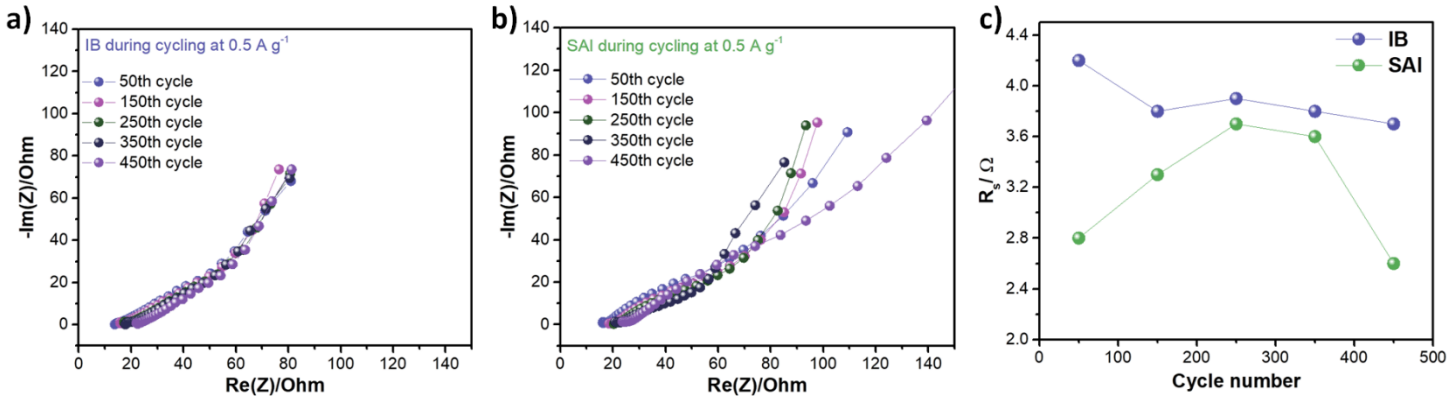

Figure 4.5. Nyquist plots of a) IB and b) SAI electrodes in half cell configuration. EIS (10 kHz–100 mHz) along cycling at 0.5 A g^{-1}; c) Resistances (R_{SEI}) obtained from fitting data every 100 cycles at 0.5 A g^{-1}. The tests were done at OCP condition.

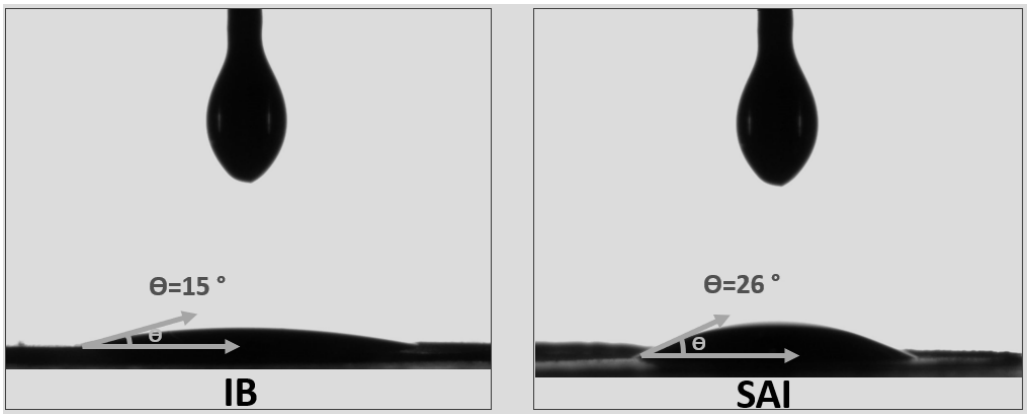

Figure 4.6. Contact angle images for IB and SAI electrodes in the presence of DOLDME-LiTFSI-$LiNO_3$ electrolyte.

The proposed mechanism for the electrochemical behavior (especially at lower current densities) of the activated and non-activated biochars in DOLDME-LiTFSI-$LiNO_3$ electrolyte is shown in Figure 4.7. Since the surface of IB biochar is enriched with functional groups such as oxygen, the hydrophilicity of this electrode is high, leading to better lithium-ion transportation compared to that of SAI. It is interesting to note that the active carbon sites at the nanopores or edges can be changed into the ether or carbonyl groups. When compared to carbon defects, these interfacial oxygen groups show less chemical activity toward electrolyte, which prevents the electrolyte decomposition during redox reactions. While the IB electrode demonstrates a steady performance because of the strong interaction between the ether or carbonyl groups and the SEI layer, the generated SEI film on the surface of SAI can be degraded during recharging as a result of the exfoliation of the graphite layer. As a result, great cycling performance is finally expected for the IB electrode. Additionally, the oxygen groups offer more sites for the lithium-ions' storage, leading to increase in the d-spacing graphitic layer and improving the capacity of the electrode. Furthermore, compared to materials made entirely (or mostly) of carbon, oxygen groups exhibit a stronger wetting behavior toward the ether electrolyte, improving the lithium-ion diffusion coefficient and ensuring excellent rate performance.

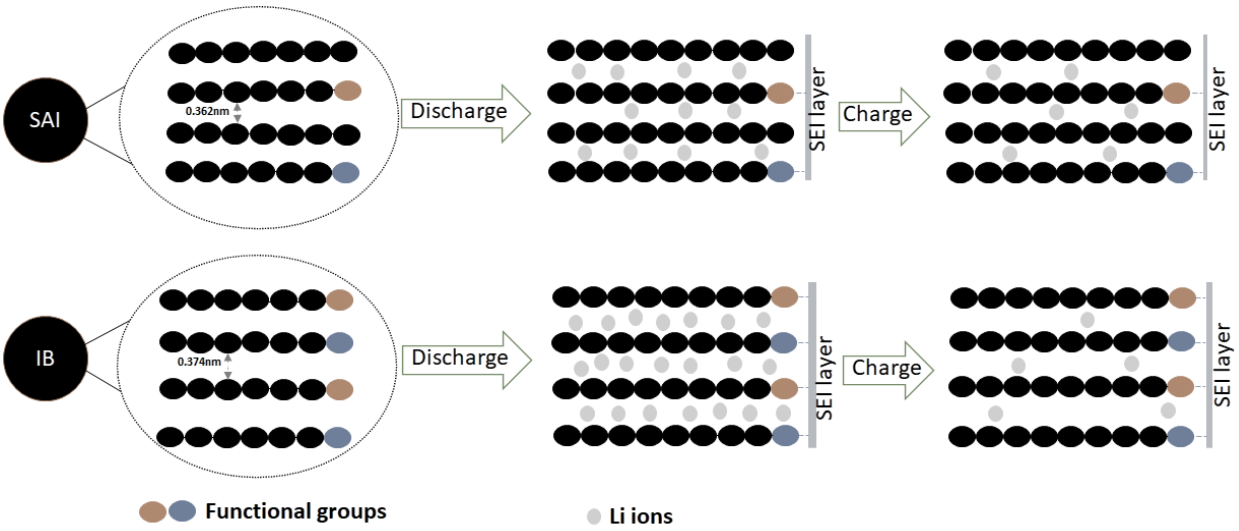

Figure 4.7. The proposed mechanism for IB and SAI electrodes in the electrolyte condition of sulfur batteries.

After the electrochemical analyses of biomass-based electrodes in half-cell configuration, IB was therefore chosen for apply in new LiMFS technology. This battery design is especially appealing for using a low-cost, high-performance, environmentally friendly, and safe anode material as an alternative to traditional graphite and metallic lithium. Before cell assembly, the IB electrode was pre-lithiated according to the procedure discussed in the experimental section. The pre-lithiation step makes the anode possible to act as a lithium reservoir in this novel energy system. Additionally, the capacity balancing between the anode and cathode is crucial to enhance the performance of the LiMFS cell. The different ratios may significantly vary the lithium-ion sulfur cell voltage and its delivered capacity. The balancing should be precisely performed to avoid the overcharge of the battery and lithium plating of the anode which causes safety issues and deteriorates the system's cycle life [203]. In our battery assembly, a slight excess of the anode capacity (i.e., anode capacity to cathode capacity is around 1.1, the typical ratio in LIBs, according to the stable capacity of the electrodes at low current density) has been considered. The lithiated IB//Sulfur cell assembled in the charged state, operated upon discharge by de-intercalation/ desorption of lithium ions at the IB anode and converting lithium polysulfides at the sulfur cathode (Figure 4.8a). Thus, LiMFS cell benefits from multiple-electron reactions (like lithium-sulfur batteries (Figure 4.8c)), low-cost and safer electrodes, unlike lithium-containing batteries which apply critical raw materials and can cause safety issues. The IB//Sulfur cell shows the initial

discharge and charge capacity of 459, and 440 mA h g^{-1}, resulting ICE of 96%. The high ICE of the cell is attributed to the as-formed SEI on the surface of the IB electrode through pre-lithiation which prevents consuming more lithium for this action. This cell reflects a combination of the anode and cathode profiles in half-cell configuration *vs.* Li/Li^+ (Figure 4.2c, and Figure 4.8c). Thus, the cell appears to have two slanted plateaus during discharge, occurring between 2 and 1.2 V, and one voltage plateau during charging, occurring between 1.15 and 2.2 V. The cell's average working potential is around 1.5 V and exhibits a stable capacity of approximately 335 mA h g^{-1} (based on sulfur active mass) with a coulombic efficiency of 99% during 100 cycling charge and discharge at 0.1C (Figure 4.8b). On the basis of the cell voltage and the delivered initial capacity, the Li_xC//Sulfur system delivers energy density of ~ 600 Wh Kg^{-1} (based on sulfur mass loading). Although the innovative cell based on biochar anode could be a very promising energy storage system, there are still some technical barriers and scientific challenges that need to be overcome to maximize the cell efficiency. One of the main challenges is related to the anode prelithiation before coupling with sulfur. Because in LiMFS battery, the anode behaves as the lithium reservoir, the complete lithiation of the anode significantly affects the overall performance of the battery. Additionally, optimizing the anode/cathode mass balancing can further improve the capacity and lifetime of the system. Apart from these, sulfur as the most promising candidate for next-generation energy storage systems is still full of thorns due to the inherent sluggish redox kinetics and severe polysulfides shuttle. Thus, a feasible approach should be studied and considered to guide the practical design of advanced sulfur cathodes for application in LiMFS technology.

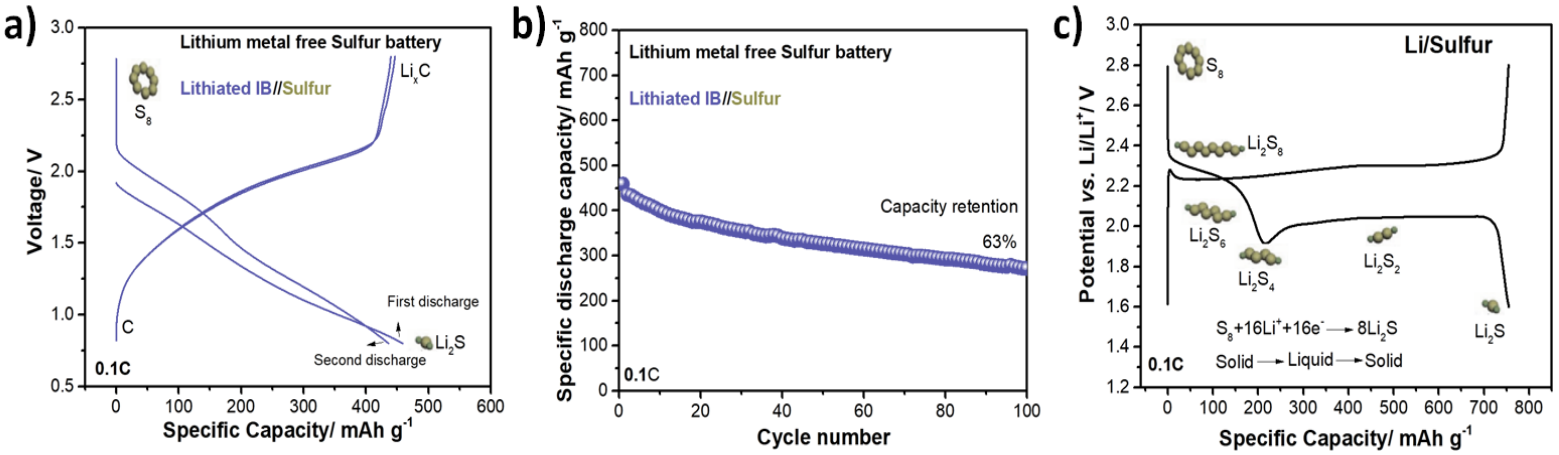

Figure 4.8. a) Galvanostatic charge and discharge profile, and b) cycling performance of LiMFS cell based on IB anode at 0.1C (1C=1675 mA g^{-1}). The specific capacity of the cell is reported considering the sulfur mass. The test is performed in the voltage range of 0.8- 2.8 V at room temperature. Electrolyte: DOLDME-LiTFSI-$LiNO_3$. c) Galvanostatic charge and discharge profile (50^{th} cycle) of Lithium-sulfur cell in the same electrolyte of LiMFS cell in the potential range of 1.6- 2.8 V.

4.4 Conclusion

The morphogical, structural, and electrochemical characteristics of carbons derived from pyrolysis (biochar) and activation (activated biochar) processes were compared for potential applications in lithium-metal free sulfur batteries, LiMFS. The environmentally friendly activation methods (i.e., steam activation) was employed to improve the surface area, and pore size of ivy biochar (IB). For both cases, the assembled lithium half-cells have demonstrated good compatibility in the electrolyte condition of sulfur batteries, with the non-activated biochar cell providing the best long cycling and highest capacity results. Differences in morphology, surface chemistry, surface area, and porosity result in different electrochemical behavior. For instance, IB with lower specific surface area demonstrated higher initial coulombic efficiency (ICE) compared to that of steam activated ivy biochar (SAI). Additionally, in comparison with SAI, IB electrode with higher functional group contents such as oxygen, exhibited a steadier capacity because of the strong interaction between the ether or carbonyl groups and the SEI layer, preventing the exfoliation of the IB's graphite layer.

It should be pointed out that the most significant contribution to the synthesis process of IB and SAI is the electricity and gas consumption during pyrolysis and steam activation. The synthesis of

SAI consumes additional electricity and gas resulting in a more energy-intensive synthesis route. Therefore, from an environmental standpoint, IB with no post-treatment process has lower potential impacts and appears to be the most promising sample for further investigation. Finally, the IB electrode was chosen for application in LiMFS cells as an innovative and green battery technology. The Li_xC//Sulfur system delivered a specific energy density of ~ 600 Wh Kg^{-1}. Although this battery could be very promising energy storage system, there are still some technical barriers and challenges that need to be overcome to enhance the cell performance such as progress in the pre-lithiation strategy, very careful cell capacity balancing, and the practical design of advanced sulfur cathodes.

Chapter 5 . Conclusions and further works

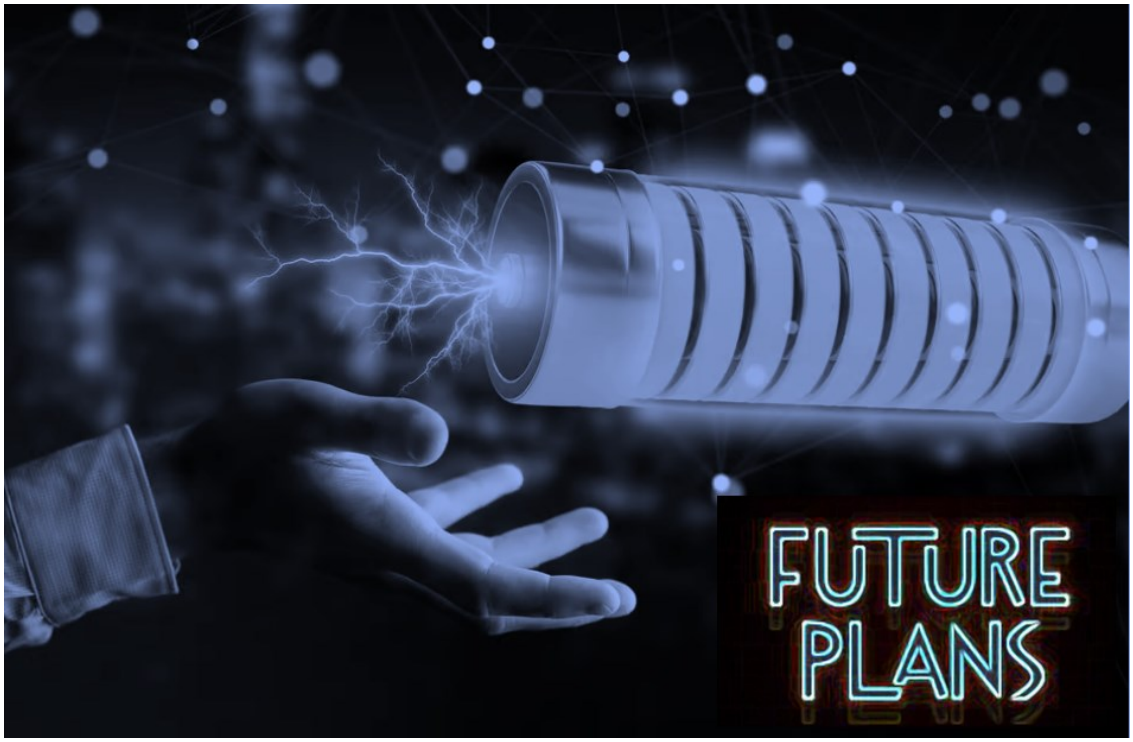

The development of biomass-derived carbons with significant effects on the reduction of carbon footprint for use in current and next-generation batteries was the subject of the research in this thesis. Waste biomass is regarded as a readily available and inexpensive source of carbon for making carbon or self-doped heteroatom carbon compounds. It has been understood that the sources of the biomass used, and their engineering have a significant impact on the performance of the electrodes in lithium-ion batteries (LIBs). The stability, high aromaticity, customizable surface characteristics, and environmental benefits of biochar make them suitable and high potential candidates for a variety of electrochemical energy storage systems, especially as the anode in LIBs. As a next-generation high performance electrode, biochar generated from various resources has been investigated in this study as a potential alternative for graphite, the well-known anode in LIBs since its commercialization. Graphite does not meet the requirement for high-energy

and high-power LIBs because of its limited storage capacity versus Li/Li^+ and its incompatibility in the next-generation sulfur battery environment.

In this project, we have tackled the sustainable batteries problem by breaking it down into its main parts, namely what kind of biomass/waste materials to exploit and their treatment to make them suitable to run as the battery anode. Additionally, the circular economy and scalability have been taken into account.

Herein, we showed that the identification of a successful strategy for the use of waste biomass in the energy storage field would open a new paradigm for massive green-battery production, hence making the proposed scheme suitable for realistic scenarios.

Even though there have been several studies, particularly in traditional LIBs, more research is still needed to fully comprehend how biochars behave in the next-generation and post-LIBs. Due to the complicated nature of biochars, the limitations of deep characterization techniques, and the lack of in-depth knowledge about the properties of biochars and their performance in LIBs, these materials are still far from the lithium battery market. The works listed below are recommended to comprehend the research needs and obstacles that must be overcome in order to maximize the use of biochar materials in electrochemical energy storage and their applications in the future:

- Life cycle assessment (LCA) study of biochar derived from different resources for electrochemical energy storage: Because of biochar's potential for application in energy, and its coproducts (bio-oil and bio-gas), it has drawn a lot of attention as one of the most promising energy resources. Additionally, the bio-based energy can positively affect the global warming, sustainable agriculture, pollutant removal, etc. Nevertheless, to confirm all advantages of biochar, the comprehensive LCA analysis on environmental and energy loads of the production cycle of each feedstock is necessary.
- Deeply understanding of the relationship between the structural properties of biochar, type of feedstock, and performance: Although many studies are done, especially in application biochars in conventional batteries, today, there is a need to fully comprehend the electrochemical behaviour of biochar as anode material to allow the further development of next-generation battery technology. More attention should be paid to understand the relationship between structural properties of feedstocks and biochars. Moreover, it would be even more beneficial to use spent biomass as feedstock. Hence, the effect of combination

of different parameters (e.g. porosity, heteroatoms, surface area, graphitization order, and graphene interlayer distance) on the biochar electrochemical performance should be considered.

- A combination of experimentation and modeling in the time (e.g. Potentiostatic Intermittent Titration Technique (PITT) and Galvanostatic Intermittent Titration Technique (GITT), and frequency (EIS): These techniques help to quantify the kinetics of charge transfer (e.g. lithium (de)insertion rate constant at electrode/electrolyte interface) and transport phenomena in the electrode materials (e.g. solid state lithium diffusion coefficient).
- Potential use of biochar in Sodium-ion batteries: Nowadays, one hot topic in electrochemistry is the development of alternative to Lithium-based battery technology. The main reason is Lithium supply. Sodium-ion batteries as alternative to LIBs, can solve this issue. Furthermore, Sodium is the seventh most abundant element in the earth's crust. On the other hand, Graphite as the most common anode electrode in LIBs, is not thermodynamically favorable for sodium insertion. The hard carbon derived from fossil fuels is the generally use in Sodium-ion batteries. The use of non-renewable resources can negatively affect the environmental balance and battery cost. Therefore, bio-based carbon derived from different resources could be a good option for application in sodium battery technology in terms of cost and environmental points of view.
- Reduction of the well-known polysulfide shuttle effect in Lithium-sulfur batteries by compositing self-doped heteroatoms carbon derived from biomass/waste with elemental sulfur: Biochar with their specific morphology, appropriate pore size, and existence of polar groups can work as the host material to embed sulfur, leading to decrease the dissolution of polysulfides, and improve the electrochemical properties.
- Potential use of biochar in other electrochemical energy storage devices such as supercapacitors, and fuel cells: A promising candidate for a sustainable carbon material may be biochar, that has a lot of surface functional groups and can be easily tuned for porosity. Because of its easily tunable surface chemistry and porosity, research conducted recently have shown that materials based on biochar offer a great deal of potential for use in energy storage and conversion.

Appendices

Li_2S@Gr synthesis, structural and electrochemical performance in Lithium half-cell configuration

The Li_2S@Graphene composite (Li_2S@Gr) was used as the cathode side to combine with a biowaste-based anode electrode to create a lithium-metal free sulfur battery in the third chapter of this thesis, which is titled: Biochar and beyond conventional LIBs: Lithium-metal free sulfur battery based on brewer's spent grain biochar anode. The synthesis process, the sample's structural characteristics, and its electrochemical behaviour are described here:

Synthesis, and structural and electrochemical characteristic of Li_2S@Gr

A solvent evaporation approach was used to synthesize a lithium sulfide-graphene active material in an inert atmosphere. Lithium sulfide from Sigma Aldrich and graphene, the latter produced via liquid-phase exfoliation of graphite, were combined in a flask with anhydrous ethanol as the solvent and dried under molecular sieves for several days in an argon-filled glove box (MBraun). The solution was successively sonicated in a sonic bath for 1.5 hours. After that, the solvent was removed by heating it to 60 °C under a 400 mbar vacuum. All the process was carried out without exposing the sample to the air. To prepare the cathode, the powder was collected and placed in a glove box.

Li_2S@Gr active material powder was investigated by scanning electron microscopy (SEM) and energy dispersive spectroscopy (EDS) using a JEOL JSM-6490LA SEM Analytical (low-vacuum) operating at an acceleration voltage of 5kV with a W filament thermionic source. Scanning transmission electron microscopy (STEM) images and energy dispersion spectroscopy (EDS) maps were acquired with a JEM 1400 Plus (JEOL) provided with a thermionic source (LaB_6) and applying an acceleration voltage of 120 kV. PANalytical Empyrean X-ray diffractometer (XRD) equipped with a 1.8 kW CuKα sealed ceramic tube also applied to structural analysis of the material.

The lithium sulfide-graphene cathode's structure and morphology were examined using XRD analysis and electron microscopy (STEM and SEM). Figure A 1a displays the diffraction pattern of the Li_2S@Gr active material which reveals the presence of the characteristic peaks ascribed to

the cubic Li_2S phase (ICDD: 98-006-0432, cyano bars). Additionally, the graphite-specific diffraction peaks can be seen (ICDD: 98-007-6767, red bars). The small residual peaks can be related to the presence of dilithium sulfate monohydrate (ICDD: 98-020-1530), probably due to the imperfect sealing of the kapton tape employed to prevent the contact with air. The SEM image of the composite electrode is reported in Figure A 1b and the related elemental maps of sulfur and carbon are reported in the insets. Lithium sulfide particles that seem to have been uniformly deposited on the carbonaceous surface are seen to be covering graphene flakes of various sizes in the SEM image. As suggested by the elemental EDS maps of sulfur (in inset, cyano shades), no evidence of sulfide aggregation is visible and the detected element shows a homogeneous overall distribution on the carbonaceous surface (in inset, red colour).

Figure A 1c presents the STEM image of the lithium sulfide-carbon composite and the corresponding EDS map. The EDS map supports the STEM photo's finding that there are tiny lithium sulfide particles anchored to the surface of the graphene sheets. The diameter of the Li_2S particles, which are dispersed at random throughout the carbon-based substrate, is in the range of 10 to 30 nm.

The Li_2S particles dimension also is calculated according to Scherrer equation through XRD pattern (Figure A 1a):

$$L=K\lambda/B.\ Cos\Theta \qquad \text{Equation 5.1}$$

L= crystallite size

K= Shape factor, for Li_2S is 0.94 because of cubic symmetry of Li_2S crystal

B=line broadening at half the maximum intensity (FWHM), after subtracting the instrumental line broadening, in radians.

θ = *the Bragg angle*

The Li_2S particles dimension is in the range 10 - 30 nm in diameter with an average crystalline size of 23 nm. This result is in line with STEM analysis.

Nano sized of Li_2S particles is necessary to overcome the initial activation barrier which is the main issue of Li_2S electrode by routine synthesis method. The conversion of Li_2S to sulfur as S_8 involves a large overpotential due to the polysulphides phase nucleation, thus requiring the cell activation at 3.5 V. However, in this work, by synthesizing non size of Li_2S particle, the activation of Li_2S takes place at 2.4 V at initial charge process.

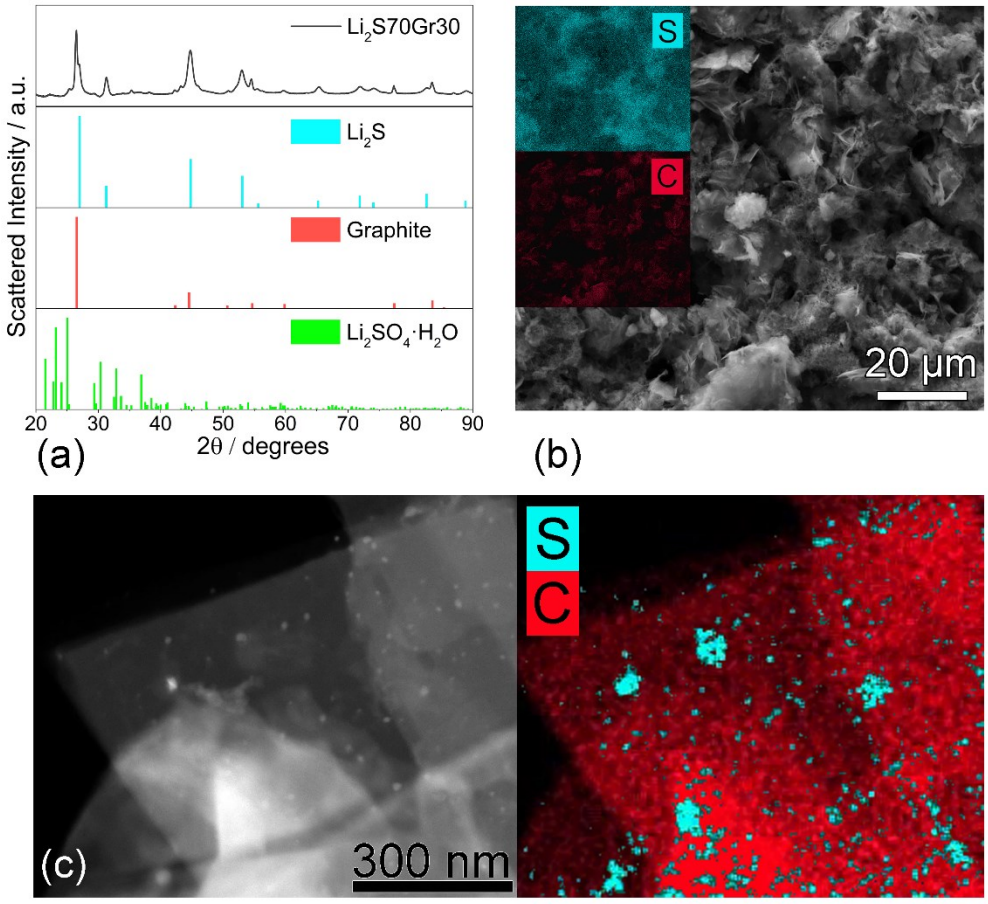

Figure A 1. (a) X-ray diffraction pattern of the Li_2S@Gr active material and reference pattern of cubic lithium sulfide (ICDD: 98-006-0432, cyano bars), graphite (ICDD: 98-007-6767, red bars) and dilithium sulfate monohydrate (ICDD: 98-020-1530, green bars), (b) SEM image of the Li_2S@Gr electrode and the relative EDS maps of sulfur and carbon, (c) STEM image of the composite material (left side) and the related EDS map (red shades for carbon and cyan shades for sulfur).

In a mortar, the lithium sulfide-graphene active material (Li2S@Gr), Super P carbon (from Imerys) as a conductive agent, and polyvinylidene difluoride PVdF (from Solvay) as a binder were mixed in an 80:10:10 weight ratio to form the Li2S@Gr electrodes. N-methylpyrrolidone (NMP, from Sigma Aldrich) was applied as solvent for slurry preparation. The slurry was casted by Doctor-Blade onto a carbon cloth current collector (AvCarb) and dried overnight at 40°C. The electrodes had an active material loading of about 0.6 mg cm^{-2}.

Lithium-metal half-cells using Li2S@Gr as the working electrode were put through testing to assess how well the cathode active material performed electrochemically. Figure A 2a

demonstrates the CV measurements carried out on the Li2S@Gr electrode in the 1.8 V – 2.6 V voltage range at the scan rate of 0.1 mV s^{-1}. The CV profiles exhibit the distinctive form attributed to the multistage interactions between lithium and elemental sulfur. It is interesting that the initial activation barrier was overcome without the requirement for overpotential. This is associated with the small Li_2S particles size and the presence of highly conductive carbonaceous material within the composite.

The first anodic peak at about 2.35 V in the first cycle appears in the following cycles at the same voltage while the second anodic peak initially at 2.5 V shifts to a lower value (2.4 V vs. Li^+/Li) in the following cycles. This latter effect could be related to overpotential reduction subsequent to the initial Li_2S activation. The oxidation of Li_2S to elemental sulfur (S_8) could be the cause of the overall anodic curve. These reactions involve the conversion of Li_2S into low-order polysulfide moieties Li_2S_x ($2 < x \leq 6$) and successively to long-chain species Li_2S_x ($6 < x \leq 8$). In the cathodic scan two reduction peaks appear at 2.4 V and at about 2.0 V, indicating the reversibility of the reaction from S_8 to Li_2S through the formation of PSs species. Figure A 2b and c report the galvanostatic cycling test carried out at 1C (1166 mA g^{-1}) exhibiting the specific capacity vs. cycle number and the relative voltage profiles, respectively.

Figure A 2b shows an initial capacity of 805 mAh g^{-1} (with respect to Li_2S mass). This value was achieved by cycling the cell at C/10 for the first cycle in order to activate the oxidation reaction and thus avoiding the application of a high voltage cut-off (overpotential) to overcome the energy barrier for the Li_2S oxidation. The cell specific capacity is 580 mAh g^{-1} at 1C and gradually drops over the period of cycling to 340 mAh g^{-1} after 350 cycles.

Figure A 2c presents the voltage profile relative to the 1C galvanostatic cycling test. The curve for the first cycle at C/10 in particular exhibits a slight charge overpotential, as seen by the red circle and highlighted in the inset. The following cycles at 1C depict the characteristic voltage profiles of the lithium-sulfur chemistry reactions. In fact, a plateau in the charge curves at about 2.35 V is attributed to the oxidation of Li_2S to elemental sulfur. At roughly 2.35 V and 2.0 V, respectively, two main redox plateaus are visible upon discharge, signifying the transformation of S8 into its

discharge product (i.e., Li_2S_2 and Li_2S). Additionally, a gradual increase in voltage hysteresis over the life of the test indicates a slight capacity loss during cycling.

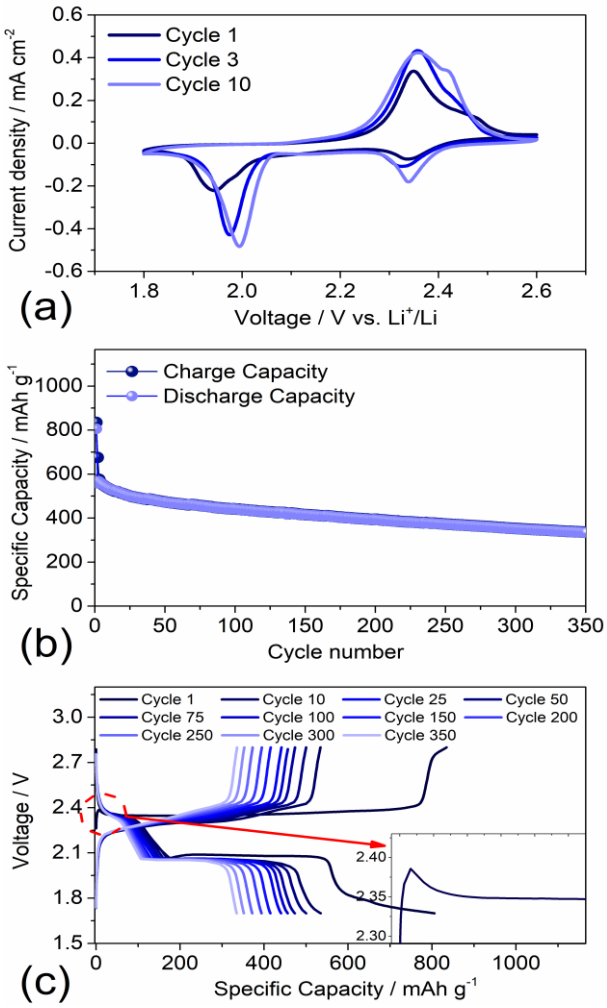

Figure A 2. (a) Cyclic voltammetry tests of Li2S@Gr electrode, performed in 2032-coin cell using DOLDME-LITFSI-$LiNO_3$ as electrolyte in 1.8 V – 2.6 V potential range with a scan rate of 0.1 mV s^{-1}. (b) Galvanostatic cycling profiles and (c) voltage profiles of the Li2S@Gr electrode performed in 2032-coin cells with DOLDME-LITFSI-$LiNO_3$ electrolyte carried out at 1C = 1166 mA g^{-1} after running the first cycle

REFERENCES

[1] T. Placke, R. Kloepsch, S. Dühnen, M. Winter, Lithium ion, lithium metal, and alternative rechargeable battery technologies: the odyssey for high energy density, J. Solid State Electrochem. 21 (2017) 1939–1964. https://doi.org/10.1007/s10008-017-3610-7.

[2] T. Kim, W. Song, D.Y. Son, L.K. Ono, Y. Qi, Lithium-ion batteries: outlook on present, future, and hybridized technologies, J. Mater. Chem. A. 7 (2019) 2942–2964. https://doi.org/10.1039/C8TA10513H.

[3] B. Scrosati, History of lithium batteries, J. Solid State Electrochem. 15 (2011) 1623–1630. https://doi.org/10.1007/s10008-011-1386-8.

[4] H.L. Lord, W. Zhan, J. Pawliszyn, Fundamentals and applications of needle trap devices, 2012. https://doi.org/10.1016/B978-0-12-381373-2.00056-9.

[5] Commission on Chronic Illness, D. Sherbrooke, D. Luca, 张浩波副教授, B. Of, R.C. Hollow, C. Columns, R. With, G. Bars, U. Concentric, E. Loads, Chapter 1 核磁共振成像基本原理, Prev. Chronic Illn. 440 (2021) 1–12. https://doi.org/10.1088/978-0-7503-4881-2ch1.

[6] C. Del Gratta, G.L. Romani, MEG: Principles, methods, and applications, Biomed. Tech. 44 (1999) 11–23. https://doi.org/10.1515/bmte.1999.44.s2.11.

[7] A. Aktaş, Y. Kirçiçek, Solar Hybrid Systems and Energy Storage Systems, 2021. https://doi.org/10.1016/b978-0-323-88499-0.00005-7.

[8] H. Abdi, B. Mohammadi-ivatloo, S. Javadi, A.R. Khodaei, E. Dehnavi, Energy Storage Systems, Elsevier Inc., 2017. https://doi.org/10.1016/B978-0-12-804208-3.00007-8.

[9] B. Sundén, Hydrogen, batteries and fuel cells, 2019. https://doi.org/10.1016/C2018-0-01247-5.

[10] J.P. Zheng, T.R. Jow, High energy and high power density electrochemical capacitors, J. Power Sources. 62 (1996) 155–159. https://doi.org/10.1016/S0378-7753(96)02424-X.

[11] V.L. Martins, H.R. Neves, I.E. Monje, M.M. Leite, P.F.M. DE OLIVEIRA, R.M. Antoniassi, S. Chauque, W.G. Morais, E.C. Melo, T.T. Obana, B.L. Souza, R.M. Torresi, An overview on the development of electrochemical capacitors and batteries – part I, An. Acad. Bras. Cienc. 92 (2020) 1–28. https://doi.org/10.1590/0001-3765202020200796.

[12] J. Xiao, Q. Li, Y. Bi, M. Cai, B. Dunn, T. Glossmann, J. Liu, T. Osaka, R. Sugiura, B. Wu, J. Yang, J.G. Zhang, M.S. Whittingham, Understanding and applying coulombic efficiency in lithium metal batteries, Nat. Energy. 5 (2020) 561–568. https://doi.org/10.1038/s41560-020-0648-z.

[13] Y. Zhou, X. Zhang, Y. Liu, X. Xie, X. Rui, X. Zhang, Y. Feng, X. Zhang, Y. Yu, K. Huang, A High-Temperature Na-Ion Battery: Boosting the Rate Capability and Cycle Life by Structure Engineering, Small. 16 (2020). https://doi.org/10.1002/smll.201906669.

[14] N. Nitta, F. Wu, J.T. Lee, G. Yushin, Li-ion battery materials: Present and future, Mater. Today. 18 (2015) 252–264. https://doi.org/10.1016/j.mattod.2014.10.040.

[15] M.A. Gialampouki, J. Hashemi, A.A. Peterson, The Electrochemical Mechanisms of Solid-Electrolyte Interphase Formation in Lithium-Based Batteries, J. Phys. Chem. C. 123 (2019) 20084–20092. https://doi.org/10.1021/acs.jpcc.9b03886.

[16] K. Xu, Nonaqueous liquid electrolytes for lithium-based rechargeable batteries, Chem. Rev. 104 (2004) 4303–4417. https://doi.org/10.1021/cr030203g.

[17] G. Wan, F. Guo, H. Li, Y. Cao, X. Ai, J. Qian, Y. Li, H. Yang, Suppression of Dendritic Lithium Growth by in Situ Formation of a Chemically Stable and Mechanically Strong Solid Electrolyte Interphase, ACS Appl.

Mater. Interfaces. 10 (2018) 593–601. https://doi.org/10.1021/acsami.7b14662.

[18] M. Nie, D.P. Abraham, Y. Chen, A. Bose, B.L. Lucht, Silicon solid electrolyte interphase (SEI) of lithium ion battery characterized by microscopy and spectroscopy, J. Phys. Chem. C. 117 (2013) 13403–13412. https://doi.org/10.1021/jp404155y.

[19] H. Lv, X. Huang, Y. Liu, Analysis on pulse charging–discharging strategies for improving capacity retention rates of lithium-ion batteries, Ionics (Kiel). 26 (2020) 1749–1770. https://doi.org/10.1007/s11581-019-03404-8.

[20] T. Gao, Z. Wang, S. Chen, L. Guo, Hazardous characteristics of charge and discharge of lithium-ion batteries under adiabatic environment and hot environment, Int. J. Heat Mass Transf. 141 (2019) 419–431. https://doi.org/10.1016/j.ijheatmasstransfer.2019.06.075.

[21] F. Leng, C.M. Tan, M. Pecht, Effect of Temperature on the Aging rate of Li Ion Battery Operating above Room Temperature, Sci. Rep. 5 (2015) 1–12. https://doi.org/10.1038/srep12967.

[22] S. Javadian, P. Salimi, H. Gharibi, A. Fathollahi, E. Kowsari, J. Kakemam, Effect of imidazolium-based ionic liquid as electrolyte additive on electrochemical performance of 18650 cylindrical Li-ion batteries at room and 60 °C temperatures, J. Iran. Chem. Soc. 16 (2019) 2123–2134. https://doi.org/10.1007/s13738-019-01683-6.

[23] D.A.C. Brownson, D.K. Kampouris, C.E. Banks, Graphene electrochemistry: Fundamental concepts through to prominent applications, 2012. https://doi.org/10.1039/c2cs35105f.

[24] T. Kim, W. Choi, H.C. Shin, J.Y. Choi, J.M. Kim, M.S. Park, W.S. Yoon, (How to read CV for batteries) Applications of voltammetry in lithium ion battery research, J. Electrochem. Sci. Technol. 11 (2020) 14–25.

[25] N. Meddings, M. Heinrich, F. Overney, J.S. Lee, V. Ruiz, E. Napolitano, S. Seitz, G. Hinds, R. Raccichini, M. Gaberšček, J. Park, Application of electrochemical impedance spectroscopy to commercial Li-ion cells: A review, J. Power Sources. 480 (2020). https://doi.org/10.1016/j.jpowsour.2020.228742.

[26] S. Schindler, M.A. Danzer, Influence of cell design on impedance characteristics of cylindrical lithium-ion cells: A model-based assessment from electrode to cell level, J. Energy Storage. 12 (2017) 157–166. https://doi.org/10.1016/j.est.2017.05.002.

[27] A. Yoshino, The birth of the lithium-ion battery, Angew. Chemie - Int. Ed. 51 (2012) 5798–5800. https://doi.org/10.1002/anie.201105006.

[28] A. Mauger, C.M. Julien, J.B. Goodenough, K. Zaghib, Tribute to Michel Armand: from Rocking Chair – Li-ion to Solid-State Lithium Batteries, J. Electrochem. Soc. 167 (2020) 070507. https://doi.org/10.1149/2.0072007jes.

[29] R. Yazami, P. Touzain, A reversible graphite-lithium negative electrode for electrochemical generators, J. Power Sources. 9 (1983) 365–371. https://doi.org/10.1016/0378-7753(83)87040-2.

[30] J. Xie, Y.C. Lu, A retrospective on lithium-ion batteries, Nat. Commun. 11 (2020) 9–12. https://doi.org/10.1038/s41467-020-16259-9.

[31] M. Winter, B. Barnett, K. Xu, Before Li Ion Batteries, Chem. Rev. 118 (2018) 11433–11456. https://doi.org/10.1021/acs.chemrev.8b00422.

[32] D. Aurbach, B. Markovsky, A. Shechter, Y. Ein-Eli, H. Cohen, A Comparative Study of Synthetic Graphite and Li Electrodes in Electrolyte Solutions Based on Ethylene Carbonate-Dimethyl Carbonate Mixtures, J. Electrochem. Soc. 143 (1996) 3809–3820. https://doi.org/10.1149/1.1837300.

[33] J.-L. Yang, X.-X. Zhao, W.-H. Li, H.-J. Liang, Z.-Y. Gu, Y. Liu, M. Du, X.-L. Wu, Advanced cathode for dual-ion batteries: Waste-to-wealth reuse of spent graphite from lithium-ion batteries, EScience. 2 (2022) 95–101. https://doi.org/10.1016/j.esci.2021.11.001.

[34] S. Megahed, W. Ebner, Lithium-ion battery for electronic applications, J. Power Sources. 54 (1995) 155–

162. https://doi.org/10.1016/0378-7753(94)02059-C.

[35] F.C. Cowlard, J.C. Lewis, Vitreous carbon - A new form of carbon, J. Mater. Sci. 2 (1967) 507–512. https://doi.org/10.1007/BF00752216.

[36] R.A. Adams, A. Varma, V.G. Pol, Carbon Anodes for Nonaqueous Alkali Metal-Ion Batteries and Their Thermal Safety Aspects, Adv. Energy Mater. 9 (2019). https://doi.org/10.1002/aenm.201900550.

[37] E.R. Buiel, A.E. George, J.R. Dahn, Model of micropore closure in hard carbon prepared from sucrose, Carbon N. Y. 37 (1999) 1399–1407. https://doi.org/10.1016/S0008-6223(98)00335-2.

[38] J.R. Dahn, W. Xing, Y. Gao, The "falling cards model" for the structure of microporous carbons, Carbon N. Y. 35 (1997) 825–830. https://doi.org/10.1016/S0008-6223(97)00037-7.

[39] L.F. Zhao, Z. Hu, W.H. Lai, Y. Tao, J. Peng, Z.C. Miao, Y.X. Wang, S.L. Chou, H.K. Liu, S.X. Dou, Hard Carbon Anodes: Fundamental Understanding and Commercial Perspectives for Na-Ion Batteries beyond Li-Ion and K-Ion Counterparts, Adv. Energy Mater. 11 (2021). https://doi.org/10.1002/aenm.202002704.

[40] A.K. Mondal, K. Kretschmer, Y. Zhao, H. Liu, H. Fan, G. Wang, Naturally nitrogen doped porous carbon derived from waste shrimp shells for high-performance lithium ion batteries and supercapacitors, Microporous Mesoporous Mater. 246 (2017) 72–80. https://doi.org/10.1016/j.micromeso.2017.03.019.

[41] P. Salimi, S. Javadian, O. Norouzi, H. Gharibi, Turning an environmental problem into an opportunity: potential use of biochar derived from a harmful marine biomass named Cladophora glomerata as anode electrode for Li-ion batteries, Environ. Sci. Pollut. Res. 24 (2017) 27974–27984. https://doi.org/10.1007/s11356-017-0181-1.

[42] Y. Wan, Y. Liu, D. Chao, W. Li, D. Zhao, Recent advances in hard carbon anodes with high initial Coulombic efficiency for sodium-ion batteries, Nano Mater. Sci. (2022). https://doi.org/10.1016/j.nanoms.2022.02.001.

[43] H.D. Asfaw, C.W. Tai, M. Valvo, R. Younesi, Facile synthesis of hard carbon microspheres from polyphenols for sodium-ion batteries: insight into local structure and interfacial kinetics, Mater. Today Energy. 18 (2020) 100505. https://doi.org/10.1016/j.mtener.2020.100505.

[44] H. Zhang, S. Zhao, F. Huang, A comparative overview of carbon anodes for nonaqueous alkali metal-ion batteries, J. Mater. Chem. A. 9 (2021) 27140–27169. https://doi.org/10.1039/d1ta07962j.

[45] H. Li, Z. Cheng, Q. Zhang, A. Natan, Y. Yang, D. Cao, H. Zhu, Bacterial-Derived, Compressible, and Hierarchical Porous Carbon for High-Performance Potassium-Ion Batteries, Nano Lett. 18 (2018) 7407–7413. https://doi.org/10.1021/acs.nanolett.8b03845.

[46] M.S. Dresselhaus, G. Dresselhaus, Advances in Physics Intercalation compounds of graphite, Adv. Phys. 51 (1981) 1–186.

[47] M. Tan, W. Zhang, C. Fan, L. Li, H. Chen, R. Li, T. Luo, S. Han, Boric Acid–Catalyzed Hard Carbon Microfiber Derived from Cotton as a High-Performance Anode for Lithium-Ion Batteries, Energy Technol. 7 (2019). https://doi.org/10.1002/ente.201801164.

[48] N. Wang, Q. Liu, B. Sun, J. Gu, B. Yu, W. Zhang, D. Zhang, N-doped catalytic graphitized hard carbon for high-performance lithium/sodium-ion batteries, Sci. Rep. 8 (2018) 1–8. https://doi.org/10.1038/s41598-018-28310-3.

[49] M. Metra, June 2015 at a glance, Eur. J. Heart Fail. 17 (2015) 535. https://doi.org/10.1002/ejhf.301.

[50] M. Winter, J.O. Besenhard, M.E. Spahr, P. Novák, Insertion electrode materials for rechargeable lithium batteries, Adv. Mater. 10 (1998) 725–763. https://doi.org/10.1002/(SICI)1521-4095(199807)10:10<725::AID-ADMA725>3.0.CO;2-Z.

[51] J.R. Dahn, T. Zheng, Y. Liu, J.S. Xue, Mechanisms for lithium insertion in carbonaceous materials, Science (80-.). 270 (1995) 590–593. https://doi.org/10.1126/science.270.5236.590.

[52] N.A. Kaskhedikar, J. Maier, Lithium storage in carbon nanostructures, Adv. Mater. 21 (2009) 2664–2680. https://doi.org/10.1002/adma.200901079.

[53] R.M. Goody, Crystallite growth in graphitizing and non-graphitizing carbons, Proc. R. Soc. London. Ser. A. Math. Phys. Sci. 209 (1951) 196–218. https://doi.org/10.1098/rspa.1951.0197.

[54] D.A. Stevens, J.R. Dahn, The Mechanisms of Lithium and Sodium Insertion in Carbon Materials, J. Electrochem. Soc. 148 (2001) A803. https://doi.org/10.1149/1.1379565.

[55] H. Hou, X. Qiu, W. Wei, Y. Zhang, X. Ji, Carbon Anode Materials for Advanced Sodium-Ion Batteries, Adv. Energy Mater. 7 (2017). https://doi.org/10.1002/aenm.201602898.

[56] G. Yang, X. Li, Z. Guan, Y. Tong, B. Xu, X. Wang, Z. Wang, L. Chen, Insights into lithium and sodium storage in porous carbon, Nano Lett. 20 (2020) 3836–3843. https://doi.org/10.1021/acs.nanolett.0c00943.

[57] S. Alvin, H.S. Cahyadi, J. Hwang, W. Chang, S.K. Kwak, J. Kim, Revealing the Intercalation Mechanisms of Lithium, Sodium, and Potassium in Hard Carbon, Adv. Energy Mater. 10 (2020). https://doi.org/10.1002/aenm.202000283.

[58] W. Long, B. Fang, A. Ignaszak, Z. Wu, Y.J. Wang, D. Wilkinson, Biomass-derived nanostructured carbons and their composites as anode materials for lithium ion batteries, Chem. Soc. Rev. 46 (2017) 7176–7190. https://doi.org/10.1039/c6cs00639f.

[59] D. Saurel, B. Orayech, B. Xiao, D. Carriazo, X. Li, T. Rojo, From Charge Storage Mechanism to Performance: A Roadmap toward High Specific Energy Sodium-Ion Batteries through Carbon Anode Optimization, Adv. Energy Mater. 8 (2018). https://doi.org/10.1002/aenm.201703268.

[60] P. Fu, S. Hu, J. Xiang, L. Sun, S. Su, S. An, Study on the gas evolution and char structural change during pyrolysis of cotton stalk, J. Anal. Appl. Pyrolysis. 97 (2012) 130–136. https://doi.org/10.1016/j.jaap.2012.05.012.

[61] Q. Wang, C. Zhao, Y. Lu, Y. Li, Y. Zheng, Y. Qi, X. Rong, L. Jiang, X. Qi, Y. Shao, D. Pan, B. Li, Y.S. Hu, L. Chen, Advanced Nanostructured Anode Materials for Sodium-Ion Batteries, Small. 13 (2017) 1–32. https://doi.org/10.1002/smll.201701835.

[62] J. Ni, Y. Huang, L. Gao, A high-performance hard carbon for Li-ion batteries and supercapacitors application, J. Power Sources. 223 (2013) 306–311. https://doi.org/10.1016/j.jpowsour.2012.09.047.

[63] L. Xie, F. Su, L. Xie, X. Guo, Z. Wang, Q. Kong, G. Sun, A. Ahmad, X. Li, Z. Yi, C. Chen, Effect of pore structure and doping species on charge storage mechanisms in porous carbon-based supercapacitors, Mater. Chem. Front. 4 (2020) 2610–2634. https://doi.org/10.1039/d0qm00180e.

[64] Y. Qian, S. Jiang, Y. Li, Z. Yi, J. Zhou, T. Li, Y. Han, Y. Wang, J. Tian, N. Lin, Y. Qian, In Situ Revealing the Electroactivity of P□O and P□C Bonds in Hard Carbon for High-Capacity and Long-Life Li/K-Ion Batteries, Adv. Energy Mater. 9 (2019). https://doi.org/10.1002/aenm.201901676.

[65] G. Liu, X. Wang, G. Han, J. Yu, H. Zhao, Earth abundant colloidal carbon quantum dots for luminescent solar concentrators, Mater. Adv. 1 (2020) 119–138. https://doi.org/10.1039/d0ma00181c.

[66] F. Xie, Z. Xu, Z. Guo, M.M. Titirici, Hard carbons for sodium-ion batteries and beyond, Prog. Energy. 2 (2020). https://doi.org/10.1088/2516-1083/aba5f5.

[67] K. Miijra, H. Nakagawa, K. Hashimoto, 95/05948 Examination of the oxidative stabilization reaction of the pitch-based carbon fiber through continuous measurement of oxygen chemisorption and gas formation rate, Fuel Energy Abstr. 36 (1995) 423. https://doi.org/10.1016/0140-6701(95)97586-9.

[68] Z. Guo, C. Wang, M. Chen, M. Li, Hard carbon derived from coal tar pitch for use as the anode material in lithium ion batteries, Int. J. Electrochem. Sci. 8 (2013) 2702–2709.

[69] H. Fujimoto, K. Tokumitsu, A. Mabuchi, N. Chinnasamy, T. Kasuh, The anode performance of the hard carbon for the lithium ion battery derived from the oxygen-containing aromatic precursors, J. Power

Sources. 195 (2010) 7452–7456. https://doi.org/10.1016/j.jpowsour.2010.05.041.

[70] F. Yu, S. Li, W. Chen, T. Wu, C. Peng, Biomass-Derived Materials for Electrochemical Energy Storage and Conversion: Overview and Perspectives, Energy Environ. Mater. 2 (2019) 55–67. https://doi.org/10.1002/eem2.12030.

[71] M. Muraleedharan Pillai, N. Kalidas, X. Zhao, V.P. Lehto, Biomass-Based Silicon and Carbon for Lithium-Ion Battery Anodes, Front. Chem. 10 (2022) 1–11. https://doi.org/10.3389/fchem.2022.882081.

[72] A. Demirbaş, Biomass resource facilities and biomass conversion processing for fuels and chemicals, Energy Convers. Manag. 42 (2001) 1357–1378. https://doi.org/10.1016/S0196-8904(00)00137-0.

[73] A.C. Caputo, M. Palumbo, P.M. Pelagagge, F. Scacchia, Economics of biomass energy utilization in combustion and gasification plants: Effects of logistic variables, Biomass and Bioenergy. 28 (2005) 35–51. https://doi.org/10.1016/j.biombioe.2004.04.009.

[74] Z. Gao, Y. Zhang, N. Song, X. Li, Biomass-derived renewable carbon materials for electrochemical energy storage, Mater. Res. Lett. 5 (2017) 69–88. https://doi.org/10.1080/21663831.2016.1250834.

[75] S. Kim, B.E. Dale, Life cycle assessment of various cropping systems utilized for producing biofuels: Bioethanol and biodiesel, Biomass and Bioenergy. 29 (2005) 426–439. https://doi.org/10.1016/j.biombioe.2005.06.004.

[76] A. El-Naggar, S.S. Lee, J. Rinklebe, M. Farooq, H. Song, A.K. Sarmah, A.R. Zimmerman, M. Ahmad, S.M. Shaheen, Y.S. Ok, Biochar application to low fertility soils: A review of current status, and future prospects, Geoderma. 337 (2019) 536–554. https://doi.org/10.1016/j.geoderma.2018.09.034.

[77] M.. Tadda, A. Ahsan, A. Shifu, M. ElSergany, T. Arunkumar, B. Jose, M. Razzaque, Abdur, N.. Daud, Nik, A Review on Activated Carbon from Biowaste : Process , Application and Prospects, J. Adv. Civ. Eng. Pract. Res. 5 (2018) 82–83.

[78] E.A. Shalaby, A Review of Selected Non-Edible Biomass Sources as Feedstock for Biodiesel Production, Biofuels - Status Perspect. (2015) 3–20. https://doi.org/10.5772/59178.

[79] E. Porpatham, A. Ramesh, B. Nagalingam, Effect of compression ratio on the performance and combustion of a biogas fuelled spark ignition engine, Fuel. 95 (2012) 247–256. https://doi.org/10.1016/j.fuel.2011.10.059.

[80] A.T. Services, Stauffer Pyrolysis Paper.Pdf, 43 (2003) 29–40.

[81] K.L. Gould, Does Coronary Flow Trump Coronary Anatomy?, JACC Cardiovasc. Imaging. 2 (2009) 1009–1023. https://doi.org/10.1016/j.jcmg.2009.06.004.

[82] A.S. Marriott, A.J. Hunt, E. Bergström, K. Wilson, V.L. Budarin, J. Thomas-Oates, J.H. Clark, R. Brydson, Investigating the structure of biomass-derived non-graphitizing mesoporous carbons by electron energy loss spectroscopy in the transmission electron microscope and X-ray photoelectron spectroscopy, Carbon N. Y. 67 (2014) 514–524. https://doi.org/10.1016/j.carbon.2013.10.024.

[83] A. Primo, P. Atienzar, E. Sanchez, J.M. Delgado, H. García, From biomass wastes to large-area, high-quality, N-doped graphene: Catalyst-free carbonization of chitosan coatings on arbitrary substrates, Chem. Commun. 48 (2012) 9254–9256. https://doi.org/10.1039/c2cc34978g.

[84] T. Tay, S. Ucar, S. Karagöz, Preparation and characterization of activated carbon from waste biomass, J. Hazard. Mater. 165 (2009) 481–485. https://doi.org/10.1016/j.jhazmat.2008.10.011.

[85] M.-M. Titirici, M. Antonietti, Chemistry and materials options of sustainable carbon materials made by hydrothermal carbonization, Chem. Soc. Rev. 39 (2010) 103–116. https://doi.org/10.1039/B819318P.

[86] A.N.A. El-Hendawy, S.E. Samra, B.S. Girgis, Adsorption characteristics of activated carbons obtained from corncobs, Colloids Surfaces A Physicochem. Eng. Asp. 180 (2001) 209–221. https://doi.org/10.1016/S0927-7757(00)00682-8.

[87] O. Norouzi, P. Salimi, F. Di Maria, S.E.M. Pourhosseini, F. Safari, Synthesis and Design of Engineered Biochars as Electrode Materials in Energy Storage Systems, in: 2019: pp. 233–265. https://doi.org/10.1007/978-981-13-3768-0_8.

[88] A. Zoghlami, G. Paës, Lignocellulosic Biomass : Understanding Recalcitrance and Predicting Hydrolysis, 7 (2019). https://doi.org/10.3389/fchem.2019.00874.

[89] H. Yang, R. Yan, H. Chen, D.H. Lee, C. Zheng, Characteristics of hemicellulose, cellulose and lignin pyrolysis, Fuel. 86 (2007) 1781–1788. https://doi.org/10.1016/j.fuel.2006.12.013.

[90] A.A.M. Daifullah, S.M. Yakout, S.A. Elreefy, Adsorption of fluoride in aqueous solutions using KMnO4-modified activated carbon derived from steam pyrolysis of rice straw, J. Hazard. Mater. 147 (2007) 633–643. https://doi.org/10.1016/j.jhazmat.2007.01.062.

[91] O. Ioannidou, A. Zabaniotou, Agricultural residues as precursors for activated carbon production-A review, Renew. Sustain. Energy Rev. 11 (2007) 1966–2005. https://doi.org/10.1016/j.rser.2006.03.013.

[92] S. Kumar, R. Kushwaha, S. Kumar, M.L. Verma, Decongestion of lignocellulosics: a critical assessment of physicochemical approaches, INC, 2022. https://doi.org/10.1016/b978-0-12-822810-4.00009-9.

[93] G. Greco, R.L.S. Canevesi, C. Di Stasi, A. Celzard, V. Fierro, J.J. Manyà, Biomass-derived carbons physically activated in one or two steps for CH4/CO2 separation, Renew. Energy. 191 (2022) 122–133. https://doi.org/10.1016/j.renene.2022.04.035.

[94] D. Prahas, Y. Kartika, N. Indraswati, S. Ismadji, Activated carbon from jackfruit peel waste by H3PO4 chemical activation: Pore structure and surface chemistry characterization, Chem. Eng. J. 140 (2008) 32–42. https://doi.org/10.1016/j.cej.2007.08.032.

[95] M.A. Lillo-Ródenas, J. Juan-Juan, D. Cazorla-Amorós, A. Linares-Solano, About reactions occurring during chemical activation with hydroxides, Carbon N. Y. 42 (2004) 1371–1375. https://doi.org/10.1016/j.carbon.2004.01.008.

[96] S. Zheng, J. Zhang, H. Deng, Y. Du, X. Shi, Chitin derived nitrogen-doped porous carbons with ultrahigh specific surface area and tailored hierarchical porosity for high performance supercapacitors, J. Bioresour. Bioprod. 6 (2021) 142–151. https://doi.org/10.1016/j.jobab.2021.02.002.

[97] J. Wang, P. Nie, B. Ding, S. Dong, X. Hao, H. Dou, X. Zhang, Biomass derived carbon for energy storage devices, J. Mater. Chem. A. 5 (2017) 2411–2428. https://doi.org/10.1039/c6ta08742f.

[98] W. Chen, M. Gong, K. Li, M. Xia, Z. Chen, H. Xiao, Y. Fang, Y. Chen, H. Yang, H. Chen, Insight into KOH activation mechanism during biomass pyrolysis: Chemical reactions between O-containing groups and KOH, Appl. Energy. 278 (2020) 115730. https://doi.org/10.1016/j.apenergy.2020.115730.

[99] J. Deng, M. Li, Y. Wang, Biomass-derived carbon: synthesis and applications in energy storage and conversion, Green Chem. 18 (2016) 4824–4854. https://doi.org/10.1039/C6GC01172A.

[100] W. Luo, B. Wang, C.G. Heron, M.J. Allen, J. Morre, C.S. Maier, W.F. Stickle, X. Ji, Pyrolysis of cellulose under ammonia leads to nitrogen-doped nanoporous carbon generated through methane formation, Nano Lett. 14 (2014) 2225–2229. https://doi.org/10.1021/nl500859p.

[101] P. Salimi, S. Javadian, O. Norouzi, H. Gharibi, Turning an environmental problem into an opportunity: potential use of biochar derived from a harmful marine biomass named Cladophora glomerata as anode electrode for Li-ion batteries, Environ. Sci. Pollut. Res. (2017). https://doi.org/10.1007/s11356-017-0181-1.

[102] B. Joffres, D. Laurenti, N. Charon, A. Daudin, A. Quignard, C. Geantet, Conversion thermochimique de la lignine en carburants et produits chimiques: Une revue, Oil Gas Sci. Technol. 68 (2013) 753–763. https://doi.org/10.2516/ogst/2013132.

[103] L. Jiang, L. Sheng, Z. Fan, Biomass-derived carbon materials with structural diversities and their applications in energy storage, Sci. China Mater. 61 (2018) 133–158. https://doi.org/10.1007/s40843-017-9169-4.

[104] M. Heidari, A. Dutta, B. Acharya, S. Mahmud, A review of the current knowledge and challenges of hydrothermal carbonization for biomass conversion, J. Energy Inst. 92 (2019) 1779–1799. https://doi.org/10.1016/j.joei.2018.12.003.

[105] B. Hu, K. Wang, L. Wu, S.H. Yu, M. Antonietti, M.M. Titirici, Engineering carbon materials from the hydrothermal carbonization process of biomass, Adv. Mater. 22 (2010) 813–828. https://doi.org/10.1002/adma.200902812.

[106] J. González-Arias, M.E. Sánchez, J. Cara-Jiménez, F.M. Baena-Moreno, Z. Zhang, Hydrothermal carbonization of biomass and waste: A review, Environ. Chem. Lett. 20 (2022) 211–221. https://doi.org/10.1007/s10311-021-01311-x.

[107] M.P. Maniscalco, M. Volpe, A. Messineo, Hydrothermal carbonization as a valuable tool for energy and environmental applications: A review, Energies. 13 (2020). https://doi.org/10.3390/en13164098.

[108] M. Liu, F. Wu, Y. Bai, Y. Li, H. Ren, R. Zhao, X. Feng, T. Song, C. Wu, Boosting Sodium Storage Performance of Hard Carbon Anodes by Pore Architecture Engineering, ACS Appl. Mater. Interfaces. 13 (2021) 47671–47683. https://doi.org/10.1021/acsami.1c14738.

[109] L. Xiao, H. Lu, Y. Fang, M.L. Sushko, Y. Cao, X. Ai, H. Yang, J. Liu, Low-Defect and Low-Porosity Hard Carbon with High Coulombic Efficiency and High Capacity for Practical Sodium Ion Battery Anode, Adv. Energy Mater. 8 (2018). https://doi.org/10.1002/aenm.201703238.

[110] G. Zou, H. Hou, C.W. Foster, C.E. Banks, T. Guo, Y. Jiang, Y. Zhang, X. Ji, Advanced Hierarchical Vesicular Carbon Co-Doped with S, P, N for High-Rate Sodium Storage, Adv. Sci. 5 (2018). https://doi.org/10.1002/advs.201800241.

[111] M. Dahbi, T. Nakano, N. Yabuuchi, T. Ishikawa, K. Kubota, M. Fukunishi, S. Shibahara, J.Y. Son, Y.T. Cui, H. Oji, S. Komaba, Sodium carboxymethyl cellulose as a potential binder for hard-carbon negative electrodes in sodium-ion batteries, Electrochem. Commun. 44 (2014) 66–69. https://doi.org/10.1016/j.elecom.2014.04.014.

[112] A. Ponrouch, A.R. Goñi, M.R. Palacín, High capacity hard carbon anodes for sodium ion batteries in additive free electrolyte, Electrochem. Commun. 27 (2013) 85–88. https://doi.org/10.1016/j.elecom.2012.10.038.

[113] J. Ding, H. Zhou, H. Zhang, T. Stephenson, Z. Li, D. Karpuzov, D. Mitlin, Exceptional energy and new insight with a sodium-selenium battery based on a carbon nanosheet cathode and a pseudographite anode, Energy Environ. Sci. 10 (2017) 153–165. https://doi.org/10.1039/c6ee02274j.

[114] M. Kohl, F. Borrmann, H. Althues, S. Kaskel, Hard Carbon Anodes and Novel Electrolytes for Long-Cycle-Life Room Temperature Sodium-Sulfur Full Cell Batteries, Adv. Energy Mater. 6 (2016). https://doi.org/10.1002/aenm.201502185.

[115] X. Wu, S. Yao, Flexible electrode materials based on WO3 nanotube bundles for high performance energy storage devices, Nano Energy. 42 (2017) 143–150. https://doi.org/10.1016/j.nanoen.2017.10.058.

[116] S. Goriparti, E. Miele, F. De Angelis, E. Di Fabrizio, R. Proietti Zaccaria, C. Capiglia, Review on recent progress of nanostructured anode materials for Li-ion batteries, J. Power Sources. 257 (2014) 421–443. https://doi.org/10.1016/j.jpowsour.2013.11.103.

[117] P. Salimi, E. Kowsari, Electrochemical Study of Li-Ion 18650 Cylindrical Rechargeable Cell at Elevated Temperature Using Geminal Dicationic Ionic Liquid as Electrolyte Additive, (2019).

[118] F. Yang, D. Wang, Y. Zhao, K.L. Tsui, S.J. Bae, A study of the relationship between coulombic efficiency and capacity degradation of commercial lithium-ion batteries, Energy. 145 (2018) 486–495. https://doi.org/10.1016/j.energy.2017.12.144.

[119] V. Mullaivananathan, R. Sathish, N. Kalaiselvi, Coir Pith Derived Bio-carbon: Demonstration of Potential Anode Behavior in Lithium-ion Batteries, Electrochim. Acta. 225 (2017) 143–150.

https://doi.org/10.1016/j.electacta.2016.12.086.

[120] U. Gulzar, T. Li, X. Bai, S. Goriparti, R. Brescia, Nitrogen-doped single wall carbon nanohorns enabling effective utilization of Ge nanocrystals for next generation lithium ion batteries, Electrochim. Acta. (2018). https://doi.org/10.1016/j.electacta.2018.11.130.

[121] X. Zhou, F. Chen, T. Bai, B. Long, Q. Liao, Y. Ren, J. Yang, Interconnected highly graphitic carbon nanosheets derived from wheat stalk as high performance anode materials for lithium ion batteries, Green Chem. 18 (2016) 2078–2088. https://doi.org/10.1039/C5GC02122G.

[122] J. Niu, R. Shao, J. Liang, M. Dou, Z. Li, Y. Huang, F. Wang, Biomass-derived mesopore-dominant porous carbons with large specific surface area and high defect density as high performance electrode materials for Li-ion batteries and supercapacitors, Nano Energy. 36 (2017) 322–330. https://doi.org/10.1016/j.nanoen.2017.04.042.

[123] J.H. Um, C.Y. Ahn, J. Kim, M. Jeong, Y.E. Sung, Y.H. Cho, S.S. Kim, W.S. Yoon, From grass to battery anode: Agricultural biomass hemp-derived carbon for lithium storage, RSC Adv. 8 (2018) 32231–32240. https://doi.org/10.1039/c8ra06958a.

[124] P. Salimi, O. Norouzi, S.E.M. Pourhosseini, Two-step synthesis of nanohusk Fe3O4 embedded in 3D network pyrolytic marine biochar for a new generation of anode materials for Lithium-Ion batteries, J. Alloys Compd. 786 (2019) 930–937. https://doi.org/10.1016/j.jallcom.2019.02.048.

[125] C. Choi, S.D. Seo, B.K. Kim, D.W. Kim, Enhanced Lithium Storage in Hierarchically Porous Carbon Derived from Waste Tea Leaves, Sci. Rep. 6 (2016) 1–10. https://doi.org/10.1038/srep39099.

[126] F. Gao, C. Geng, N. Xiao, J. Qu, J. Qiu, Hierarchical porous carbon sheets derived from biomass containing an activation agent and in-built template for lithium ion batteries, Carbon N. Y. 139 (2018) 1085–1092. https://doi.org/10.1016/j.carbon.2018.08.010.

[127] Y. Yao, F. Wu, Naturally derived nanostructured materials from biomass for rechargeable lithium/sodium batteries, Nano Energy. 17 (2015) 91–103. https://doi.org/10.1016/j.nanoen.2015.08.004.

[128] S.J. Yang, M. Antonietti, N. Fechler, Self-Assembly of Metal Phenolic Mesocrystals and Morphosynthetic Transformation toward Hierarchically Porous Carbons, J. Am. Chem. Soc. 137 (2015) 8269–8273. https://doi.org/10.1021/jacs.5b04500.

[129] B. Zhu, K. Li, J. Liu, H. Liu, C. Sun, C.E. Snape, Z. Guo, Nitrogen-enriched and hierarchically porous carbon macro-spheres-ideal for large-scale CO2 capture, J. Mater. Chem. A. 2 (2014) 5481–5489. https://doi.org/10.1039/c4ta00438h.

[130] J. Liu, N.P. Wickramaratne, S.Z. Qiao, M. Jaroniec, Molecular-based design and emerging applications of nanoporous carbon spheres, Nat. Mater. 14 (2015) 763–774. https://doi.org/10.1038/nmat4317.

[131] Z.Y. Sui, Q.H. Meng, J.T. Li, J.H. Zhu, Y. Cui, B.H. Han, High surface area porous carbons produced by steam activation of graphene aerogels, J. Mater. Chem. A. 2 (2014) 9891–9898. https://doi.org/10.1039/c4ta01387e.

[132] F. Guo, X. Jia, S. Liang, X. Jiang, K. Peng, L. Qian, Design and Synthesis of Highly Porous Activated Carbons from Sargassum as Advanced Electrode Materials for Supercapacitors, J. Electrochem. Soc. 166 (2019) A3109–A3118. https://doi.org/10.1149/2.0191914jes.

[133] Y.C. Zhang, Y. You, S. Xin, Y.X. Yin, J. Zhang, P. Wang, X. sheng Zheng, F.F. Cao, Y.G. Guo, Rice husk-derived hierarchical silicon/nitrogen-doped carbon/carbon nanotube spheres as low-cost and high-capacity anodes for lithium-ion batteries, Nano Energy. 25 (2016) 120–127. https://doi.org/10.1016/j.nanoen.2016.04.043.

[134] S.E.M. Pourhosseini, O. Norouzi, P. Salimi, H.R. Naderi, Synthesis of a Novel Interconnected 3D Pore Network Algal Biochar Constituting Iron Nanoparticles Derived from a Harmful Marine Biomass as High-Performance Asymmetric Supercapacitor Electrodes, ACS Sustain. Chem. Eng. 6 (2018) 4746–4758.

https://doi.org/10.1021/acssuschemeng.7b03871.

[135] A.L. Tasca, M. Puccini, Leather tanning: Life cycle assessment of retanning, fatliquoring and dyeing, J. Clean. Prod. 226 (2019) 720–729. https://doi.org/10.1016/j.jclepro.2019.03.335.

[136] M. Parisi, A. Nanni, M. Colonna, Recycling of chrome-tanned leather and its utilization as polymeric materials and in polymer-based composites: A review, Polymers (Basel). 13 (2021) 1–23. https://doi.org/10.3390/polym13030429.

[137] Y.S. Hedberg, C. Lidén, I. Odnevall Wallinder, Chromium released from leather - I: Exposure conditions that govern the release of chromium(III) and chromium(VI), Contact Dermatitis. 72 (2015) 206–215. https://doi.org/10.1111/cod.12329.

[138] M. Ashokkumar, N.T. Narayanan, A.L. Mohana Reddy, B.K. Gupta, B. Chandrasekaran, S. Talapatra, P.M. Ajayan, P. Thanikaivelan, Transforming collagen wastes into doped nanocarbons for sustainable energy applications, Green Chem. 14 (2012) 1689–1695. https://doi.org/10.1039/c2gc35262a.

[139] N. Konikkara, L.J. Kennedy, J.J. Vijaya, Preparation and characterization of hierarchical porous carbons derived from solid leather waste for supercapacitor applications, J. Hazard. Mater. 318 (2016) 173–185. https://doi.org/10.1016/j.jhazmat.2016.06.037.

[140] R. Soni, reaction electrocatalyst derived from waste leather, (2019) 7893–7902. https://doi.org/10.1039/c9nr00977a.

[141] D. Bresser, D. Buchholz, A. Moretti, A. Varzi, S. Passerini, Alternative binders for sustainable electrochemical energy storage-the transition to aqueous electrode processing and bio-derived polymers, Energy Environ. Sci. 11 (2018) 3096–3127. https://doi.org/10.1039/c8ee00640g.

[142] G. Berckmans, M. Messagie, J. Smekens, N. Omar, L. Vanhaverbeke, J. Van Mierlo, Cost projection of state of the art lithium-ion batteries for electric vehicles up to 2030, Energies. 10 (2017). https://doi.org/10.3390/en10091314.

[143] D.L. Wood, J. Li, C. Daniel, Prospects for reducing the processing cost of lithium ion batteries, J. Power Sources. 275 (2015) 234–242. https://doi.org/10.1016/j.jpowsour.2014.11.019.

[144] M. Valvo, A. Liivat, H. Eriksson, C.W. Tai, K. Edström, Iron-Based Electrodes Meet Water-Based Preparation, Fluorine-Free Electrolyte and Binder: A Chance for More Sustainable Lithium-Ion Batteries?, ChemSusChem. 10 (2017) 2431–2448. https://doi.org/10.1002/cssc.201700070.

[145] N. Susarla, S. Ahmed, D.W. Dees, Modeling and analysis of solvent removal during Li-ion battery electrode drying, J. Power Sources. 378 (2018) 660–670. https://doi.org/10.1016/j.jpowsour.2018.01.007.

[146] N.L. Panwar, A. Pawar, Influence of activation conditions on the physicochemical properties of activated biochar: a review, Biomass Convers. Biorefinery. (2020). https://doi.org/10.1007/s13399-020-00870-3.

[147] B. Sajjadi, W.Y. Chen, N.O. Egiebor, A comprehensive review on physical activation of biochar for energy and environmental applications, Rev. Chem. Eng. 35 (2019) 735–776. https://doi.org/10.1515/revce-2017-0113.

[148] H. Wan, X. Hu, Nitrogen doped biomass-derived porous carbon as anode materials of lithium ion batteries, Solid State Ionics. 341 (2019) 115030. https://doi.org/10.1016/j.ssi.2019.115030.

[149] H. Shan, X. Li, Y. Cui, D. Xiong, B. Yan, D. Li, A. Lushington, X. Sun, Sulfur/Nitrogen Dual-doped Porous Graphene Aerogels Enhancing Anode Performance of Lithium Ion Batteries, Electrochim. Acta. 205 (2016) 188–197. https://doi.org/10.1016/j.electacta.2016.04.105.

[150] D. Angin, Effect of pyrolysis temperature and heating rate on biochar obtained from pyrolysis of safflower seed press cake, Bioresour. Technol. 128 (2013) 593–597. https://doi.org/10.1016/j.biortech.2012.10.150.

[151] J.M. de la Rosa, M. Paneque, A.Z. Miller, H. Knicker, Relating physical and chemical properties of four different biochars and their application rate to biomass production of Lolium perenne on a Calcic Cambisol

during a pot experiment of 79 days, Sci. Total Environ. 499 (2014) 175–184. https://doi.org/10.1016/j.scitotenv.2014.08.025.

[152] Y. Liu, Z. He, M. Uchimiya, Comparison of Biochar Formation from Various Agricultural By-Products Using FTIR Spectroscopy, Mod. Appl. Sci. 9 (2015) 246–253. https://doi.org/10.5539/mas.v9n4p246.

[153] B. Ma, Y. Huang, Z. Nie, X. Qiu, D. Su, G. Wang, J. Yuan, X. Xie, Z. Wu, Facile synthesis of: Camellia oleifera shell-derived hard carbon as an anode material for lithium-ion batteries, RSC Adv. 9 (2019) 20424–20431. https://doi.org/10.1039/c9ra03345a.

[154] T.L.P. Dantas, F.M.T. Luna, I.J. Silva, D.C.S. de Azevedo, C.A. Grande, A.E. Rodrigues, R.F.P.M. Moreira, Carbon dioxide-nitrogen separation through adsorption on activated carbon in a fixed bed, Chem. Eng. J. 169 (2011) 11–19. https://doi.org/10.1016/j.cej.2010.08.026.

[155] P. Wang, J. Bai, K. Li, H. Ma, W. Li, X. Zhu, Y. Sun, B. Zhao, NiCo2N hollow sphere with interconnected nanosheets shell: A potential anode material for high performance lithium-ion batteries, Chem. Eng. J. 425 (2021) 130607. https://doi.org/10.1016/j.cej.2021.130607.

[156] S.W. Lee, N. Yabuuchi, B.M. Gallant, S. Chen, B.S. Kim, P.T. Hammond, Y. Shao-Horn, High-power lithium batteries from functionalized carbon-nanotube electrodes, Nat. Nanotechnol. 5 (2010) 531–537. https://doi.org/10.1038/nnano.2010.116.

[157] L.J. Kennedy, T. Ratnaji, N. Konikkara, J.J. Vijaya, Value added porous carbon from leather wastes as potential supercapacitor electrode using neutral electrolyte, J. Clean. Prod. 197 (2018) 930–936. https://doi.org/10.1016/j.jclepro.2018.06.244.

[158] P. González-García, S. Gamboa-González, I. Andrade Martínez, T. Hernández-Quiroz, Preparation of activated carbon from water hyacinth stems by chemical activation with K2CO3 and its performance as adsorbent of sodium naproxen, Environ. Prog. Sustain. Energy. 39 (2020) 1–13. https://doi.org/10.1002/ep.13366.

[159] L. Huang, Y. Sun, W. Wang, Q. Yue, T. Yang, Comparative study on characterization of activated carbons prepared by microwave and conventional heating methods and application in removal of oxytetracycline (OTC), Chem. Eng. J. 171 (2011) 1446–1453. https://doi.org/10.1016/j.cej.2011.05.041.

[160] E. Hao, W. Liu, S. Liu, Y. Zhang, H. Wang, S. Chen, F. Cheng, S. Zhao, H. Yang, Rich sulfur doped porous carbon materials derived from ginkgo leaves for multiple electrochemical energy storage devices, J. Mater. Chem. A. 5 (2017) 2204–2214. https://doi.org/10.1039/C6TA08169J.

[161] C. Marino, J. Cabanero, M. Povia, C. Villevieille, Biowaste Lignin-Based Carbonaceous Materials as Anodes for Na-Ion Batteries, J. Electrochem. Soc. 165 (2018) A1400–A1408. https://doi.org/10.1149/2.0681807jes.

[162] C. Liu, G. Han, Y. Chang, Y. Xiao, M. Li, W. Zhou, D. Fu, W. Hou, Properties of Porous Carbon Derived from Cornstalk Core in High-Performance Electrochemical Capacitors, ChemElectroChem. 3 (2016) 323–331. https://doi.org/10.1002/celc.201500376.

[163] E.M. Lotfabad, J. Ding, K. Cui, A. Kohandehghan, W.P. Kalisvaart, M. Hazelton, D. Mitlin, High-density sodium and lithium ion battery anodes from banana peels, ACS Nano. 8 (2014) 7115–7129. https://doi.org/10.1021/nn502045y.

[164] X. Gu, C.J. Tong, S. Rehman, L.M. Liu, Y. Hou, S. Zhang, Multifunctional Nitrogen-Doped Loofah Sponge Carbon Blocking Layer for High-Performance Rechargeable Lithium Batteries, ACS Appl. Mater. Interfaces. 8 (2016) 15991–16001. https://doi.org/10.1021/acsami.6b02378.

[165] Y. Gong, D. Li, C. Luo, Q. Fu, C. Pan, Highly porous graphitic biomass carbon as advanced electrode materials for supercapacitors, Green Chem. 19 (2017) 4132–4140. https://doi.org/10.1039/c7gc01681f.

[166] S. Qiu, L. Xiao, M.L. Sushko, K.S. Han, Y. Shao, M. Yan, X. Liang, L. Mai, J. Feng, Y. Cao, X. Ai, H. Yang, J. Liu, Manipulating Adsorption–Insertion Mechanisms in Nanostructured Carbon Materials for

High-Efficiency Sodium Ion Storage, Adv. Energy Mater. 7 (2017) 1–11. https://doi.org/10.1002/aenm.201700403.

[167] J. Zhao, Y. Liu, X. Quan, S. Chen, H. Zhao, H. Yu, Nitrogen and sulfur co-doped graphene/carbon nanotube as metal-free electrocatalyst for oxygen evolution reaction: The enhanced performance by sulfur doping, Electrochim. Acta. 204 (2016) 169–175. https://doi.org/10.1016/j.electacta.2016.04.034.

[168] D. GĄSIOR, W.J. TIC, Application of the Biochar-Based Technologies as the Way of Realization of the Sustainable Development Strategy, Econ. Environ. Stud. 17 (2017) 597–611. https://doi.org/10.25167/ees.2017.43.9.

[169] F.L. Braghiroli, H. Bouafif, C.M. Neculita, A. Koubaa, Performance of Physically and Chemically Activated Biochars in Copper Removal from Contaminated Mine Effluents, Water. Air. Soil Pollut. 230 (2019) 1–14. https://doi.org/10.1007/s11270-019-4233-7.

[170] K. Xu, Y. Li, J. Xiong, X. Ou, W. Su, G. Zhong, C. Yang, Activated Amorphous Carbon With High-Porosity Derived From Camellia Pollen Grains as Anode Materials for Lithium/Sodium Ion Batteries, Front. Chem. 6 (2018) 1–10. https://doi.org/10.3389/fchem.2018.00366.

[171] C. Yu, H. Hou, X. Liu, L. Han, Y. Yao, Z. Dai, D. Li, The recovery of the waste cigarette butts for N-doped carbon anode in lithium ion battery, Front. Mater. 5 (2018) 1–9. https://doi.org/10.3389/fmats.2018.00063.

[172] Z. Nie, Y. Huang, B. Ma, X. Qiu, N. Zhang, X. Xie, Z. Wu, Nitrogen-doped Carbon with Modulated Surface Chemistry and Porous Structure by a Stepwise Biomass Activation Process towards Enhanced Electrochemical Lithium-Ion Storage, Sci. Rep. 9 (2019) 1–9. https://doi.org/10.1038/s41598-019-50330-w.

[173] L. Yan, J. Yu, J. Houston, N. Flores, H. Luo, Biomass derived porous nitrogen doped carbon for electrochemical devices, Green Energy Environ. 2 (2017) 84–99. https://doi.org/10.1016/j.gee.2017.03.002.

[174] D. Bhattacharjya, H.Y. Park, M.S. Kim, H.S. Choi, S.N. Inamdar, J.S. Yu, Nitrogen-doped carbon nanoparticles by flame synthesis as anode material for rechargeable lithium-ion batteries, Langmuir. 30 (2014) 318–324. https://doi.org/10.1021/la403366e.

[175] J. Ou, Y. Zhang, L. Chen, H. Yuan, D. Xiao, Heteroatom doped porous carbon derived from hair as an anode with high performance for lithium ion batteries, RSC Adv. 4 (2014) 63784–63791. https://doi.org/10.1039/C4RA12121J.

[176] J. Xiong, Q. Pan, F. Zheng, X. Xiong, C. Yang, D. Hu, C. Huang, N/S Co-doped carbon derived from cotton as high performance anode materials for Lithium ion batteries, Front. Chem. 6 (2018) 1–9. https://doi.org/10.3389/fchem.2018.00078.

[177] X. Sun, X. Wang, N. Feng, L. Qiao, X. Li, D. He, A new carbonaceous material derived from biomass source peels as an improved anode for lithium ion batteries, J. Anal. Appl. Pyrolysis. 100 (2013) 181–185. https://doi.org/10.1016/j.jaap.2012.12.016.

[178] J. Ou, Y. Zhang, L. Chen, Q. Zhao, Y. Meng, Y. Guo, D. Xiao, Nitrogen-rich porous carbon derived from biomass as a high performance anode material for lithium ion batteries, J. Mater. Chem. A. 3 (2015) 6534–6541. https://doi.org/10.1039/C4TA06614F.

[179] B. Campbell, R. Ionescu, Z. Favors, C.S. Ozkan, M. Ozkan, Bio-Derived, Binderless, Hierarchically Porous Carbon Anodes for Li-ion Batteries, Sci. Rep. 5 (2015) 1–9. https://doi.org/10.1038/srep14575.

[180] K. Yu, Y. Wang, X. Wang, W. Liu, J. Liang, C. Liang, Preparation of porous carbon anode materials for lithium-ion battery from rice husk, Mater. Lett. 253 (2019) 405–408. https://doi.org/10.1016/j.matlet.2019.07.126.

[181] P. Yan, F. Ai, C. Cao, Z. Luo, Hierarchically porous carbon derived from wheat straw for high rate lithium ion battery anodes, J. Mater. Sci. Mater. Electron. 30 (2019) 14120–14129. https://doi.org/10.1007/s10854-019-01778-z.

[182] V. Selvamani, R. Ravikumar, V. Suryanarayanan, D. Velayutham, S. Gopukumar, Garlic peel derived high

capacity hierarchical N-doped porous carbon anode for sodium/lithium ion cell, Electrochim. Acta. 190 (2016) 337–345. https://doi.org/10.1016/j.electacta.2016.01.006.

[183] Y. Li, C. Li, H. Qi, K. Yu, C. Liang, Mesoporous activated carbon from corn stalk core for lithium ion batteries, Chem. Phys. 506 (2018) 10–16. https://doi.org/10.1016/j.chemphys.2018.03.027.

[184] W. Chen, D. Xu, S. Kuang, Z. Wu, H. Hu, M. Zheng, X. Yu, Hierarchically porous SiOx/C and carbon materials from one biomass waste precursor toward high-performance lithium/sodium storage, J. Power Sources. 489 (2021) 229459. https://doi.org/10.1016/j.jpowsour.2021.229459.

[185] M. Curcio, S. Brutti, L. Caripoti, A. De Bonis, R. Teghil, Laser irradiation of a bio-waste derived carbon unlocks performance enhancement in secondary lithium batteries, Nanomaterials. 11 (2021). https://doi.org/10.3390/nano11123183.

[186] Y. Li, F. Wang, J. Liang, X. Hu, K. Yu, Preparation of disordered carbon from rice husks for lithium-ion batteries, New J. Chem. 40 (2016) 325–329. https://doi.org/10.1039/C5NJ01970B.

[187] Q. Huang, J. Hu, S. Wen, X. Zhang, G. Liu, S. Chang, Y. Liu, Sulfur-Doped and Bio-Resin-Derived Hard Carbon@rGO Composites as Sustainable Anodes for Lithium-Ion Batteries, Front. Chem. 8 (2020) 1–10. https://doi.org/10.3389/fchem.2020.00241.

[188] M. Drews, J. Büttner, M. Bauer, J. Ahmed, R. Sahu, C. Scheu, S. Vierrath, A. Fischer, D. Biro, Spruce Hard Carbon Anodes for Lithium-Ion Batteries, ChemElectroChem. 8 (2021) 4750–4761. https://doi.org/10.1002/celc.202101174.

[189] X. Lu, K. Xiang, W. Zhou, Y. Zhu, X. Chen, Porous carbons derived from tea-seed shells and their improved electrochemical performance in lithium-ion batteries and supercapacitors, Mater. Technol. 7857 (2018) 1–8. https://doi.org/10.1080/10667857.2018.1466511.

[190] F. Luna-Lama, D. Rodríguez-Padrón, A.R. Puente-Santiago, M.J. Muñoz-Batista, A. Caballero, A.M. Balu, A.A. Romero, R. Luque, Non-porous carbonaceous materials derived from coffee waste grounds as highly sustainable anodes for lithium-ion batteries, J. Clean. Prod. 207 (2019) 411–417. https://doi.org/10.1016/j.jclepro.2018.10.024.

[191] T. Wang, X. Yu, M. Fan, Q. Meng, Y. Xiao, Y.X. Yin, H. Li, Y.G. Guo, Direct regeneration of spent LiFePO4 via a graphite prelithiation strategy, Chem. Commun. 56 (2019) 245–248. https://doi.org/10.1039/c9cc08155k.

[192] W. Wang, Y. Sun, B. Liu, S. Wang, M. Cao, Porous carbon nanofiber webs derived from bacterial cellulose as an anode for high performance lithium ion batteries, Carbon N. Y. 91 (2015) 56–65. https://doi.org/10.1016/j.carbon.2015.04.041.

[193] X. Zhang, X. Du, Y. Yin, N.W. Li, W. Fan, R. Cao, W. Xu, C. Zhang, C. Li, Lithium-Ion Batteries: Charged by Triboelectric Nanogenerators with Pulsed Output Based on the Enhanced Cycling Stability, ACS Appl. Mater. Interfaces. 10 (2018) 8676–8684. https://doi.org/10.1021/acsami.7b18736.

[194] J. Ahn, S. Yoon, S.G. Jung, J.H. Yim, K.Y. Cho, A conductive thin layer on prepared positive electrodes by vapour reaction printing for high-performance lithium-ion batteries, J. Mater. Chem. A. 5 (2017) 21214–21222. https://doi.org/10.1039/c7ta05591a.

[195] Y. Abe, N. Hori, S. Kumagai, Electrochemical impedance spectroscopy on the performance degradation of LiFePO4/graphite lithium-ion battery due to charge-discharge cycling under different c-rates, Energies. 12 (2019) 1–14. https://doi.org/10.3390/en12234507.

[196] W. Tang, Y. Zhang, Y. Zhong, T. Shen, X. Wang, X. Xia, J. Tu, Natural biomass-derived carbons for electrochemical energy storage, Mater. Res. Bull. (2016). https://doi.org/10.1016/j.materresbull.2016.12.025.

[197] P. Salimi, S. Tieuli, S. Taghavi, E. Venezia, S. Fugattini, S. Lauciello, M. Prato, S. Marras, T. Li, M. Signoretto, P. Costamagna, R. Proietti Zaccaria, Sustainable lithium-ion batteries based on Metals-free

tannery waste biochar, Green Chem. (2022). https://doi.org/10.1039/d1gc04772h.

[198] M.S. Zafar, M. Zahid, A. Athanassiou, D. Fragouli, Biowaste-Derived Carbonized Bone for Solar Steam Generation and Seawater Desalination, Adv. Sustain. Syst. 5 (2021). https://doi.org/10.1002/adsu.202100031.

[199] D.A. Teigiserova, L. Hamelin, M. Thomsen, Towards transparent valorization of food surplus, waste and loss: Clarifying definitions, food waste hierarchy, and role in the circular economy, Sci. Total Environ. 706 (2020) 136033. https://doi.org/10.1016/j.scitotenv.2019.136033.

[200] J. Niu, R. Shao, M. Liu, Y. Zan, M. Dou, J. Liu, Z. Zhang, Y. Huang, F. Wang, Porous Carbons Derived from Collagen-Enriched Biomass: Tailored Design, Synthesis, and Application in Electrochemical Energy Storage and Conversion, Adv. Funct. Mater. 29 (2019) 1–23. https://doi.org/10.1002/adfm.201905095.

[201] J. Niu, R. Shao, J. Liang, M. Dou, Z. Li, Y. Huang, F. Wang, Biomass-derived mesopore-dominant porous carbons with large specific surface area and high defect density as high performance electrode materials for Li-ion batteries and supercapacitors, Nano Energy. 36 (2017) 322–330. https://doi.org/10.1016/j.nanoen.2017.04.042.

[202] J. Christensen, J. Newman, Stress generation and fracture in lithium insertion materials, J. Solid State Electrochem. 10 (2006) 293–319. https://doi.org/10.1007/s10008-006-0095-1.

[203] A. Benítez, D. Di Lecce, G.A. Elia, Á. Caballero, J. Morales, J. Hassoun, A Lithium-Ion Battery using a 3 D-Array Nanostructured Graphene–Sulfur Cathode and a Silicon Oxide-Based Anode, ChemSusChem. 11 (2018) 1512–1520. https://doi.org/10.1002/cssc.201800242.

[204] A. Boskey, N. Pleshko Camacho, FT-IR imaging of native and tissue-engineered bone and cartilage, Biomaterials. 28 (2007) 2465–2478. https://doi.org/10.1016/j.biomaterials.2006.11.043.

[205] M.P.M. Marques, D. Gonçalves, A.P. Mamede, T. Coutinho, E. Cunha, W. Kockelmann, S.F. Parker, L.A.E. Batista de Carvalho, Profiling of human burned bones: oxidising versus reducing conditions, Sci. Rep. 11 (2021) 1–13. https://doi.org/10.1038/s41598-020-80462-3.

[206] G. Gunawan, A. Arifin, I. Yani, M. Indrajaya, Characterization of porous hydroxyapatite-alumina composite scaffold produced via powder compaction method, IOP Conf. Ser. Mater. Sci. Eng. 620 (2019). https://doi.org/10.1088/1757-899X/620/1/012107.

[207] U.E. Pazzaglia, T. Congiu, M. Raspanti, F. Ranchetti, D. Quacci, Anatomy of the intracortical canal system: Scanning electron microscopy study in rabbit femur, Clin. Orthop. Relat. Res. 467 (2009) 2446–2456. https://doi.org/10.1007/s11999-009-0806-x.

[208] M. Figueiredo, A. Fernando, G. Martins, J. Freitas, F. Judas, H. Figueiredo, Effect of the calcination temperature on the composition and microstructure of hydroxyapatite derived from human and animal bone, Ceram. Int. 36 (2010) 2383–2393. https://doi.org/10.1016/j.ceramint.2010.07.016.

[209] J. Deng, M. Li, Y. Wang, Biomass-derived carbon: synthesis and applications in energy storage and conversion, Green Chem. (2016). https://doi.org/10.1039/C6GC01172A.

[210] S.W. Han, D.W. Jung, J.H. Jeong, E.S. Oh, Effect of pyrolysis temperature on carbon obtained from green tea biomass for superior lithium ion battery anodes, Chem. Eng. J. 254 (2014) 597–604. https://doi.org/10.1016/j.cej.2014.06.021.

[211] Z. Parviz, P. Salimi, S. Javadian, H. Gharibi, A. Morsali, E. Bayat, L. Leoncino, S. Lauciello, R.P. Zaccaria, Fabrication of Sustainable Hybrid MOF/Silica Electrodes for Current Lithium-ion Batteries and Beyond, (2022). https://doi.org/10.1021/acsaem.2c02821.

[212] J. Feng, N.A. Chernova, F. Omenya, L. Tong, A.C. Rastogi, M. Stanley Whittingham, Effect of electrode charge balance on the energy storage performance of hybrid supercapacitor cells based on LiFePO4 as Li-ion battery electrode and activated carbon, J. Solid State Electrochem. 22 (2018) 1063–1078. https://doi.org/10.1007/s10008-017-3847-1.

[213] M. Kwiecien, Electrochemical Impedance Spectroscopy on Lead-Acid Cells during Aging, (2019) 1–14.

[214] J. Xu, R.D. Deshpande, J. Pan, Y.-T. Cheng, V.S. Battaglia, Electrode Side Reactions, Capacity Loss and Mechanical Degradation in Lithium-Ion Batteries, J. Electrochem. Soc. 162 (2015) A2026–A2035. https://doi.org/10.1149/2.0291510jes.

[215] S. Brutti, J. Hassoun, B. Scrosati, C.Y. Lin, H. Wu, H.W. Hsieh, A high power Sn-C/C-LiFePO 4 lithium ion battery, J. Power Sources. 217 (2012) 72–76. https://doi.org/10.1016/j.jpowsour.2012.05.102.

[216] M.S. Balogun, W. Qiu, Y. Luo, H. Meng, W. Mai, A. Onasanya, T.K. Olaniyi, Y. Tong, A review of the development of full cell lithium-ion batteries: The impact of nanostructured anode materials, Nano Res. 9 (2016) 2823–2851. https://doi.org/10.1007/s12274-016-1171-1.

[217] X. Zhang, V. Aravindan, P.S. Kumar, H. Liu, J. Sundaramurthy, S. Ramakrishna, S. Madhavi, Synthesis of TiO2 hollow nanofibers by co-axial electrospinning and its superior lithium storage capability in full-cell assembly with olivine phosphate, Nanoscale. 5 (2013) 5973–5980. https://doi.org/10.1039/c3nr01128c.

[218] G.N. Zhu, L. Chen, Y.G. Wang, C.X. Wang, R.C. Che, Y.Y. Xia, Binary Li4Ti5O12-Li2Ti 3O7 nanocomposite as an anode material for Li-ion batteries, Adv. Funct. Mater. 23 (2013) 640–647. https://doi.org/10.1002/adfm.201201741.

[219] A. Varzi, D. Bresser, J. Von Zamory, F. Müller, S. Passerini, ZnFe2O4-C/LiFePO4-CNT: A novel high-power lithium-ion battery with excellent cycling performance, Adv. Energy Mater. 4 (2014). https://doi.org/10.1002/aenm.201400054.

[220] Y. Ma, R. Younesi, R. Pan, C. Liu, J. Zhu, B. Wei, K. Edström, Constraining Si Particles within Graphene Foam Monolith: Interfacial Modification for High-Performance Li+ Storage and Flexible Integrated Configuration, Adv. Funct. Mater. 26 (2016) 6797–6806. https://doi.org/10.1002/adfm.201602324.

[221] S. Choi, Y.G. Cho, J. Kim, N.S. Choi, H.K. Song, G. Wang, S. Park, Mesoporous Germanium Anode Materials for Lithium-Ion Battery with Exceptional Cycling Stability in Wide Temperature Range, Small. 13 (2017) 1–10. https://doi.org/10.1002/smll.201603045.

[222] Z.P. Cano, D. Banham, S. Ye, A. Hintennach, J. Lu, M. Fowler, Z. Chen, Batteries and fuel cells for emerging electric vehicle markets, Nat. Energy. 3 (2018) 279–289. https://doi.org/10.1038/s41560-018-0108-1.

[223] W. Li, R. Long, H. Chen, J. Geng, A review of factors in fl uencing consumer intentions to adopt battery electric vehicles, Renew. Sustain. Energy Rev. 78 (2017) 318–328. https://doi.org/10.1016/j.rser.2017.04.076.

[224] J. Hassoun, B. Scrosati, A High-Performance Polymer Tin Sulfur Lithium Ion Battery, Angew. Chemie. 122 (2010) 2421–2424. https://doi.org/10.1002/ange.200907324.

[225] Z.H. Chen, X.L. Du, J.B. He, F. Li, Y. Wang, Y.L. Li, B. Li, S. Xin, Porous coconut shell carbon offering high retention and deep lithiation of sulfur for lithium-sulfur batteries, ACS Appl. Mater. Interfaces. 9 (2017) 33855–33862. https://doi.org/10.1021/acsami.7b09310.

[226] Y. Su, Challenges and Prospects of Lithium À Sulfur Batteries, 46 (2013) 1125–1134.

[227] F. Xu, X. Li, F. Xiao, S. Xu, X. Zhang, P. He, H. Zhou, A battery with sulphur cathode and lithiated graphite anode based on Lithium shuttle reaction, Mater. Technol. 31 (2016) 517–520. https://doi.org/10.1080/10667857.2016.1196564.

[228] B. Uzakbaiuly, A. Mentbayeva, A. Konarov, I. Kurmanbayeva, Y. Zhang, Z. Bakenov, Evaluating Sulfur-Composite Cathode Material with Lithiated Graphite Anode in Coin Cell and Pouch Cell Configuration, Front. Energy Res. 8 (2020) 1–8. https://doi.org/10.3389/fenrg.2020.595481.

[229] J. Jiang, Q. Fan, S. Chou, Z. Guo, K. Konstantinov, H. Liu, J. Wang, Li2S-Based Li-Ion Sulfur Batteries: Progress and Prospects, Small. 1903934 (2019) 1–24. https://doi.org/10.1002/smll.201903934.

[230] L. Lin, F. Liang, K. Zhang, H. Mao, J. Yang, Y. Qian, Lithium phosphide/lithium chloride coating on lithium for advanced lithium metal anode, J. Mater. Chem. A. 6 (2018) 15859–15867. https://doi.org/10.1039/c8ta05102j.

[231] L. Carbone, J. Peng, M. Agostini, M. Gobet, M. Devany, B. Scrosati, S. Greenbaum, J. Hassoun, Carbon Composites for a High-Energy Lithium–Sulfur Battey with a Glyme-Based Electrolyte, ChemElectroChem. 4 (2017) 209–215. https://doi.org/10.1002/celc.201600586.

[232] Biomass-based materials in Li-S, (n.d.).

[233] D. Su, D. Zhou, C. Wang, G. Wang, Toward High Performance Lithium–Sulfur Batteries Based on Li2S Cathodes and Beyond: Status, Challenges, and Perspectives, Adv. Funct. Mater. 28 (2018) 1–23. https://doi.org/10.1002/adfm.201800154.

[234] A. Manthiram, Y. Fu, S. Chung, C. Zu, Y. Su, Rechargeable Lithium − Sulfur Batteries, (2014).

[235] A. Hayashi, R. Ohtsubo, M. Tatsumisago, Electrochemical performance of all-solid-state lithium batteries with mechanochemically activated Li2S-Cu composite electrodes, Solid State Ionics. 179 (2008) 1702–1705. https://doi.org/10.1016/j.ssi.2008.03.008.

[236] Z. Li, S. Zhang, C. Zhang, K. Ueno, T. Yasuda, R. Tatara, K. Dokko, M. Watanabe, One-pot pyrolysis of lithium sulfate and graphene nanoplatelet aggregates: In situ formed Li2S/graphene composite for lithium-sulfur batteries, Nanoscale. 7 (2015) 14385–14392. https://doi.org/10.1039/c5nr03201f.

[237] H. El-Shinawi, E.J. Cussen, S.A. Corr, A facile synthetic approach to nanostructured Li2S cathodes for rechargeable solid-state Li-S batteries, Nanoscale. 11 (2019) 19297–19300. https://doi.org/10.1039/c9nr06239d.

[238] G. Tan, R. Xu, Z. Xing, Y. Yuan, J. Lu, J. Wen, C. Liu, L. Ma, C. Zhan, Q. Liu, T. Wu, Z. Jian, R. Shahbazian-Yassar, Y. Ren, D.J. Miller, L.A. Curtiss, X. Ji, K. Amine, Burning lithium in CS2 for high-performing compact Li2S–graphene nanocapsules for Li–S batteries, Nat. Energy. 2 (2017) 1–10. https://doi.org/10.1038/nenergy.2017.90.

[239] H. Jha, I. Buchberger, X. Cui, S. Meini, H.A. Gasteiger, Li-S Batteries with Li 2 S Cathodes and Si/C Anodes , J. Electrochem. Soc. 162 (2015) A1829–A1835. https://doi.org/10.1149/2.0681509jes.

[240] Z. Li, Y. Kamei, M. Haruta, T. Takenaka, A. Tomita, T. Doi, S. Zhang, K. Dokko, M. Inaba, M. Watanabe, Si/li2s battery with solvate ionic liquid electrolyte, Electrochemistry. 84 (2016) 887–890. https://doi.org/10.5796/electrochemistry.84.887.

[241] L. Borchardt, M. Oschatz, S. Kaskel, Carbon Materials for Lithium Sulfur Batteries - Ten Critical Questions, Chem. - A Eur. J. 22 (2016) 7324–7351. https://doi.org/10.1002/chem.201600040.

[242] N.A. Cañas, K. Hirose, B. Pascucci, N. Wagner, K.A. Friedrich, R. Hiesgen, Investigations of lithium-sulfur batteries using electrochemical impedance spectroscopy, Electrochim. Acta. 97 (2013) 42–51. https://doi.org/10.1016/j.electacta.2013.02.101.

[243] F. Ye, H. Noh, H. Lee, H.T. Kim, An Ultrahigh Capacity Graphite/Li2S Battery with Holey-Li2S Nanoarchitectures, Adv. Sci. 5 (2018) 1–8. https://doi.org/10.1002/advs.201800139.

[244] Y. Chen, S. Lu, Y. Li, W. Qin, X. Wu, A high-performance Li 2 S/MnO 2 rechargeable battery, Mater. Lett. 248 (2019) 157–160. https://doi.org/10.1016/j.matlet.2019.04.018.

[245] Z. Wang, N. Zhang, M. Yu, J. Liu, S. Wang, J. Qiu, Boosting redox activity on MXene-induced multifunctional collaborative interface in high Li2S loading cathode for high-energy Li-S and metallic Li-free rechargeable batteries, J. Energy Chem. 37 (2019) 183–191. https://doi.org/10.1016/j.jechem.2019.03.012.

[246] J. Hassoun, B. Scrosati, A high-performance polymer tin sulfur lithium ion battery, Angew. Chemie - Int. Ed. 49 (2010) 2371–2374. https://doi.org/10.1002/anie.200907324.

[247] S. Wang, H. Chen, Z. Zhong, X. Hou, S. Hu, J. Wu, Graphene-decorated sphere Li2S composite prepared by spray drying method as cathode for lithium-sulfur full cell, Ionics (Kiel). 24 (2018) 3385–3392. https://doi.org/10.1007/s11581-018-2493-7.

[248] P. Salimi, O. Norouzi, S.E.M. Pourhoseini, P. Bartocci, A. Tavasoli, F. Di Maria, S.M. Pirbazari, G. Bidini, F. Fantozzi, Magnetic biochar obtained through catalytic pyrolysis of macroalgae: A promising anode material for Li-ion batteries, Renew. Energy. 140 (2019) 704–714. https://doi.org/10.1016/j.renene.2019.03.077.

[249] P. Salimi, K. Askari, O. Norouzi, Improving the Electrochemical Performance of Carbon Anodes Derived from Marine Biomass by Using Ionic-Liquid-Based Hybrid Electrolyte for LIBs, 3 (2018).

[250] K.M. Lynch, E.J. Steffen, E.K. Arendt, Brewers' spent grain: a review with an emphasis on food and health, J. Inst. Brew. 122 (2016) 553–568. https://doi.org/10.1002/jib.363.

[251] R. dos S.M. Thiago, P.M. de M. Pedro, F.C.S. Eliana, Solid wastes in brewing process: A review, J. Brew. Distill. 5 (2014) 1–9. https://doi.org/10.5897/jbd2014.0043.

[252] C. Kerby, F. Vriesekoop, An overview of the utilisation of brewery by-products as generated by british craft breweries, Beverages. 3 (2017). https://doi.org/10.3390/beverages3020024.

[253] S. Huang, Z. Li, B. Wang, J. Zhang, Z. Peng, R. Qi, J. Wang, Y. Zhao, N-Doping and Defective Nanographitic Domain Coupled Hard Carbon Nanoshells for High Performance Lithium/Sodium Storage, Adv. Funct. Mater. 28 (2018) 1–10. https://doi.org/10.1002/adfm.201706294.

[254] W. Yu, H. Wang, S. Liu, N. Mao, X. Liu, J. Shi, W. Liu, S. Chen, X. Wang, N, O-codoped hierarchical porous carbons derived from algae for high-capacity supercapacitors and battery anodes, J. Mater. Chem. A. 4 (2016) 5973–5983. https://doi.org/10.1039/C6TA01821A.

[255] J. Brückner, S. Thieme, F. Böttger-Hiller, I. Bauer, H.T. Grossmann, P. Strubel, H. Althues, S. Spange, S. Kaskel, Carbon-based anodes for lithium sulfur full cells with high cycle stability, Adv. Funct. Mater. 24 (2014) 1284–1289. https://doi.org/10.1002/adfm.201302169.

[256] L. Jin, C. Shen, Q. Wu, A. Shellikeri, J. Zheng, C. Zhang, J.P. Zheng, Pre-Lithiation Strategies for Next-Generation Practical Lithium-Ion Batteries, Adv. Sci. 2005031 (2021) 1–21. https://doi.org/10.1002/advs.202005031.

[257] M. Lu, W. Yu, J. Shi, W. Liu, S. Chen, X. Wang, H. Wang, Self-doped carbon architectures with heteroatoms containing nitrogen, oxygen and sulfur as high-performance anodes for lithium- and sodium-ion batteries, Electrochim. Acta. 251 (2017) 396–406. https://doi.org/10.1016/j.electacta.2017.08.131.

[258] J.M. de la Rosa, M. Paneque, A.Z. Miller, H. Knicker, Relating physical and chemical properties of four different biochars and their application rate to biomass production of Lolium perenne on a Calcic Cambisol during a pot experiment of 79 days, Sci. Total Environ. 499 (2014) 175–184. https://doi.org/10.1016/j.scitotenv.2014.08.025.

[259] X. Lian, Z. Sun, Q. Mei, Y. Yi, J. Zhou, M.H. Rümmeli, J. Sun, Biomass Template Derived Boron/Oxygen Co-Doped Carbon Particles as Advanced Anodes for Potassium-Ion Batteries, Energy Environ. Mater. 5 (2022) 344–352. https://doi.org/10.1002/eem2.12183.

[260] J. Tu, L. Hu, S. Jiao, J. Hou, H. Zhu, Core–shell Si–N-doped C assembled via an oxidative template for lithium-ion anodes, Phys. Chem. Chem. Phys. 15 (2013) 18549. https://doi.org/10.1039/c3cp52777h.

[261] S. Wacharasindhu, S. Likitmaskul, L. Punnakanta, K. Chaichanwatanakul, K. Angsusingha, C. Tuchinda, Serum IGF-I and IGFBP-3 Levels for Normal Thai Children and their Usefulness in Clinical Practice, J. Med. Assoc. Thail. 81 (1998) 420–430.

[262] M. Gao, K. Zou, Y. Deng, Z. Zhao, Y. Li, G. Chen, An Unprecedented Case: A Low Specific Surface Area Anatase/N-Doped Carbon Nanocomposite Derived from a New Single Source Precursor Affords Fast and Stable Lithium Storage, ACS Appl. Mater. Interfaces. 9 (2017) 28527–28536.

https://doi.org/10.1021/acsami.7b07869.

[263] W. Luo, C. Bommier, Z. Jian, X. Li, R. Carter, S. Vail, Y. Lu, J.J. Lee, X. Ji, Low-surface-area hard carbon anode for Na-ion batteries via graphene oxide as a dehydration agent, ACS Appl. Mater. Interfaces. 7 (2015) 2626–2631. https://doi.org/10.1021/am507679x.

[264] Y. Li, S. Xu, X. Wu, J. Yu, Y. Wang, Y.S. Hu, H. Li, L. Chen, X. Huang, Amorphous monodispersed hard carbon micro-spherules derived from biomass as a high performance negative electrode material for sodium-ion batteries, J. Mater. Chem. A. 3 (2015) 71–77. https://doi.org/10.1039/c4ta05451b.

[265] L. Carbone, M. Gobet, J. Peng, M. Devany, B. Scrosati, S. Greenbaum, J. Hassoun, Polyethylene glycol dimethyl ether (PEGDME)-based electrolyte for lithium metal battery, J. Power Sources. 299 (2015) 460–464. https://doi.org/10.1016/j.jpowsour.2015.08.090.

[266] X. Zhang, C. Fan, P. Xiao, S. Han, Effect of vinylene carbonate on electrochemical performance and surface chemistry of hard carbon electrodes in lithium ion cells operated at different temperatures, Electrochim. Acta. 222 (2016) 221–231. https://doi.org/10.1016/j.electacta.2016.10.149.

[267] N. Wang, N. Zhao, C. Shi, E. Liu, C. He, F. He, L. Ma, In situ synthesized Li2S@porous carbon cathode for graphite/Li2S full cells using ether-based electrolyte, Electrochim. Acta. 256 (2017) 348–356. https://doi.org/10.1016/j.electacta.2017.10.053.

[268] F. Ye, M. Liu, X. Yan, J. Li, Z. Pan, H. Li, Y. Zhang, In Situ Electrochemically Derived Amorphous-Li2S for High Performance Li2S/Graphite Full Cell, Small. 14 (2018) 1–7. https://doi.org/10.1002/smll.201703871.

[269] D. Lv, P. Yan, Y. Shao, Q. Li, S. Ferrara, H. Pan, G.L. Graff, B. Polzin, C. Wang, J.G. Zhang, J. Liu, J. Xiao, High performance Li-ion sulfur batteries enabled by intercalation chemistry, Chem. Commun. 51 (2015) 13454–13457. https://doi.org/10.1039/c5cc05171a.

[270] P. Zeng, Y. Han, X. Duan, G. Jia, L. Huang, Y. Chen, A stable graphite electrode in superconcentrated LiTFSI-DME/DOL electrolyte and its application in lithium-sulfur full battery, Mater. Res. Bull. 95 (2017) 61–70. https://doi.org/10.1016/j.materresbull.2017.07.018.

[271] D.I. Lee, H.-W. Yang, W.S. Kang, J. Kim, S.-J. Kim, Optimal Condition of Solid-Electrolyte-Interphase Prepared by Controlled Prelithiation for High Performance Li-Ion Batteries, J. Electrochem. Soc. 166 (2019) A787–A792. https://doi.org/10.1149/2.1201904jes.

[272] Z. Li, S. Zhang, S. Terada, X. Ma, K. Ikeda, Y. Kamei, C. Zhang, K. Dokko, M. Watanabe, Promising Cell Configuration for Next-Generation Energy Storage: Li2S/Graphite Battery Enabled by a Solvate Ionic Liquid Electrolyte, ACS Appl. Mater. Interfaces. 8 (2016) 16053–16062. https://doi.org/10.1021/acsami.6b03736.

[273] S. Thieme, J. Brückner, A. Meier, I. Bauer, K. Gruber, J. Kaspar, A. Helmer, H. Althues, M. Schmuck, S. Kaskel, A lithium-sulfur full cell with ultralong cycle life: Influence of cathode structure and polysulfide additive, J. Mater. Chem. A. 3 (2015) 3808–3820. https://doi.org/10.1039/c4ta06748g.

[274] M. Agostini, J. Hassoun, J. Liu, M. Jeong, H. Nara, T. Momma, T. Osaka, Y.K. Sun, B. Scrosati, A lithium-ion sulfur battery based on a carbon-coated lithium-sulfide cathode and an electrodeposited silicon-based anode, ACS Appl. Mater. Interfaces. 6 (2014) 10924–10928. https://doi.org/10.1021/am4057166.

[275] K. Zhang, L. Wang, Z. Hu, F. Cheng, J. Chen, Ultrasmall Li2S nanoparticles anchored in graphene nanosheets for high-energy lithium-ion batteries, Sci. Rep. 4 (2014) 1–7. https://doi.org/10.1038/srep06467.

[276] T. Takeuchi, H. Kageyama, K. Nakanishi, T. Ohta, A. Sakuda, T. Sakai, H. Kobayashi, H. Sakaebe, K. Tatsumi, Z. Ogumi, Application of graphite-solid electrolyte composite anode in all-solid-state lithium secondary battery with Li2S positive electrode, Solid State Ionics. 262 (2014) 138–142. https://doi.org/10.1016/j.ssi.2013.09.046.

[277] R.K. Bhardwaj, H. Lahan, V. Sekkar, B. John, A.J. Bhattacharyya, High-Performance Li-Metal-Free Sulfur

Battery Employing a Lithiated Anatase TiO2 Anode and a Freestanding Li2S-Carbon Aerogel Cathode, ACS Sustain. Chem. Eng. 10 (2022) 410–420. https://doi.org/10.1021/acssuschemeng.1c06581.

[278] J. Zhang, J. Wang, M. Qian, B. Zhao, R. Wang, X. Hao, X. Huang, R. Shao, Z. Xing, J. Xie, B. Xu, Y. Su, F. Wu, G. Tan, Lithiothermic-Synchronous Construction of Mo-Li2S-Graphene Nanocomposites for High-Energy Li2S//Si-C Battery, Adv. Funct. Mater. 32 (2022) 1–9. https://doi.org/10.1002/adfm.202108305.

[279] M. Tutak, J. Brodny, Renewable energy consumption in economic sectors in the EU-27. The impact on economics, environment and conventional energy sources. A 20-year perspective, J. Clean. Prod. 345 (2022). https://doi.org/10.1016/j.jclepro.2022.131076.

[280] D. Tong, D.J. Farnham, L. Duan, Q. Zhang, N.S. Lewis, K. Caldeira, S.J. Davis, Geophysical constraints on the reliability of solar and wind power worldwide, Nat. Commun. 12 (2021) 1–12. https://doi.org/10.1038/s41467-021-26355-z.

[281] A. Masias, J. Marcicki, W.A. Paxton, Opportunities and Challenges of Lithium Ion Batteries in Automotive Applications, ACS Energy Lett. 6 (2021) 621–630. https://doi.org/10.1021/acsenergylett.0c02584.

[282] F.C. Krause, J.P. Ruiz, S.C. Jones, E.J. Brandon, E.C. Darcy, C.J. Iannello, R. V. Bugga, Performance of Commercial Li-Ion Cells for Future NASA Missions and Aerospace Applications, J. Electrochem. Soc. 168 (2021) 040504. https://doi.org/10.1149/1945-7111/abf05f.

[283] L. Wang, Z. Schnepp, M.M. Titirici, Rice husk-derived carbon anodes for lithium ion batteries, J. Mater. Chem. A. 1 (2013) 5269. https://doi.org/10.1039/c3ta10650k.

[284] P. Salimi, K. Askari, O. Norouzi, Improving the Electrochemical Performance of Carbon Anodes Derived from Marine Biomass by Using Ionic-Liquid-Based Hybrid Electrolyte for LIBs, 48 (2019) 951–963. https://doi.org/10.1007/s11664-018-6826-0.

[285] W. Lv, F. Wen, J. Xiang, J. Zhao, L. Li, L. Wang, Z. Liu, Y. Tian, Peanut shell derived hard carbon as ultralong cycling anodes for lithium and sodium batteries, Electrochim. Acta. 176 (2015) 533–541. https://doi.org/10.1016/j.electacta.2015.07.059.

[286] I. Kovalenko, B. Zdyrko, A. Magasinski, B. Hertzberg, Z. Milicev, R. Burtovyy, I. Luzinov, G. Yushin, A Major Constituent of Brown Algae for Use in High-Capacity Li-Ion Batteries, Science (80-.). 334 (2011) 75–79. https://doi.org/10.1126/science.1209150.

[287] H. Parsimehr, A. Ehsani, S.A. Payam, Electrochemical energy storage electrodes from rice biochar, Biomass Convers. Biorefinery. (2022). https://doi.org/10.1007/s13399-021-02089-2.

[288] S. Marzeddu, A. Cappelli, A. Ambrosio, M.A. Décima, P. Viotti, M.R. Boni, A life cycle assessment of an energy-biochar chain involving a gasification plant in Italy, Land. 10 (2021). https://doi.org/10.3390/land10111256.

[289] E. Sierocinski, F. Holzinger, J.F. Chenot, Ivy leaf (Hedera helix) for acute upper respiratory tract infections: an updated systematic review, Eur. J. Clin. Pharmacol. 77 (2021) 1113–1122. https://doi.org/10.1007/s00228-021-03090-4.

[290] R.W.F. Cameron, J. Taylor, M. Emmett, A Hedera green façade - Energy performance and saving under different maritime-temperate, winter weather conditions, Build. Environ. 92 (2015) 111–121. https://doi.org/10.1016/j.buildenv.2015.04.011.

[291] W. Vercruysse, J. Smeets, T. Haeldermans, B. Joos, A. Hardy, P. Samyn, J. Yperman, K. Vanreppelen, R. Carleer, P. Adriaensens, W. Marchal, D. Vandamme, Biochar from raw and spent common ivy: Impact of preprocessing and pyrolysis temperature on biochar properties, J. Anal. Appl. Pyrolysis. 159 (2021) 105294. https://doi.org/10.1016/j.jaap.2021.105294.

[292] P. Salimi, E. Venezia, S. Taghavi, S. Tieuli, L. Carbone, M. Prato, M. Signoretto, J. Qiu, R. Proietti Zaccaria, Lithium-Metal Free Sulfur Battery Based on Waste Biomass Anode and Nano-Sized Li2S Cathode, Energy Environ. Mater. (2022) 1–9. https://doi.org/10.1002/eem2.12567.

[293] L. Zhou, D.L. Danilov, F. Qiao, J. Wang, H. Li, R.A. Eichel, P.H.L. Notten, Sulfur Reduction Reaction in Lithium–Sulfur Batteries: Mechanisms, Catalysts, and Characterization, Adv. Energy Mater. 2202094 (2022). https://doi.org/10.1002/aenm.202202094.

[294] T. Haeldermans, M.A. Lataf, G. Vanroelen, P. Samyn, D. Vandamme, A. Cuypers, K. Vanreppelen, S. Schreurs, Numerical prediction of the mean residence time of solid materials in a pilot-scale rotary kiln, Powder Technol. 354 (2019) 392–401. https://doi.org/10.1016/j.powtec.2019.06.008.

[295] American Standard of Testing Material, Standard Test Method for Total Ash Content of Activated Carbon, Astm D 2866-11. 15 (2011) 1–2. https://doi.org/10.1520/D2866-11.2.

[296] G. Vázquez, G. Antorrena, J. Gonzalez, S. Freire, FTIR, 1H and 13C NMR characterization of acetosolv-solubilized pine and eucalyptus lignins, Holzforschung. 51 (1997) 158–166. https://doi.org/10.1515/hfsg.1997.51.2.158.

[297] Z. Yang, H. Peng, W. Wang, T. Liu, Crystallization behavior of poly(ε-caprolactone)/layered double hydroxide nanocomposites, J. Appl. Polym. Sci. 116 (2010) 2658–2667. https://doi.org/10.1002/app.

[298] G. Bekiaris, G. Koutrotsios, P.A. Tarantilis, C.S. Pappas, G.I. Zervakis, FTIR assessment of compositional changes in lignocellulosic wastes during cultivation of Cyclocybe cylindracea mushrooms and use of chemometric models to predict production performance, J. Mater. Cycles Waste Manag. 22 (2020) 1027–1035. https://doi.org/10.1007/s10163-020-00995-7.

[299] G. Müller, C. Schöpper, H. Vos, A. Kharazipour, A. Polle, FTIR-ATR spectroscopic analyses of changes in wood properties during particleand fibreboard production of hardand softwood trees, BioResources. 4 (2009) 49–71. https://doi.org/10.15376/biores.4.1.49-71.

[300] A.M. Raspolli Galletti, A. D'Alessio, D. Licursi, C. Antonetti, G. Valentini, A. Galia, N. Nassi O Di Nasso, Midinfrared FT-IR as a tool for monitoring herbaceous biomass composition and its conversion to furfural, J. Spectrosc. 2015 (2015). https://doi.org/10.1155/2015/719042.

[301] T. Haeldermans, J. Claesen, J. Maggen, R. Carleer, J. Yperman, P. Adriaensens, P. Samyn, D. Vandamme, A. Cuypers, K. Vanreppelen, S. Schreurs, Microwave assisted and conventional pyrolysis of MDF – Characterization of the produced biochars, J. Anal. Appl. Pyrolysis. 138 (2019) 218–230. https://doi.org/10.1016/j.jaap.2018.12.027.

[302] P. Salimi, O. Norouzi, S.E.M. Pourhoseini, P. Bartocci, A. Tavasoli, F. Di Maria, S.M. Pirbazari, G. Bidini, F. Fantozzi, Magnetic biochar obtained through catalytic pyrolysis of macroalgae: A promising anode material for Li-ion batteries, Renew. Energy. 140 (2019) 704–714. https://doi.org/10.1016/j.renene.2019.03.077.

[303] H. Moon, A. Innocenti, H. Liu, H. Zhang, M. Weil, M. Zarrabeitia, S. Passerini, Bio-Waste-Derived Hard Carbon Anodes Through a Sustainable and Cost-Effective Synthesis Process for Sodium-Ion Batteries, ChemSusChem. (2022). https://doi.org/10.1002/cssc.202201713.

[304] C. Quan, R. Su, N. Gao, Preparation of activated biomass carbon from pine sawdust for supercapacitor and CO2 capture, Int. J. Energy Res. 44 (2020) 4335–4351. https://doi.org/10.1002/er.5206.

[305] H. Xie, Z. Wu, Z. Wang, N. Qin, Y. Li, Y. Cao, Z. Lu, Solid electrolyte interface stabilization via surface oxygen species functionalization in hard carbon for superior performance sodium-ion batteries, J. Mater. Chem. A. 8 (2020) 3606–3612. https://doi.org/10.1039/c9ta12429b.

[306] A. Tomczyk, Z. Sokołowska, P. Boguta, Biochar physicochemical properties: pyrolysis temperature and feedstock kind effects, Rev. Environ. Sci. Biotechnol. 19 (2020) 191–215. https://doi.org/10.1007/s11157-020-09523-3.

[307] S. Guo, Y. Chen, L. Shi, Y. Dong, J. Ma, X. Chen, H. Song, Nitrogen-doped biomass-based ultra-thin carbon nanosheets with interconnected framework for High-Performance Lithium-Ion Batteries, Appl. Surf. Sci. 437 (2018) 136–143. https://doi.org/10.1016/j.apsusc.2017.12.144.

[308] P. Salimi, S. Javadian, O. Norouzi, H. Gharibi, Turning an environmental problem into an opportunity: potential use of biochar derived from a harmful marine biomass named Cladophora glomerata as anode electrode for Li-ion batteries, Environ. Sci. Pollut. Res. 24 (2017) 27974–27984. https://doi.org/10.1007/s11356-017-0181-1.

[309] X. Lin, Y. Liu, H. Tan, B. Zhang, Advanced lignin-derived hard carbon for Na-ion batteries and a comparison with Li and K ion storage, Carbon N. Y. 157 (2020) 316–323. https://doi.org/10.1016/j.carbon.2019.10.045.

[310] Y. Morikawa, S. ichi Nishimura, R. ichi Hashimoto, M. Ohnuma, A. Yamada, Mechanism of Sodium Storage in Hard Carbon: An X-Ray Scattering Analysis, Adv. Energy Mater. 10 (2020) 1–9. https://doi.org/10.1002/aenm.201903176.

[311] K. Yu, J. Li, H. Qi, C. Liang, High-capacity activated carbon anode material for lithium-ion batteries prepared from rice husk by a facile method, Diam. Relat. Mater. (2018). https://doi.org/10.1016/j.diamond.2018.04.019.